A Thesis Submitted for the Degree of PhD at the University of Warwick

Characterisation of Order/Disorder in Mixed Metal Oxide Catalyst Materials by Reverse Monte Carlo Modelling of X-ray and Neutron Total Scattering

By

Aron C. N. Summer

Thesis

Submitted to the University of Warwick

for the degree of

Doctor of Philosophy in Analytical Science

Department of Chemistry

March 2023

Table of Contents

Table of Figures

Acknowledgements

A great deal of thanks goes to my supervisor Richard Walton for his guidance, understanding and endless effort over the last 6 years which has been vital during these troubled years and required for the ultimate completion of this thesis.

Secondly my appreciation goes to my second supervisor, Helen Playford who assisted a great deal in understanding and application of Total scattering data reduction and RMCProfile. Without her keen insights and tutoring at key times the data analysis aspect of this work would have been insurmountable.

Third I would like to thank the MAS-CDT staff and students past and present, a great deal of community was felt which certainly helped to make Warwick University a second home. Additional thanks goes directly to Steven Brown and Elanor Edwards who were vital in allowing me to take a year away from the university during Covid-19 restrictions to take the opportunity to fill a temporary industrial role at Johnson Matthey which has ultimately led to permanent employment.

Additional thanks also goes to the greater Walton group (past and present) with specific thanks going to James Annis and Lucy McLeod for their assistance during beamtime and valuable office/coffee discussions.

I am grateful for the understanding and flexibility of my team at Johnson Matthey, in particular Hoi Jobson who’s fully supported a flexible working routine to allow for the completion of this Thesis. Special thanks also goes to Lucy McLeod here as well for not so subtly hinting I should apply for the temporary role at Johnson Matthey.

Special thanks goes to my partner Ronnie who’s been a source of stability in uncertain times and has constantly helped keep me afloat during the completion of this Thesis while progressing my career.

Lastly, I am eternally grateful to my daughter Alice who’s shown compassion and understanding during these long years.

Declaration

This thesis is submitted to the University of Warwick in support of my application for the degree of Doctor of Philosophy. It has been entirely composed by myself and has not been submitted in any previous application for any degree.

The work presented (including data generated and data analysis) was carried out by the author except in the cases outlined below:

- Several cerium zirconium oxide samples studied were provided by Janet Fisher at Johnson Matthey, a full list is provided in Chapter 2.
- Sample synthesis, preparation and data collection of neutron diffraction data relating to the Ce containing TiO_2 samples discussed in Chapter 5 were undertaken by Juliana de Lima and Richard Walton predating the start of this work.

Work relating to Chapter 3 of this thesis have been published by the author:

A. Summer, H. Y. Playford, L. R. Owen, J. M. Fisher, A. Kolpin, D. Thompsett and R. I. Walton, *APL Mater.*, 2023, **11**, 031113.

Abstract

A deep dive into structural disorder of cerium zirconium oxides relevant for catalysis is undertaken focusing on a reverse Monte Carlo approach driven by total scattering X-ray and neutron data collected at synchrotron facilities. Cation nano-domains and interstitial oxygen are discovered after a atomic scale solid solution $Ce_{0.75}Zr_{0.25}O_2$ material is is heated to 1050 °C under H_2 paired with a subsequent reoxidation via heating under air at 400 °C. An overall loss of oxygen storage capacity is observed and rationalised as consequence of the nanoscale cation segregation clearly outweighs the beneficial properties of the inclusion of interstitial oxygen.

In another reverse Monte Carlo study relating to stoichiometric ceria zirconia it is shown that synthesis route dramatically impacts the presence and types of local cation structures observed as shown by Clapp configuration analysis. A statistical approach to characterising local structures within face centred cubic atomic arrangements. For the first time a κ-$CeZrO_4$ phase, prepared by reduction at 1050 °C followed by oxidation at 400 °C, is modelled via a large box reverse Monte Carlo approach revealing significant cation and oxide disorder. The disorder relating to the cation sites are characterised and shown to be a heavily defected pyrochlore-like cation ordering. The oxide lattice disorder is shown to be myriad with significant concentrations of interstitial sites occupied, split sites and more generalised anisotropy within the oxide lattice present, shining light on the origins of the high oxygen storage capacity associated to κ-$CeZrO_4$ materials prepared at relatively low reduction temperatures.

The $Ce_{0.5}Zr_{0.5}O_2$ transition to pyrochlore ordering at ~1000+ °C is observed in an in-situ X-ray pair distribution study and shows a distinct mis-alignment between changes in the local structure and the average cation ordered structure that is determined form the super lattice Bragg reflections.

Chapter 1: Introduction and Background

1.1 Crystalline materials

All materials are made up of constituent atoms, ions, or molecules, and when these sub-units are arranged in a 3-dimensional repeating structure the material is defined as a crystalline material. In the cases where there is no repeating structure present such as the case with gases, most liquids[1], and certain solids such as glass or wood, these materials are known as amorphous. While the use of the term “crystalline” can be traced back to the 14th century the understanding that crystal like materials adopt shapes based on the arrangement of their sub-units was only introduced in the late 17th century by Kepler looking at snowflake shapes[2] and Hooke who noted that the various shapes of flint shards could be explained by close packed globules in a rhombohedral arrangement, he also identified a cubic structure for sea-salt and Sal-gem (Rock-salt),[3] both now commonly known to be the rock-salt structure.

This description of close packed globule sub-units crudely described the repeating atomic arrangements now known as unit cells and came prior to the first modern atomistic model[4] introduced by John Dalton in the 1800’s which eventually led to Erwin Schrödinger’s quantum mechanical model[5] of the atom in 1926 which is still used today.

While the original 14th century term ‘crystalline’ (crystal like) and the observations of Johannes Kepler and Robert Hooke in the late 17th century were based on the external shape/appearance of a material, the modern definition is entirely based on the repeating atomic structure of a material. This repeating atomic structures can be on the micrometres or even nanometres in scale with no “crystal like” features visible to the eye and is the case for crystalline powders or polycrystalline materials which show no clear relationship to the shape of their atomic scale arrangement. This makes modern crystallography the study of internal atomic order, and not the exclusive study of gemstones.

Unit cells form the base repeating unit of crystalline materials fundamentally describing a repeating arrangement of atoms. Unit cells are comprised of 3D atomic coordinates within a symmetry constrained volume of variable dimensions, with the shape and symmetry of this volume dictating which of the 230 crystallographic space groups[6] represents it.

While the idea of crystalline materials had been recorded as early as the 14th century it wasn't until 1895 when Röntgen discovered and initially characterised an unknown type of radiation, referred to as 'X-rays' by him for the sake of brevity. The characterisation of X-rays led directly to Sommerfeld calculating the approximate wavelength of X-rays in 1912 fulfilling the final criteria for von Laue's[7] initial theory of crystal diffraction, subsequently proven experimentally by Friedrich and Knippling. It would be the interpretations and experiments of William Lawrence Bragg and his father by the end of 1913 that would prove that X-rays had more than a single discrete wavelength[8] and go on to construct the first X-ray ionisation spectrometer[9] forming the beginning X-ray diffraction today.[10]

1.1.1 Local structure and defects

While a crystalline material is defined by having a repeating 3-dimensional structure, it is common for materials to contain defects where the repeating crystalline structure is imperfect. It is well known that the types and magnitudes of defects present in a material have significant impact on the physical properties, such as textile strength, plasticity, thermal stability, and catalytic activity.

Crystalline defects[11–13] can be broadly characterised as point defects[12], line defects, surface defects and volume defects. Some common examples of point defects include missing atoms forming vacancy sites or atoms occupying otherwise unoccupied interstitial sites, substitutional defects can also occur when considering additional atomic species, which can either be from impurities or intentionally doped into the material. When stochimetricly matched vacancies occur with cation and anion pairs it is known as otherwise known as Schottky defect. When an atom present in the material shifts to an interstitial site forming a vacancy in the process it is known as a Frenkel defect[14]. Point defects usually distort or shift their local environment causing inhomogeneous strain but otherwise do little to disrupt the overall crystalline order of a system. Solid solutions, where two or more atom species share the same crystallographic site are an example of substitution defects where (in)homogeneity of the atomic species does not provide a uniquely ordered arrangement. Various point defects are illustrated in Figure 1.1.

Line defects can be further broken down into edge defects or screw defects, both of which can significantly disrupt the crystalline order in one or more lattice plane. Edge defects occur where partial rows of atoms are inserted or absent from the structure, causing the material to expand or contract resulting in a break or shift of crystalline order in an otherwise homogeneous material. Screw defects are a result of sheer strain applied over a cutting plane of the material, resulting in two parts partially sliding out of phase resulting in a region of bridging between two planes of atoms. Line defects are 1 dimensional and do not fully disrupt the crystalline order of a material alone but are likely to impact the crystalline order of specific crystal planes.

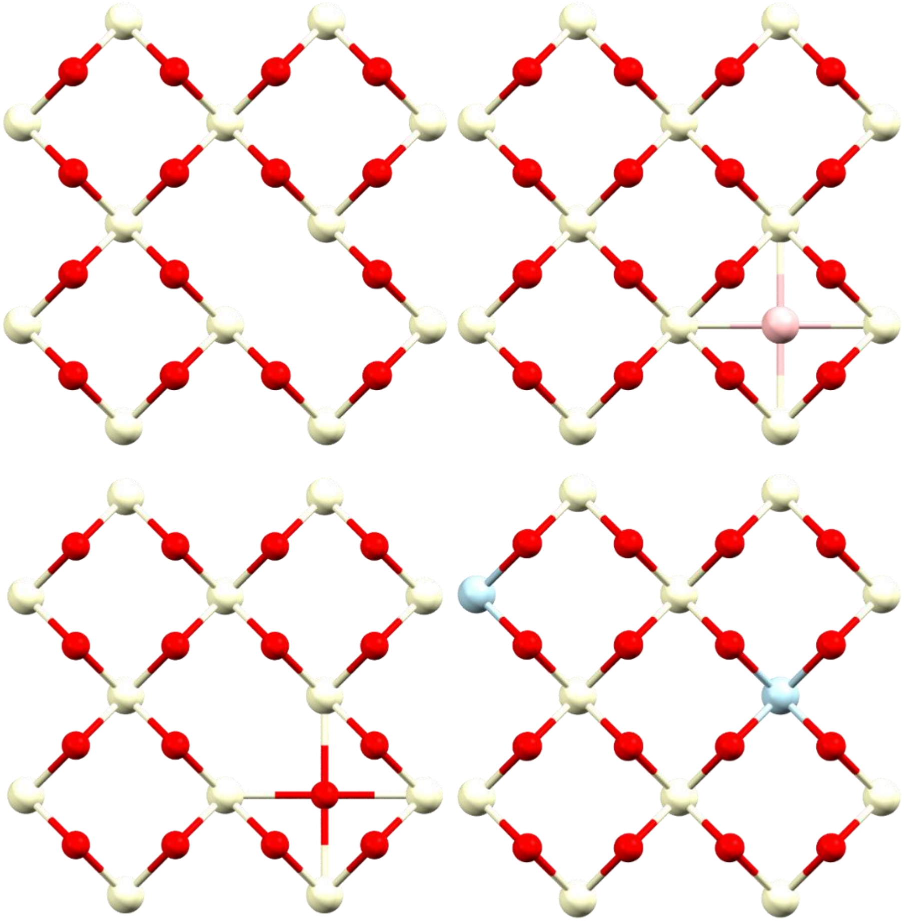

Figure 1.1: Four examples of point defects; atomic vacancies (top left); interstitial insertion of a foreign atom (top right); shift of native atom to an interstitial site, Frenkel defects (bottom left); atomic substitutions of a native atom with a foreign atom (bottom right).

Surface defects can be further subdivided into two types, material surface defects and grain boundary defects. Material surface defects are where the surface of a crystalline domain is exposed to the environment where additional surface chemistry, not described by the crystalline order of the material, may occur such as oxide termination in the case of most metals. The grain boundary is where two or more crystallites within a single particle terminate, the crystallites are not in alignment so cannot be considered a single crystalline domain even if their relative crystalline order is otherwise identical. Some level of surface defects is expected as no material is infinite, however some extreme examples of surface defects can further disrupt the crystalline order within a crystallite, such as stacking faults found in graphite, where a 2-dimensional plane can shift out of phase along the 3rd dimension causing a break in crystalline order of that plane. Figure 1.2

shows visual examples of a line defect (edge) and a surface defect (grain boundary).

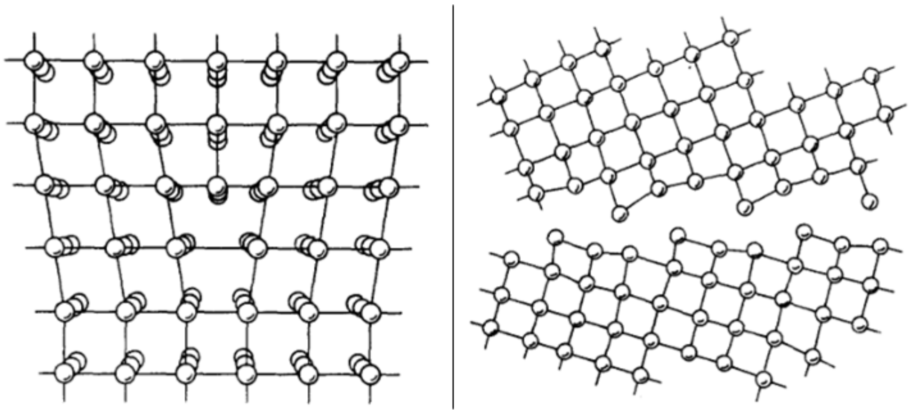

Figure 1.2: Graphical depictions of a dislocation edge type line defect (left) and grain boundary type surface defect (right) in a simple cubic system, taken from Gleiter, 1989.[15]

Volume defects describe when a cluster of atoms are missing from a structure, forming a pore or void within the material. It is important to distinguish that some crystalline materials have voids or pores described within their crystalline structure, and as such aren't considered a crystal defect. Some examples of materials with voids or pores as part of the defined crystal structure are zeolites and Metal-Organic Frameworks (MOF's) often studied for their numerous applications including catalysis,[16] gas storage,[17] molecular sieves[18] and nuclear waste stabilisation[19], properties often closely tied to the size and shapes of the voids present.

When solid solution materials such as $Ce_{1-x}Zr_xO_2$ are considered, an additional form of order/disorder must be addressed based not on individual point defects or the inclusion or omission of matter but rather the relative occupancies of otherwise crystal graphically equivalent atomic sites on a scale too short to observe Bragg diffraction. Such as the formation of sub-nanometre domains of cation rich volumes, or short-range structures comprised of specific cations.

A similar form of local scale disorder is that of an atomic split site, where an atom has significant probabilities of existing in either of two sites, these sites are distinct but too close in proximity to be simultaneously occupied. The average structure would describe both sites as having some value of occupancy without consideration of the local impact of which site was occupied, but rather an average blur of the effect of both true local structures overlaid.

For real materials defects are fundamentally part of structure as the perfectly crystalline assumption is that of a material that perfectly repeats its atomic order infinitely, which is a truly unachievable assumption. As such defects in their various forms can occur on much larger than trace scale while preserving the average structure making a clear case for the importance of combining local and average structure characterisation techniques to properly study the property/structure relationship of any material.[15,20–24]

1.1.2 Properties and local structure

The properties of a material are intrinsically tied to the local atomic and average structure and as such defects play a major role on the observed properties of a material.[23–25] It is not uncommon to observe two materials with identical compositions and near-identical average structures but drastically different properties. This may cause confusion and irreproducibility in properties; one example relevant to this thesis is that of the various phases of cerium zirconium oxide materials, where the sample history and synthesis route[26] is often credited with observed differences in properties unexplained by the average structure model.[27–30]

To complicate this, functional materials often have crystallite-size-dependant properties[15,31] which is often credited to the increased surface area of the material, however surface area alone often falls short in explaining the differences in properties[32].

1.2 Investigating short range order

While the emphasis on the characterisation of short range order is gaining increasing attention in materials science, the characterisation of local vs average structure remains a significant challenge. Different analytical techniques each have their limitations and sensitivities which intrinsically convolve the results they produce. While cross technique studies are a powerful tool, they also have the strong potential to produce misleading results if the technique dependant convolutions are not properly understood.

Classical diffraction-based techniques focus entirely on the relatively sharp, pronounced Bragg peaks, which reflects the bulk average repeating structural information of the material. A sole focus on these features results in the exclusion of the broad low intensity diffuse scattering which contains local structure information. Bragg diffraction modelling techniques such as Pawley fitting or Rietveld modelling simulate a diffraction pattern based on the periodic crystal structure using a least squares[33] matrix minimalisation approach and are fundamentally limited to description of an "average" model by the small-box periodic nature of the method. Rietveld analysis software packages such as TOPAS[34] and GSAS2[35] have developed significantly now including the iterative modelling of various forms of crystal phenomenon, such as stacking faults and anisotropic crystallite shapes, however due to the limitations intrinsically included by the small box modelling method their inability to tackle local scale deviations such as nano-scale inhomogeneity remains.

This exclusive focus on the Bragg features of the diffraction pattern has caused one of the greatest strengths of diffraction techniques, their sensitivity to the crystalline structure of a material, to effectively overshadow the additional structural information captured in the data which is often discounted as background noise. Total scattering[36–38] experiments aim to extract the full scattering characteristics of a material via meticulous data processing and extraction of known instrumental convolutions and artifacts, such as sample environment and air scatter leaving only the sample dependant scattering for analysis. This processed pattern can be Fourier transformed[39–41] to obtain a pair distribution function (PDF) that represents all atom-atom correlation distances present in the sample. While obtaining the PDF of a material requires rigorous data processing, the PDF itself is expressed in real-space, as a plot of atomic pair scattering intensity by pair-distance for all atom-atom pairs within the sample. This means the PDF is an easily interpretable local structure weighted function of the atom-atom pairings of the material studied. Common approaches to the analysis of PDF data for crystalline solids is the comparison to simulated patterns based on average structure, using fitting software such as PDFgui[42] which uses a small box fitting approach similar to the Rietveld method but with symmetry constraints relaxed. While the Total scattering technique and PDF have been introduced here in context of crystalline materials, it's important to acknowledge that the technique can be applied to non-crystalline materials and even molecular substances[43]. Indeed the history of the method is founded in non-crystalline materials, namely amorphous glasses and liquids where information of the first shell atomic correlations could be extracted from diffraction data void of Bragg peaks or well defined features, recognised previously as the radial distribution function[44–47].

X-ray Absorption Spectroscopy (XAS) techniques such as X-ray absorption near edge structure (XANES) and X-ray absorption fine structure (XAFS) are intrinsically elementally specific techniques capable of shining insight into the local electronic structure of a material. Information relating to oxidation states and coordination environments of the first, second or third coordination shell are extractable given ideal data and processing. These methods are intrinsically elemental specific and are limited by the mean free path of the electron excited from the probed atom, providing a highly convolved depiction of the local structure of a specific element present.

In materials chemistry, one can only discuss local structure for so long before mentioning transmission electron microscopy (TEM) and atomic force microscopy[48] (AFM) due to their intrinsically local scale imaging of materials. These incredibly powerful tools are commonly used for aiding in the visualisation of materials on the nano-scale. When sufficiently high resolution is achieved TEM and AFM have been used to observe grain boundaries and crystalline order.[15,49] While these techniques are powerful tools, they are fundamentally very low volume surface techniques and do little to shine insight into the bulk material or average local environments. TEM instruments also have the benefit of being easily equipped with a detector for electron diffraction[49] (ED) experiments, providing the potential for a true local scale diffraction experiment of single crystallites. However, due to the complexity of sample preparation, instrumental use, data collection and data analysis, ED has seen comparably limited application in the broader research community than its X-ray and neutron counterparts. A core limitation of microscopy methods is the extensive sample preparation required and the truly tiny volumes of sample studied, causing significant potential for sampling bias, such as micro-scale sample inhomogeneity and human bias relating to which images are recorded.

Nuclear magnetic resonance (NMR) is another spectroscopic technique capable of local structure insight allowing for the determination and characterisation of elementally specific inequivalent local environments. While NMR can be applied to a great many materials, the experiment requires the specific nuclei of interest to possess a non-zero nuclear spin. One common example of a relevant element which is difficult to study with NMR is oxygen, which requires isotropic enrichment (^{17}O) to receive meaningful experimental signal. One example of a material with no naturally occurring isotopes with non-zero magnetic spin is cerium, which is one of the key elements studied within this thesis.

While experimental data form the backbone of scientific understanding, atomic scale structural modelling methods such as density functional theory (DFT) have been increasingly applied to materials science in recent years. While the application and scope of DFT is extensive, it is limited in scale by computational cost often requiring extensive computer clusters or access to super computer facilities such as ARCHER UK National Supercomputing Service[50] to stretch the scope of the simulation out of the 100-1000 atom range.

Recent advances and interest in the Monte Carlo modelling methods[22,51–55] used in predictive models to capture the effects of randomness on a system, routinely used for weather forecasts and stock market predictions. The Monte Carlo method at its core is an iterative process where some portions of ‘bad’ moves are allowed to enable the method to overcome false minimal without explicit user input. The whole model is then run a multitude of times where the key outputs of the whole set can be read as a probability distribution.

The application of the reverse Monte Carlo[56] (RMC) method to study materials where the ‘goal’ is defined by experimental data and the starting model is semi-randomised has seen increased interest in recent years. RMC software packages such as RMCProfile[57] have seen significant development and are capable of modelling non-symmetry constrained structures of 20,000+ atoms, fitting to various forms of data from the atomic supercell configuration and using the Monte Carlo method to drive minimalisation of the observed vs calculated difference from multiple experimental datasets, allowing for a combined local and average structure approach. This makes use of the contrasting sensitivity of multiple techniques and probes. The RMCProfile fitting remains computationally cheap enabling it's use on personal computers even when addressing structures upwards of 216,000 Å^3 (60 Å × 60 Å × 60 Å) with over 20,000 atoms encouraging continued growth of its use in materials science research.[58]

While a range of techniques are available for the study of local structure, the focus of the work undertaken in this thesis was the application of diffraction-based techniques for the simultaneous study of average and local structure of mixed metal oxides.

1.3 Diffraction

While the discovery of X-rays and observation of their scattering from crystal planes was the summation of the work of several scientists, it was work of William Lawrence Bragg that would show the conditions for Bragg peaks, the constructive interference between the incident wavelength (λ), lattice interplanar spacing (d) and the incident angle (Θ), in Bragg's law below, n is any integer.

$$n\lambda = 2dsin(\theta)$$

Bragg's law shows the relationship between incident (probe) wavelength (λ) used and the of crystal spacings (d), allowing for different crystal spacings to be probed by varying incident angle Θ, or incident wavelength λ. Experimentally however most diffractometer instruments have access to only a single X-ray source or wavelength (or subset thereof for cathode tubes) at a time such as Cu (K-α, λ = 1.5406 Å; K-α2 λ = 1.5444 Å; K-β, λ = 1.3922 Å) so varying diffraction angle is by far the most common approach.

1.3.1 Choice of diffraction probe

Diffraction of a wave-probe from the interspacing of atoms within a structure may be the foundations of why diffraction techniques provide atomic scale structural information, the choice of wave-probe used is equally important. X-rays are often the most readily available as X-ray lab sources are commercially available. Neutrons can offer a contrasting elemental sensitivity and electrons can be used to perform diffraction on single crystallites within a polycrystalline sample. While electron diffraction can be a powerful tool, it was excluded due to the intrinsically non-ambient nature of the data collection where key research questions in this thesis relate to oxide disorder, so environments which would would likely reduce the samples studied during data collection would make the data collected inherently incompatible with ambient/near ambient environment data collection of X-rays and neutrons.

While elemental sensitivity is important, the purpose of the data collection must also be addressed. When probing local disorder it is of paramount importance that the low intensity broad oscillations in the data be captured with a high degree of certainty, these data collections are referred to as total scattering experiments and aim to collect a wide range of data with good resolution on the environmental and sample environments through extra data collections of the empty sample container and instrument allowing for all non-sample scattering to be subtracted from the data. This range is usually expressed in terms of Q where Q is the momentum transfer of the incident probe upon diffraction. Q_{max} refers to the maximum measurable Q range; the units for Q are Å^{-1}.

$$Q = \left(4.\frac{\pi}{\lambda}\right).\sin(\theta)$$

Q has the merit of being independent of incident wavelength, shorter wavelengths provide a larger accessible Q range which is vital for total scattering experiments. All of the diffraction data shown in this thesis are presented in d spacing as it has the dual benefit of structurally related physical meaning and removal of the wavelength dependence of the presented data, Q and d have the following relationship.

$$Q = \frac{2\pi}{d}$$

1.3.1.1 X-rays

X-ray sources are easily available on laboratory scale for Bragg scattering experiments and are commercially available with a range of elemental targets such as Cu, Ni, Co, Mo and Ag each with different X-ray flux and wavelengths. While good resolution and X-ray flux can be achieved on laboratory scale, when total scattering experiments are the focus, most laboratory X-ray sources fail to provide meaningful Q_{max} ranges.

Ag and Mo sources can produce a Q_{max} ~17 Å^{-1}, where the I15-1 XPDF beamline at the Diamond Light Source (DLS) routinely provides a Q_{max} of 28 Å^{-1} and Polaris a total scattering neutron diffractometer at the ISIS neutron and muon source routinely measure data to a Q_{max} of 40 Å^{-1} and above.

Synchrotron X-ray sources such as the Diamond Light Source (DLS) or the European Synchrotron Radiation Facility (ESRF) can generate X-rays with much lower wavelengths allowing a larger Q_{max}. X-rays however are limited in practice due to electron scattering form factor falloff and the limited elemental sensitivity. Due to X-rays scattering from electron density, X-rays also reach a relative sensitivity limitation when investigating materials with similar electron counts. Additional difficulties are experienced when studying materials where the electron count difference is large between the elements, such as CeO_2 (Ce = 58, O = 8) where the X-ray scattering from the element with the larger electron density dominates the observed data.

1.3.1.2 Neutrons

Neutrons were first discovered by Chadwick in 1932 and were first used in a diffraction experiment by Wollan in 1945, then again by Shull in 1946 at the Oak Ridge graphite reactor. Together they established the basic principles of neutron diffraction and proved it as a valuable tool for investigating magnetic moments and crystal structures.[59]

Neutron diffraction is used in a similar manner to X-ray diffraction to determine and understand the atomic structure of materials via diffraction.

While X-rays diffract from the electron density of a material, neutrons diffract from the nucleus which give rise to several valuable differences[60]; neutron scattering length is not a function of electron count/density, is isotopically sensitive and is also scattered by magnetic moments. The magnitude of scattering can be positive or negative, allowing for "null scattering alloys" which generate no coherent neutron scattering making them essentially neutron invisible. $Ti_{0.67}Zr_{0.33}$ is one example of a null scattering alloy which is already finding applications in neutron diffraction. The neutron diffraction work undertaken in this thesis used exclusively near-neutron transparent vanadium sample cans, which have an exceptionally low negative coherent bound scattering length.

While X-ray diffraction can be a readily accessible technique afforded by the availability of lab scale X-ray diffractometers, the same cannot be said for neutron diffraction due to the difficulties and hazards associated to the generation of neutrons for research. Neutrons for research are generated via two types of sources, spallation source (SNS, ISIS, J-PARC) which generate neutrons by colliding a high energy proton beam with a Tungsten target causing the spallation of neutrons from the target, and reactor sources (ILL, NIST) which use nuclear fission to generate neutrons.

Due to the use of a particle accelerator which can easily generated "packets" of particles, spallation neutron sources are often pulsed allowing for time-of-flight (TOF) data collection based on the speed of the neutron diffracted which allows for a high accessible Q-max which is highly beneficial for total scattering experiments.

Reactor sources (ILL, NIST), use nuclear fission to generate a neutron beam with high flux and a wide spread of wavelengths, resulting in the need to monochromate the neutron beam prior to use in diffraction instruments. TOF data collection can be performed at a reactor neutron source but requires a precisely timed physical block of the white-light neutron beam, this is generally less efficient than use of a monochromator and often cannot accommodate for the high energy neutrons. This results in a lower effective

Q-max at a reactor source than a spallation source due to the loss of higher wavelength thermal neutrons.

All neutron diffraction data discussed in this thesis was collected on the Polaris instrument at the ISIS neutron and muon source.[61]

1.4 Materials

Cerium oxide has been a material of keen interest in the scientific literature due to its highly accessible Ce^{3+} to Ce^{4+} redox properties enabling effective storage of oxygen, or oxygen storage capacity (OSC).[32,62–65] The beneficial OSC and accessible redox properties of CeO_2 lend themselves to a multitude of applications from it’s well established roles in air purification[66] and three way catalysis[63] to the less known applications in the water gas shift reaction, photocatalysis[67], solid oxide fuel cells[68], and potential biomedical applications as a antimicrobial agent[69] and as a reactive hydroxide radial scavenger[70,71] and sunscreen UV shielding[72] among many other emerging applications. The literature surrounding CeO_2 is exceedingly large with constant new applications in a wide range of fields. Indeed the review article by Montini *et al.* in 2016[67] focussing on CeO_2 applications in catalysis alone was 26 pages long with 660 references cited; another review article by Devaiah in 2018[26] focusing on synthesis methods and applications of ceria zirconia based materials span 100 pages with 308 references. The expansive literature expands further when doped CeO_2 and applications outside of catalysis are considered.

While reduction of CeO_2 occurs at relatively low temperatures it relies on surface availability of the crystallites and does not readily undergo full reduction to Ce_2O_3, to complicate matters cerium oxide suffers from thermal sintering further reducing the available surface area for further redox. For this reason, doped cerium oxides are a common topic of study within the literature where the thermal stability and accessible OSC properties of CeO_2 are further tuned.

Cerium oxide is found in the fluorite MX_2 (space group = $Fm\bar{3}m$) structure where the Ce occupies a face centred cubic (FCC) arrangement with the O tetrahedrally coordinated to the Ce. CeO_2 exists in the $Fm\bar{3}m$ space group where Ce occupies the 4a and O occupied the 8C Wyckoff positions,[73] with a Ce-O bond length of 2.34 Å. The unit cell for cubic CeO_2 is shown in Figure 1.3.

Zirconium oxide is a well established additive to cerium oxide[65,67] known for its thermal resistance and use in ceramics[74]. ZrO_2 exists naturally in three structures, a monoclinic structure below 1170 °C, a tetragonal structure above 1170 °C and 2370 °C and a cubic phase above 2370°C. The tetragonal and cubic phase of ZrO_2 can be stabilised at room temperature via the doping, the addition of cerium stabilises the tetragonal phase and the addition of yttrium stabilises the cubic phase. The tetragonal structure (space group = $P4_2/nmc$) of ZrO_2 is of interest in this work and is described by tetragonal body centred arrangement of Zr atoms where the O are tetrahedrally coordinated to Z with two Zr-O bond distances of 2.09 Å and 2.39 Å.[75] The unit cell for tetragonal ZrO_2 is shown in Figure 1.3.

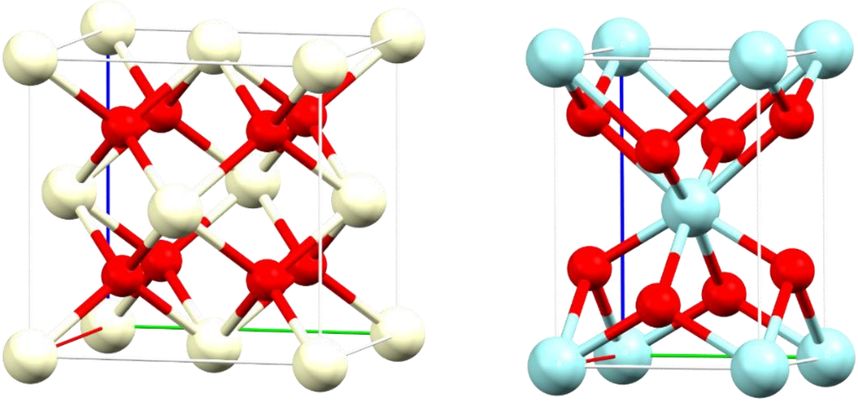

Figure 1.3: Unit cells of CeO_2 (left) and ZrO_2 (right), Ce atoms in pale yellow, Zr atoms in pale blue, O atoms in red. Unit cell atomic positions are related by a 45 ° rotation around the c axis, marked by the blue line.

Ceria zirconia materials have been widely studied within the literature with several phase diagrams published[76,77] with several meta-stable intermediate phases identified. Even so the topic of ceria zirconia materials with composition nearing $Ce_{0.5}Zr_{0.5}O_2$ has been a topic of debate, not least because it heavily depends on sample preparation and thermal history. To complicate matters small crystallite sizes with large surface areas are catalytical desirable but broaden the features of the diffraction pattern adding ambiguity to the analysis which blurs the already limited difference observed via X-ray diffraction between the cubic ($Fm\bar{3}m$) and t” ($P4_2/nmc$) phases of ceria zirconia[78], where t” is defined as a cubic arrangement of Ce/Zr cations but where tetragonal displacement in the oxygen site is still present.

When considering improvements to CeO_2, why stop at one doped constituent? Double-doped CeO_2 have become increasingly common place in the literature for both experimental and computational studies[79] which aim to further finetune key properties of ceria zirconia. One such study by Croisé *et al.*[80] showed that substituting some of the zirconia for praseodymium in a ceria zirconia solid solution resulted in a lower reduction temperature with a larger total reduction achieved over ceria zirconia for oxidation of H_2, this was matched with a drastic decrease in oxidation of CO showing significant preference for specific reducing agent. Additional problems were encountered with the catalyst formulation when loading the praseodymium substituted ceria zirconia with WO_3 or Nb_2O_5 as the active catalyst, both of which were found to significantly inhibit the redox behaviours of the Pr substituted material. These results highlight the potential of highly specialised and selective cerium oxide based catalysts tailored for specific reactions.

The potential for highly specialised cerium oxide based catalysts further reinforces the importance of studying the local disorder present within these materials and to fully understand the impact that dopants and thermal history have on these defects which are proving increasingly vital to the properties of these catalyst materials. Notably much of the activity in cerium oxide based catalysts is related to the overall mobility and activity of the oxygen sublattice, which due to a relatively low electron density compared to cerium results in minimal sensitivity to oxygen via X-ray diffraction, as such neutron diffraction which has significantly larger sensitivity to oxygen is a solid choice for studying disorder in metal oxides, especially in the application of total scattering experiments which aim to capture the diffuse scattering which arises from local scale deviations in the crystal structure.

1.5 Focus of work in this thesis

The focus of the work detailed in this thesis is to highlight a combined experimental and modelling approach employing laboratory and central facility diffraction-based techniques used to probe the atomic-scale structural nature of solid solution mixed-metal oxides. This thesis shows how a combined approach can shine insight into structural defects of key mixed metal oxides relevant in industrial catalysis.

This has been achieved through synchrotron X-ray and spallation source neutron total scattering experiments to generate the X-ray and neutron pair distribution functions (PDF) for several cerium zirconium oxide materials complimented with laboratory X-ray diffraction. Chapters 3 and 4 describe how X-ray/neutron PDF and Bragg diffraction data used with an RMC modelling approach can shine insights into local structures beyond that which is clearly visible to an analyst in the data. Chapter 3 focuses on the $Ce_{0.75}Zr_{0.25}O_2$ composition[58] detailing an exemplar study on two materials which appear nominally identical. Chapter 4 discusses the $Ce_{0.5}Zr_{0.5}O_2$ composition which includes research on observed oxygen disorder in the κ-$CeZrO_4$ phase and X-PDF in-situ study of pyrochlore formation at the I15-1 XPDF beamline at the Diamond Light Source. Chapter 5 discusses several other cerium zirconium materials including titanium doped ceria zirconia and cerium doped titania drawing conclusions based on X-ray and neutron Bragg diffraction data and highlighting potential future work on these materials. Chapter 6 collates cross chapter results not explicitly discussed in any other chapter and broader areas of further work relating to the study of ceria zirconia oxides using combined data approaches.

Johnson Matthey provided key cerium zirconium oxide samples for study to further understand of the local-structure properties correlation within industrially relevant samples. The provided samples include the $Ce_{0.75}Zr_{0.25}O_2$ F800 and SRMO1050 samples discussed in Chapter 3, the $Ce_{0.5}Zr_{0.5}O_2$ (industrially provided, SRMO1050 and SRMO1200) samples discussed in Chapter 4 and the $Ce_{0.25}Zr_{0.75}O_2$ (F800 and SRMO) and $Ce_{0.5}Zr_{0.3}Ti_{0.2}O_2$ (F800 and SRMO900, SRMO900 treatment done at Warwick) samples discussed in Chapter 5.

1.6 Bibliography

1 G. Singh, S. Kumar and S.-W. Kang, in *Reference Module in Materials Science and Materials Engineering*, Elsevier, 2016.

2 J. Kepler, *The Six-Cornered Snowflake*, Paul Dry Books, 2010.

3 R. Hooke, *Micrographia, or some physiological descriptions of minute bodies made by magnifying glasses: with observations and inquiries thereupon.*, London, UK, 1665.

4 J. Law and R. Rennie, in *A Dictionary of Physics*, eds. J. Law and R. Rennie, Oxford University Press, 7th edn., 2015.

5 J. Law and R. Rennie, in *A Dictionary of Physics*, eds. J. Law and R. Rennie, Oxford University Press, 7th edn., 2015.

6 T. Hahn, *International Tables for Crystallography*, SPRINGER, London, 5th edn., 2005, vol. A.

7 M. von Laue, in *Fifty Years of X-Ray Diffraction: Dedicated to the International Union of Crystallography on the Occasion of the Commemoration Meeting in Munich July 1962*, ed. P. P. Ewald, Springer US, Boston, MA, 1962, pp. 278–307.

8 P. W. H. Bragg and W. L. Bragg, 1913, **17**, 428–438.

9 S. W. H. Bragg, *Proc. Phys. Soc. London*, 1920, **33**, 222.

10 N. Robotti, *Rend. Lincei*, 2013, **24**, 7–18.

11 A. P. Sutton, *Phys. Elast. Cryst. Defects*, 2020.

12 H. J. Wollenberger, in *Physical Metallurgy*, eds. R. W. CAHN and P. HAASEN†, North-Holland, Oxford, 4th edn., 1996, pp. 1621–1721.

13 J. Law and R. Rennie, in *A Dictionary of Physics*, eds. J. Law and R. Rennie, Oxford University Press, 7th edn., 2015.

14 J. Frenkel, *Zeitschrift für Phys.*, 1926, **35**, 652–669.

15 H. Gleiter, *Prog. Mater. Sci.*, 1989, **33**, 223–315.

16 Z. Z. Bu, Xian-He, Michael J. Zaworotko, Ed., *Metal-organic*

framework: from design to applications., Springer International Publishing, 2020.

17 H. Li, L. Li, R. B. Lin, W. Zhou, Z. Zhang, S. Xiang and B. Chen, *EnergyChem*, 2019, **1**, 100006.

18 H. Fan, M. Peng, I. Strauss, A. Mundstock, H. Meng and J. Caro, *Nat. Commun.*, 2021, **12**, 1–10.

19 S. K. Elsaidi, M. H. Mohamed, A. S. Helal, M. Galanek, T. Pham, S. Suepaul, B. Space, D. Hopkinson, P. K. Thallapally and J. Li, *Nat. Commun.*, 2020, **11**, 1–8.

20 R. W. Siegel, *Nanostructured Mater.*, 1993, **3**, 1–18.

21 V. Krayzman, E. Cockayne, A. C. Johnston-Peck, G. Vaughan, F. Zhang, A. J. Allen, L. Y. Kunz, M. Cargnello, L. H. Friedman and I. Levin, *Chem. Mater.*, 2020, **32**, 286–298.

22 J. L. Payne, M. G. Tucker and I. R. Evans, *J. Solid State Chem.*, 2013, **205**, 29–34.

23 S. Luo, M. Li, V. Fung, B. G. Sumpter, J. Liu, Z. Wu and K. Page, *Chem. Mater.*, 2021, **33**, 3959–3970.

24 Y. Xu, F. Wang, X. Liu, Y. Liu, M. Luo, B. Teng, M. Fan and X. Liu, *J. Phys. Chem. C*, 2019, **123**, 18889–18894.

25 S. Damyanova, B. Pawelec, K. Arishtirova, M. V. M. Huerta and J. L. G. Fierro, *Appl. Catal. A Gen.*, 2008, **337**, 86–96.

26 D. Devaiah, L. H. Reddy, S. E. Park and B. M. Reddy, *Catal. Rev. - Sci. Eng.*, 2018, **60**, 177–277.

27 S. Urban, I. Djerdj, P. Dolcet, L. Chen, M. Möller, O. Khalid, H. Camuka, R. Ellinghaus, C. Li, S. Gross, P. J. Klar, B. Smarsly and H. Over, *Chem. Mater.*, 2017, **29**, 9218–9226.

28 S. Urban, P. Dolcet, M. Möller, L. Chen, P. J. Klar, I. Djerdj, S. Gross, B. M. Smarsly and H. Over, *Appl. Catal. B Environ.*, 2016, **197**, 23–34.

29 S. Otsuka-Yao-Matsuo, T. Omata, N. Izu and H. Kishimoto, *J. Solid State Chem.*, 1998, **138**, 47–54.

30 H. Kishimoto, T. Omata, S. Otsuka-Yao-Matsuo, K. Ueda, H. Hosono and H. Kawazoe, *J. Alloys Compd.*, 2000, **312**, 94–103.

31 C. Suryanarayana, *Jom*, 2002, **54**, 24–27.

32 E. Mamontov, T. Egami, R. Brezny, M. Koranne and S. Tyagi, *J. Phys. Chem. B*, 2000, **104**, 11110–11116.

33 W. I. F. David, *J. Res. Natl. Inst. Stand. Technol.*, 2004, **109**, 107–123.

34 A. A. Coelho, *J. Appl. Crystallogr.*, 2018, **51**, 210–218.

35 B. H. Toby and R. B. Von Dreele, *J. Appl. Crystallogr.*, 2013, **46**, 544–549.

36 T. L. Christiansen, S. R. Cooper and K. M. O. Jensen, *Nanoscale Adv.*, 2020, **2**, 2234–2254.

37 T. Proffen and H. Kim, *J. Mater. Chem.*, 2009, **19**, 5078–5088.

38 D. S. Sivia, *Elementary Scattering Theory: For X-ray and Neutron Users*, Oxford University Press, 1st edn., 2011.

39 D. A. Keen, *Crystallogr. Rev.*, 2020, **26**, 141–199.

40 R. B. Neder and T. Proffen, *J. Appl. Crystallogr.*, 2020, **53**, 710–721.

41 D. A. Keen, *J. Appl. Crystallogr.*, 2001, **34**, 172–177.

42 C. L. Farrow, P. Juhas, J. W. Liu, D. Bryndin, E. S. Božin, J. Bloch, T. Proffen and S. J. L. Billinge, *J. Phys. Condens. Matter*, 2007, **19**, 335219.

43 M. W. Terban and S. J. L. Billinge, *Chem. Rev.*, 2022, **122**, 1208–1272.

44 J. G. Kirkwood and E. M. Boggs, *J. Chem. Phys.*, 1942, **10**, 394–402.

45 F. Li and J. S. Lannin, *Phys. Rev. Lett.*, 1990, **65**, 1905–1908.

46 J. Wilhelm and E. Frey, *Phys. Rev. Lett.*, 1996, **77**, 2581–2584.

47 B. H. Zimm, *J. Chem. Phys.*, 1948, **16**, 1093–1099.

48 C. F. Quate, *Surf. Sci.*, 1994, **299–300**, 980–995.

49 L. A. Bendersky and F. W. Gayle, *J. Res. Natl. Inst. Stand. Technol.*, 2001, **106**, 997–1012.

50 ARCHER UK National Supercomputing Service, http://www.archer.ac.uk, (accessed 19 March 2023).

51 M. T. Dove, M. G. Tucker and D. A. Keen, *Eur. J. Mineral.*, 2002, **14**, 331–348.

52 L. Pusztai and R. L. McGreevy, *Phys. B Condens. Matter*, 1997, **234–236**, 357–358.

53 V. M. Nield, *Nucl. Inst. Methods Phys. Res. A*, 1995, **354**, 30–37.

54 T. R. Welberry and D. J. Goossens, *Acta Crystallogr. Sect. A Found. Crystallogr.*, 2008, **64**, 23–32.

55 H. Y. Playford, L. R. Owen, I. Levin and M. G. Tucker, *Annu. Rev. Mater. Res.*, 2014, **44**, 429–449.

56 R. L. Mcgreevy and L. Pusztai, *Mol. Simul.*, 1988, **1**, 359–367.

57 R. L. McGreevy, *J. Phys. Condens. Matter*, 2001, **13**, R887–R913.

58 A. Summer, H. Y. Playford, L. R. Owen, J. M. Fisher, A. Kolpin, D. Thompsett and R. I. Walton, *APL Mater.*, 2023, **11**, 031113.

59 C. G. Shull, *Rev. Mod. Phys.*, 1995, **67**, 753–757.

60 V. F. Sears, *Neutron News*, 1992, **3**, 26–37.

61 R. I. Smith, S. Hull, M. G. Tucker, H. Y. Playford, D. J. McPhail, S. P. Waller and S. T. Norberg, *Rev. Sci. Instrum.*, 2019, **90**, 115101.

62 H. F. Wang, Y. L. Guo, G. Z. Lu and P. Hu, *Angew. Chem - Int. Ed.*, 2009, **48**, 8289–8292.

63 R. Di Monte and J. Kašpar, *Top. Catal.*, 2004, **28**, 47–58.

64 Y. Goto, A. Morikawa, M. Iwasaki, M. Miura and T. Tanabe, *Chem. Commun.*, 2018, **54**, 3528–3531.

65 M. Sugiura, *Catal. Surv. from Asia*, 2003, **7**, 77–87.

66 Y. Shan, Y. Liu, Y. Li and W. Yang, *Sep. Purif. Technol.*, 2020, **250**, 117181.

67 T. Montini, M. Melchionna, M. Monai and P. Fornasiero, *Chem. Rev.*, 2016, **116**, 5987–6041.

68 P. Arunkumar, M. Meena and K. S. Babu, *Nanomater. Energy*, 2012, **1**, 288–305.

69 M. Nadeem, R. Khan, K. Afridi, A. Nadhman, S. Ullah, S. Faisal, Z. U. Mabood, C. Hano and B. H. Abbasi, *Int. J. Nanomedicine*, 2020, **15**, 5951–5961.

70 A. Dhall and W. Self, *Antioxidants*, 2018, **7**, 1–13.

71 S. Rajeshkumar and P. Naik, *Biotechnol. Reports*, 2018, **17**, 1–5.

72 S. Parwaiz, M. M. Khan and D. Pradhan, *Mater. Express*, 2019, **9**, 185–202.

73 R. W. G. Wyckoff, *The analytical expression of the results of the theory of space-groups*, Carnegie Institution of Washington, Washington, 1922.

74 L. Treccani, T. Yvonne Klein, F. Meder, K. Pardun and K. Rezwan, *Acta Biomater.*, 2013, **9**, 7115–7150.

75 Neetu, D. Singh, N. Kumar and J. Gangwar, *Mater. Res. Express*, 2019, **6**, 1150f8.

76 P. Duran, M. Gonzalez, C. Moure, J. R. Jurado and C. Pascual, *J. Mater. Sci.*, 1990, **25**, 5001–5006.

77 M. Yashima, K. Morimoto, N. Ishizawa and M. Yoshimura, *J. Am. Ceram. Soc.*, 1993, **76**, 1745–1750.

78 M. Yashima, *Catal. Today*, 2015, **253**, 3–19.

79 E. A. Khera, H. Ullah, F. Hussain, M. Imran, R. M. A. Khalil, M. A. Sattar, A. M. Rana, C. Mahata and S. Kim, *Phys. E Low-Dimensional Syst. Nanostructures*, 2020, **119**, 114025.

80 C. Croisé, R. Pointecouteau, J. Akil, A. Demourgues, N. Bion, X. Courtois and F. Can, *Appl. Catal. B Environ.*, 2021, **298**, 120563.

Chapter 2: Experimental and Analysis Methodology

This chapter aims to introduce the experimental techniques, analysis methodologies and data processing tools used throughout this thesis.

2.1 Sample origin and preparation

Samples labelled with the F### formalism refer to a thermal treatment involving firing in air at ###, usually at ### = 800 °C for 2 hours in a muffle furnace using a 10 °C / min heating rate unless otherwise specified.

Samples labelled with the SRMO#### formalism refer to a high temperature thermal reduction (strong reduction, SR) at #### (#### = 1050, 1200 or 900) under a reducing atmosphere (H_2 or 5% H_2 in N_2) in a tube furnace followed by cooling to room temperature before exposing the sample to air, a second thermal treatment involving a lower temperature thermal oxidation (moderate oxidation, MO) of usually 400 °C in air for 1 hour. Unless otherwise stated, heating rates were 10 °C / min.

Most samples discussed in this thesis were provided by Johnson Matthey where the sample synthesis method is not disclosed. These samples include the $Ce_{0.75}Zr_{0.25}O_2$ (F800 and SRMO1050) samples discussed in Chapter 3, three $Ce_{0.5}Zr_{0.5}O_2$ (industrially provided, SRMO1050, SRMO1200) samples discussed in Chapter 4 and the $Ce_{0.25}Zr_{0.75}O_2$ (F800, SRMO1050), Ce0.5Zr0.3Ti0.2O2 (F800, SRMO900) and $Ce_{0.3}Zr_{0.5}Ti_{0.2}$ (F800, SRMO900) samples discussed in Chapter 5.

The alkoxide synthesised $Ce_{0.5}Zr_{0.5}O_2$ sample discussed in Chapter 4 was prepared at Warwick via a solvothermal synthesis method using alkoxide precursors. The sample was synthesised by mixing a 1:4.6 weight ratio (1:1, Ce:Zr molar ratio) of 18-20 wt/% cerium(IV) 2-methoxyethoxide in 2-methoxyethanol and 80 wt/% zirconium n-butoxide in 1-butanol. The precursor mixture was placed into a Teflon autoclave liner and mixed with a magnetic stirrer for 1 hour. Once mixed the autoclave was assembled and placed in an oven at 200 °C and left for 24 hours. The synthesised product was washed with butanol and filtered using vacuum filtration then left to dry at 80 °C in a drying cabinet. The dried product was ground using a pestle and mortar then fired in a muffle furnace at 800 °C for 2 hours.

The cerium containing anatase titanium oxide samples discussed in Chapter 5 were previously made by de Lima[1] via a solvothermal synthesis method in ethanol. Appropriate ratios of titanium(IV) isopropoxide (Acros Organics) and cerium nitrate hexahydrate (Sigma-Aldrich, 99%) solutions were added to a Teflon autoclave liner and stirred for 1 hour prior to autoclave assembly and placed into a pre-heated oven at 240 °C for 24 hours, the cerium to titanium atom ratios synthesised were 0 %, 1 %, 5 % and 10%. The pale yellow solids were recovered by vacuum filtration and dried in air at 70 °C prior, subsamples were fired at 400 °C in air for 4 hours.

2.2 Experimental methods

2.2.1 X-ray and neutron diffraction

Braggs law is fundamental for X-ray and neutron diffraction and is clearly derived in many textbooks[2] in great detail so has not been derived here. Braggs law relates the atomic interplanar spacings of a crystal structure (d), the wavelength (λ) of incident beam and the angle of diffraction (θ) and any non-zero integer (n). In essence, Braggs law describes the conditions for a diffraction peak is that the incident and scattered waves are in phase. The two waves are in phase if they have experienced a path difference that is an integer number of wavelengths ($n \times \lambda$). Diffracted X-rays are observed as peaks where Braggs law is observed and are referred to as 'reflections' of the interplanar *d* spacing they relate to.

$$n\lambda = 2dsin(\theta)$$

The interplanar spacing (d) is a function of the crystalline order of a material which is generally unknown. Wavelength (λ) is defined by the source of incident radiation and is commonly fixed in laboratory X-ray diffractometer setups. For X-rays the wavelength employed is usually limited by the X-ray source. Laboratory diffractometers generate X-rays by using a cathode tube. Within the cathode tube a tungsten filament is used to generate a electron beam which strikes a metallic target causing the metal to emit X-rays with a wavelength profile primarily based on the element of the target. Due to this process being destructive X-ray cathode tubes lose X-ray flux over time and require replacement once the target has eroded.

For most diffraction instruments use of a fixed wavelength and collection of as wide as possible angular range of diffraction is best option for probing a wide range of d spacings. While large 2D detectors and detector arrays capable of simultaneously collecting diffracted X-rays from a wide angular range exist they are prohibitively expensive for use in most lab diffractometers which instead use a much smaller detector moved by a robotic arm. The immediate drawback of this method is such that during an hour long data collection, any given 2theta value may only see a few seconds of data collection depending on the functional collection angle of the detector resulting in a relatively slow data collection process which discards the vast majority of diffracted intensity.

All laboratory powder X-ray diffraction data displayed in this thesis were collected via the Warwick X-ray diffraction research technology platform using a Panalytical X-Pert Pro MPD equipped with a Cu Kα1 focusing Johansson monochromator on the incident beam. The average data collection was between 10° and 120° 2θ over a 12 h (overnight) scan duration.

2.2.1.1 Synchrotron X-rays

Large 2D detectors and detector arrays are used at specialised instruments at synchrotron facilities where the trade off between X-ray generation cost and detector cost becomes less of a concern. Advanced detectors combined with exceptionally high X-ray flux at facilities such as the Diamond Light Source (DLS) result in excellent data quality collected within seconds.

Synchrotron facility X-ray generation is via the acceleration of electrons in a ring shaped continuous particle accelerator, at the DLS one linear accelerator and two synchrotron rings are used. First electrons are generated fired from an electron gun and accelerated in the linear accelerator to energies of ~ 100 million eV. Electrons then enter the second particle accelerator, the ‘booster’ ring where the electrons are repeatedly accelerated until energies of ~3 giga eV are reached before entering the third particle accelerator, the storage ring. The storage ‘ring’ at the DLS is not actually a ring at all, but rather comprised of 24 straight segments which use dipole magnet pairs at each junction to bend the electron beam at given points, this change in velocity of a high energy electron beam generates the synchrotron X-rays. The use of straight segments provides the significant advantage of X-ray generation at fixed points of the synchrotron rather than true ring design which generates X-rays throughout the whole ring due to the curved trajectory required. The generated X-rays can be further tuned by the use of a wiggler insertion devices which consist of an array of magnets that changes the linear path of the electron beam to a wiggling oscillation causing the emission of a wide range of X-ray wavelengths, providing access to ultra-low wavelengths useful in high energy applications such as total scattering experiments. Undulators are another form of insertion device used at DLS which produces a highly focused monochromatic X-ray beam.

Synchrotron X-ray data were acquired on the I15-1 XPDF beamline at the Diamond Light Source, Rutherford Appleton Labo*r*atory, UK.[3] Small volumes of the sample were loaded into 0.1 mm quartz capillaries with a 0.01 mm wall thickness before being manually loaded into the beamline and aligned using a motorized sample stage. Data were collected using a 2D Perkin Elmer detector, with raw diffraction data processed into 1D diffraction patterns automatically using the DAWN (Data Analysis WorkbeNch) software at the Diamond Light Source.[4] GudrunX was used for total scattering data reduction and processing to obtain the X-PDF patterns for the studied samples.[5] Ex-situ data collections were 5 minutes in duration.

In-situ Synchrotron X-ray data discussed in Chapter 4 was also collected at the I15-1 XPDF beamline, where the sample was bedded into a horizontal 10 mm outer diameter quartz capillary and filled to approximately half the depth of the capillary allowing free gas flow over the sample. The loaded capillary was then kept horizontal and mounted into the centre of the DLS HELIOS[6] IR Furnace and connected to the gas system using steel fittings. The HELIOS IR furnace borrowed from the I12 beamline at the DLS, uses four high intensity IR lamps housed within a reflective dome to generate a 2 × 2 × 2 mm hotspot at the centre of the cell. Due to the use of infrared light the heating efficiency varies for samples of different colour, to validate the thermal trends of the dark grey Si/Al_2O_3 thermal calibrant and the pale yellow ceria zirconia samples a type-S thermocouple was embedded into the sample with care taken to avoid any overlap of the thermocouple with the X-ray beam or IR furnace hotspot. The thermocouple readout was used to validate the trend of the Rietveld refined calibration vs the trend observed for the samples studied which were found to have a slight offset but were highly comparable across the whole furnace power range used. Gas (4% H_2 in Ar or 20% O_2 in N_2) was passed over the sample and data collected at room temperature before applying power to the IR furnace. Thermal calibration of IR furnace power to temperature was performed by heating a synthetic mixture of high purity NIST Si and Al_2O_3 at set furnace powers up to 80 % as shown in Figure 2.1. A fault in the communication between the experimental hutch controller and the HELIOS IR furnace controller was noted where the HELIOS furnace power setting would not update correctly, This fault was observed in the thermal calibration data and is observed in Figure 2.1 but was solved for collection of the experimental data. In-situ data collections were fifteen 1 minute data collections, where thermal equilibrium in the observed data was achieved after ~3 minutes. Data processing and reduction to obtain the Xray-PDF patterns was performed using data obtained after 5 minutes (scans 6+), where diffraction data from I15-1 is shown the 10th scan is displayed.

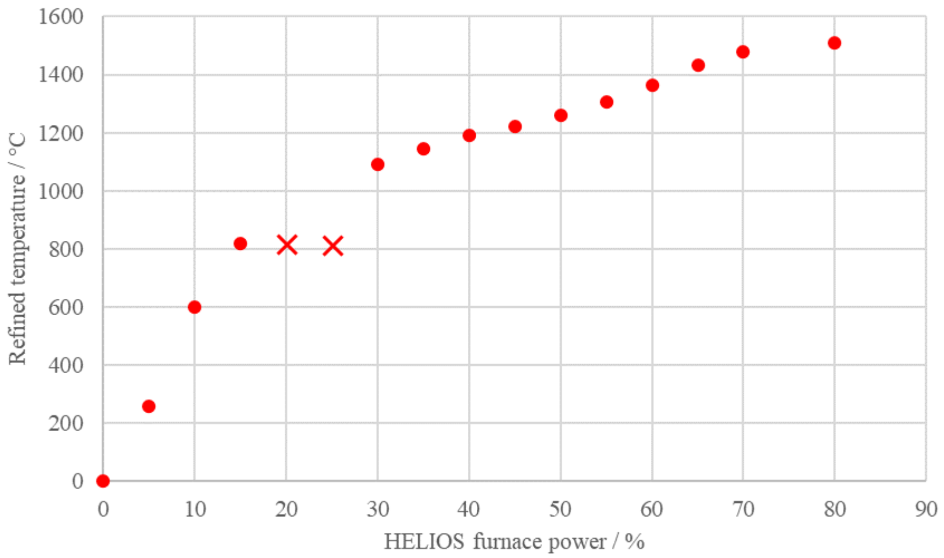

Figure 2.1: HELIOS IR furnace Rietveld refined temperature calibration using a synthetic Si/Al_2O_3 mixture. Thermal expansion coefficients[7], Si = 3.6×10^{-6} / °C, Al_2O_3 = 8.1×10^{-6} / °C. Red crosses are data collected where a communication error prevented the IR furnace power updating from 15 %.

2.2.1.2 Spallation source neutrons

As mentioned above the conditions for constructive interference which generates Bragg peaks can be probed by either changing detection angle or the incident wavelength. One example of where the incident wavelength is varied instead of diffracted angle is a time-of-flight (TOF) neutron diffractometer which is able to collect data as a function of time by exploiting the highly precise timings of neutron generation at a spallation source enabling the time of travel to be measured, and thus the velocity of the detected neutron to be calculated by the initial creation time (t_0), time of detection (t_1) and path length (L).

$$v = \frac{t_1 - t_0}{L}$$

Once the velocity (v) and mass (m) are known the de Broglie wavelength (λ) can be calculated by using Planck's constant (h) for that particle using the de Broglie equation below.[8]

$$\lambda = \frac{h}{m.v}$$

A practical guide to how the relationship between TOF and d spacing is exploited was produced by Smith[9] and deserves a mention here. In his guide ZERO and DIFC represent different parts of the path length while DIFA is path length correction due to sample absorption of neutrons, and as such is an experimentally derived parameter unique to each sample composition.

With the wavelength of neutrons at any given detection time is known, TOF data collected become a function of neutron wavelength allowing for the use of a ‘white light’ neutron source without the need for a monochromator. Neutron spallation sources provide high energy neutrons without the need for a monochromator allowing for larger accessible Q ranges. While high energy X-ray sources can provide significant advantages in beam intensity, X-ray form factor intensity fall off at higher Q results in a practically limited Q_{max} for X-rays of below 30 in most cases. This means that total scattering experiments at neuron spallation sources routinely exceed X-ray total-scattering experiments in terms of useable Q range. The usable Q range being defined as the Q range at which discernible sample signal above noise is observed. As mentioned, neutron flux is dramatically lower than synchrotron X-rays making useable total scattering data collections orders of magnitudes different in terms of collection time, with 2+ hours routinely used for neutrons at Polaris and 1+ minutes routinely used for X-rays at I15-1.

Figure 2.2 shows the neutron coherent bound scattering lengths by atomic number. The use of neutrons as a scattering probe has several useful properties, here we will discuss five of these useful properties.

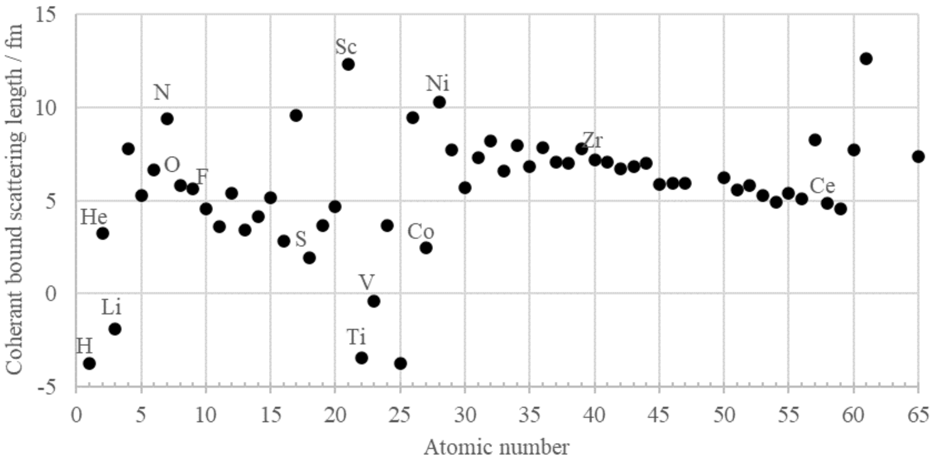

Figure 2.2: Neutron coherent bound scattering lengths by atomic number, natural isotope abundance assumed.[10]

First is their independence to atomic number allowing for meaningful scattering intensity difference from neighbouring elements such as Co and Ni which are indistinguishable via X-ray diffraction, making the two techniques highly compatible and complementary, rather than merely repetitions.

Secondly is the isotopic sensitivity of the neutron scattering allowing for isotopically labelled studies, or the isotope enrichment of elements such as ^{1}H which have a problematically large incoherent scattering length which contributes to significant background noise when present. The coherent bound scattering length observed for naturally abundant elements is a weighted average of their isotropic coherent bound scattering lengths, the case for Ti and its isotopes are shown in Figure 2.3 as an example.

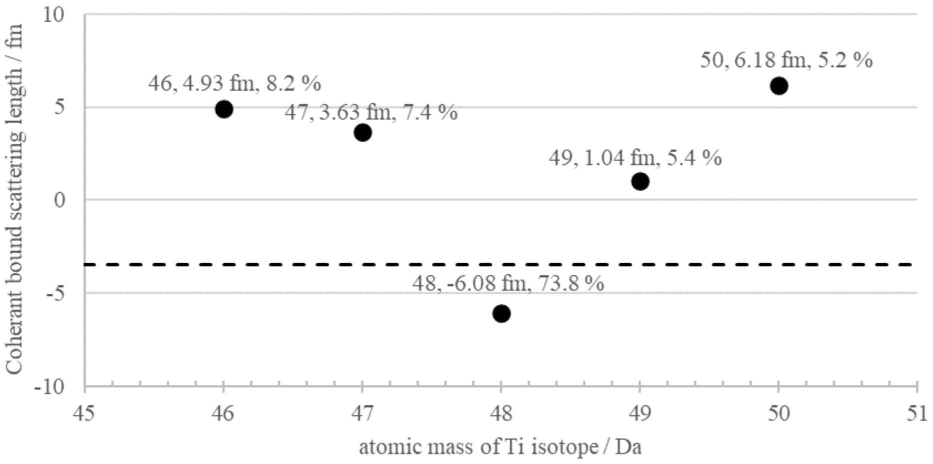

Figure 2.3: Coherent bound scattering lengths of Ti isotopes, isotope atomic mass, coherent bound scattering length and relative abundance labelled. Dashed line showing the Ti coherent bound scattering length for natural abundance Ti.[10]

Third is the is the overall magnitude of scattering power across the periodic table spanning with the largest neutron scattering length belonging to ^{26}Ar at 24.6 fm with most elements of natural abundance being in the 3 – 10 fm range, meaning there are relatively few systems where there isn't a meaningful elemental sensitivity to the observed data allowing for both heavy and light elements in a structure such as CeO_2 (Ce, $Z = 58$; O, $Z = 8$) to be studied with comparable weighting in the data.

Fourth is the existence of negative scattering lengths where the diffracted neutron is subject to attractive forces prior to diffraction rather than a repulsive force resulting in a phase shift of 180° of the diffracted neutrons. The importance of this becomes apparent when solid solution alloys of net zero scattering can be designed which give rise to no coherent neutron scattering, allowing for the fabrication of neutron invisible sample environments. Naturally abundant vanadium has low negative coherent scattering length and is a commonly used material.

Lastly, while not exploited in this study, neutrons possess a small magnetic moment allowing them to scatter based on the magnetic structure of a material, known as magnetic scattering.

While reactor sources are discussed briefly in the introduction, no reactor source neutron experiments or data are used in this thesis.

All neutron data presented in this thesis were obtained on the Polaris instrument beamline at the STFC ISIS Neutron and Muon Source, Rutherford Appleton Laboratory, UK.[11] Polaris is a high intensity, medium resolution powder diffractometer with five fixed angle detector banks covering the angular ranges of 6.7-14.0° 2θ (bank 1), 19.5 - 34.1 °2θ (bank 2), 40.4-66.4 °2θ (bank 3), 75.2-112.9 °2θ and 134.6-167.4 °2θ, a diagram of the vacuum chamber housed detector banks of Polaris is shown in Figure 2.4. The Polaris instrument routinely achieves an accessible Q_{max} of 40 Å^{-1}, with 50 Å^{-1} being achievable with ideal materials, it is commonly used for total scattering experiments. Raw collected data were first processed using Mantid[12], this calibration involved summation of individual detector counts based on recent calibration of the instrument to produce 5 histograms of normalised intensity vs TOF data. The data were normalised to the scattering of a vanadium rod of known density and dimensions allowing for the use of an absolute scale on the data generated.

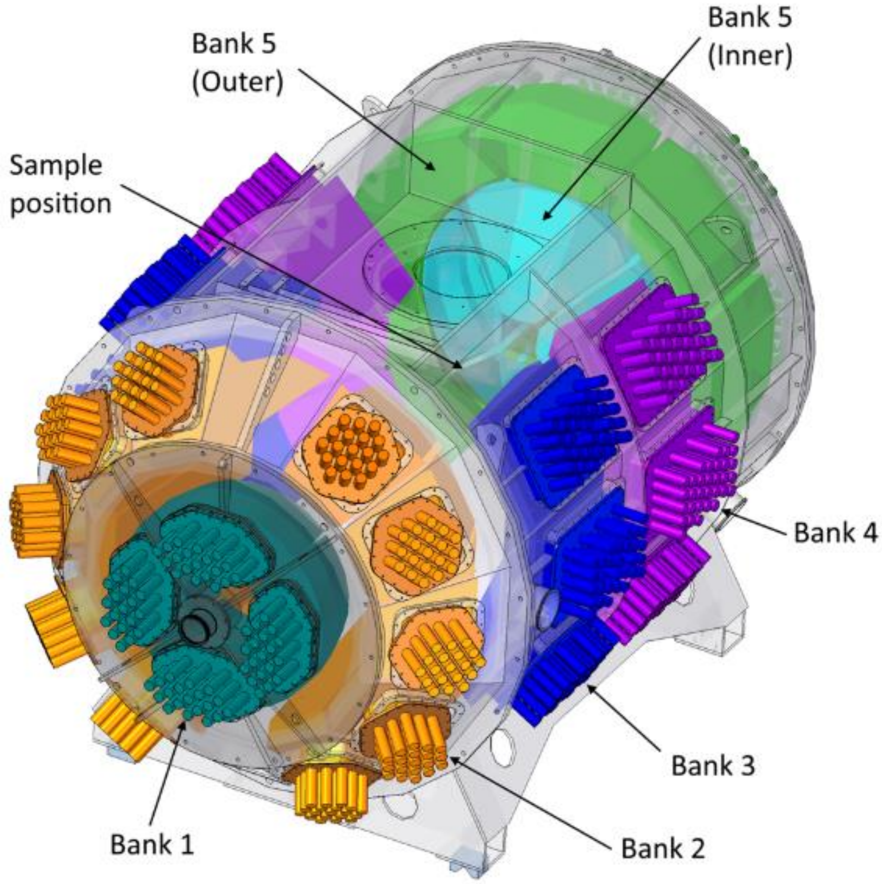

Figure 2.4: Arrangement of the detector banks within vacuum tank of the Polaris neutron diffractometer at ISIS neutron and muon source, samples loaded through a hatch on the top. Diagram obtained from Smith et al.[11]

All samples were ground to ensure a fine powder and loaded into (8 or 6 mm, depending on available volume) vanadium cans. The filled vanadium cans were then affixed onto an automatic sample changer and placed into the Polaris detector tank before the tank was evacuated. Data were collected under vacuum in 300 μAmps (∼1 h) scans, n-PDF data was processed using the summation of eight 300 μAmp collections. Raw data were processed using MantidPlot.[12] Total scattering data reduction and processing to generate the pair distribution function was performed using GudrunN[5,13] using all data from all five detector banks. Useable $Q_{\max}$ values of 33.5 to 40 Å^{-1} were observed for the samples studied correlating with the sharpness of the observed reflections.

2.1.3 Total scattering to PDF

A total scattering experiment aims to decouple the instrumental and environmental contributions to the observed diffraction data. The standard approach to this involves collecting diffraction data of the sample, the sample environment, and the sample container to as large a Q range as experimentally possible with excellent signal to noise ratio. In practice this involves the collection of several long duration datasets allowing the contributions from the instrument and sample environment to be subtracted from the observed data. This theoretically results in a dataset which contains only the observed scattering from the sample, however particularly high levels of care must be taken to avoid introducing artifacts to the data. For neutrons this dataset can be normalised to an absolute scale based on the scattering observed from a vanadium rod used as a convenient normalisation standard, routinely done as at Polaris as a data normalisation step. For multi-detector neutron diffractometers such as Polaris all used detector banks need merging to a single dataset to obtain the best Q range from the low and high angle detectors.

No such convenient normalisation tool is available for X-rays and their relatively stronger interaction with matter leaves few materials suitable for sample environments. In general a larger highly repeatable background representative to the sample background is favoured over less precise lower intensity backgrounds, as such the use of highly precise 100 nm walled capillaries are favoured over thinner options with larger variance. The I15-1 beamline at diamond is equipped with two detectors, however one is solely used to collect Bragg diffraction data and plays no role in the data processing of X-PDF data.

Once a diffraction dataset containing only scattering from the sample of interest is obtained it can be Fourier transformed to obtain the pair distribution function (PDF) for the material, this in essence is a transformation of the data from reciprocal space into real space, fundamentally both the processed total scattering diffraction pattern and the PDF contain the same structural information but presented from different views. The striking features in reciprocal space (diffraction pattern, *x* axis = *d*, *q*, 2θ) are due to average structure weighted long range atomic order where the features in real space (PDF, *x* axis = radial distance, Å) are most striking at the low r regions of the data which displays the average shortest atom-atom correlation distances highlighting short range order.

GUDRUN-N[5,13] was used to process the neutron total scattering data while GUDRUN-X was used to process the X-ray total scattering data to obtain the X-ray/neutron G(r) and D(r) PDFs presented as part of this thesis

2.2.3 Raman Spectroscopy

Raman spectra were collected via the Warwick Spectroscopy Research Technology Platform on a Renishaw inVia Raman Microscope equipped with a 514 nm DPSS laser. The collected data range was nominally from 100 to 3200 cm^{-1} using 10 s irradiations at 10 % laser exposure.

2.3.4 Temperature Programmed Reduction (TPR)

Temperature programmed reduction (TPR) shown in Chapter 4 for $Ce_{0.75}Zr_{0.25}O_2$ samples was measured at Johnson Matthey by the thermal conductivity of 10 % H_2 in N_2 at a flow rate of 30 ml min^{-1} before and after contact with a 0.05–0.10 g sample as a function of temperature. A trap after the sample was used to absorb the water created by H_2 oxidation. The temperature was increased linearly as a function of time. Quantification of hydrogen consumption was enabled by the addition of a known quantity (1 ml) of N_2 into the H_2/N_2 gas stream before the experiment began to create a calibration peak. The quantification of H_2 consumption was carried out by the integration of the TPR profile as a function of time, and the results are presented as the amount of H atoms oxidized per cerium atoms reduced. The error is estimated to be ± 5 % for the total gram of sample, mmol(H) g^{-1}, which can be related to the fraction of H_2 consumption in these measurements. Temperature programmed oxidation after the reduction of $Ce_{0.75}Zr_{0.25}O_2$ samples discussed in Chapter 4 show that reoxidation readily takes place around 200 °C.

2.4 Analysis Methodology

2.4.1 Rietveld refinements of Bragg diffraction data

The Rietveld refinement method was first developed by Rietveld in the late 1960's,[14] where he showed at diffraction data from crystalline powders could be successfully modelled using an iterative process to simulate the observed 2D patterns. Powder diffraction data are a 2D summary of the 3D diffraction sphere of countless individual crystallites and is the sum of heavily overlapped Bragg reflections. The method works by iteratively simulating a powder diffraction pattern from a model, then using the experimental vs calculated difference to drive the least squares algorithm to iteratively refine user defined instrumental or structural parameters until a satisfactory fit between the experimental and calculated powder diffraction patterns is achieved.

This refinement driven structural modelling method allows not just the extraction of lattice parameters, crystallite size and inhomogeneous strain from powder diffraction data, but also structural details such as atomic site positions, site occupancies and thermal parameters which sets the Rietveld method apart from similar non-structural whole powder pattern modelling methods such as the Pawley[15] and Le Bail[16,17] methods. The Rietveld refinement method has since been well established in Rietveld refinement programs such as GSAS[18], GSAS-II[19] and TOPAS[20].

All Bragg diffraction data analysis undertaken in this thesis was analysed Rietveld refinements with full structural models in GSAS-II.

2.4.2 Pair Distribution Function analysis (small box)

One of the strongest advantages to the PDF is that meaningful insight can be gained by inspection of the function, such as the first metal to oxygen (M-O) bond lengths and peak splitting of single atom-atom distances due to a multiple modal nature in mixed metal oxides. A common data analysis approach is fitting a 'small box' model to the PDF data using software such as PDFgui[21] with PDFfit2 in a process similar to Rietveld refinement. Larger portions of the PDF can then be matched against a simulated average structure enabling key areas of mismatch to be more easily identified. While small box PDF fitting approaches do use an average crystal structure, the local symmetry is usually relaxed to $P1$ symmetry to allow for explorative refinement of otherwise symmetrically related atomic positions, the unit cell maintains periodic boundary conditions and thus is truly incapable of modelling certain varieties of disorder relating to the nanostructures of solid solution materials. This approach while useful for probing anisotropic disorder quickly runs into limitations when applied to larger more complicated unit cells where the number of free parameters exceeds that which can be sensibly probed by the analyst.

All small box PDF fitting undertaken in this work was performed using PDFgui with PDFfit2, although it should be noted that both TOPAS and GSAS-II (also using PDFfit2) are now capable of fitting PDF data. Small box refined parameters from PDF data were exceedingly difficult to obtain for certain key samples and rarely insightful beyond visual inspection of the PDF patterns, in part due to the fitting of an intrinsically bulk model to local structure weighted data.

2.4.3 Reverse Monte Carlo modelling

Monte Carlo modelling (also called simulation) relies on solving a question of probability using randomness. The method is appliable to assess the likely outcomes of a process impacted by random variation and is used to applications in meteorology relating to weather prediction and finance for portfolio valuation.

The approach is quite simple, a model representing current data is generated (weather today, current stock price etc) as a known starting point. Next a random change is applied to a random parameter of the model, simulate the effect of that random change and accept the change if a) the change shifts the simulated parameter towards the minima, or b) accept the change with a given probability regardless of if the change was towards the minima. This iterative process is then repeated for a given number of iterations. The whole process is then repeated for a given number of repeats; these repeats can then be viewed collectively as a probability profile of outcomes after the influence of random variation. A cone shaped plot of the simulated parameter which gets wider with more steps in the iterative ‘length’ of the simulation, representing the increased impact of additive random choice.

The reverse Monte Carlo (RMC) modelling method applied in crystallography[22–25] follows the same methodology but in a “reversed” state. Rather than starting from a known position (weather today, current stock price) and predicting the probability of the unknown (weather in 3 weeks, stock price in 6 months), the starting arrangement of atoms can be random and experimentally obtained data of the system is used to drive the minimalisation of an atomic supercell. This then “reverses” the process, as the experimental data the model should match becomes the known with the starting model randomised where possible. While classic Monte Carlo simulated parameters become less accurate the longer the simulation is run, due to the minimalisation against experimental data the opposite is true for the reverse Monte Carlo process resulting in a parameter variation decreasing as a function of iterations run.

RMCProfile[26] is a program which makes use of the reverse Monte Carlo process applied to crystallographic datasets. The program is designed to allow for multiple datasets to drive the minimalisation process allowing for a truly multi-technique driven data analysis approach by combining local and average structure weighted data such as the observed Bragg diffraction combined with X-ray and neutron PDF data using models in scale capable of explicitly describing a wide range local structures while maintaining the overall average structure.

Due to the low computational cost of the reverse Monte Carlo method compared to MD or DFT simulations, RMCProfile is increasingly used to explore local-scale structures (average scale defects) through the use of supercell models with 10,000+ atoms earning this type of large scale fitting the name “large box” modelling.

While minimalisation to observed data proves to be a powerful tool, the brutal truth of the RMC process is that the analysis of colossal unit cells with 10s of thousands of explicitly described atoms is no easy task. RMCProfile includes a variety of useful sub-programs for manipulation of these supercells however due to the unique nature of material defects most analysis tools and constructed with specific relating to specific materials and systems in mind. Probing the relative local structures of every atom in a model of 27,648 entities requires not only the use of computational tools but also rigorous analysis methodology.

Due to the extensive data processing steps involved in the generation of a PDF, some artifacts of data processing are to be expected. When fitting with small box models or drawing conclusions visually these features can easily be ignored, missed or simply built into the comparison. Incorrect normalisations would be consistent across a series of similar samples. The PDFs would be relative to each other, while some oddities in fitting scales would be observed it's unlikely to have a significant impact on the analysis as a whole. The same cannot be said for PDF data used in the RMC method, the RMC method has no inherent chemical sense and will attempt to fit all features of the data, including all artifacts still present. As such it's vitally important that PDFs for use in RMC methods are processed to a very high standard as to not drive the conclusions of the model.

Analysis of RMCProfile generated configurations employed a combination of personally developed code using MATLAB[27] designed to extract key structural descriptors while assessing the overall health of the refined RMCProfile configurations coupled with the use of Clapp configuration analysis code developed by, and graciously provided with usage and editing permissions by Dr Owen[28] which enabled detailed analysis of all unique local arrangements of cations in the FCC structures studied within this work.

RMCProfile has been extensively used with supercells of 60 Å^3 in volume with over 20,000 simulated atoms present with two RMCProfile studies presented in Chapter 3 and three RMCProfile studies presented in Chapter 4.

2.4.3.1 Clapp configuration analysis

While achieving an exceptionally good fit to experimental data is one immediate benefit to the RMC method, ensuring the generated model has physical meaning and probing the generated large box configuration for local structure is not as straight forward as extracting refined parameters from its small box counterparts. Fundamentally, the large box model requires ways to reduce the exceptional volume of data down to meaningful conclusions. There is also the additional need to understand the statistically expected conclusions for the material studied are. When considering atomic sites shared by two or more elements the statistics of any given arrangement must be understood.

One such way of reducing the large box problem is to separate the larger system to characterizable individual components. Each cation in fluorite $Ce_{0.5}Zr_{0.5}O_2$ has an anion first shell of 8 oxide ions and a first cation shell of 12 Ce/Zr ions. This system can be simplified by only investigating the cation order independent of the oxide ions allowing for the construction of a suite of individual and correlated analysis to paint the paint the conclusions of the analysis as a whole. The analysis methodology below was applied to the FCC arranged metal sites in the fluorite structure effectively ignoring the oxygen sites of the mixed metal oxides discussed in Chapter 3 and 4, effectively describing the local structure of the FCC cations in terms of a binary alloy.

In 1971 Clapp[29] published a full list of the 144 orientationally unique first shell configurations of a FCC binary alloy (with only 22 for the 8 nearest neighbours of a BCC lattice).

To enable this assignment of Clapp configurations each of the 12 nearest neighbours are assigned a unique relative label to each other. Figure 2.5 shows a diagram of the 12 nearest neighbours of a central atom (0) and their site numbers as defined by Clapp.

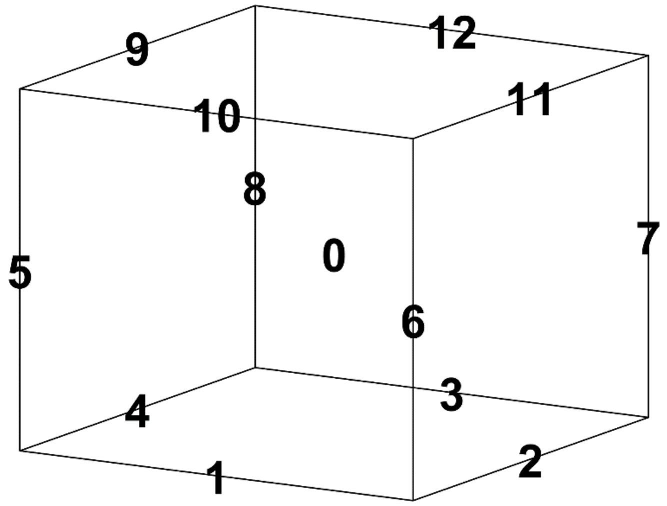

Figure 2.5: Site numbering for Clapp configuration analysis of a binary alloy.

These configurations (hereby referred to as C#, or Clapp configurations) are labelled C1 to C87 for structures where the central atom is the same type as the majority of the nearest 12 neighbours, and C-1 to C-57 where the central atom is of the opposite type as the majority of the 12 nearest neighbours. The configurations are numbered in order of configurations with ‘unlike’ atoms in their 12 nearest neighbours, C1 represents the structure where all 12 atomic neighbours are ‘like’ as the central atom. C-1 is the inversion of this where all 12 neighbours are ’unlike’ the central atom. On the other end of the scale configurations C58 to C87 are all configurations with 6 like and 6 unlike neighbours, making the negative Clapp configurations for these structures an orientational copy of another Clapp configuration in this range. A full list of Clapp configurations and their exact relative structures is available in Clapp’s paper.[29]

144 orientationally unique configurations are a much more manageable analysis than the 4096 (2^{12}) possible arrangements when orientation of the configuration is not accounted for. Similar to rolling two six sided dice, if we consider an outcome of 1 and 6 to be equivalent to 6 and 1 then we collapse the possible outcomes from 36, to only 11 (2-12) orientationally unique outcomes, the likelihood of each of these outcomes is not equal and must be addressed to understand deviations from the statistical outcome. In the same way Clapp configurations have a statistical probability based on how many possible orientations of the configuration there are, multiplied by

the relative composition of element in the binary alloy they relate to. These compositionally defined statistical probabilities allows the observed occurrences to be normalised per configuration providing a statistically defined baseline hypothesis describing a true solid solution with no only compositionally statistical local order. This normalisation is paired with an enhancement factor (β) for each Clapp configuration, defined as the number of observed configurations (x) away from the statistically calculated abundance (μ) in terms of statistically expected standard deviations (σ) so that $\beta = \frac{x-\mu}{\sigma}$. Use of the statistically defined baseline and enhancement factor allow for a plot of observed Clapp configurations where each configuration's counts are displayed in terms of their statistical significance above or below a 0 value which represents a statistical solid solution. An example of how this is plotted is shown in Figure 2.6.

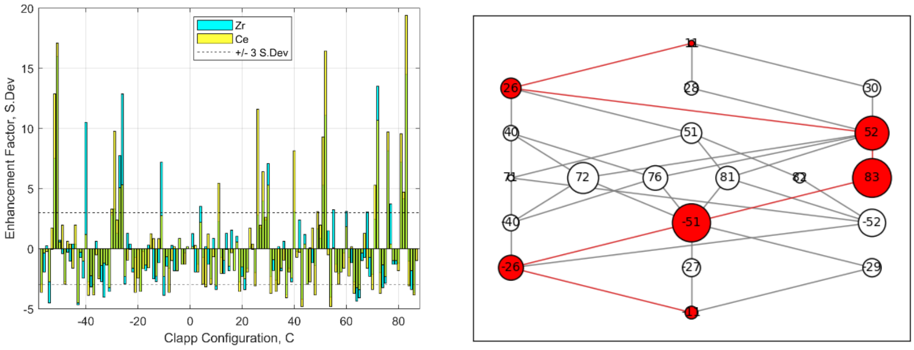

Figure 2.6: Example plots of Clapp configuration analysis, enhanced Clapp configurations by central atom (left), Clapp configuration degrade pathway showing which enhanced configurations are related by single atom type swaps (right). Data shown from the $Ce_{0.5}Zr_{0.5}O_2$ SRMO1050 RMCProfile study highlighting a defective κ-$CeZrO_4$ structure (ideal κ-$CeZrO_4$ structure would be entirely C83).

Clapp analysis can be summarised as the observed rate of occurrence of relative atomic structures in a binary alloy described in terms of the statistical likelihood of its occurrence, thus enabling a characterisation methodology for the local cation structures present in a mixed metal oxide FCC large box model.

As mentioned above, the application of the Clapp analysis method was exploited by the provision of code developed by Dr Owen who also provided the "Degrade pathways" code which highlights the relationships between enhanced Clapp configurations, these relationships are represented visually with each relative like – unlike ratio separated by tier, connecting lines show which configurations are related by a single atom site type swap, configurations in red show the most enhanced configuration for each like – unlike ratio, red lines simply show where the most enhanced configurations for each ratio are connected by single site swaps.

2.4.3.2 MATLAB scripts

As part of this work a substantial amount of time was dedicated to the construction of data analysis scripting tools to assist in mining useful structural data from the 20,000 + atom cubic supercells investigated, with RMCProfile fitting being a fundamentally iterative process these analysis scripts were also required to probe the chemical sense and overall stability of the RMCProfile configurations generated.

Ideally a healthy RMC configuration is one that fits all available data to a high standard while making fundamental chemical sense and while using the fewest possible user applied constraints.

The two primary analysis scripts developed, what they aim to extract and some of the detailed of how this is achieved are discussed below.

RMC_Compare (v7) contrasts one or more RMCProfile configurations (.rmc6f) against a reference configuration. As part of this contrast atomic displacements per species are extracted based on the site coordinates from the reference configuration and generates the atomic displacement and site occupancy (metal and O) histograms as seen in Chapters 3 and 4. The script also served as a translation tool for translating the $P2_13$ κ-$CeZrO_4$ model to describe it in terms of its FCC underpinning fluorite cation arrangement compatible with the Clapp analysis script provided by Dr. Owen. The script generates figures and reports relative to the reference configuration for each configuration run allowing for the inspection of how key structural conclusions change as a function of RMCProfile run time, helping to observe when suitable minima were reached and guiding any modifications applied to the next iterations of RMCProfile runs. Each configuration of ~27,000 atoms took approximately 1 minute on the personal computers used where early versions of this tool routinely took up to 10 minutes, this reduction in run time was critical to allowing “in-situ” assessments of the health of a running RMCProfile configuration.

Script Roles: Displacement analysis, Site occupancy analysis, ‘in-situ’ RMCProfile configuration assessing tool, patch translation for $P2_13$ to $Fm\bar{3}m$ for Clapp configuration analysis.

RMC_Analyse (v6) extracts the coordinates and atomic species of each atom present within a specific RMCProfile configuration in .cif format, it then imparts periodic boundary conditions and collates all atom-atom distances in a user defined window. This allows for the extraction of nearest neighbour cation pairs (or metal oxygen distances, although this feature is not reported) providing insight into localised clusters which deviate from the average stoichiometry. The script also outputs a O-interstitial report file listing all interstitial O and the ratio of their cation nearest neighbours if present in the input structure. Valence information is also extracted where it flags instances of when more or fewer atoms of a given type are observed within the nearest neighbour window, significant numbers of under/over coordinated atoms were observed as a clear indicator of poor model health.

Script Roles: Atom-Atom distance and type analysis, valency extractor, detector of under/over coordinated atoms.

2.5 Bibliography

1 J. Fonseca De Lima, M. H. Harunsani, D. J. Martin, D. Kong, P. W. Dunne, D. Gianolio, R. J. Kashtiban, J. Sloan, O. A. Serra, J. Tang and R. I. Walton, *J. Mater. Chem. A*, 2015, **3**, 9890–9898.

2 B. D. Cullity and S. R. Stock, *Elements of X-Ray Diffraction: Pearson New International Edition*, Pearson Education UK, Harlow, UNITED KINGDOM, 2013.

3 T. Connolley, C. M. Beavers and P. Chater, *Synchrotron Radiat. News*, 2020, **33**, 31–36.

4 M. Basham, J. Filik, M. T. Wharmby, P. C. Y. Chang, B. El Kassaby, M. Gerring, J. Aishima, K. Levik, B. C. A. Pulford, I. Sikharulidze, D. Sneddon, M. Webber, S. S. Dhesi, F. Maccherozzi, O. Svensson, S. Brockhauser, G. Náray and A. W. Ashton, *J. Synchrotron Radiat.*, 2015, **22**, 853–858.

5 A. K. Soper, *RAL Rep. RAL-TR-2011-013*.

6 Diamond Light Source, HELIOS IR furnace, https://www.diamond.ac.uk/Instruments/Imaging-and-Microscopy/I12/Sample-Environments.html, (accessed 28 March 2023).

7 W. M. Yim and R. J. Paff, *J. Appl. Phys.*, 1974, **45**, 1456–1457.

8 L. de Broglie, *Ann. Phys.*, 1925, **10**, 22–128.

9 R. Smith, *Crystallogr. Group, ISIS Facil. Rutherford Applet. Lab.*, 2011, 1–4.

10 V. F. Sears, *Neutron News*, 1992, **3**, 26–37.

11 R. I. Smith, S. Hull, M. G. Tucker, H. Y. Playford, D. J. McPhail, S. P. Waller and S. T. Norberg, *Rev. Sci. Instrum.*, 2019, **90**, 115101.

12 O. Arnold, J. C. Bilheux, J. M. Borreguero, A. Buts, S. I. Campbell, L. Chapon, M. Doucet, N. Draper, R. Ferraz Leal, M. A. Gigg, V. E. Lynch, A. Markvardsen, D. J. Mikkelson, R. L. Mikkelson, R. Miller,

K. Palmen, P. Parker, G. Passos, T. G. Perring, P. F. Peterson, S. Ren, M. A. Reuter, A. T. Savici, J. W. Taylor, R. J. Taylor, R. Tolchenov, W. Zhou and J. Zikovsky, *Nucl. Instruments Methods Phys. Res. Sect. A Accel. Spectrometers, Detect. Assoc. Equip.*, 2014, **764**, 156–166.

13 A. K. Soper, *GudrunN and GudrunX*, 2012.

14 H. M. Rietveld, *J. Appl. Crystallogr.*, 1969, **2**, 65–71.

15 G. S. Pawley, *J. Appl. Crystallogr.*, 1981, **14**, 357–361.

16 J. L. F. A. Le Bail , H. Duroy, *Mat. Res. Bull.*, 1988, **23**, 447–452.

17 A. Le Bail, *Powder Diffr.*, 2005, **20**, 316–326.

18 A. C. L. and R. B. Von Dreele, *General Structure Analysis System (GSAS)*, 2004.

19 B. H. Toby and R. B. Von Dreele, *J. Appl. Crystallogr.*, 2013, **46**, 544–549.

20 A. A. Coelho, *J. Appl. Crystallogr.*, 2018, **51**, 210–218.

21 C. L. Farrow, P. Juhas, J. W. Liu, D. Bryndin, E. S. Božin, J. Bloch, T. Proffen and S. J. L. Billinge, *J. Phys. Condens. Matter*, 2007, **19**, 335219.

22 R. L. Mcgreevy and L. Pusztai, *Mol. Simul.*, 1988, **1**, 359–367.

23 R. L. McGreevy, *J. Phys. Condens. Matter*, 2001, **13**, R887–R913.

24 R. Evans, *Mol. Simul.*, 1990, **4**, 409–411.

25 M. C. Tucker, M. T. Dove and D. A. Keen, *J. Appl. Crystallogr.*, 2001, **34**, 630–638.

26 M. G. Tucker, D. A. Keen, M. T. Dove, A. L. Goodwin and Q. Hui, *J. Phys. Condens. Matter*, 2007, **19**, 335218.

27 The MathWorks Inc., 2020.

28 L. R. Owen, H. Y. Playford, H. J. Stone and M. G. Tucker, *Acta Mater.*, 2017, **125**, 15–26.

29 P. C. Clapp, *Phys. Rev. B*, 1971, **4**, 255–270.

Chapter 3: Cerium-rich cerium zirconium oxides

The work detailed in this chapter has also been published by the authors prior to submission of this thesis.[1]

3.1 Introduction to cerium-rich cerium zirconium oxide

The materials covered in this chapter are a commercial cerium zirconium oxide solid solution with a composition of $Ce_{0.75}Zr_{0.25}O_2$ after having undergone two different thermal treatments. The industrial $Ce_{0.75}Zr_{0.25}O_2$ material investigated is very poorly crystalline in the provided 'as-made' form and required a firing step to be sufficiently crystalline to be effectively studied by diffraction techniques.

The first treatment aims to increase crystallinity by firing to improve crystallinity without inducing a phase change, keeping the material close to the 'as-made' material as such 800 °C in air was chosen as these materials are known to undergo a phase degradation to CeO_2 and ZrO_2 when fired above 900 °C in air.[2–4]

The second treatment consists of a high temperature reduction at 1050 °C for 4 hours under a reducing atmosphere, with pure H_2 used in this case. This reduction is followed by a mild oxidation; 400 °C under air for 2 hours was used in this case. This treatment is known as 'Strong Reduction Mild Oxidation' (SRMO) and may be referred to with the reduction temperature used (SRMO1050) when describing to specific samples. As described in Chapter 1, in the $Ce_{0.5}Zr_{0.5}O_2$ composition this treatment is known to form supercell cation ordering on reduction (pyrochlore phase, $Fd\bar{3}m$, $Ce_2Zr_2O_7$)[5–7] while maintaining the cation ordering on subsequent oxidation resulting in the kappa (κ-$CeZrO_4$) structure with significantly improved OSC, the SRMO1050 treatment also mimics the extreme side of the TPR-TPO experiment commonly used to look at OSC in automotive conditions. While there is no prior evidence of significant cation ordering of the pyrochlore or kappa structure forming in the $Ce_{0.75}Zr_{0.25}O_2$ composition, the treatment was chosen to investigate any nano-structural effects even in the absence of changes to the long-range order, such as nano domains of κ-$CeZrO_4$ too small in volume for Bragg reflections to be observed.

While cerium zirconium oxides have been a common topic of study for well over 40 years, nominally due to their favourable OSC properties, the cerium rich compositions are generally of less interest due to its comparatively poor OSC and more CeO_2 like behaviour compared to the more commonly studied $Ce_{0.5}Zr_{0.5}O_2$ composition. However this CeO_2 similarity favours it for theoretical and understanding focused studies such as the work undertaken by Yuxing Xu *et al.*[8] in 2019 which uses a Density Functional Theory (DFT) approach to understand the structural behaviours which result in the Raman spectra observed in CeO_2, $Ce_{0.75}Zr_{0.25}O_2$ and $Ce_{0.75}Y_{0.25}O_2$. Another DFT study undertaken by Jason Kim *et al.*[9] shows their lowest energy $Ce_{0.75}Zr_{0.25}O_2$ DFT models have a range of Ce-O and Zr-O bond distances, with Zr-O having distinctly lower average coordination numbers. Another study by Gargi Dutta *et al.*[10] in 2006 which employed a combined first principles calculations and EXAFS to study $Ce_{0.5}Zr_{0.5}O_2$ and $Ce_{0.75}Zr_{0.25}O_2$ showed evidence of long and short M-O bonds, which they related to strong and weakly bound oxygen and correlated to OSC performance. The $Ce_{0.75}Zr_{0.25}O_2$ composition was chosen for this work to act as an exemplar study closer to pure CeO_2 in order to establish methodology for studying the more complicated observations in the $Ce_{0.5}Zr_{0.5}O_2$ composition samples. To appreciate the pyrochlore cation ordering it was first important to characterise the local structures and nano-domain phase segregation present in cerium rich materials presenting a single crystalline phase material by bulk diffraction techniques.

In this work long-range and local atomic structure has been studied via laboratory X-ray and central facility X-ray and neutron diffraction techniques employing the classical Rietveld refinement method[11] and X-ray and neutron total scattering experiments undertaken to study the local structure via the Pair Distribution Function (PDF)[12–14]. The Reverse Monte Carlo[15] modelling method was employed to simulate possible atomic arrangements within a supercell which remain consistent with both the observed long range Bragg diffraction and local structure sensitive PDF giving insight into possible local-scale structures present in these materials.

3.2 Average Structure: Small-box Refinements

3.2.1 800AIR – Fired in Air at 800C

Based on existing phase diagrams[2] of cerium-zirconium oxide systems the Ce = 0.75 composition is expected to adopt the cubic $Fm\bar{3}m$ space group. Initially observed reflections via laboratory powder X-ray diffraction (pXRD) agree with this prediction and as such the initial model used to investigate these two materials was the cubic $Fm\bar{3}m$ structure. No evidence of phase segregation or additional crystalline features were observed indicating a phase pure material prior to neutron data collection.

Rietveld refinements shown in Figure 3.1 show a satisfactory match to the observed X-ray and neutron diffraction data with a wR value of 2.37 %, refined parameters of this fit are shown in Table 3.1.

While no clear evidence of an alternative phase was observed in the X-ray data, a persistent broad feature was observed in the neutron data at ~2.2 Å which would match the expected position for the forbidden (2 1 0) reflection, disallowed in face centred cubic (fcc) symmetry such as the $Fm\bar{3}m$ space group. The sample container used for the neutron experiment was made of vanadium metal, which is used for low, but non-zero, coherent scattering length giving rise to very low intensity Bragg reflections for neutron diffraction. The most intense reflection for vanadium metal is expected at 2.15 Å, and indeed a crystalline reflection barely above noise is observed at 2.15 Å in the neutron diffraction patterns shown. This instrumental environment feature is mentioned to rule it out as a cause for the broad feature noted at ~2.2 Å and discussed further below.

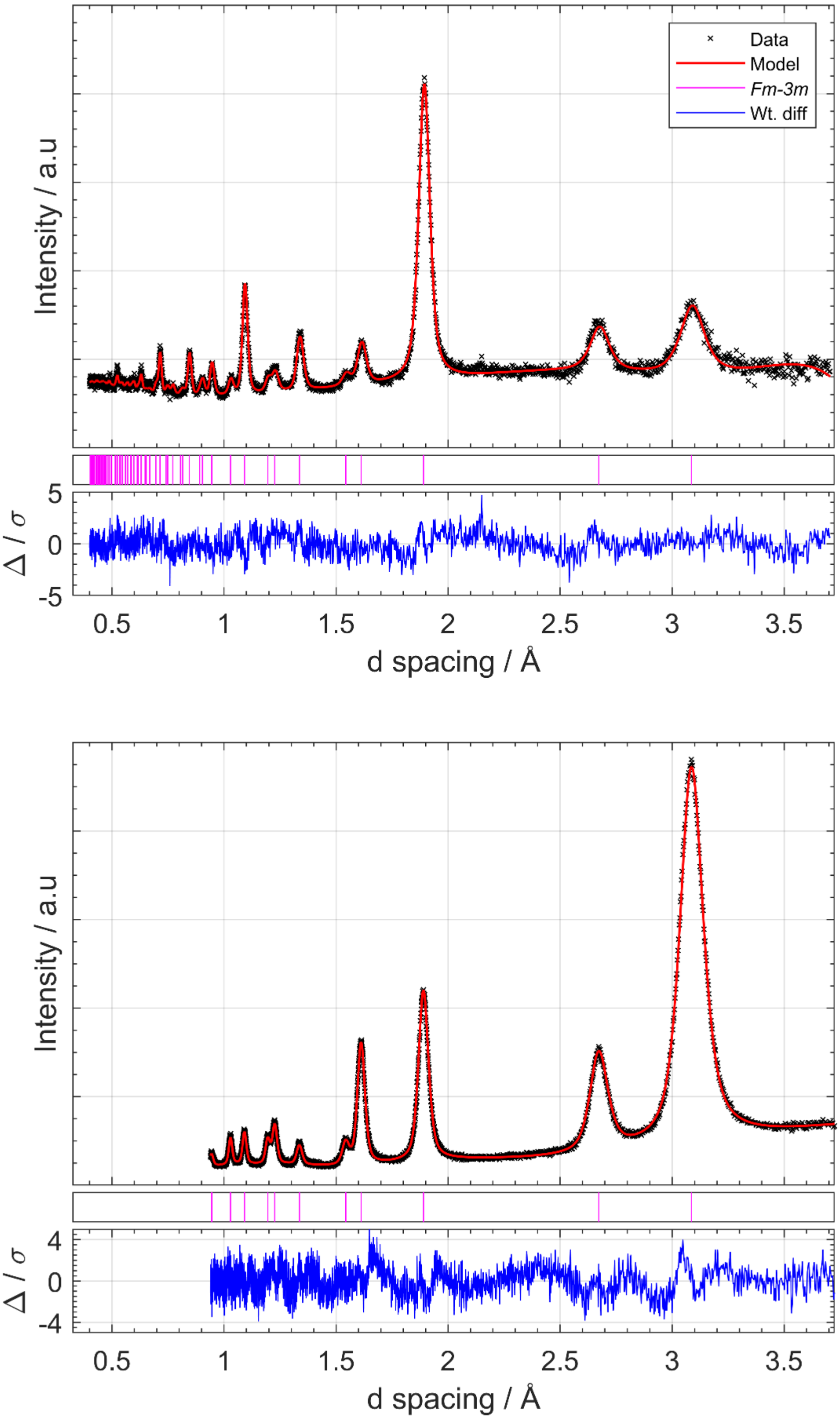

Figure 3.1: Rietveld refinement of $Ce_{0.75}Zr_{0.25}O_2$ *fired in air at 800 °C, model refined against 5 banks of neutron data and 1 bank of X-ray data using the* $Fm\bar{3}m$ *space group; Top) Neutron data obtained from Polaris neutron diffractometer, ISIS neutron spallation source, detector bank 3 of 5 shown; Bottom) X-ray data shown obtained from a monochromatic Cu K-α1 laboratory diffractometer.*

Due to the observation of the broad feature matching the fcc forbidden (2 1 0) reflection, the alternative tetragonal $P4_2/nmc$ space group usually observed in the Zr rich compositions for cerium zirconium oxides is suggested. While the volumes and unit cells of the $Fm\bar{3}m$ and $P4_2/nmc$ are visually distinct, they both describe a near identical structure shown in Figure 3.2.

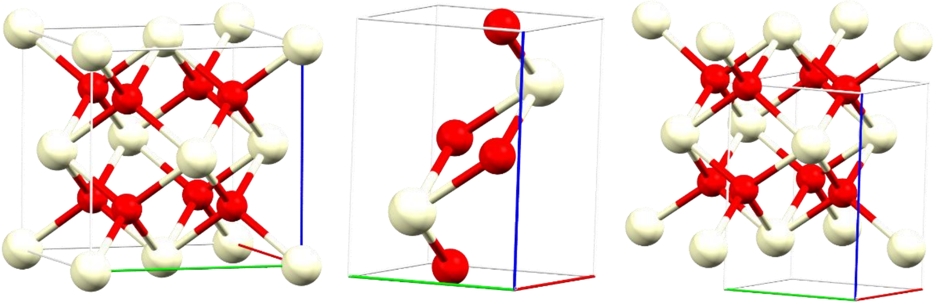

Figure 3.2: Two common cerium zirconium oxide models. Left; $Fm\bar{3}m$ unit cell. Middle; $P4_2/nmc$:2 unit cell using the 2nd origin. Right; $P4_2/nmc$:2 expanded to highlight the real space similarity between the two models. Pale yellow = metal sites (Ce/Zr), red = oxygen sites. Red line is the a lattice plane, green line is the b lattice planes with the blue line as the c lattice plane.

The lower symmetry of the tetragonal $P4_2/nmc$ space group allows for two key differences in the atomic structures when compared with the $Fm\bar{3}m$ model. First the $P4_2/nmc$ space group being a tetragonal space group allows for an independent *c* lattice parameter. While the reflection profile observed for the F800 treated sample is relatively broad, no distinctive reflection splitting was observed in the data showing that the bulk average structure remains in a ‘cubic’ like arrangement where metal-metal distances are the same regardless of which lattice direction they span. Due to the 45 ° difference in orientation and the different real space used in the unit cell descriptions, the ‘cubic’ lattice parameter *a* / *c* ratio where the $P4_2/nm$ space group described a cubic structure is $\frac{1}{\sqrt{2}}$ or approximately 0.7071… which would result in lattice plane independent cation distances.

The second more important key difference afforded by the lower symmetry of the $P4_2/nmc$ space group is the general *z* coordinate of the oxygen site allowing it to sit slightly off the idealised cubic description giving two marginally different M-O bond distances, 2.29 Å and 2.34 Å for the $Ce_{0.75}Zr_{0.25}O_2$ F800 sample discussed here. The second difference allows some degree of asymmetry for the oxygen atoms which is forbidden in a true cubic space group. The primary reflection affected by the O site *z* coordinate displacement is the fcc forbidden (2 1 0), or (0 1 2) in the $P4_2/nmc$ setting. As such a “pseudo”-cubic unit cell using the $P4_2/nmc$ space group was investigated for this cerium rich composition and all others where the fcc forbidden reflection was observed.

Figure 3.3 shows the observed X-ray and neutron data and Rietveld calculated $P4_2/nmc$ fits of the $Ce_{0.75}Zr_{0.25}O_2$ material fired in air at 800 °C. The model matched the observed data well with a wR value of 2.22 % which is marginally better fit than that of the $Fm\bar{3}m$ structure. The visual fit across all banks is also slightly better for the $P4_2/nmc$ description however this difference is minor and correlates with the expected outcome when adding additional parameters to any model.

The $P4_2/nmc$ (0 1 2) reflection does provide a good match to the broad feature at ~2.2 Å while also not fitting intensity from the vanadium peak at 2.15 Å as is highlighted best in the difference curve of Figure 3.3. This reflection is caused by the oxygen site not being ideally positioned between the four nearest cations, this discrepancy is allowed in the $P4_2/nmc$ structure as the oxygen z coordinate is not special or fixed.

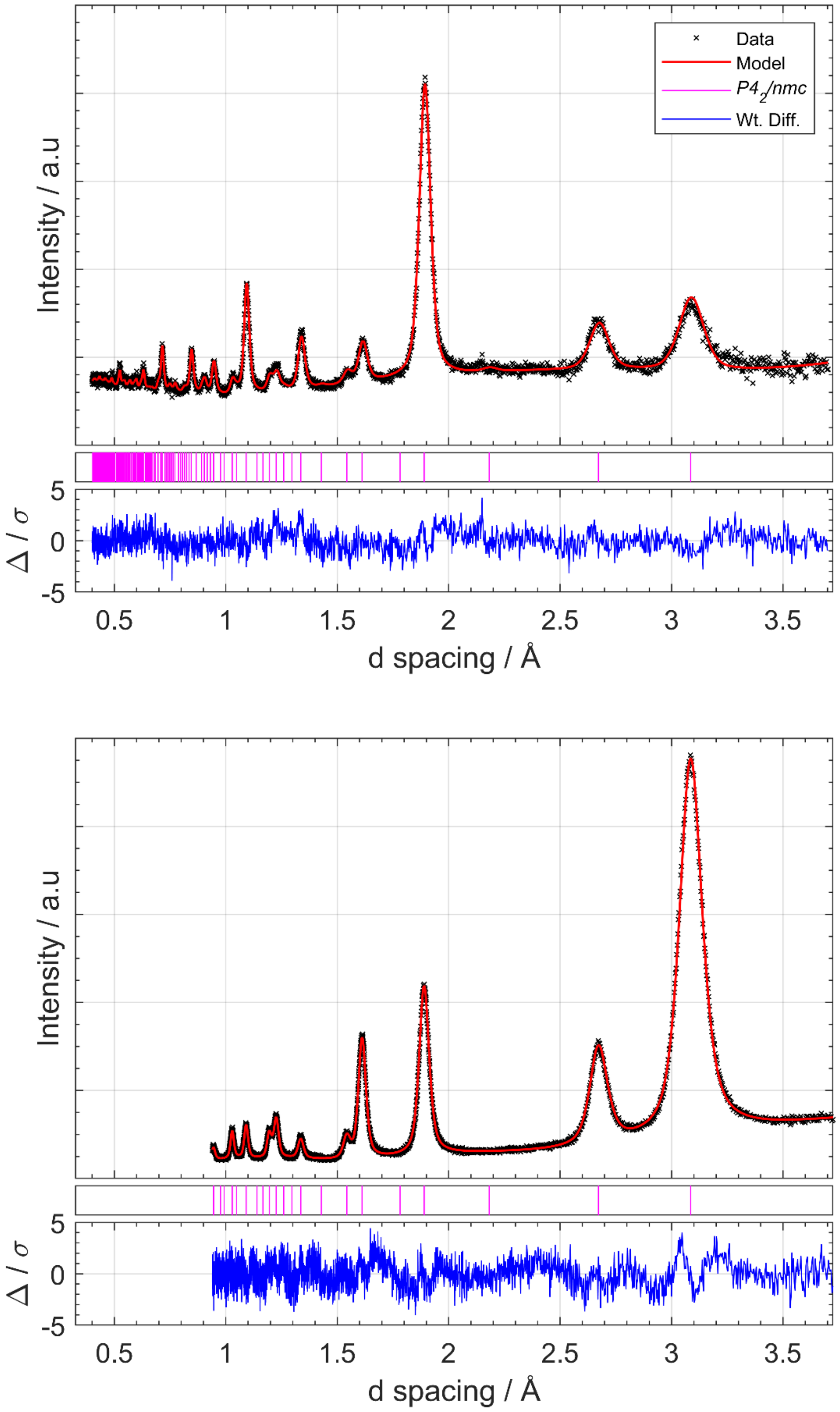

Figure 3.3: Rietveld refinement of $Ce_{0.75}Zr_{0.25}O_2$ *fired in air at 800 °C, model refined against 5 banks of neutron data and 1 bank of X-ray data using the* $P4_2/nmc$ *space group; Top) Neutron data obtained from Polaris neutron diffractometer, ISIS neutron spallation source, detector bank 3 of 5 shown; Bottom) X-ray data shown obtained from a monochromatic Cu K-α1 laboratory diffractometer.*

Table 3.1 shows the Rietveld refined parameters for the $Fm\bar{3}m$ model fit to data collected on the $Ce_{0.75}Zr_{0.25}O_2$ refined $Fm\bar{3}m$ model, while the observed fit could easily be considered good enough, closer inspection shows an abnormally large O Uiso value.

Table 3.1: Refined parameters for $Ce_{0.75}Zr_{0.25}O_2$ *using the face centred cubic* $Fm\bar{3}m$ *space group, a = 5.34580(13). Calculated density 7.0471 g/cm*^{3} *wR = 2.37 %*

Atom	Wyck.	x	y	z	Uiso / Å^2	Occ.
Ce	4a	0	0	0	0.00802(12)	0.75
Zr						0.25
O	8c	¼	¼	¼	0.01772(14)	1

Total oxygen site displacement in the Ce0.75Zr0.25O2 F800 sample comes to ~ 0.07 Å offset from the idealised cubic O site.

Table 3.2 shows the refined *a* and *c* lattice parameters had an *a*/*c* ratio very close the ideal cubic ratio of $\frac{1}{\sqrt{2}}$ or 0.7071 showing that the cubic cation sites of CeO_2 were adopted which would be consistent with the $Fm\bar{3}m$ model. However the oxygen *z* coordinate did not refine to 0.5 as would be expected in an idealised CeO_2 arrangement and indicate true $Fm\bar{3}m$ symmetry showing that while the metal sites and overall unit cell was cubic a low level of oxygen displacement remained forbidding face centred cubic symmetry. Occupancies were refined periodically but found to be stable, as such they were fixed to minimise the number of free parameters during the final refinements. Total oxygen site displacement in the $Ce_{0.75}Zr_{0.25}O_2$ F800 sample comes to ~ 0.07 Å offset from the idealised cubic O site.

Table 3.2: Refined parameters for $Ce_{0.75}Zr_{0.25}O_2$ *using the tetragonal* $P4_2/nmc$ *space group in the 2*nd *origin, a = 3.7802(6), c = 5.3436(16), a/c ratio = 0.7074 (ideal cubic ratio = 0.7071…). Calculated density = 6.954 g/cm*^{3}*, oxygen 'displacement' from cubic z coordinate = 0.0134 (0.072 Å), wR = 2.22 %*

Atom	Wyck.	x	y	z	Uiso / Å^2	Occ.
Ce	2a	¼	-¼	¼	0.00448(14)	0.75
Zr						0.25
O	4d	¼	¼	0.4866(3)	0.00949(17)	1

Note; The 2nd origin of the $P4_2/nmc$ space group was used due to the use of GSAS2, in the 2nd origin, the idealised 'cubic' oxygen *z* position equivalent is at z = 0.5.

While not shown yet in this thesis, the forbidden reflection at 2.2 Å is more visually observable other compositions of ceria zirconia studied with trends in the oxygen *z* position being inversely linear with Ce % across the Ce = 0.25, 0.5 and 0.75 compositions studied. Trends observed are discussed more in Chapter 9 and are a large reason for the proposal of the $P4_2/nmc$ structure for Rietveld refinements for the Ce = 0.75 composition.

3.2.2 1050H2 – SRMO treated

As described above, the same $Ce_{0.75}Zr_{0.25}O_2$ bulk material was exposed to a separate SRMO treatment with reduction at 1050 °C and subsequent oxidation at 400 °C for 2 hours in air. The treatment aimed to mimic conditions known to cause a phase change in the $Ce_{0.5}Zr_{0.5}O_2$ system, and while no bulk phase change was expected the question was focused on any nano structural changes that may give a deeper understanding to why the system appears to maintain a solid solution, rather than undergoing a partial phase change to κ-$CeZrO_4$ and CeO_2, nor to CeO_2 and ZrO_2 as would be expected if heated to 1050 °C under air.

The initial expectation was that this material was in the cubic $Fm\bar{3}m$ phase, especially as any deviations from the cubic cation lattice would be clear to observe due to the sharper reflection profile of this sample. The sharp reflection clearly observed in the weighted difference in all neutron diffraction pattern at 2.15 Å matches the most intense reflection expected from vanadium metal sample can.

No reflection splitting was observed, which due to the sharper reflection profile increases the confidence that this material's average structure exists as a single phase composition with cubic symmetry. However due to the relatively sharper reflection profile post SRMO treatment, the fcc forbidden (2 1 0) reflection is clearly observed in the weighted difference plot of Figure 3.4, seen as a broad hump at 2.2 Å slightly overlapping with the sharp vanadium reflection at 2.15 Å. As described for the F800 treated sample above, this reflection is the (0 1 2) reflection of the tetragonal $P4_2/nmc$ space group so as such, the SRMO1050 treated sample was also investigated using the $P4_2/nmc$ space group expected for the 'pseudo-cubic' t" phase of $Ce_{1-x}Zr_xO_2$ most likely where x = ~0.5, and a known requirement in the literature for forming the kappa phase with SRMO treatment.[5,16–18]

As with the F800 sample discussed above, the $Fm\bar{3}m$ model fit (wR 3.68 %) shown in Figure 3.4 was slightly worse than the $P4_2/nmc$ model fit (wR: 3.44 %) shown in Figure 3.5 which could likely be accounted for by the additional two parameters (*c* lattice parameter, oxygen *z* coordinate) afforded by the lower symmetry of the *P*4$_2$/*nmc* structural description of cerium zirconium oxide.

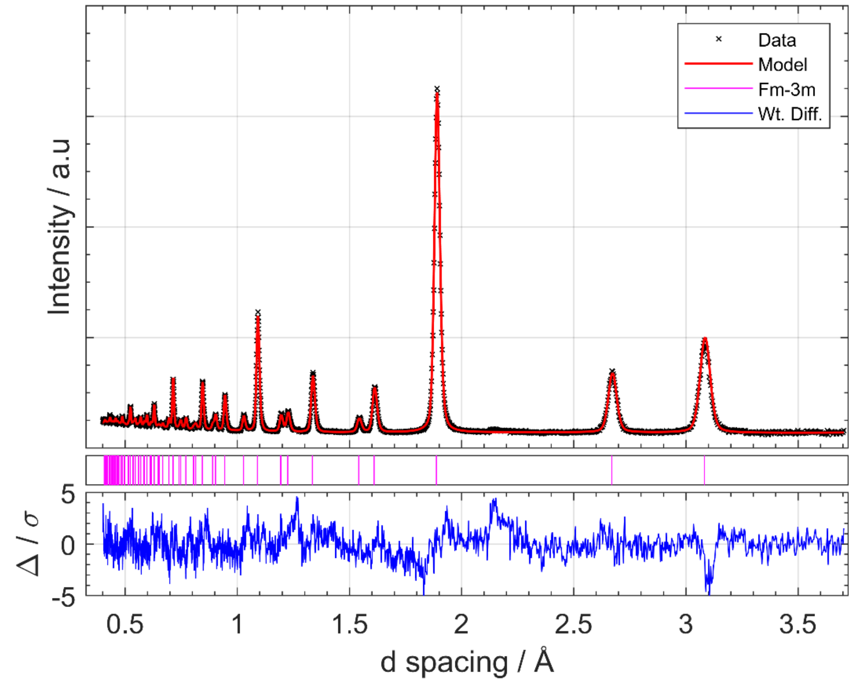

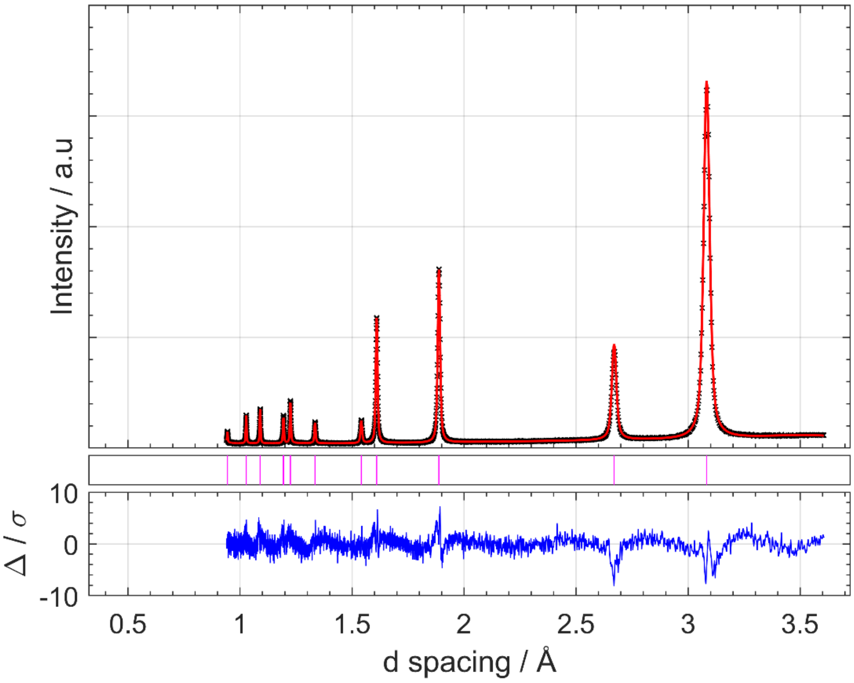

Figure 3.4: Rietveld refinement of SRMO treated $Ce_{0.75}Zr_{0.25}O_2$*, model refined against 5 banks of neutron data and 1 bank of X-ray data using the* $Fm\overline{3}m$ *space group; Top) Neutron data obtained from Polaris neutron diffractometer, ISIS neutron spallation source, detector bank 3 of 5 shown; Bottom) Data shown obtained from a monochromatic Cu K-α1 laboratory diffractometer.*

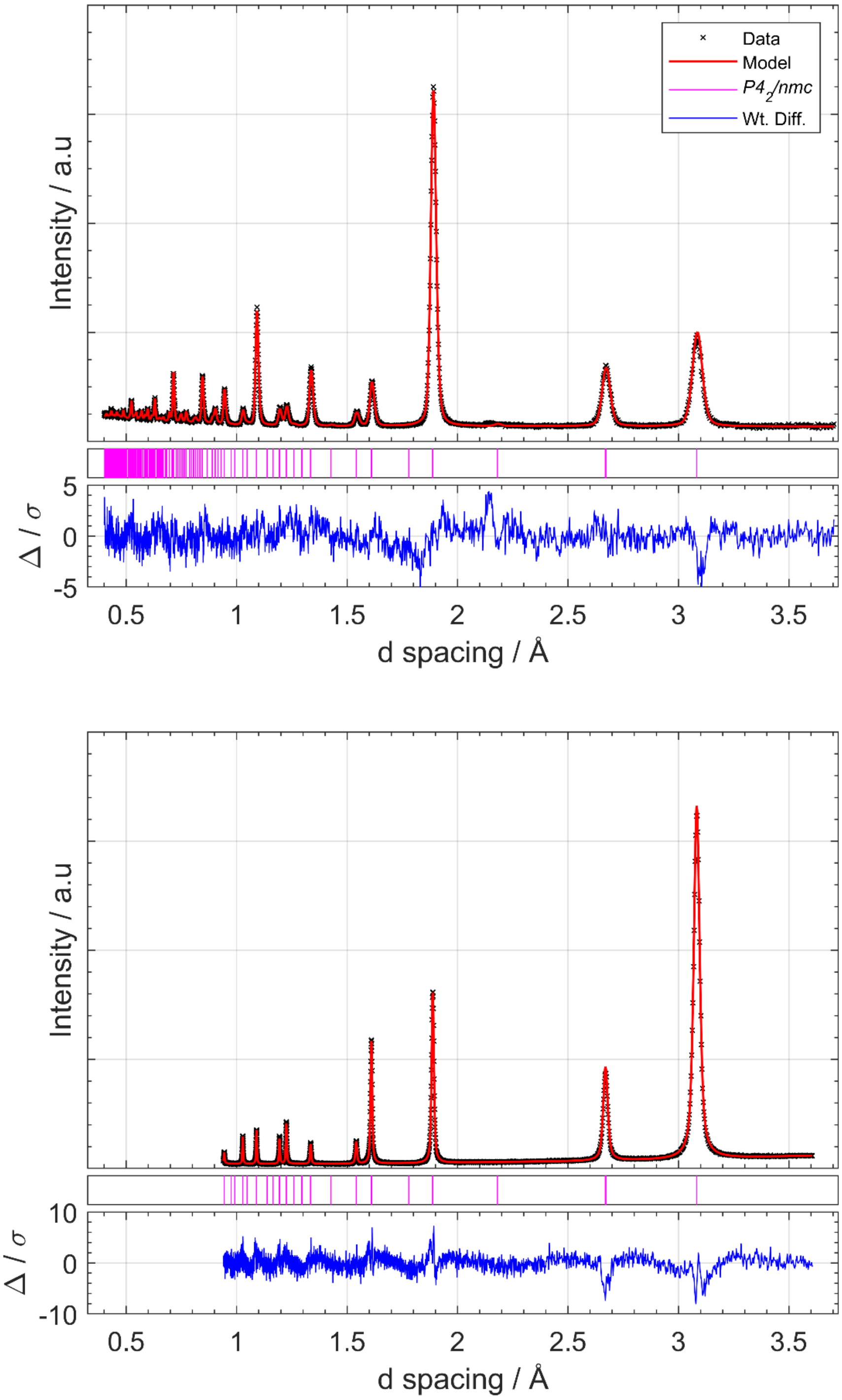

Figure 3.5: Rietveld refinement of SRMO treated $Ce_{0.75}Zr_{0.25}O_2$*, model refined against 5 banks of neutron data and 1 bank of X-ray data using the* $P4_2/nmc$ *space group; Top) data obtained from Polaris neutron diffractometer, ISIS neutron spallation source, detector bank 3 of 5 shown; Bottom) Data shown obtained from a monochromatic Cu K-α1 laboratory diffractometer.*

Perhaps a more obvious difference between the F800 and SRMO1050 data sets which has not yet been discussed in detail is the distinct difference in reflection profile. While not a source of focus in this investigation this difference can be accredited to a difference in crystallite size and strain, with the F800 data showing smaller crystallites and higher degree of inhomogeneous lattice strain. Both a decrease in strain and an increase in crystallite size is associated to sintering and higher temperature treatments, as such the sharper more distinct reflections of the SRMO1050 diffraction pattern is entirely expected due to the higher temperature treatment. An important note on the Rietveld refinement method is that sharper line profiles lead to a higher degree of precision on refined parameters, as such it comes as no surprise that the two SRMO1050 models have a high degree of agreement on Uiso values and calculated density shown in Table 3.3 and Table 3.4, while the F800 models show a weaker agreement on these parameters. Occupancies were refined periodically but found to be relatively stable at the expected values, during the final refinements they were fixed to minimise the number of free parameters. Total oxygen site displacement in the $Ce_{0.75}Zr_{0.25}O_2$ SRMO1050 sample comes to ~ 0.05 Å offset from the idealised cubic O site.

Table 3.3: Refined parameters for $Ce_{0.75}Zr_{0.25}O_2$ using the face centred cubic $Fm\bar{3}m$ space group, a = 5.33935(5). Calculated density = 6.977 g/cm^3, wR = 3.68 %.

Atom	**Wyck.**	**x**	**y**	**z**	**Uiso / Å^2**	**Occ.**
Ce Zr	4a	0	0	0	0.00442(5)	0.75 0.25
O	8c	¼	¼	¼	0.01062(5)	1

Table 3.4: Refined parameters for $Ce_{0.75}Zr_{0.25}O_2$ using the tetragonal $P4_2/nmc$ space group in the 2nd origin, a = 3.77438(13), c = 5.3422(3), a/c ratio = 0.7065 (ideal cubic ratio = 0.7071…). Calculated density = 6.977 g/cm^3, oxygen 'displacement' from cubic z coordinate = 0.0091 (0.049 Å), wR = 3.44 %.

Atom	**Wyck.**	**x**	**y**	**z**	**Uiso / Å^2**	**Occ.**
Ce Zr	2a	¼	-¼	¼	0.00430(5)	0.75 0.25
O	4d	¼	¼	0.49089(11)	0.00958(6)	1

3.2.3 Average Structure PDF refinements

While Bragg diffraction informs on the average long-range repeating atomic structure, the PDF informs on the average short to mid-range atomic structure making these two structural diffraction-based techniques complementary when considering local and bulk atomic structure. As with the Rietveld study of Bragg diffraction data above, both the $Fm\overline{3}m$ and $P4_2/nmc$ space groups were considered when fitting a structural model to the observed data. Due to transformation of the unit cell to $P1$ for fitting in PDFgui and the removal of symmetry constraints, some additional tools could be employed to study the importance of the oxygen z position independently from the a/c lattice parameter ratio. This was achieved by constraining the a/c lattice parameter ratio of the $P4_2/nmc$ model to 0.7071, forcing a cubic arrangement of cations. The two models studied by PDF fitting can be summarised as 'True cubic' and a 'Pseudo-cubic' unit cell. The 'True cubic' was consistent with the $Fm\overline{3}m$ space group with true cubic symmetry. The 'Pseudo-cubic' is based on the $P4_2/nmc$ structure constrained to a cubic unit cell allowing displacements in the oxygen z coordinate; this resulted in the oxygen z coordinate being the only structural difference in these two models.

While both 'True-cubic' and 'Pseudo-cubic' structures were tested, due to the highly similar visual nature of both fits only the better fitting 'Pseudo-cubic' fits are shown in Figure 3.6. All PDFgui fitted parameters are shown in Tables 3.5-3.8. The impact of a refined oxygen z coordinate manifests as a subtle improvement to the overall fit across the whole r range.

The first clear difference shown in Figure 3.6 between the two sample treatments is the significant dampening on the F800 sample which is characteristic of smaller crystallite domain sizes which was also observed in the Bragg diffraction in the form of reflection profile broadness. The main characteristics and peak positions in the short range $r < 10$ Å are highly similar for both PDFs showing that the average local structure of both samples remains the same.

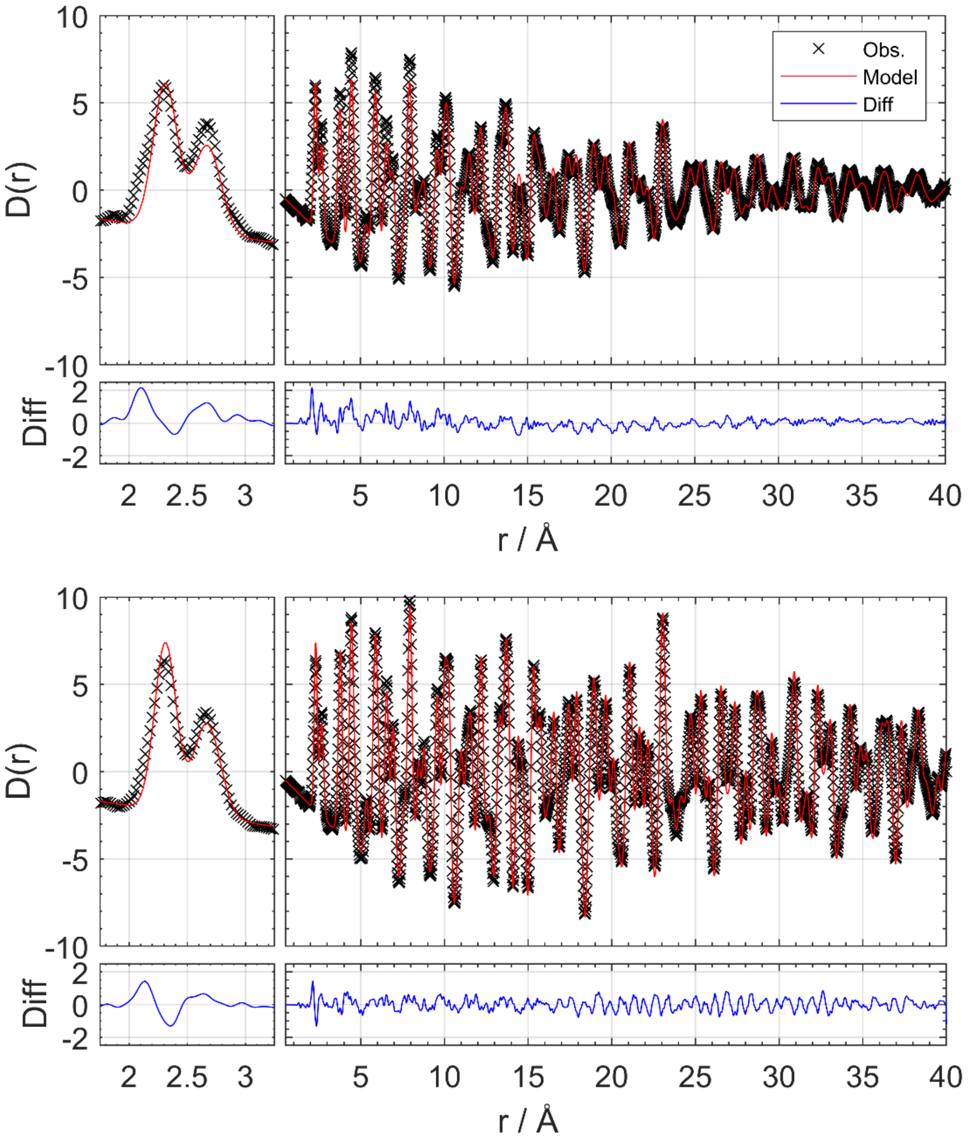

Figure 3.6: Neutron pair distribution functions (D(r)) and calculated patterns of $Ce_{0.75}Zr_{0.25}O_2$ *in the 'Pseudo-Cubic' structure. Top; Sample fired in air at 800 °C. Bottom; SRMO1050 treated sample. Neutron total scattering data acquired from Polaris.*

While both samples show good match to the same long range structure, the short-medium range of the F800 sample shows significant mismatch in the < 10 Å region, while the precise cause of this mismatch has not been fully solved in this study the mismatch region of < 10 Å could be due to a crystalline surface phase such as one found in CeO_2 nano-crystals by Luo *et al.*[19] where they used neutron total scattering data to show that the primary defects in CeO_2 nano-crystals were partially reduced Ce_3O_{5+x} surface phases.

Given the relatively large surface area of the F800 sample it is highly plausible that such a surface structure would be significantly more distinct in the more poorly crystalline F800 treated sample than the more crystalline SRMO1050 treated sample. However, no such investigative study has been performed for the F800 data to confirm this surface reduced phase hypothesis.

Due to the constrained lattice parameters of the "pseudo cubic" fits where $a = 0.7071 \times c$, only the lattice parameter c is reported in Table 3.6 and Table 3.8 which is directly comparable to the "True-cubic" lattice parameter a.

Table 3.5 shows the refined parameters for the "True cubic" model fit against neutron diffraction data of the $Ce_{0.75}Zr_{0.25}O_2$ F800 sample shown as a baseline for the "Pseudo-cubic" model parameters reported in Table 3.6.

Table 3.5: Refined parameters from small-box PDF fitting of F800 treated $Ce_{0.75}Zr_{0.25}O_2$ using the 'True-cubic' model based on the $Fm\bar{3}m$ space group, a = 5.3533(8), crystallite diameter = 78(3) nm, Rw = 0.1706.

Atom	Wyck.	x	y	z	Uiso / Å^2	Occ.
Ce Zr	4a	0	0	0	0.0127(9)	0.75 0.25
O	8c	¼	¼	¼	0.0176(7)	1

Table 3.6: Refined parameters from small-box PDF fitting of F800 treated $Ce_{0.75}Zr_{0.25}O_2$ using the 'Pseudo-cubic' model based on the $P4_2/nmc$ space group in the 2nd origin with cubic cation spacing, c = 5.3532(8), oxygen 'displacement' from cubic z coordinate = 0.111 (0.059 Å), crystallite diameter = 76(3) nm, Rw = 0.1685.

Atom	Wyck.	x	Y	z	Uiso / Å^2	Occ.
Ce Zr	2a	¼	-¼	¼	0.0123(9)	0.75 0.25
O	4d	¼	¼	0.489(2)	0.0163(8)	1

Table 3.7 shows the refined parameters for the "True cubic" model fit against neutron diffraction data of the $Ce_{0.75}Zr_{0.25}O_2$ SRMO1050 sample shown as a baseline for the "Pseudo-cubic" model parameters reported in Table 3.8

Table 3.7: Refined parameters from small-box PDF fitting of SRMO1050 treated $Ce_{0.75}Zr_{0.25}O_2$ using the ‘True-cubic’ model based on the $Fm\bar{3}m$ space group, a = 5.3481(3), crystallite diameter = 233(16) nm, Rw = 0.0948.

Atom	Wyck.	x	Y	z	Uiso / Å^2	Occ.
Ce Zr	4a	0	0	0	0.0077(4)	0.75 0.25
O	8c	¼	¼	¼	0.0137(3)	1

Table 3.8: Refined parameters from small-box PDF fitting of SRMO1050 treated $Ce_{0.75}Zr_{0.25}O_2$ using the ‘Pseudo-cubic’ model based on the $P4_2/nmc$ space group in the 2nd origin with cubic cation spacing, c = 5.3480(3), oxygen ‘displacement’ from cubic z coordinate = 0.087 (0.046 Å), crystallite diameter = 227(15) nm, Rw = 0.0928.

Atom	Wyck.	x	y	z	Uiso / Å^2	Occ.
Ce Zr	2a	¼	-¼	¼	0.0076(3)	0.75 0.25
O	4d	¼	¼	0.4913(16)	0.0128(4)	1

3.3 RMC Modelling

To better understand local structure, Reverse Monte Carlo modelling was undertaken using neutron total scattering data acquired from the Polaris neutron diffractometer. The aim of the modelling was to probe the local atomic nature of the solid-state material by simulating structures which are consistent with the long range average structure data informed by the Bragg scattering and the short-mid range PDF structural data. The RMC method is described in greater detail in Chapter 2.

While neutron diffraction indicates that oxygen displacement is present in these materials which disfavours the $Fm\bar{3}m$ space group, the cubic space group was still chosen as the starting model used to generate the 12 × 12 × 12 supercells. This was chosen for three primary reasons, namely the a/c lattice parameter ratio of the $P4_2/nmc$ structure formed a cubic description of the cation sites, as such using a cubic unit cell would allow for a clearer description of the supercell. Second the oxygen z position flexibility afforded by the $P4_2/nmc$ space group would be inherently allowed in the RMCProfile generated supercell as all symmetry constraints of the original unit cell would be relaxed. Lastly by using a true cubic starting description, it would be significantly easier to build scripts and use existing tools to analyse features of the supercell, such as displacement, unit cell site occupancies and preferred local structures present in the resulting 20,736 atom supercell.

To probe for nanostructures, reduce the impact of initial model bias and allow for true solid solutions to manifest, swaps were allowed between cerium and zirconium atoms. All RMC models were weighted to be driven by locally weighted PDF data while also adhering to the medium range PDF and Bragg data; this was to give local structures the ability to deviate from the average structure, while keeping the supercell consistent with the experimentally observed long range average structure.

Effort was made to keep the RMC models and processing consistent between datasets; however due to the intensive setup of the RMC models and the unique data processing features encountered for each dataset some inconsistencies between the approaches used for each sample remain. The inclusions of additional X-ray total scattering F(*Q*) data for the $Ce_{0.75}Zr_{0.25}O_2$ SRMO1050 treated sample; the applied inverse crystallite size function to the $Ce_{0.75}Zr_{0.25}O_2$ F800 which corrects for the *r*-range dampening observed due to a crystallite size of ~90 nm. These non-standard corrections are discussed and explained as appropriate with the data/models they relate to.

To enable analysis of the 20,736 atom supercells (an additional 6912 if vacancy sites are considered) MATLAB scripts were developed to probe the models generated, a summary of these scripts and their roles can be found in Chapter 2. A significant portion of the work undertaken involved the development, and use of these unique tools to probe the distance from ideal site, interatomic distances between atoms, nearest neighbour species, reduced unit cell occupancies and vacancy site occupancies. Additional tools were used to complement those generated such as the Clapp configuration analysis script written by Dr Lewis Owen[20,21] who gave permission for its use in this work. The Clapp configurations shown in this work are reported as the mean enhancement of 100 RMCProfile refined configurations in order to eliminate the impact spurious configurations through statistical means, while the initial configurations were refined in an accessible run duration of ~24 hours, achieving a statistically significant number of RMCProfile refined configurations required use of a computational cluster, the SCARF[22] computation cluster at the ISIS neutron and muon source was used to generate the 100 RMCProfile refined configurations used for Clapp configuration analysis for both the F800 and SRMO1050 treated samples discussed below.

3.3.1 Initial setup for F800 supercell model

Initial setup of the RMC model follows the method described in Chapter 2 with the following exceptions. It was noted that the PDF generated by STOG was dampened by the finite crystallite size of the sample, which is a feature of the data that is not normally accounted for during data processing. To ensure the model was as comparable as possible to models using data from more crystalline systems, such as that of the $Ce_{0.75}Zr_{0.25}O_2$ SRMO1050 sample, this finite crystallite size dampening required accounting for. RMCProfile v 6.7.8 lacks a sufficient crystallite size function so the crystallite size dampening envelope function from PDFgui was employed and inverted to enhance the raw data rather than dampen it. This correction was applied to the G(r) data after STOG processing but prior use with the RMC model, and a crystallite size of 90 nm was found to be approximately appropriate for this dataset.

3.3.2 Initial setup for SRMO1050 supercell model

During trial runs of this model, it became apparent that additional atomic sites were required to best fit the data; this manifested in the form of movement of atoms from their original site to an interstitial site in the $Fm\bar{3}m$ (4b, 0.5, 0.5, 0.5, $m\bar{3}m$) structure. Based on charge constraints this additional site was deemed a Frenkel type defect, in this case believed to be an oxide ion occupying a interstitial position leaving a vacancy in the oxide lattice. Additional support for this is the X-O and X-M bond distances for this interstitial site being comparable to existing O-O and O-M distances. To accommodate this and probe the volume of interstitial oxygen present, a special vacancy atom (Va) was used within the RMCProfile model with no scattering or mass and the same atomistic constraints as oxygen, the oxygen and vacancy atoms were allowed to swap positions with a given probability, keeping overall stoichiometry of the supercell balanced. This Va atom gives the SRMO1050 model an additional 6912 atomic sites over the F800 model while maintaining the same number of Ce, Zr and O atoms.

Figure 3.7 shows the final RMCProfile supercell models, collapsed unit cells and classical starting models used for the two treatments of $Ce_{0.75}Zr_{0.25}O_2$ investigated and highlights the need for bulk analysis tools and scripted analysis to extract useful information from the raw supercells.

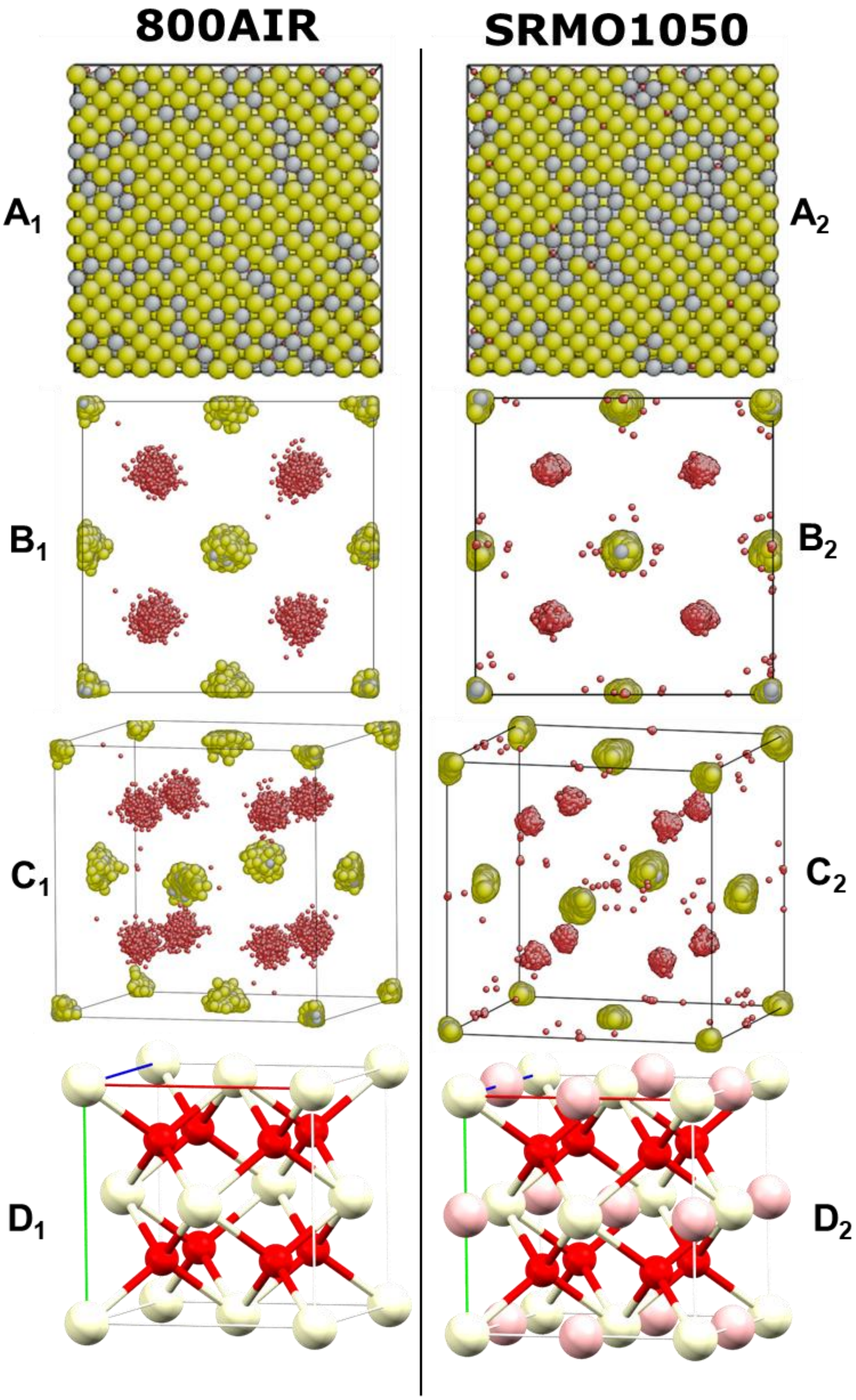

Figure 3.7: 12 × 12 × 12 supercell generated from RMC based on the fluorite unit cell. A) RMC generated supercell containing 20736 atoms. B) Supercell collapsed into a single fluorite unit cell, viewing angle from a single face. C) Viewing angle offset for additional perspective, yellow = cerium, grey = zirconium, red = oxygen. D) Classical view of the starting model. red = regular oxygen site, white = metal site, pink = interstitial oxygen site. Left, X_1) Model refined against the F800 treated sample. Right, X_2) Model refined against the SRMO1050 treated sample.

3.3.3 Results of RMC fitting of F800 data

Figure 3.8 shows fitted pattern of the RMCProfile generated 12 × 12 × 12 supercell is in good agreement with the observed data as shown in Figure 3.8. In particular the short-range PDF shows a significantly improved fit over the small box PDF fit shown earlier in Figure 3.6 in this chapter.

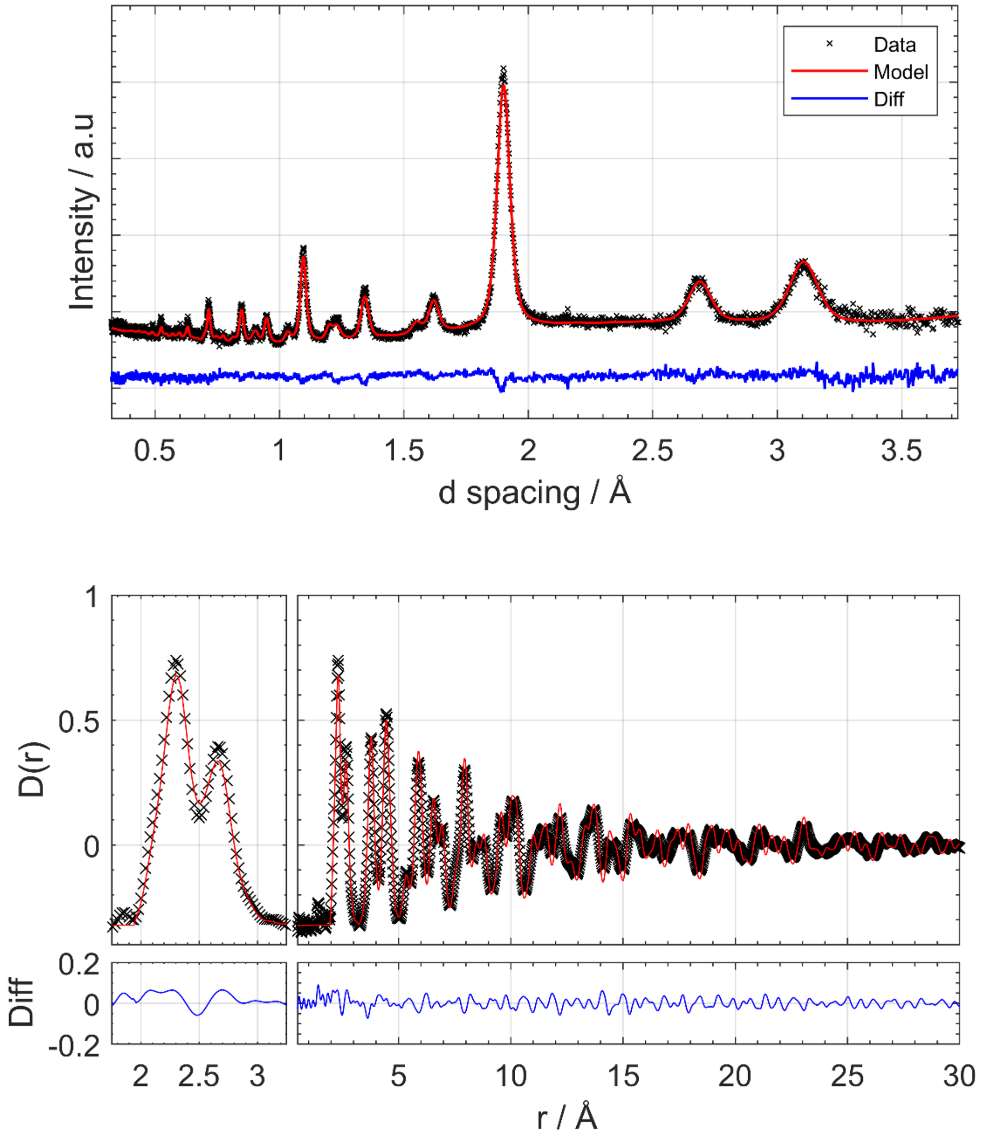

Figure 3.8: Datasets and calculated patterns from the RMC generated 12 × 12 × 12 supercell for the F800 treated sample. Top: TOF neutron data acquired on Polaris bank 3. Bottom: Short range 0-10 Å neutron pair distribution function acquired on Polaris, full fitted region extends to ~30 Å.

The Figure 3.9 shows a histogram of the atomic displacement from the initial ideal crystallographic site. RMCProfile has no explicit thermal motion corrections such as Uiso or Beq values leaving the only method available for accounting for thermal motion is for the atoms to physically deviate from these sites, so even in an ideal system some displacement would be expected. It is observed that the Ce appears to be marginally more displaced compared to the Zr with nearly all Zr displacements being smaller than 0.3 Å while Ce displacement is still evident to 0.4 Å.

The magnitude of oxygen displacement fits roughly what is expected from thermal motion, however a small portion of oxygen appears to trail off with significant levels of displacement, this could be evidence of small regions of oxygen *z* position displacement.

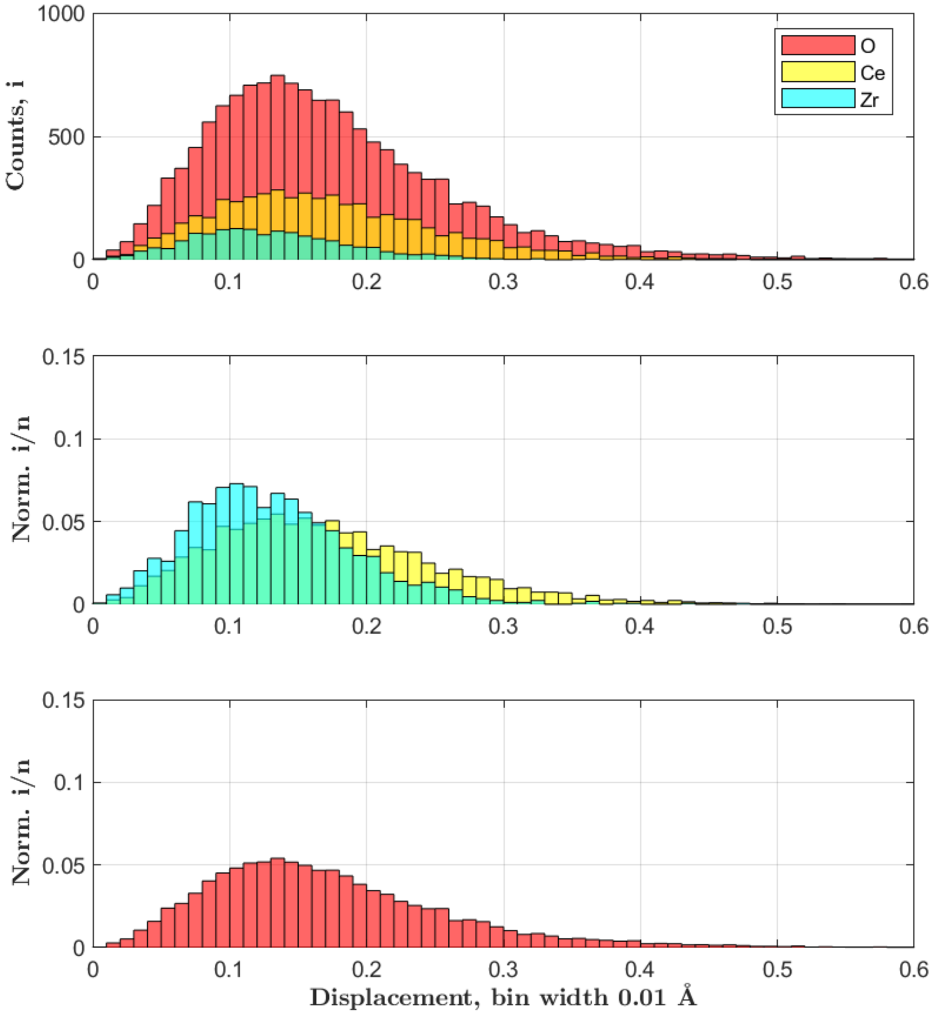

Figure 3.9: Histogram of atomic displacement counts by species for the F800 treated sample. Counts, Total = 20,736; Ce = 5184; Zr = 1728; O = 13824. Displacement distance measured from the Fm$\bar{3}$m idealised coordinate. Top; All displacements by atomic species. Middle; Cation (Ce, Zr) site displacements by atomic species. Bottom; Anion (O) site displacements by atomic species.

Figure 3.10 shows the collapsed unit cell site occupancy information extracted from the supercell model. When considering the atomic site occupancies of the 12 × 12 × 12 supercell model, made up of 1728 individual cubic unit cells, with each explicitly describing the 4 cation and 8 oxygen sites each of the 12 sites. In the original $Fm\bar{3}m$ space group all 4 of these cation sites and all 8 of the oxygen sites are equivalent, however as the RMC supercell is described with no symmetry constraints each of these equivalent sites become independent and were each assigned a 'Primitive site ID' number for ease of analysis. Primitive site ID's (*P*1) 1-4 being the symmetrically equivalent Ce/Zr occupied 0, 0, 0 *m*3*m* site and 5-12 the being the symmetrically equivalent ¼, ¼, ¼, -43*m* O occupied site of the original $Fm\bar{3}m$ structure, P1 site ID's and ideal atomic coordinates are shown in Table 3.9.

The occupancy histograms show that all four cation sites are approximately Ce = ~75 %, Zr = ~25 % with a small level of deviation indicating that within each unit cell no repeating arrangement of Ce/Zr is forming which shows the model is correctly constrained to avoid long range order which would be evident in the Bragg diffraction if such structures were indeed present. Due to the model being built with full oxygen occupancy assumed for charge balance, no abnormal behaviour was expected or observed in the oxygen sites the occupancy of these 8 sites was not informative in this system.

Table 3.9: P1 transcription of the $Fm\bar{3}m$ unit cell of ceria zirconia with final site occupancy of the 1728 base unit cells.

Atom	*P*1 Site ID	Wyck.	x	y	z	Occ. / %
Ce : Zr	1	4a	0	0	0	77.9 : 22.1
Ce : Zr	2	4a	0.5	0.5	0	75.4 : 24.6
Ce : Zr	3	4a	0.5	0	0.5	73.7 : 26.3
Ce : Zr	4	4a	0	0.5	0.5	72.9 : 27.1
O	5	8c	0.25	0.25	0.25	1
O	6	8c	0.75	0.75	0.25	1
O	7	8c	0.75	0.25	0.75	1
O	8	8c	0.25	0.75	0.75	1
O	9	8c	0.75	0.75	0.75	1
O	10	8c	0.25	0.25	0.75	1
O	11	8c	0.25	0.75	0.25	1
O	12	8c	0.75	0.25	0.25	1

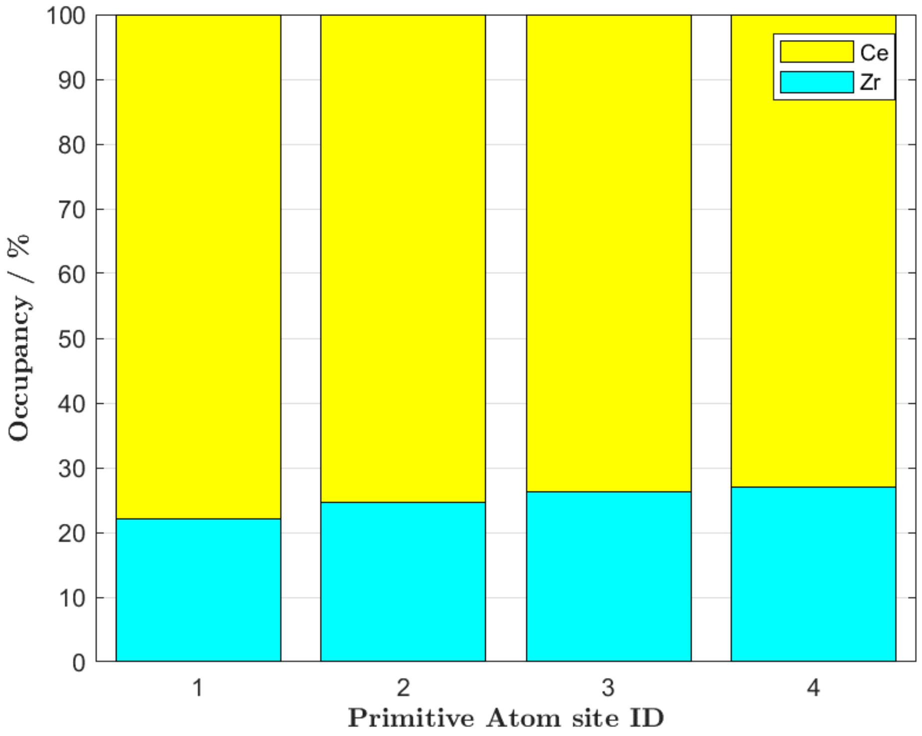

Figure 3.10: Cation site occupancy by individual unit cell cation sites for the F800 treated sample. All sites are symettrically equivlent in the original structure.

Figure 3.11 visualises an investigation of the nearest cation neighbour species and distance of all 6,912 cations present within the model. The cation species and the magnitude of interatomic distances between each of these pairings matched the statistically expected values for a solid solution. Combined with the atom site occupancy information discussed above this information indicates that on average there was no specific ordering of cations on each symmetrically equivalent site, and no clustering of cations across nano regions of the big box model. In summary this paints the picture that this model fits the classical description of a solid-solution material with no unexpected local structures present.

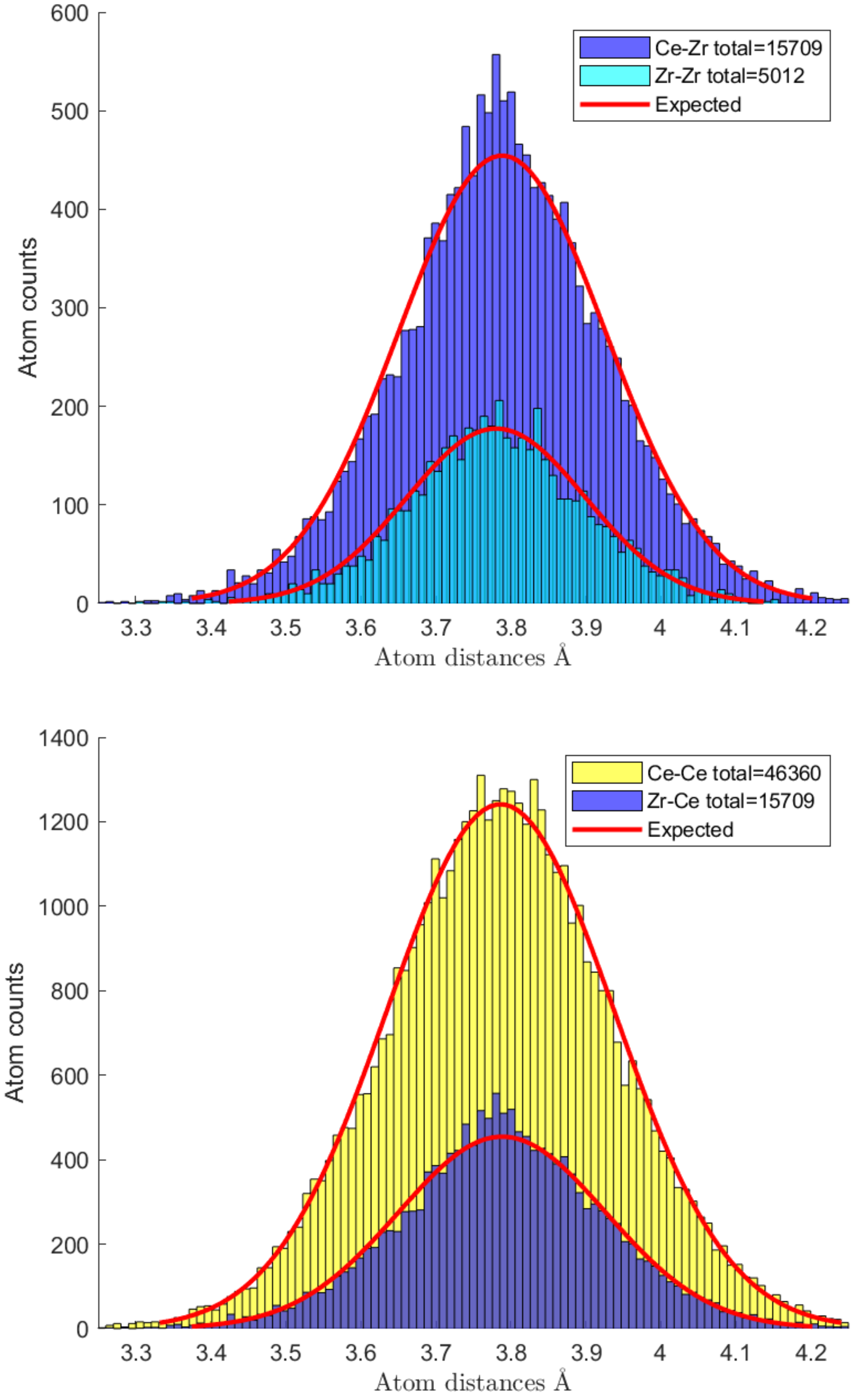

Figure 3.11: Histogram of nearest neighbour cation count and distance by species, for the F800 treated sample. The red line shows the expected intensity profile for single distribution which is compositionally defined. Top: Zr-Zr and Zr-Ce. Bottom: Ce-Ce and Ce-Zr.

Figure 3.11 shows an investigation of the relative local structure of the cerium and zirconium fluorite lattice undertaken via the Clapp configuration analysis[20,21] method. By ignoring the oxygen present and reducing the system to a binary alloy a more detailed statistical analysis of the cation structures present is allowed, and the method as described by Clapp[23] was undertaken. Clapp configuration analysis in this example focuses on the nearest cation neighbour shell of each individual cation. In a fcc binary system there are 12 atoms in the nearest cation neighbour shell, with the inclusion of the central atom there is a total of 144 possible symmetrically unique configurations that these 13 (1 central, 12 nearest neighbours) atoms can arrange in. These symmetrically unique configurations are labelled with positive or negative numbers based on the shell consisting of primarily ‘like’ or ‘unlike’ atoms respectively, relative to the central atom. Labels close to 0 represent configurations with large numbers of like (positive) or unlike (negative) atomic neighbours. As such configuration C1 represents a case where all C12 nearest neighbours are the same atomic species as the central atom, where configuration C-1 would be where all nearest cation 12 neighbours are not the same species as the central atom. For clarity there is no configuration labelled 0.

For the F800 model it was statistically significant that no significant configurations were observed that all 144 possible configurations occurred firmly within 0.5 standard deviations of the statistically expected profile, far below the implied threshold of significance at +/- 3 standard deviations. This strongly supports the hypothesis that the material is a homogeneous solid solution with a compositionally average local structure as an exceptionally good fit to observed data has been achieved with only compositionally defined statistical localised cation arrangements observed.

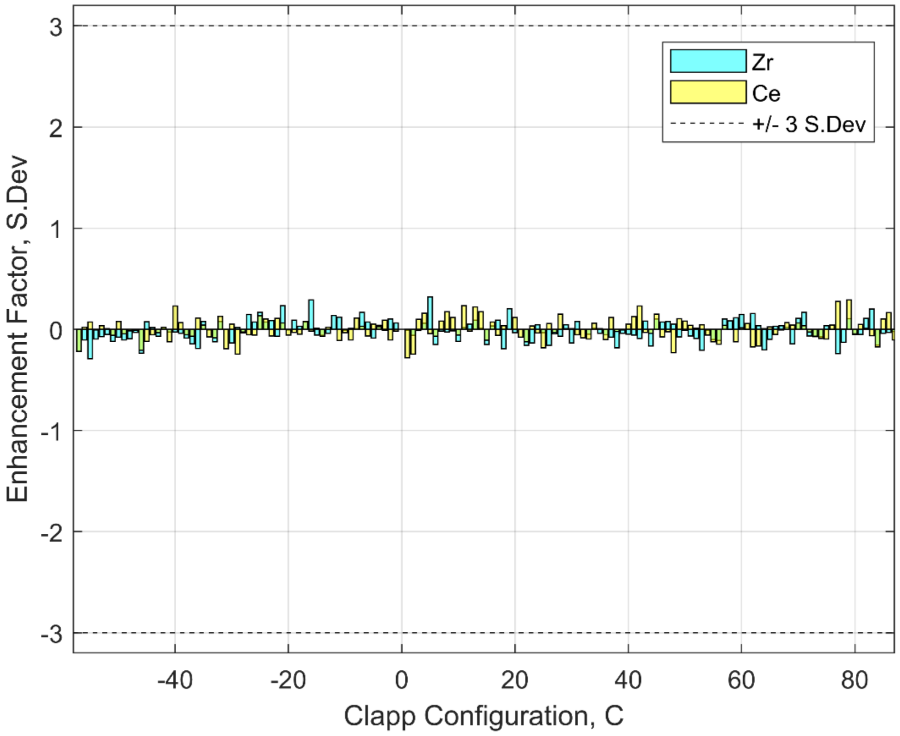

Figure 3.12: Histograms of Clapp configurations observed within the 12 × 12 × 12 supercell for the F800 treated sample. Clapp enhancement factors plotted are a mean of 100 independent RMCProfile refinemed configurations using randomised starting cation arrangements but otherwise identical parameters.

3.3.4 Results of RMC fitting of SRMO1050 data

Figure 3.13 shows the RMC model calculated fits vs the observed neutron Bragg diffraction pattern, neutron PDF and X-ray F(Q) data. The RMC supercell model proves an excellent fit to the neutron Bragg and PDF data and a good fit to the X-ray F(Q) pattern. The X-ray F(Q) pattern mismatch is likely due to anomalies in the data processing rather than the model; however due to time limitations and limited experience processing X-ray total scattering data these artifacts were not removed, instead the X-ray F(Q) data was employed as additional data and was weighted as supporting data as to avoid driving the model to account for data processing artifacts.

Notably the supercell model for the SRMO1050 treated sample matches the observed PDF significantly better than what was achieved for the F800 model discussed above, this is likely to do with the additional data processing steps required to crudely account for the significantly higher lattice strain and smaller crystallite sizes, the difference curves between these two models are nearly a magnitude of order in difference.

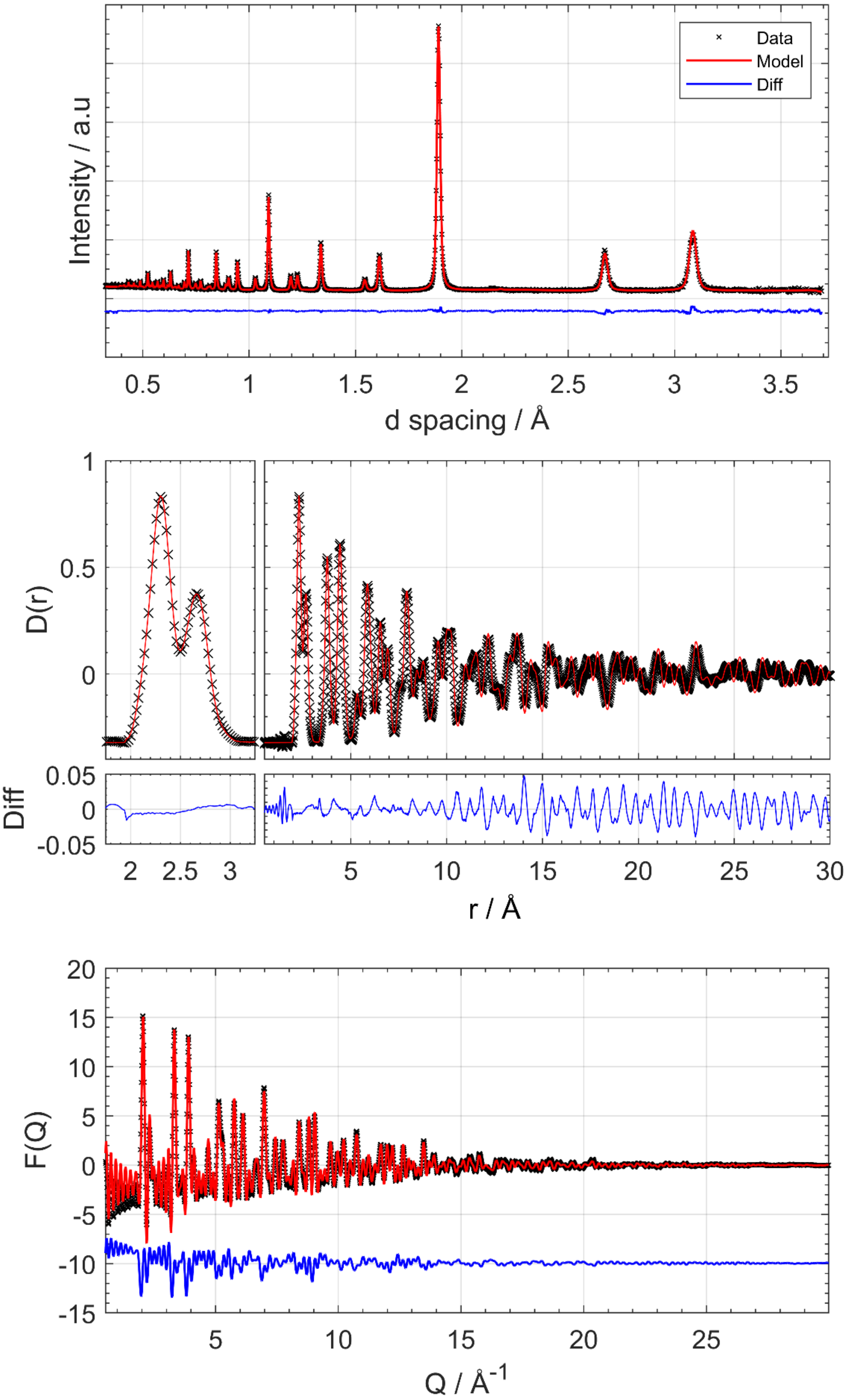

Figure 3.13: Datasets and calculated patterns from the RMC generated 12 × 12 × 12 supercell for the SRMO1050 treated sample. Top; TOF neutron diffraction spectra acquired on Polaris bank 4. Middle; Short range 0-10 Å. Neutron pair distribution function acquired on Polaris, full fitted region extends to ~30 Å. Bottom; X-ray F(Q) data acquired from I15-1

Figure 3.14 shows a histogram of atomic displacement observed for the 1050SRMO model which showed several key differences compared to the F800 model. The first was the obvious difference in displacement profiles for Ce and Zr. Zr appears to be more uniform in displacement with a slightly less average displacement, while Ce appears to have a bimodal displacement profile. The trace Zr dispersed beyond 0.2 Å could easily be artifacts due to Ce-Zr swaps which have been allowed due to the inbuild error acceptance of the RMCProfile process. A simple hypothesis for this bimodal Ce displacement could be that the heat treatment applied caused more ordering in the lighter O and Zr atoms present, while the heavier Ce atoms have only partially undergone the thermal induced changes and maintain a higher relative strain.

The interstitial oxygen displacement appears to have two profiles, one sharp at ~ 0.05 Å and another broader, similar to the average oxygen displacement, observed at ~ 0.16 Å. A sharp distribution was expected due to the interstitial site simply having less space than the regular oxygen site, the second profile observed is broad in nature and more like the bulk O profile, however this could simply be an artefact of the RMC modelling process due to the relatively few interstitial oxygens present, totalling to only 2.115 % of the overall oxygen content.

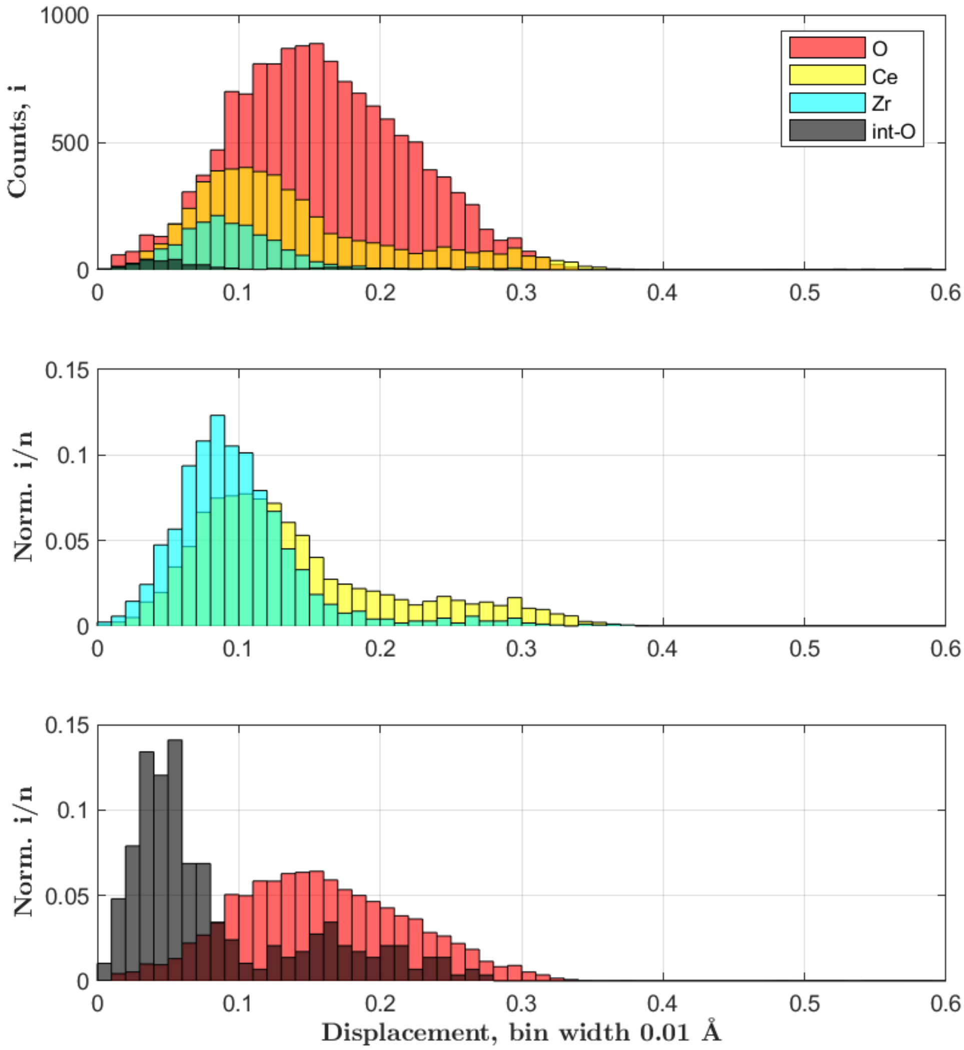

Figure 3.14: Top) Histogram of atomic displacement counts by species for the SRMO1050 treated sample. Middle) Cerium (yellow) and zirconium (cyan) displacements normalised to relative atom count. Bottom) Bulk oxygen (red) and interstitial oxygen (black) normalised to relative atom count. Counts, Total = 20,736; Ce = 5184; Zr = 1728; O = 13824, int-O = 291. Displacement distance measured from the Fm$\bar{3}$m idealised coordinate.

Figure 3.15 shows the cation occupancy for the SRMO1050 treated model which shows no average structure preference based symmetrically equivalent sites confirming the model has not formed any long-range features which haven't been observed in the Bragg diffraction, and that the idealised ratio of 75 % Ce and 25 % Zr is approximately maintained across each cation site within each unit cell across the supercell model. Table 3.10 shows the original sites and the mean final atomic occupancies of the base 1728 unit cells.

Table 3.10: P1 transcription of the Fm$\bar{3}$m unit cell used for the RMC SRMO1050 model of ceria zirconia with interstitial sites with final site occupancies.

Atom	***P1* Site ID**	**Wyck.**	**x**	**y**	**z**	**Occ. / %**
Ce : Zr	1	4a	0	0	0	74.1 : 25.9
Ce : Zr	2	4a	0.5	0.5	0	74.9 : 25.1
Ce : Zr	3	4a	0.5	0	0.5	76.7 : 23.3
Ce : Zr	4	4a	0	0.5	0.5	74.3 : 25.7
O : Va	5	8c	0.25	0.25	0.25	98.8 : 1.2
O : Va	6	8c	0.75	0.75	0.25	97.8 : 2.2
O : Va	7	8c	0.75	0.25	0.75	98.6 : 1.4
O : Va	8	8c	0.25	0.75	0.75	98.1 : 1.9
O : Va	9	8c	0.75	0.75	0.75	97.8 : 2.2
O : Va	10	8c	0.25	0.25	0.75	97.4 : 2.6
O : Va	11	8c	0.25	0.75	0.25	97.6 : 2.4
O : Va	12	8c	0.75	0.25	0.25	97.1 : 2.9
Interstitial O sites						
O : Va	13	4b	0.5	0.5	0.5	4.3 : 95.7
O : Va	14	4b	0	0	0.5	4.6 : 95.4
O : Va	15	4b	0	0.5	0	3.4 : 96.6
O : Va	16	4b	0.5	0	0	4.5 : 95.5

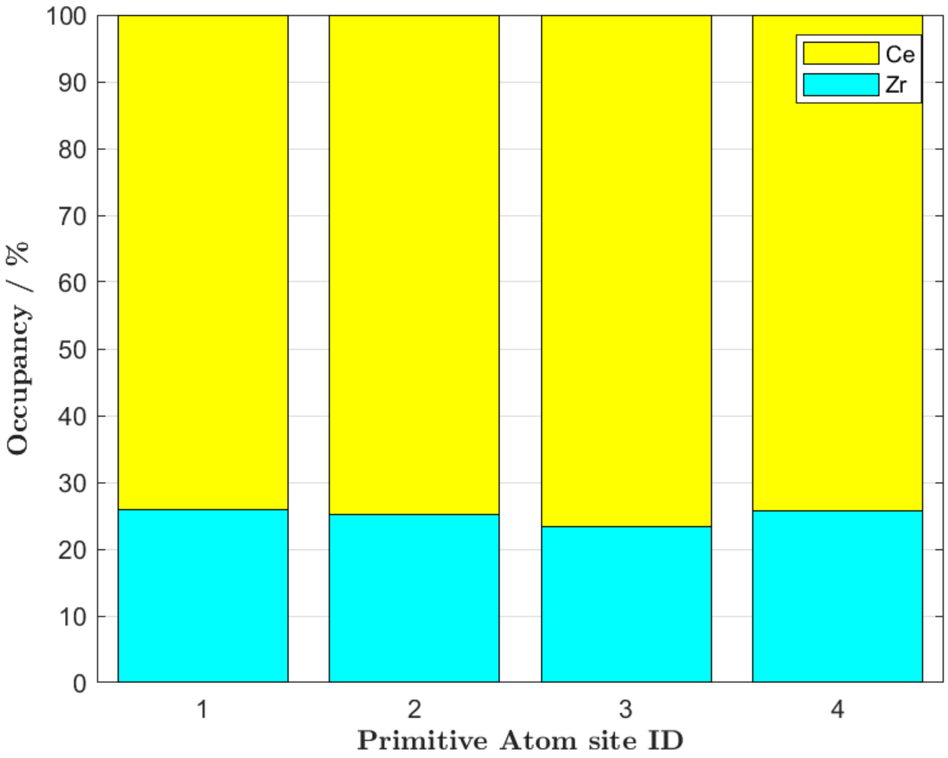

Figure 3.15: Cation site occupancy by individual unit cell cation sites for the SRMO1050 treated sample. All sites (1-4) are symmetrically equivalent in the original structure.

Figure 3.16 shows the 8 original oxygen sites (Primitive Atom site ID 5-12) within the $Fm\bar{3}m$ model alongside the 4 interstitial oxygen sites (Primitive Atom site ID 13-16). The relative occupancies of the model were probed to help identify how much interstitial oxygen was present and if there was a site preference which would form vacancies. Due to all 8 original oxygen sites being symmetrically equivalent and the same being true for all 4 interstitial sites it was expected that vacancies would form equivalently across the regular oxygen sites and the interstitial sites would be equivalently occupied. The overall oxygen content refined to the interstitial sites equated to 2.105% of the overall oxygen present, giving the system studied the formula of $Ce_{0.75}Zr_{0.25}O_{1.958}(Oi)_{0.042}$ where (Oi) is the Frenkel type interstitial oxygen described above.

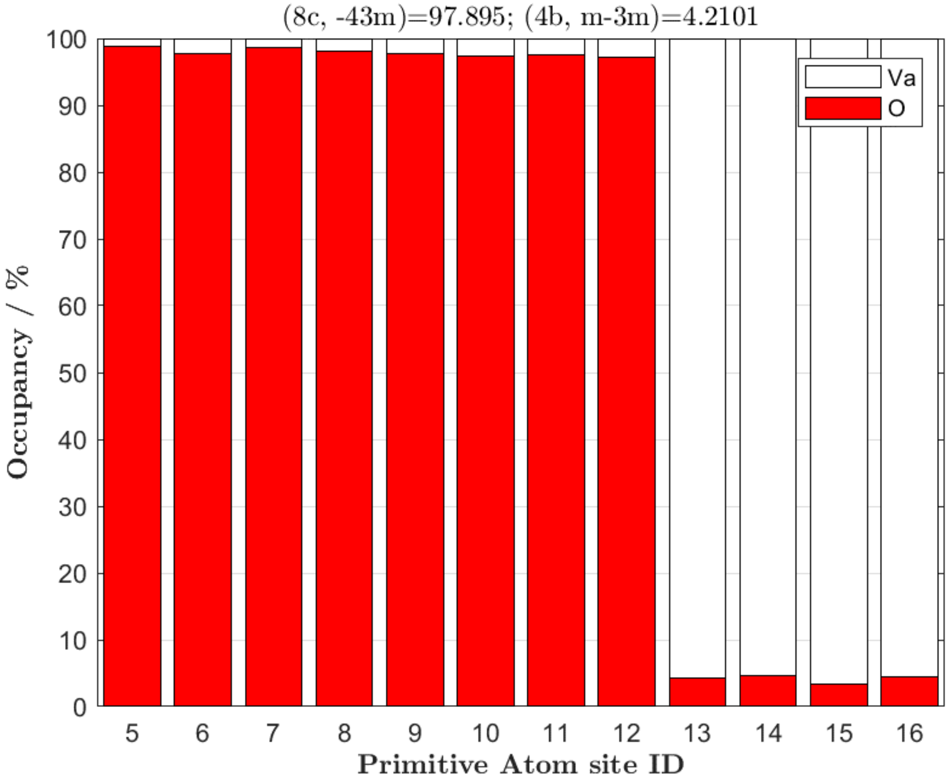

Figure 3.16: Oxygen site occupancy by individual unit cell oxygen and interstitial sites for the SRMO1050 treated sample. Sites (5-12) are symmetrically equivalent bulk oxygen sites, while sites 13-16 are symmetrically equivalent interstitial oxygen sites.

Interstitial oxygen sites in ceria based materials have been mentioned in the literature previously, Luo *et al.*[19] undertook a Raman spectroscopy and neutron total scattering study investigating surface oxygen defects in CeO_2 and related the importance of these defects to the observed OSC properties.

Similarly a study by Andriopoulou[24] et al. used powder X-ray diffraction and in-situ Raman spectroscopy study cerium zirconium oxides and rare earth [La, Nd, Y, Pr] doped cerium rich cerium zirconium oxides relating to synthesis route, they show that the synthesis route highly impacts the observed oxide species present and observed average structure phases and claim that the low temperature OSC properties of ceria zirconia can be primarily attributed to the mobility of oxygen in these interstitial sites. A study by Mamontov and Egami[25] introduced earlier used neutron diffraction, Electron Paramagnetic Resonance and TPR to study oxygen vacancies and interstitial oxygen defects in CeO_2 and $Ce_{0.7}Zr_{0.3}O_2$, they concluded that the presence of zirconia played a stabilising role on these defects via the reduction of Ce^{4+} to Ce^{3+} giving increased resistance to thermal sintering. They claim that interstitial oxygen defects are the source of cerium zirconium oxides OSC properties and that further stabilisation of these defects would further improve thermal resistance of these supports.

Figure 3.17 shows a histogram of the cation-cation distances by species. Unlike with the F800 series data, the ratio of nearest neighbours observed for the SRMO1050 treated model was not equivalent to the stoichiometry defined ratios with a distinct preference for same species cation neighbours.

This neighbouring preference strongly implies the existence of same species clustering within the structure. These domains only occur over short length scales, a few nanometers at most since Bragg diffraction provides no evidence of long-range phase separation. Inhomogeneous nano-domains has been observed in ceria-zirconia based materials before by E. Mamontov *et al.*[26] in 2003 who undertook a pulsed neutron scattering study on various $Ce_{0.5}Zr_{0.5}O_2$ samples and found that their samples were better described as nano-regions of $Ce_{0.4}Zr_{0.6}O_2$ in a matrix of $Ce_{0.7}Zr_{0.3}O_2$, the OSC properties of their materials also showed no correlation with crystallite size as is often accredited to OSC in the literature, but rather showed an inverse correlation with the domain sizes of the $Ce_{0.4}Zr_{0.6}O_2$ regions. While the composition clearly differs, the observation of Zr rich nano-domains agrees with the results indicated by this RMC study.

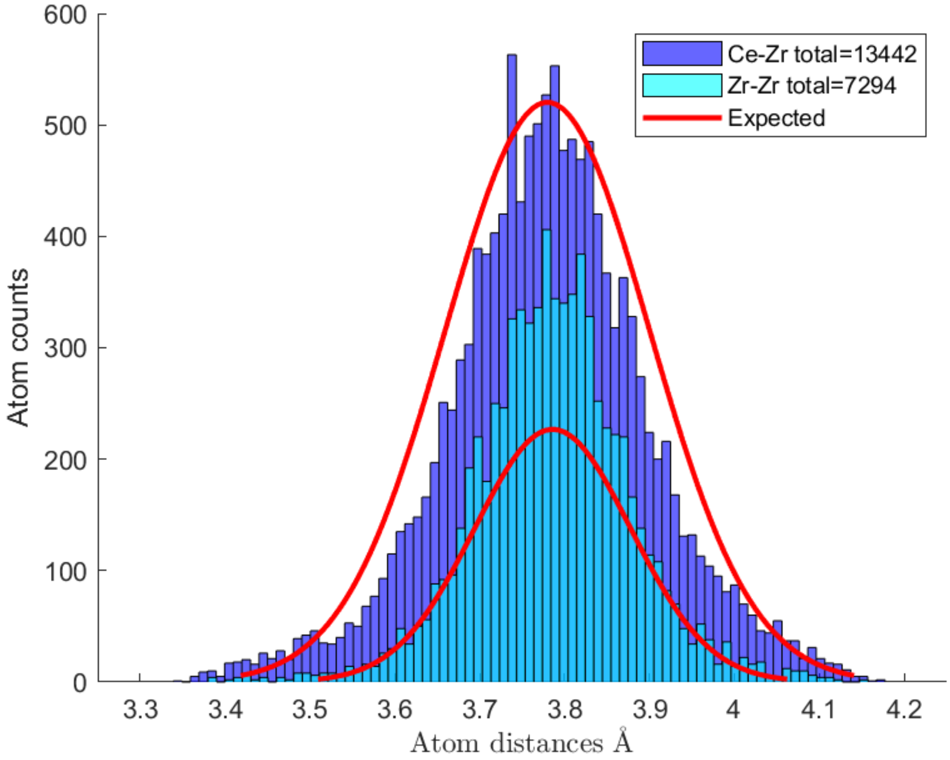

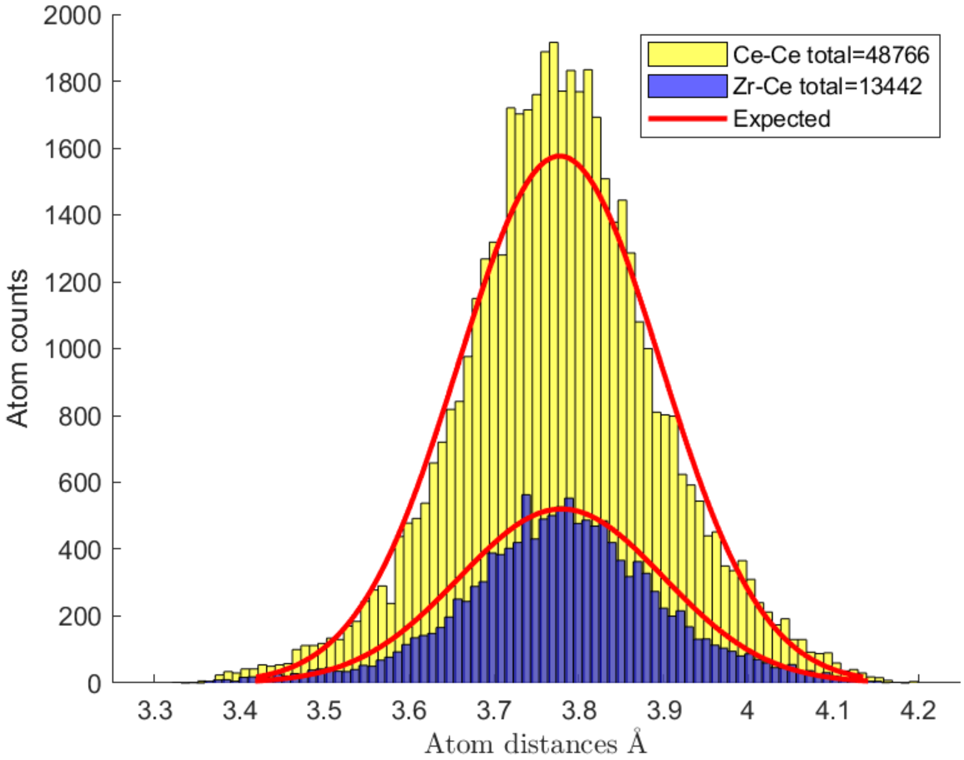

Figure 3.17: Histogram of nearest neighbour cation count and distance by species for the SRMO1050 treated sample. The red line shows the expected intensity profile for single distribution which is compositionally defined. Top: Zr-Zr and Zr-Ce. Bottom: Ce-Ce and Ce-Zr.

The preference for local like-like clustering of cations is confirmed by the Clapp configuration analysis shown in Figure 3.18. Unlike the true solid solution implied for the F800 sample discussed earlier, the SRMO1050 sample shows a significant number Clapp configurations with enhancement factors significantly greater than the implied threshold of 3 representing a 99.7 % significance against random chance. In particular both Ce and Zr centred configurations showed statistically significant enhancements of C1 and C2 which contain 12 and 11 like nearest neighbours respectively suggesting both Ce and Zr are increasing the like-like local correlations, however the statistical importance of these enhancements differs due to the stoichiometric difference of Ce and Zr in this system.

Ce centred configurations C1 and C2 benefit from Ce making up 75 % of the cations in the material, we would expect a significant number of occurrences with a large predicted standard deviation meaning the observed enhancement in Ce centred C1 and C2 configurations is particularly significant and is visually highlighted when considering the magnitude of the standard deviation error bars for Ce configurations C1 and C2 in shown in Figure 3.18(a).

The Zr shows an increase in the positive Clapp configurations (in particularly C1 to C57) and a decrease in the negative configurations (C-1 to C-8). Low numbered positive Clapp configurations have a higher local concentration of like-atoms, suggesting that Zr atoms preferentially form local environments with increase Zr. This is in agreement with the observation from the Ce, as the increase in Ce-Ce correlations, will result in a decrease in Ce-Zr, and a comparative increase in Zr-Zr. It should be noted that as the concentration of Zr is low in the material – the predicted standard deviation in the number of configurations with high local concentrations of Zr will be exceptionally small. Consequently, as a multiple of standard deviations, the increase in the low positive Clapp configurations (e.g. C1 to C16) will appear very large, even for a small increase in these configurations, for instance, due to the stoichiometry difference, a single occurrence of Zr fully surrounded by Zr cations would produce an enhancement factor of 98 due to the extreme statistically unlikelihood of occurrence, however with such few observed occurrences the statistical significance of the observed Zr centred C1 configuration is not robust, as is highlighted by the magnitude of the error bars shown in Figure 3.18(a). For the same reason the Ce centred *C*-1 configuration also suffers from statistical unreliability.

By probing the configurations with good statistical reliability, the conclusion of a statistically significant increase in Ce-Ce nearest neighbour correlations and a significant decrease in Ce-Zr nearest neighbour correlations can be drawn, strongly indicating the presence of cation rich nano-domains.

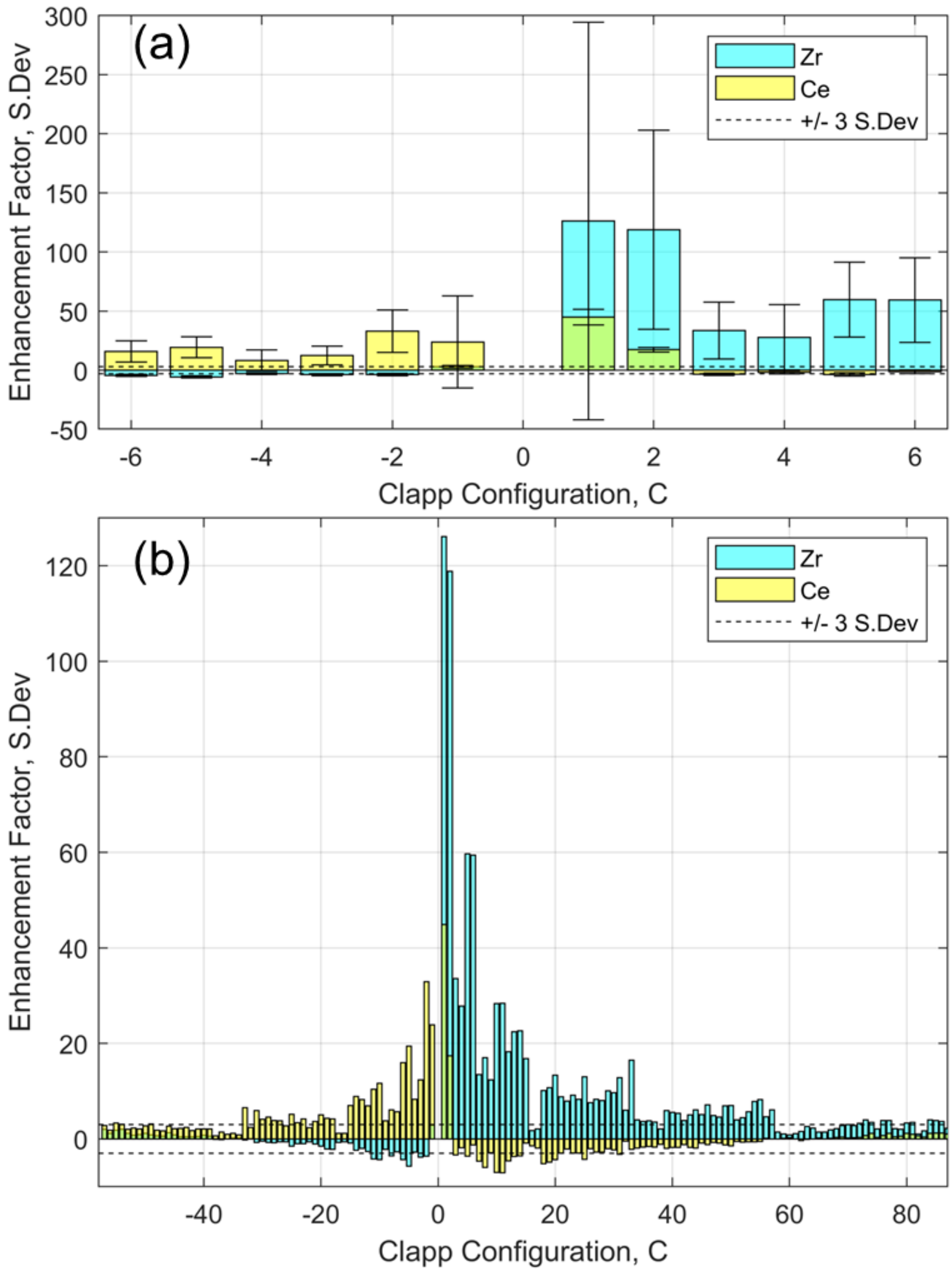

Figure 3.18: Histograms of Clapp configurations observed within the 12 × 12 × 12 supercell for the SRMO1050 treated sample. Enhancement factors displayed are a mean of 100 RMCProfile refined configurations. a) A inset of C1 to C6 (positive and negative) covering 0 to 2 'unlike' (C1 to C6) and 0-2 'like' (C-1 to C-6) neighbours, error bars represent standard deviation in terms of the observed 100 RMCProfile refined configurations. b) full range of observed Clapp configurations.

3.4 Additional analysis

The two materials were also probed ex-situ by Raman spectroscopy as shown in Figure 3.19. The primary Raman band of both spectra noted at 475 cm^{-1} is associated to the highly symmetric M-O bond distances of the $Fm\bar{3}m$

structure. This band is broadened compared to that expected for CeO_2 structure[27,28] showing that a degree of disorder in the M-O vibrational states is observed. Two moderate features are noted at ~300 cm^{-1} and ~600 cm^{-1} matching the major two features of the *t*-ZrO_2 ($P4_2/nmc$) structure. This supports the combined X-ray and neutron diffraction conclusions that the structure present cannot be fully explained in the $Fm\bar{3}m$ space group. But can be described by a cubic unit cell with a distorted oxygen lattice, referred to as the pseudo-cubic t" structure more recognised in $Ce_{0.5}Zr_{0.5}O_2$ compositions.[3,29]

While both materials have highly similar Raman spectra seen in Figure 3.19, there are notably two key differences, nominally the post-SRMO1050 material has two additional minor bands at ~ 420 cm^{-1} and ~ 575 cm^{-1} indicating additional atomic environments absent in the F800 series sample. These additional bands do not match any band expected in the CeO_2 or t-ZrO_2 structures. Andriopoulou *et al.*[24] identified a similar broad band at ~630 cm^{-1} during the reduction and oxidation of $Ce_{0.8}Zr_{0.2}O_2$ and accredited the band to Frenkel type defected oxygen occupying interstitial sites, so this assignment would be consistent with the conclusions of the RMC model generated for the SRMO1050 treated material. The Raman band at ~ 425 cm^{-1} remains unassigned at this stage, however one hypothesis for this band could be nano-domain phase segregation giving rise to a minority of more CeO_2 like M-O vibrations which would be expected to be red-shifted from the bulk solid state band, which itself appears to be blue-shifted compared to the F800 material.

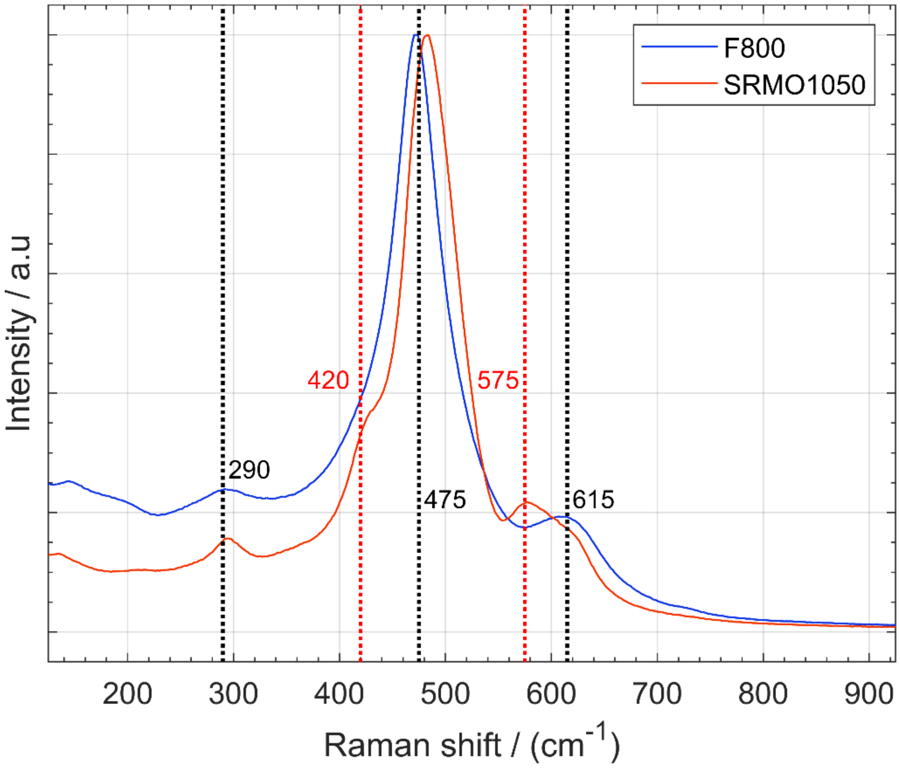

Figure 3.19: Raman Spectra of both F800 and SRMO1050 treated $Ce_{0.75}Zr_{0.25}O_2$ *obtained using 514 nm CO laser. Black dotted lines indicate* CeO_2 *or* ZrO_2 *like bands present in both samples. Red dotted lines indicate bands only observed in the SRMO1050 sample.*

Figure 3.20 shows the temperature programmed reduction (TPR) profile obtained for the F800 and SRMO1050 treated $Ce_{0.75}Zr_{0.25}O_2$ samples discussed in this chapter. The samples were heated to 930 °C under a constant flow of 5 % H_2 in N_2 with hydrogen uptake measured by voltage change at a cathode detector. Both samples were measured twice to gauge thermal stability and are referred to as TPR 1 and TPR 2. An intermediate mild oxidation was applied between each TPR. The profiles clearly show some distinctive differences between the two samples with the F800 sample providing H_2 uptake at slightly lower temperatures and slightly more reduction achieved overall at 2.85 (TPR 1) and 2.93 (TPR 2) mmol H atoms/g indicating a Ce^{4+} to Ce^{3+} reduction of 60.8 and 62.5 % respectively. The SRMO1050 sample showed more uniform reduction between TPR1 and TPR2 which was expected as the sample has already undergone a high temperature reduction as part of the SRMO1050 treatment, however it showed marginally poorer H_2 uptake with 2.77 (TPR 1) and 2.78 (TPR 2) mmol H /g indicating 59.0 and 59.2 % Ce^{4+} to Ce^{3+} reduction respectively.

Crystallite size differences could be partially responsible for the difference in redox properties as smaller crystallites are associated with more surface area and thus active cerium atoms, however various studies have found that crystallite size itself is not the defining factor but rather the removal of oxygen defects that also accompanies sintering.[25] The difference in TPR results between the two samples comes as no surprise if you consider the nano-domain phase segregation present in the SRMO1050 treated sample indicated by the RMC supercell model, well mixed ceria zirconia solid solutions are known to have better performance than systems with visible CeO_2/ZrO_2 phase segregation, with some detailed studies such as this XAFS investigation by Nagai *et.al* drawing the same conclusions at the local scale.[30] As such the TPR result supports the RMC supercell models in that the SRMO1050 system had formed Ce/Zr rich nano-domains while the F800 system appears to be a ceria zirconia solid solution.

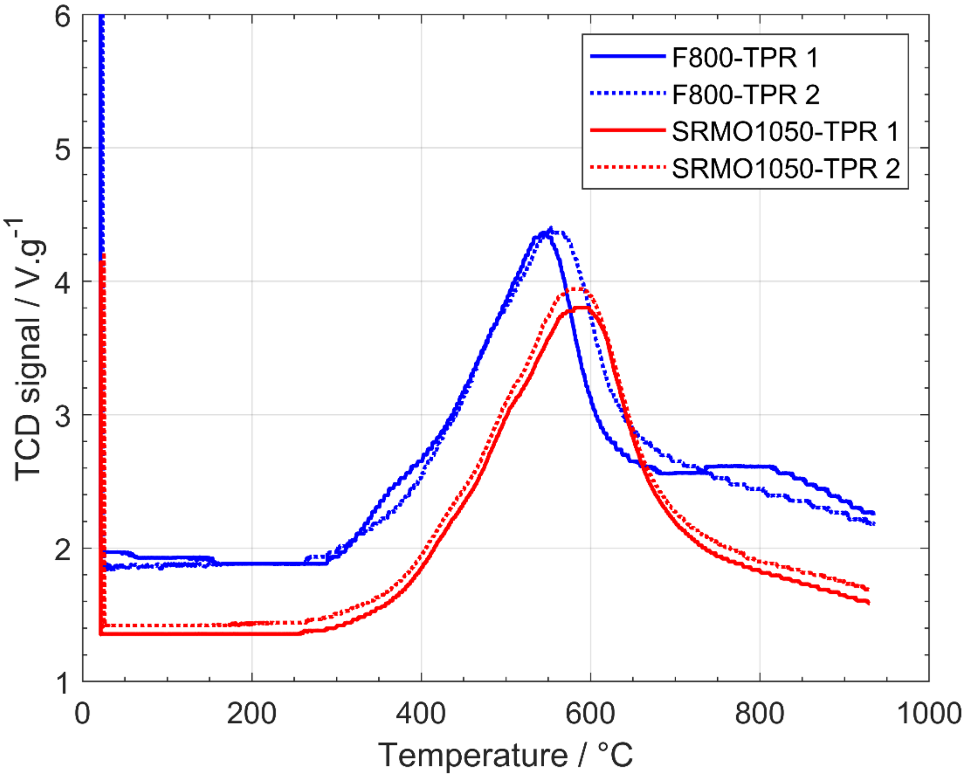

Figure 3.20: Temperature Programmed Reduction profiles of F800 and SRMO1050 treated $Ce_{0.75}Zr_{0.25}O_2$*. Data was collected at Johnson Matthey.*

3.4 Conclusions

X-ray and neutron Bragg diffraction shows the F800 treated $Ce_{0.75}Zr_{0.25}O_2$ exists as a single, nominally cubic bulk phase. Neutron diffraction highlights the presence of a fcc forbidden reflection while showing no evidence of reflection splitting showing that while the primary cation lattice remains cubic, the oxygen lattice has become distorted resulting in a structure with a single M-M nearest neighbour distance (3.78 Å), but two M-O bond distances (2.29 Å and 2.34 Å) resulting in a cubic-tetragonal duality between the cation and oxygen sub-lattices, as such the tetragonal P4/2nmc space group was favoured as it could simultaneously describe a cubic cation arrangement and allow for oxygen *z* coordinate displacement, this duality is supported by the observed Raman spectra which cannot be solely explained by the $Fm\bar{3}m$ fluorite structure. Small-box PDF refinements of the F800 sample support the existence and magnitude of the oxygen displacement observed in the Bragg diffraction and show that only a mediocre fit could be achieved using a small-box model, particularly for the short range < 10 Å region of the PDF.

RMC supercell fitting of the F800 sample shows a significantly improved fit to the observed PDF while maintaining a good agreement with the observed Bragg diffraction pattern. Clapp configuration analysis shows this fit was achieved using a model with only statistical distribution of cations with no statistically significant occurrences of specific cation arrangements or cation clustering. The 12 × 12 × 12 supercell model showed a broad displacement from the idealised sites which would be consistent with a poorly crystalline, highly strained system. Conclusions for the F800 sample indicate that the material exists as a true cubic cation solid solution with displaced oxide behaviour resulting in some tetragonal character on the local scale.

Bragg diffraction of the SRMO1050 treated $Ce_{0.75}Zr_{0.25}O_2$ showed the sample was a single crystalline phase showing a cubic cation lattice arrangement with oxygen *z* coordinate displacement described above for the F800 sample. The largest differences in observed diffraction pattern are the increased sharpness of the reflection profile observed, this difference was accredited to increased crystallite size and decreased strain which are both expected due to the higher temperature treatment undertaken. The compared to the F800 treated $Ce_{0.75}Zr_{0.25}O_2$ sample the SRMO1050 treated $Ce_{0.75}Zr_{0.25}O_2$ sample showed only slight decrease in lattice parameters with an oxygen site *z* coordinate slightly closer to the idealised cubic position, neither of these Rietveld refined differences appears to hold significance beyond that expected with a higher firing temperature.

PDF refinements probing the local structure showed some key differences in the short range < 10 Å region when compared to the F800 treated sample and were overall able to obtain a comparatively better fit using a small-box model.

RMC supercell fitting for the SRMO1050 sample showed several interesting features, firstly the model required the inclusion of interstitial oxygen and favoured them so heavily that their omission resulted in excessive atom ‘migration’ to interstitial sites or simply failed models where a good fit to the observed data was never reached. The interstitial oxygen present in the model accounted for ~ 2.1 % of the total oxygen present and appeared to sit much closer to the idealised interstitial coordinates indicating a relatively constrained atomic environment. Andriopoulou *et al.*[24] observed a Raman active band associated to interstitial oxygen in cerium zirconium oxides at 630 cm^{-1}, and while not a perfect match the additional Raman band at ~575 cm^{-1} observed only in the SRMO1050 spectra only may be associated to these interstitial oxygen.[19,24–26,31]

Investigation into the cation sublattice of the SRMO1050 supercell model showed more occurrences of like-like nearest cation neighbours than was expected, Clapp configuration analysis showed distinct regions of cation clustering with significantly higher occurrences, well beyond the 99.7 % confidence against random chance interval. These cation segregated nano-domains could indicate the beginnings of bulk phase segregation into CeO_2 and ZrO_2 and may well explain anomalous features in the Raman spectra and Bragg diffraction pattern observed for the SRMO1050 sample, namely the blue shift of the main cubic band at 475 cm^{-1} and the lesser red-shifted shoulder marked at 420 cm^{-1} of the Raman spectra shown in Figure 3.19 and the profile/intensity mismatch for the largest d spacing reflection at 3.1 Å in Figure 3.4 and Figure 3.5. This nano-domain cation segregation could explain the decrease in TPR performance and may explain the relatively constrained profile of interstitial oxygen displacements observed in the RMC model as local regions of CeO_2 or ZrO_2 may introduce trapping environments for otherwise mobile oxygen. As such the observed evidence and modelling indicate the SRMO1050 treatment of a poorly crystalline solid solution $Ce_{0.75}Zr_{0.25}O_2$ has resulted in the formation of Frenkel type oxygen defects and nano-domain cation segregation in sub-Bragg diffraction domain sizes which has resulted in a more uniform, but overall weaker TPR performance.

No evidence of any kappa phase formation was observed indicating that in the $Ce_{0.75}Zr_{0.25}O_2$ system the nano-phase segregation is preferable to the pyrochlore formation of cation ordering under high temperature reduction conditions.

3.5 Bibliography

1 A. Summer, H. Y. Playford, L. R. Owen, J. M. Fisher, A. Kolpin, D. Thompsett and R. I. Walton, *APL Mater.*, 2023, **11**, 031113.

2 P. Duran, M. Gonzalez, C. Moure, J. R. Jurado and C. Pascual, *J. Mater. Sci.*, 1990, **25**, 5001–5006.

3 M. Yashima, *Catal. Today*, 2015, **253**, 3–19.

4 M. Yashima, K. Morimoto, N. Ishizawa and M. Yoshimura, *J. Am. Ceram. Soc.*, 1993, **76**, 1745–1750.

5 S. Urban, P. Dolcet, M. Möller, L. Chen, P. J. Klar, I. Djerdj, S. Gross, B. M. Smarsly and H. Over, *Appl. Catal. B Environ.*, 2016, **197**, 23–34.

6 J. L. Payne, M. G. Tucker and I. R. Evans, *J. Solid State Chem.*, 2013, **205**, 29–34.

7 S. N. Achary, S. K. Sali, N. K. Kulkarni, P. S. R. Krishna, A. B. Shinde and A. K. Tyagi, *Chem. Mater.*, 2009, **21**, 5848–5859.

8 Y. Xu, F. Wang, X. Liu, Y. Liu, M. Luo, B. Teng, M. Fan and X. Liu, *J. Phys. Chem. C*, 2019, **123**, 18889–18894.

9 J. Kim, D. H. Kim, J. S. Kim and Y. C. Kim, *Comput. Mater. Sci.*, 2017, **138**, 219–224.

10 G. Dutta, U. V. Waghmare, T. Baidya, M. S. Hegde, K. R. Priolkar and P. R. Sarode, *Catal. Letters*, 2006, **108**, 165–172.

11 H. M. Rietveld, *J. Appl. Crystallogr.*, 1969, **2**, 65–71.

12 M. J. Cliffe, M. T. Dove, D. A. Drabold and A. L. Goodwin, *Phys. Rev. Lett.*, 2010, **104**, 1–4.

13 S. J. L. Billinge and M. G. Kanatzidis, *Chem. Commun.*, 2004, **4**, 749–760.

14 D. A. Keen, *J. Appl. Crystallogr.*, 2001, **34**, 172–177.

15 R. L. McGreevy, *J. Phys. Condens. Matter*, 2001, **13**, R887–R913.

16 H. F. Wang, H. Y. Li, X. Q. Gong, Y. L. Guo, G. Z. Lu and P. Hu, *Phys. Chem. Chem. Phys.*, 2012, **14**, 16521–16535.

17 S. Otsuka-Yao-Matsuo, T. Omata, N. Izu and H. Kishimoto, *J. Solid State Chem.*, 1998, **138**, 47–54.

18 H. Kishimoto, T. Omata, S. Otsuka-Yao-Matsuo, K. Ueda, H. Hosono and H. Kawazoe, *J. Alloys Compd.*, 2000, **312**, 94–103.

19 S. Luo, M. Li, V. Fung, B. G. Sumpter, J. Liu, Z. Wu and K. Page, *Chem. Mater.*, 2021, **33**, 3959–3970.

20 L. R. Owen, H. Y. Playford, H. J. Stone and M. G. Tucker, *Acta Mater.*, 2016, **115**, 155–166.

21 L. R. Owen, H. Y. Playford, H. J. Stone and M. G. Tucker, *Acta Mater.*, 2017, **125**, 15–26.

22 S. Fletcher, O. Glynn, P. King, E. Mobley, T. Rutter, E. Welch, C. Wilcox and D. Clements, 2015, 1–80.

23 P. C. Clapp, *Phys. Rev. B*, 1971, **4**, 255–270.

24 C. Andriopoulou, A. Trimpalis, K. C. Petallidou, A. Sgoura, A. M. Efstathiou and S. Boghosian, *J. Phys. Chem. C*, 2017, **121**, 7931–7943.

25 E. Mamontov, T. Egami, R. Brezny, M. Koranne and S. Tyagi, *J. Phys. Chem. B*, 2000, **104**, 11110–11116.

26 E. Mamontov, R. Brezny, M. Koranne and T. Egami, *J. Phys. Chem. B*, 2003, **107**, 13007–13014.

27 S. Damyanova, B. Pawelec, K. Arishtirova, M. V. M. Huerta and J. L. G. Fierro, *Appl. Catal. A Gen.*, 2008, **337**, 86–96.

28 V. Sánchez Escribano, E. Fernández López, M. Panizza, C. Resini, J. M. Gallardo Amores and G. Busca, *Solid State Sci.*, 2003, **5**, 1369–1376.

29 F. Zhang, C. H. Chen, J. C. Hanson, R. D. Robinson, I. P. Herman and S. W. Chan, *J. Am. Ceram. Soc.*, 2006, **89**, 1028–1036.

30 Y. Nagai, T. Yamamoto, T. Tanaka, S. Yoshida, T. Nonaka, T. Okamoto, A. Suda and M. Sugiura, *J. Synchrotron Radiat.*, 2001, **8**, 616–618.

31 E. Mamontov and T. Egami, *J. Phys. Chem. Solids*, 2000, **61**, 1345–1356.

Chapter 4: Structural study of $Ce_{0.5}Zr_{0.5}O_2$ oxides

4.1 Introduction to $Ce_{0.5}Zr_{0.5}O_2$

Ceria zirconia materials boast improved oxygen storage capacity (OSC) and reduced thermal sintering compared to cerium oxide materials. This change in properties greatly improves the material for use as catalysts supports which is covered briefly in the introduction of this thesis. There is particular interest in $Ce_{0.5}Zr_{0.5}O_2$ composition due to its beneficial OSC and in more recent years its role as a precursor for the formation of a cation ordered κ-$CeZrO_4$ phase. The κ-$CeZrO_4$ phase of cerium zirconium oxide, with strictly alternating ordering of Ce and Zr as seen in $A_2B_2O_7$ pyrochlores, has been a target of study for over 20 years since the phase was first identified by Otsuka *et al.* in 1995 and named the κ-$CeZrO_4$ phase in a later publication in 1998,[1] with further characterisation studies reported in 1999.[2] The phase had been observed by other authors around the same time with Thomson *et al.* publishing a chemical synthesis route to an oxygen rich pyrochlore phase $Ce_2Zr_2O_{7.36}$ in 1996,[3] and subsequently a fully oxidised pyrochlore with composition $Ce_2Zr_2O_8$ 1999.[4] Masui *et al.*[5] published a synthesis method in 2000 where a pyrochlore with composition $CeZrO_{3.75}$ was achieved with a ordered arrangement of oxygen vacancies characterised using high resolution electron microscopy, however even though X-ray diffraction is mentioned in the study, it is unclear from the paper published if cation ordering was present in their material.

The pyrochlore phase can be described as a cation ordered, oxygen deficient 2 × 2 × 2 fluorite supercell with composition $Ce_2Zr_2O_6O'$. Figure 4.1 shows the fluorite-pyrochlore relationship. The local oxygen environments of the pyrochlore structure are not so simply described however, as the bulk O_6 site sits with equal cation neighbours (Ce_2, Zr_2), the O' sits with all Ce neighbours (Ce_4), additionally among the average O6 site there is also a preference for shorter Zr-O bonds and longer Ce-O bonds.

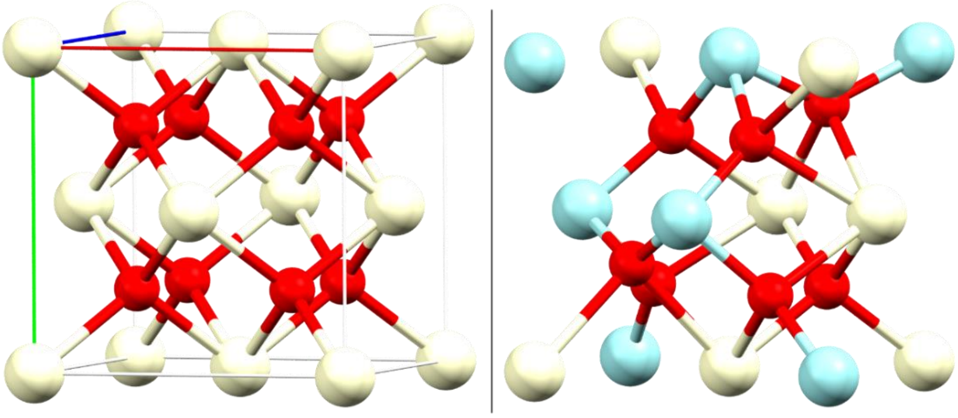

Figure 4.1: Fluorite ($Fm\bar{3}m$) (left) a solid solution with mixed cation sites and pyrochlore ($Fd\bar{3}m$) (right) with cation ordering. Fluorite-like subset of atoms shown for comparison. Fluorite composition A_4O_8 (A = Ce/Zr, pale yellow), pyrochlore composition $A_2B_2O_6O'_1$ (A = Ce pale yellow, B = Zr blue), oxygen sites shown in red.

The κ-$CeZrO_4$ phase has been a keen topic of study due to its rapid and low temperature OSC properties which show a low oxygen release onset temperature of 250 °C and peak release of ~ 1.8×10^{-10} mol.s^{-1} at 400 °C under reducing conditions while the t'-$Ce_{0.5}Zr_{0.5}O_2$ cation mixed precursor phase shows oxygen release onset at 400 °C with a peak release of ~ 1.0×10^{-10} mol.s^{-1} at 650 °C.[1,2,6–8]

While initially suspected to be in the pyrochlore $Fd\bar{3}m$ space group, Kishimoto *et al.* showed in 2000[9] that a large number of very low intensity reflections were present for the κ-$CeZrO_4$ phase prepared at 1200 °C which were forbidden by the $Fd\bar{3}m$ symmetry, so instead explored the $P2_13$, $P23$ and $P\bar{4}3m$ space groups and $P2_13$ was found to be the best match with their observed data. More recently Urban *et al.*[10,11] published papers in 2016 and 2017 showing that more extreme initial reduction with conditions of at least 1500 °C was required to fully force the cation ordering and subsequent phase transition, however the materials produced at this higher reduction temperature showed poor OSC and catalytic properties which the authors accredit to the poor surface area due to higher sintering. While surface area is likely to have played a role, such a high temperature treatment would also likely have removed much of the oxygen site disorder known to improve OSC properties, a topic seemingly overlooked by the authors.

Structural solutions for the κ-$CeZrO_4$ phase reported in the literature are not consistent but it is generally agreed that the κ-$CeZrO_4$ phase is a cation ordered fluorite $2 \times 2 \times 2$ supercell[9,10,12] which gives rise to characteristic supercell reflections most notably observed at a d-spacing of 6.0 Å (or 14 °2θ using a Cu X-ray source). The oxygen site behaviour however is significantly less clear cut much of the literature relying on X-ray diffraction data which is inherently insensitive to lighter elements in the presence of significantly heavier elements. To complicate matters Otsuka-Yao-Matsuo *et al.*[1] have shown from early studies of the κ-$CeZrO_4$ phase that the OSC properties are sensitive to the material's synthesis route[13] and thermal history, with the precursor pyrochlore phase formed at temperatures of ~1000 °C or above. A wide range of synthesis routes have been explored in the literature making direct comparisons difficult.

Figure 4.2 shows the simulated pXRD patterns from structures reported by Thompson ($R\overline{3}m$, 1999), Kishimoto ($P2_13$, 2000), Achary ($P2_13$, 209) and Urban 2016 ($P2_13$, 2016) overlaid with the data from samples SRMO1050 and SRMO1200 discussed in this chapter. Whilst differences between the observed experimental patterns and the simulated Thompson and Achary patterns are clearly visible as additional reflections, the Kishimoto and Urban simulated patterns showed a good observational match to the observed X-ray diffraction data. Differences between these two structures were minimal and Kishimoto's structure was chosen as a suitable starting model due to more similar synthesis temperatures to the samples studied here.

To summarise the main features of Kishimoto's $P2_13$ model, it is a $2 \times 2 \times 2$ fluorite supercell with pyrochlore cation ordering, using the $P2_13$ space group this is described by two cation sites for each cation (Ce1, Ce2, Zr3 & Zr4). The oxygen lattice consists of 3 local environments, 8 oxygen sites surrounded by four Ce atoms (O1 & O2), 8 oxygen sites surrounded by four Zr atoms (O3 & O4) corresponding to the missing 8b oxygen site in the pyrochlore structure. The remaining 48 oxygen sites have two Ce and two Zr neighbours (O5, O6, O7 & O8). Interstitial oxygen sites were not explicitly stated as an avenue of investigation by either Kishimoto in 2000 or Urban in

2016, however Urban did find some oxygen vacancies from sites O1 and O3 in the sample they reduced at 1500 °C.

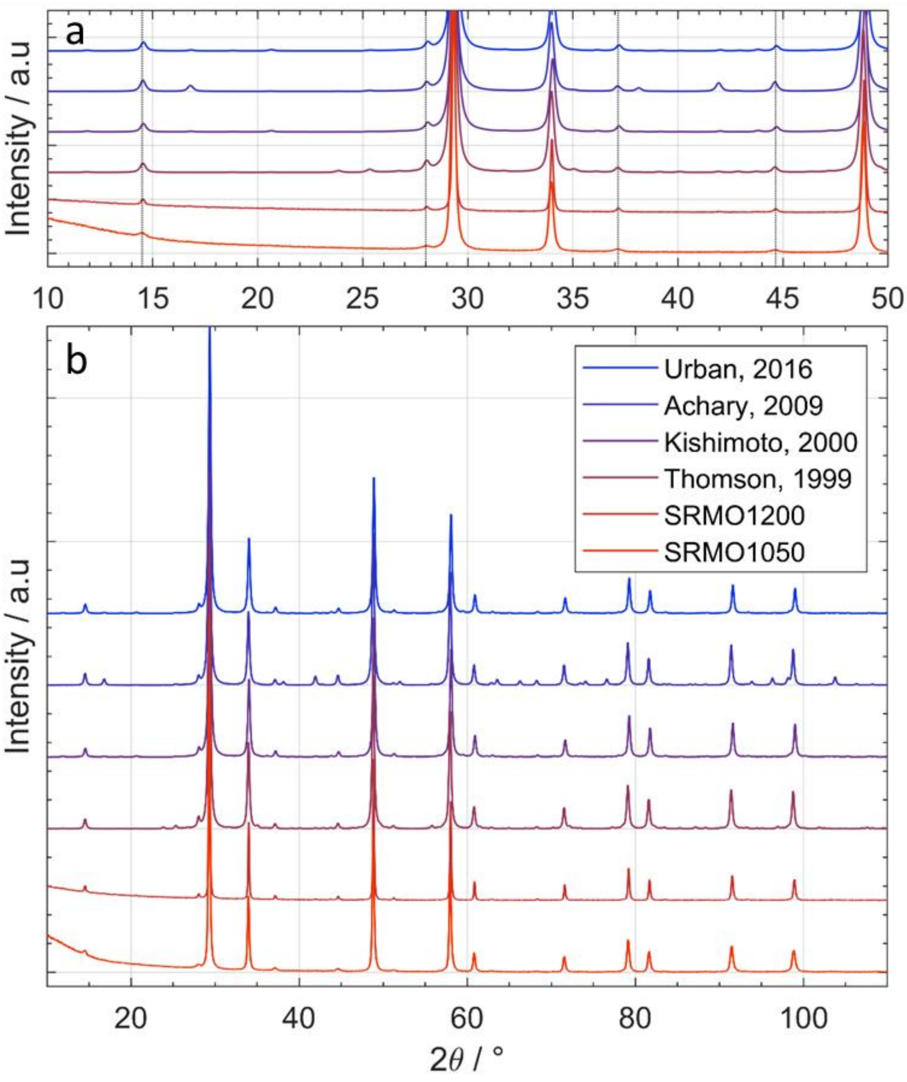

Figure 4.2: Simulated pXRD patterns from kappa structures in the literature compared to observed SRMO1050 and SRMO1200 sample, monochromatic Cu$_{\alpha 1}$ source (1.5406 Å). Urban 2016, Achary 2009 and Kishimoto 2000 all use the P2$_1$3 space group. Thompson 1999 employed the R$\bar{3}$m space group. a) Zoomed region of the comparison with dashed lines to highlight the experimentally observed supercell reflections. b) Full range comparison of predicted reflections for various κ-CeZrO$_4$ phase models vs observed diffraction pattern for SRMO1050 and SRMO1200 samples.

4.2 Average Structure: Small-box refinements of diffraction data

4.2.1 As provided industrial $Ce_{0.5}Zr_{0.5}O_2$

Chapter 4 mentions the nature of the *'cubic-tetragonal'* duality in ceria zirconia materials which is a characteristic of the t"-$Ce_{0.5}Zr_{0.5}O_2$ phase[14]. The industrial $Ce_{0.5}Zr_{0.5}O_2$ sample investigated here shows a significantly larger O site *z* coordinate displacement clearly observed by neutron diffraction, however as this displacement is solely a shift in oxygen coordinate, the change to the Bragg scattering related to this structural feature remains unobservable to X-ray diffraction at this magnitude. This highlights the difficulty of observing this duality via more accessible laboratory X-ray diffractometers. Figure 4.3 shows the Rietveld refined $P4_2/nmc$ model and obtained simultaneous fits against the observed X-ray and neutron diffraction data obtained on bank 3 of Polaris, with the refined parameters displayed in Table 4.1. No reflections with d-spacings above 3.2 Å were observed for this industrial solid solution (ss)-$Ce_{0.5}Zr_{0.5}O_2$ material.

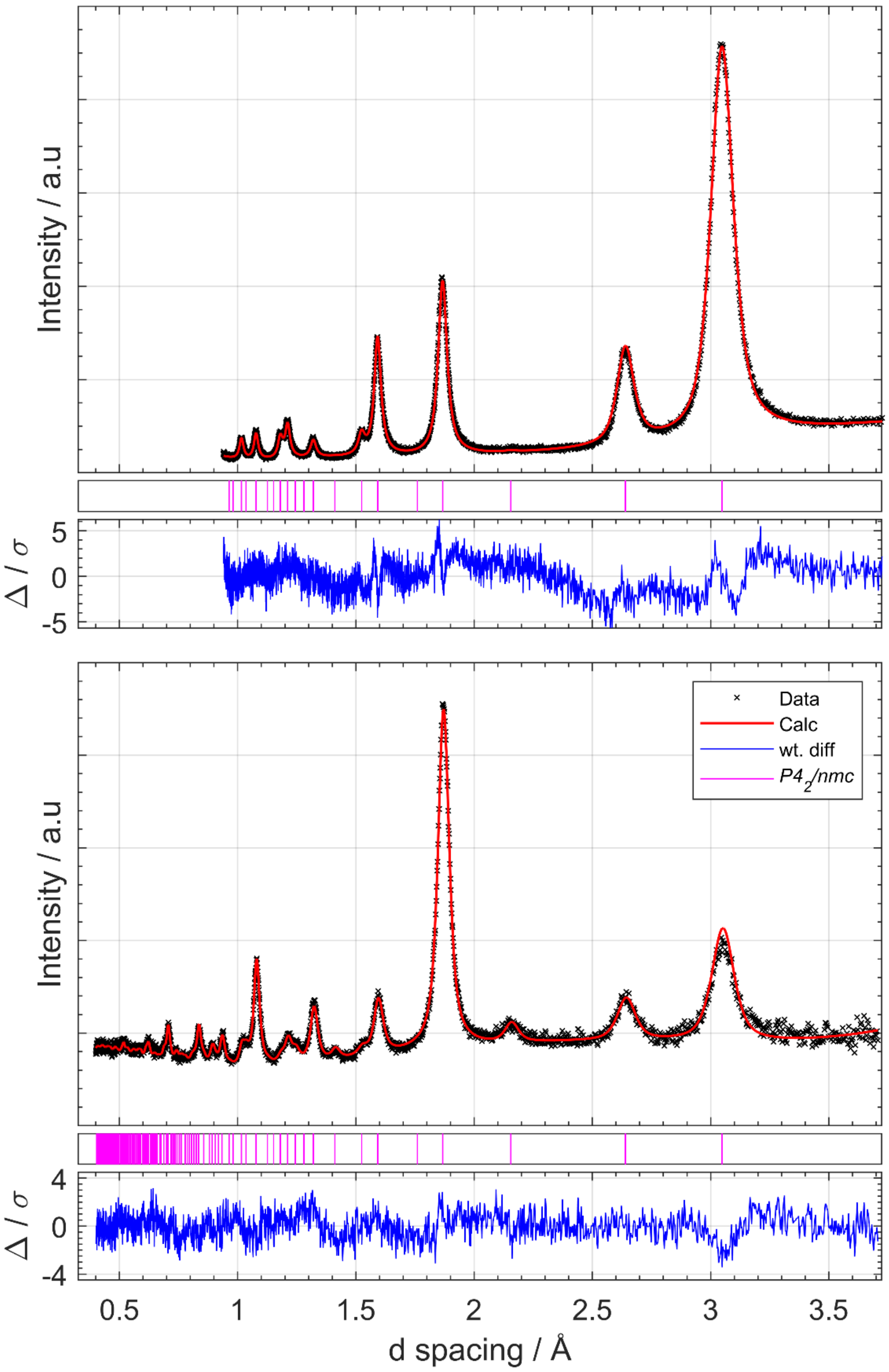

Figure 4.3: Rietveld refinements of industrially provided $Ce_{0.5}Zr_{0.5}O_2$*, model refined against 5 banks of neutron data and 1 bank of X-ray data using the* $P4_2/nmc$ *structure; Top) X-ray data obtained from a monochromatic Cu K-α1 laboratory diffractometer. Bottom) Neutron data obtained from Polaris, bank 3 shown.*

Table 4.1: Refined parameters for industrially provided $Ce_{0.5}Zr_{0.5}O_2$ using the tetragonal $P4_2/nmc$ space group in the 2nd origin, a = 3.7344(6), c = 5.2774(13), a/c ratio = 0.7076 (ideal cubic ratio = 0.7071…). Calculated density = 6.6636 g/cm^3, oxygen 'displacement' from cubic z coordinate = 0.0289 (0.153 Å), wR = 2.51 %.

Atom	**Label**	**Wyck.**	***x***	***y***	***z***	**Uiso / Å²**	**Occ.**
Ce	Ce	2a	0.25	-0.25	0.25	0.00343(17)	0.5
Zr	Zr						0.5
O	O	4d	0.25	0.25	0.4711(2)	0.0106(3)	1

4.2.2 SRMO1200 treated industrial $Ce_{0.5}Zr_{0.5}O_2$

The SRMO1200 treated $Ce_{0.5}Zr_{0.5}O_2$ sample is introduced before the SRMO1050 $Ce_{0.5}Zr_{0.5}O_2$ sample here due to the more intense features relating to the κ-$CeZrO_4$ phase providing a clearer introduction to the various forms of order/disorder present in both the SRMO1050 and SRMO1200 samples discussed. The neutron Bragg diffraction pattern for the SRMO1200 $Ce_{0.5}Zr_{0.5}O_2$ sample had a more defined profile of supercells reflections and was the first material to be successfully Rietveld fitted using combined X-ray and neutron diffraction data.

The as provided industrial $Ce_{0.5}Zr_{0.5}O_2$ material was subjected to a high reduction temperature (1200 °C under H_2) followed by a mild oxidation (400 °C under air) to study the material's thermal behaviour. The resulting material showed features that matched the primary reflections of the fluorite supercell κ-$CeZrO_4$ phase of cerium zirconium oxide.

Initial models based on the laboratory X-ray diffraction data proved a poor match to the observed neutron diffraction data, which suggested that the SRMO1200 treatment had introduced significant oxide disorder to which neutron diffraction is sensitive while the average cation positions remained close to that of the cation ordered fluorite supercell.

Fourier density maps were employed to assist in resolving the structural anomalies within this material. These Fourier density maps were generated from the raw neutron diffraction patterns and used throughout the refinement process to highlight sources of mismatch between observed and calculated scattering density. These Fourier maps revealed the existence of interstitial oxygen sites and a selection of z slices from the raw Fourier density map are shown in Figure 4.4. In addition to interstitial sites, the Fourier maps showed poorly defined scattering density from one of the fluorite-like bulk oxygen sites (O7) showing scattering density from sites too close to be distinct, the two sites describe a fluorite-like oxygen position and one slightly displaced towards an interstitial site. Anisotropic thermal parameters were tested, but they proved insufficient to describe the feature and as such it was assumed this could only indicate a split-site with partial occupancy (O7-split). Inclusion of the X-ray diffraction data to the Rietveld refinement added additional scattering contrast to the model which highlighted some supercell reflection intensity mismatch. This could not be accounted for by interstitial oxygen, and was believed to be some anti-site cation disorder where some Ce was present on the Zr sites and some Zr was present on the Ce sites. Decoupling this intensity mismatch using Rietveld refinement was only possible due to the complementary elemental scattering intensities of the combined X-ray and neutron diffraction joint refinement approach.

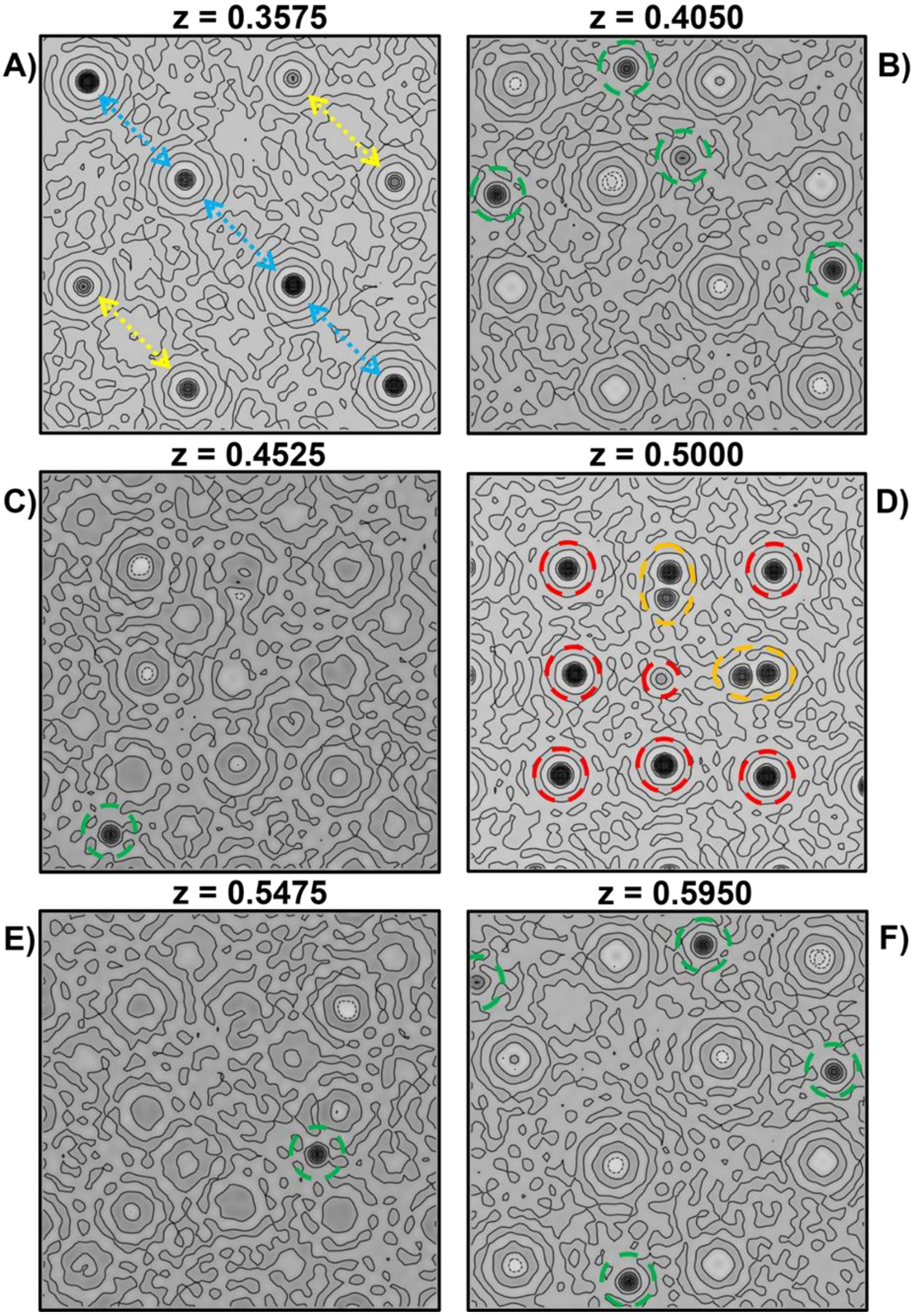

Figure 4.4: Six slices of the Fourier scattering density map obtained from 5 banks of Polaris data, all subfigures show the x & y coordinates = 0.02 to 0.98 slice of the stated z. A; z = 0.3575 slice showing 8 cation sites in plane. B; z= 0.4050 slice showing scattering from four interstitial sites. C; z = 0.4525 slice showing interstitial oxygen site. D; z = 0.5000 showing fluorite oxygen lattice with split scattering density, central O site slightly off z-plane. E; z = 0.5475 showing interstitial O site. F; z = 0.5950 slice showing four oxygen interstitial sites. Colour map; Darker = high scattering density values; lighter = low scattering density values; scaled to each individual z plane. Yellow arrows = Ce sites. Blue arrows = Zr sites. Green dashed circles = Interstitial oxygen sites. Red dashed circles = fluorite-like oxygen sites. Orange dashed ovals = oxygen split sites.

Both the inclusion of the oxygen split site and interstitial oxygen sites were required to obtain a good Rietveld fit to data with wR value of below 5 % (best fit prior to oxygen inclusion of oxygen disorder was ~10 % wR with clear supercell intensity mismatch in the pattern). Figure 4.5 shows the observed data, calculated fit and (observed – calculated)/sigma difference plot for Polaris bank 2 and laboratory pXRD data showing the fit to the supercell reflection at 6 Å. Figure 4.6 shows the fit to Polaris bank 4 with better resolution on a larger number of reflections, and refined parameters for this simultaneous fit against 5 banks of Polaris neutron data and 1 laboratory p-XRD pattern are shown in Table 4.2. Freely refining oxygen site occupancies resulted in excess oxygen beyond that allowed by the maximum charge balance of Ce^{4+} and Zr^{4+}. To avoid this non-physical situation the overall composition of the Rietveld model was constrained to the $CeZrO_4$ composition as the sample had been fired in air at 400 °C for 2 hours which was expected to fully oxidise all Ce^{3+} to Ce^{4+}.

Cation anti-site disorder was noted due to the elemental scattering contrast between X-rays and neutrons, and refinement showed approximately 11% of Ce sites were occupied by Zr and vice-versa. The cation anti-site disorder was constrained to be equivalent across all four defined cation sites. This anti-site disorder likely indicates incomplete cation ordering during the reduction to pyrochlore and is likely to be disorder in the κ-$CeZrO_4$ phase rather than existing as a minor volume of solid solution phase crystallites. This conclusion was supported by the relatively crystalline Bragg reflections observed with no evidence of any anisotropic peak broadening or shoulders.

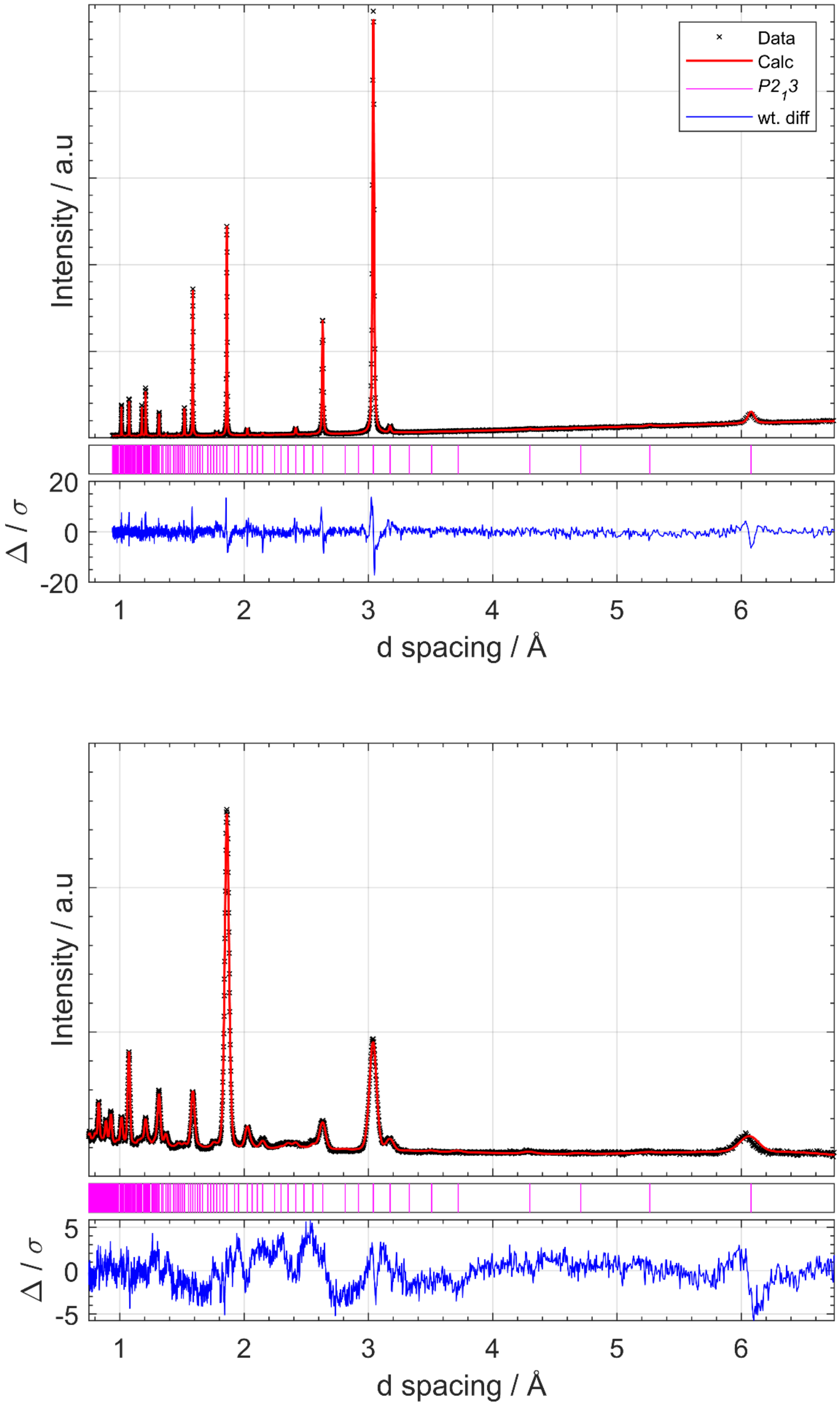

Figure 4.5: Rietveld refinement of $Ce_{0.5}Zr_{0.5}O_2$ SRMO1200 fitted with the κ-$CeZrO_4$ phase. Refined parameters are shown in Table 4.2. Top) X-ray data shown obtained from a monochromatic Cu K-α1 laboratory diffractometer showing the primary cation ordering supercell reflection at 6.0 Å. Bottom) Neutron TOF data obtained from Bank 2 showing X-ray/neutron scattering contrast.

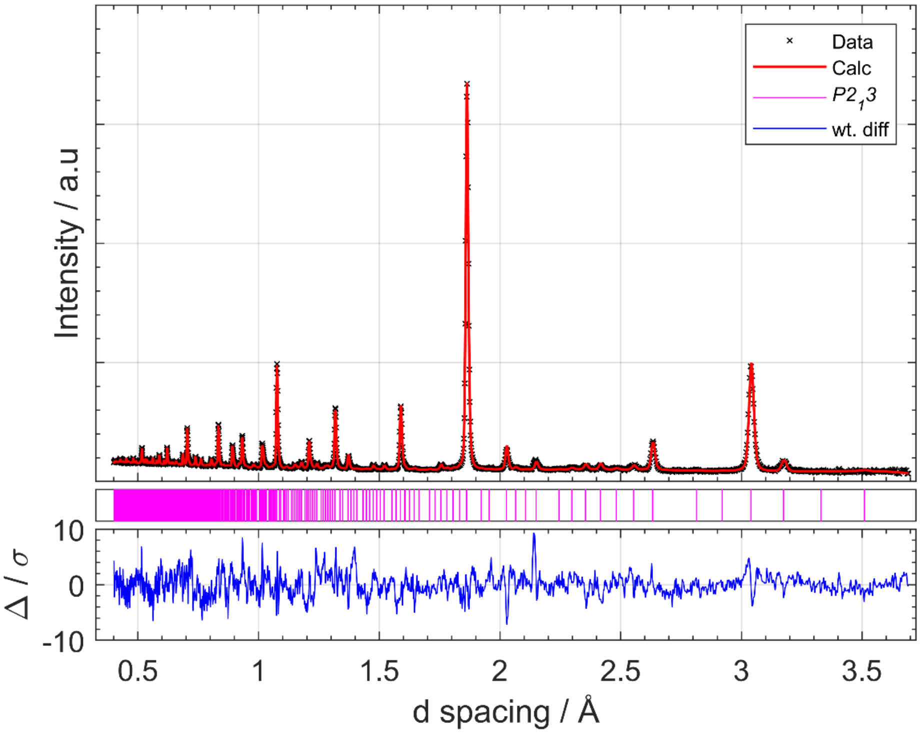

Figure 4.6: Rietveld refinement of $Ce_{0.5}Zr_{0.5}O_2$ SRMO1200 fitted with the κ-$CeZrO_4$ phase. Refined parameters are shown in Table 4.2. Neutron TOF data shown obtained from Polaris Bank 4.

Some constraints were employed to stabilise the refinement where atomic environments were similar, and these constraints are shown as shared parameters or with symbols in Table 4.2. Special consideration was given to the O7 and O7-split site due to a site-site distance of 0.662 Å. These sites are too close to be considered distinct, as such occupancy across both sites was constrained to sum to 1. Full combined occupancy of these O7-O7 split sites were constrained as refinements of the original O5-O8 site occupancies indicated approximately full occupancy in each. Anisotropic thermal parameters were explored to explain the split characteristic of O7 and O7-split but did not provide any significant improvement to the fit, as such the split site structural description was chosen to best explain this feature.

*Table 4.2: Refined parameters for SRMO1200 κ-$CeZrO_4$ using the $P2_13$ space group, a = 10.52943(11). Calculated density = 6.7216 g/cm^3, wR = 3.62 %, * Oint3 and Oint4 showed no evidence of oxygen occupancy, however they are included for completeness. $^{+/-}$ Cation anti-site disorder constrained to be equivalent, $^{+}$ indicates primary cation, $^{-}$ indicates anti-cation.*

Atom	Label	Wyck.	*x*	*y*	*z*	Uiso / Å^2	Occ.
Ce	Ce1	4a	0.1240(5)	0.1240(5)	0.1240(5)	0.00459(12)	0.890(4)$^{+}$
Zr	Zr1						0.110(4)$^{-}$
Ce	Ce2	12b	0.1226(3)	0.3715(3)	0.3752(5)		0.890(4)$^{+}$
Zr	Zr2						0.110(4)$^{-}$
Ce	Ce3	4a	0.6327(4)	0.6327(4)	0.6327(4)		0.110(4)$^{-}$
Zr	Zr4						0.890(4)$^{+}$
Ce	Ce4	12b	0.6253(3)	0.8683(4)	0.8695(5)		0.110(4)$^{-}$
Zr	Zr4						0.890(4)$^{+}$
O	O1	4a	-0.0071(6)	-0.0071(6)	-0.0071(6)	0.0026(6)	0.701(13)
O	O2	4a	0.2491(6)	0.2491(6)	0.2491(6)		0.955(13)
O	O3	4a	0.4882(12)	0.4882(12)	0.4882(12)	0.0119(13)	0.333(13)
O	O4	4a	0.7518(9)	0.7518(9)	0.7518(9)		0.905(16)
O	O5	12b	0.2411(5)	0.2470(4)	-0.0108(4)	0.0043(2)	0.972(13)
O	O6	12b	0.2419(5)	0.2511(5)	0.5042(3)		1.029(14)
O	O7	12b	-0.0008(7)	-0.0047(9)	0.2563(5)		0.585(8)
O	O7-split	12b	-0.0043(12)	-0.0020(10)	0.3190(5)		0.415(8)
O	O8	12b	-0.0032(4)	0.0057(5)	0.7241(4)		0.949(13)
O	Oint1	12b	0.456(3)	0.188(3)	0.106(3)	0.0046(13)	0.095(7)
O	Oint2	12b	0.9131(10)	0.0986(15)	0.952(14)		0.323(6)
O	Oint3*	4a	0.875	0.875	0.875	-	0
O	Oint4*	4a	0.375	0.375	0.375		0

4.2.3 SRMO1050 treated industrial $Ce_{0.5}Zr_{0.5}O_2$

The as provided industrial $Ce_{0.5}Zr_{0.5}O_2$ sample was subjected to a high temperature reduction at 1050 °C under pure H_2 followed by a mild oxidation (400 °C under air). This temperature is just barely over the phase transition temperature expected for $Ce_{0.5}Zr_{0.5}O_2$ to start forming the partially reduced cation ordered $Ce_2Zr_2O_7$ pyrochlore phase[3,5,15] with subsequent oxidation forming the κ-$CeZrO_4$ phase. The reduction temperature was chosen to assist in understanding the pseudo-fluorite to fluorite supercell phase transitions, which have not been observed in $Ce_{0.5}Zr_{0.5}O_2$ materials below 1000 °C to the author's knowledge or experience. The fitted structure of the SRMO1200 $Ce_{0.5}Zr_{0.5}O_2$ sample shown in Table 4.2 proved to be a reasonable starting structure for the SRMO1050 $Ce_{0.5}Zr_{0.5}O_2$ sample.

Figure 4.7 shows the fit obtained for the SRMO1050 treated sample. As with the SRMO1200 treated sample, oxygen interstitials, O7 split site and cation anti-site disorder was observed. This cation site disorder accounted for ~18 % site occupancy by the second cation and is likely indicative of incomplete cation ordering from the solid solution cerium zirconium oxide. This anti-site disorder could exist in two forms: as statistically dispersed cation anti-site disorder where the overall cation ordering is maintained but remains imperfect, or as ~18 % of the sample volume existing as discrete solid solution $Ce_{0.5}Zr_{0.5}O_2$ crystallites of near identical crystallinity to the bulk κ-$CeZrO_4$ phase. This second possibility is highly unlikely due to the sharp well defined Bragg peaks observed with no clear evidence of reflection asymmetry or peak splitting.

The pattern shows some notable diffuse scattering in the form of a very broad feature spanning between 1.9 Å and 2.7 Å. This feature is not observed in the X-ray diffraction pattern but is clearly observed in the difference patterns of neutron bank 2 in Figure 4.7 and neutron bank 4 shown in Figure 4.8 which could be an indicator of significant local oxide disorder.

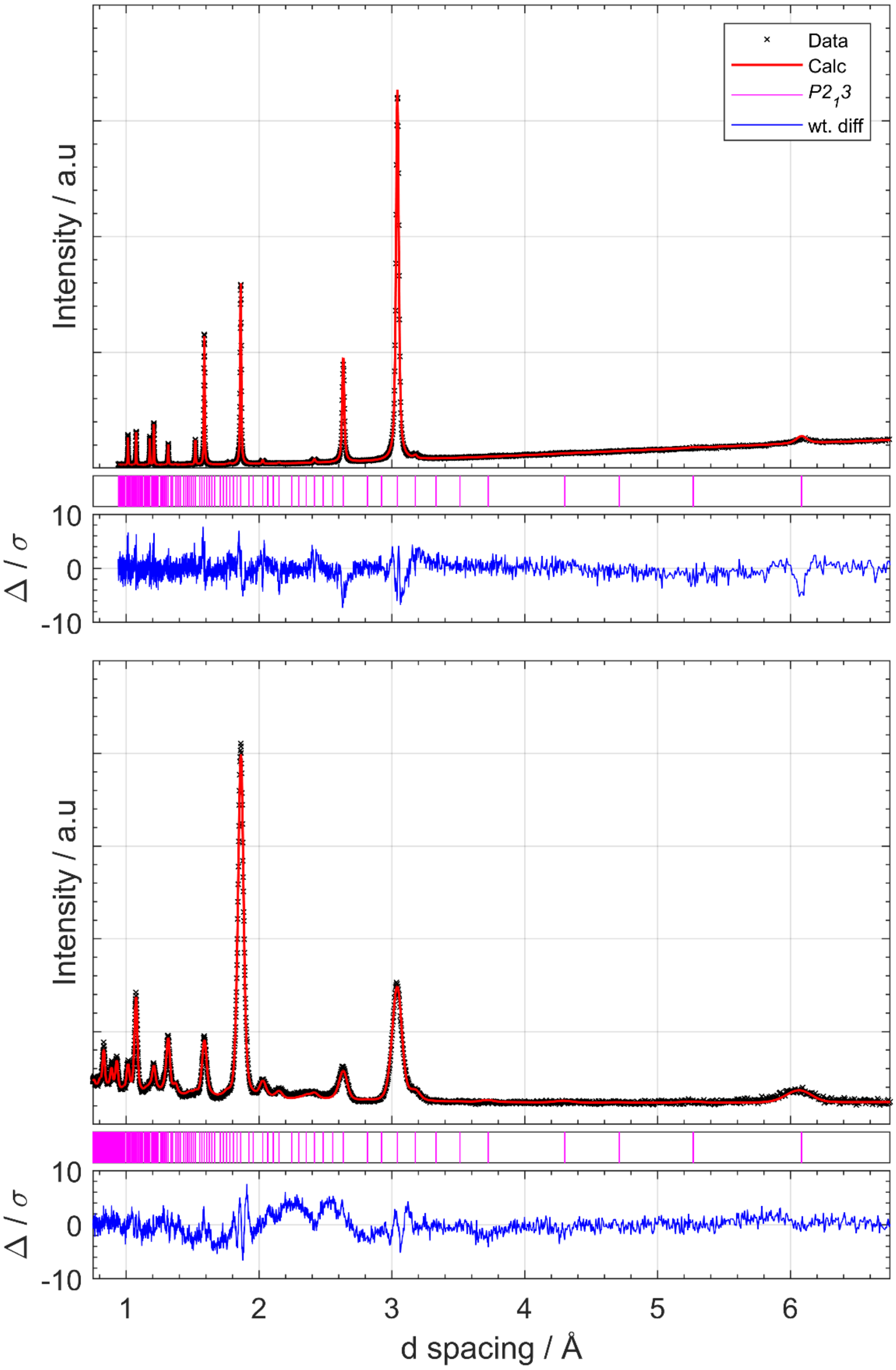

Figure 4.7: Rietveld refinement of $Ce_{0.5}Zr_{0.5}O_2$ SRMO1050 fitted with the κ-$CeZrO_4$ phase. Refined parameters are shown in Table 4.3. Top) X-ray data shown obtained from a monochromatic Cu K-α1 laboratory diffractometer showing the primary cation ordering supercell reflection at 6.0 Å. Bottom) Neutron TOF data obtained from Bank 2 showing X-ray/neutron scattering contrast.

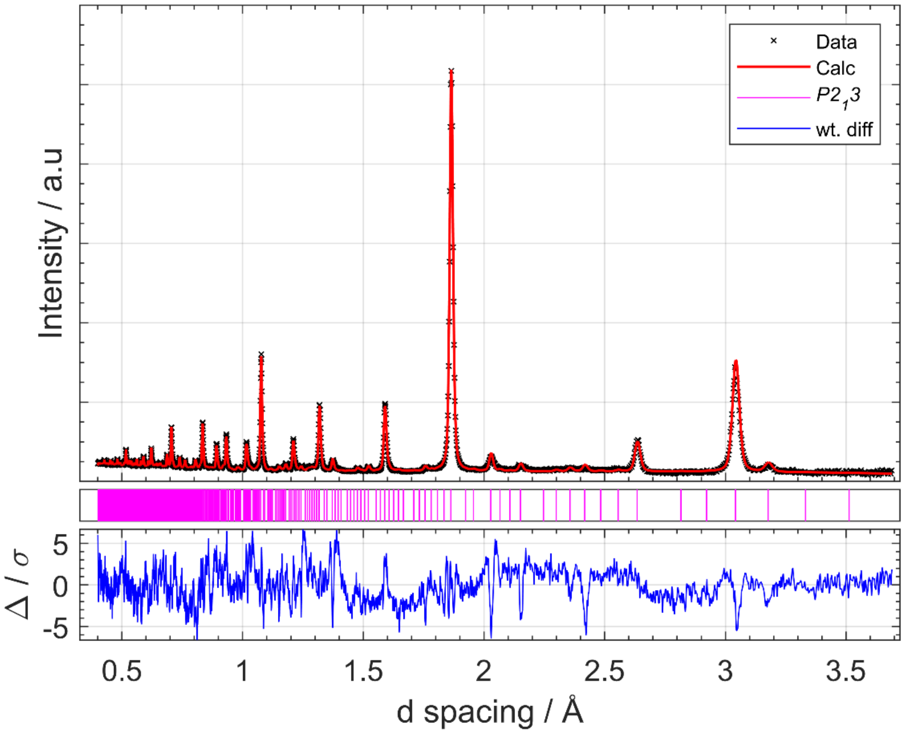

Figure 4.8: Rietveld refinement of $Ce_{0.5}Zr_{0.5}O_2$ *SRMO1050 fitted with the κ-*$CeZrO_4$ *phase. Refined parameters are shown in Table 4.3. Neutron TOF data shown was obtained from Polaris Bank 4.*

Table 4.3 shows the refined parameters from the fits shown in Figure 4.7 and Figure 4.8. These refined parameters show significant cation anti-site disorder in the region of ~20 % occupancy. Other curious features include significant but uneven oxygen interstitial occupancy accounting for ~5.5 % of overall oxygen content. Constraints used within this model are identical to the SRMO1200 Rietveld model and are discussed further there.

*Table 4.3: Refined parameters for SRMO1050 κ-$CeZrO_4$ using the $P2_13$ space group, a = 10.53683(17). Calculated density = 6.7234 g/cm^3, wR = 4.55 %. * Oint3 and Oint4 showed no evidence of oxygen occupancy, however they are included for completeness. $^{+/-}$ Cation anti-site disorder constrained to be equivalent, $^{+}$ indicates primary cation, $^{-}$ indicates off-cation.*

Atom	**Label**	**Wyck.**	***x***	***y***	***z***	**Uiso / Å^2**	**Occ.**
Ce	Ce1	4a	0.1230(6)	0.1230(6)	0.1230(6)	0.00488(14)	0.804(5)$^{+}$
Zr	Zr1						0.196(5)$^{-}$
Ce	Ce2	12b	0.1261(5)	0.3751(6)	0.3742(4)		0.804(5)$^{+}$
Zr	Zr2						0.196(5)$^{-}$
Ce	Ce3	4a	0.6285(5)	0.6285(5)	0.6285(5)		0.804(5)$^{+}$
Zr	Zr4						0.196(5)$^{-}$
Ce	Ce4	12b	0.6269(5)	0.8705(5)	0.8691(5)		0.804(5)$^{+}$
Zr	Zr4						0.196(5)$^{-}$
O	O1	4a	-0.0143(5)	-0.0143(5)	-0.0143(5)	0.0093(11)	0.865(17)
O	O2	4a	0.2524(11)	0.2524(11)	0.2524(11)		0.915(16)
O	O3	4a	0.5129(16)	0.5129(16)	0.5129(16)	0.0122(13)	0.261(13)
O	O4	4a	0.7487(13)	0.7487(13)	0.7487(13)		0.977(18)
O	O5	12b	0.2434(6)	0.2436(6)	-0.0070(6)	0.0059(2)	0.915(17)
O	O6	12b	0.2470(7)	0.2554(7)	0.5067(6)		1.061(17)
O	O7	12b	-0.0041(7)	-0.0035(10)	0.2531(5)		0.739(13)
O	O7-split	12b	-0.0006(17)	-0.0058(18)	0.3205(8)		0.349(9)
O	O8	12b	-0.00122(6)	0.0027(7)	0.7235(4)		0.994(16)
O	Oint1	12b	0.577(10)	0.229(11)	0.113(10)	0.000(2)	0.028(8)
O	Oint2	12b	0.9209(10)	0.1074(16)	0.0977(14)		0.301(6)
O	Oint3*	4a	0.875	0.875	0.875	-	0
O	Oint4*	4a	0.375	0.375	0.375		0

4.2.4 $Ce_{0.5}Zr_{0.5}O_2$ prepared by alkoxide synthesis

An alkoxide precursor synthesised $Ce_{0.5}Zr_{0.5}O_2$ sample was prepared via a solvothermal method using a 1:4.6 weight ratio (1:1, Ce:Zr molar ratio) of 18-20 wt/% cerium(IV) 2-methoxyethoxide in 2-methoxyethanol and 80 wt/% zirconium n-butoxide in 1-butanol. This sample is referred to as the “alkoxide synthesised” $Ce_{0.5}Zr_{0.5}O_2$ material. The precursor mixture was poured into a Teflon autoclave liner and mixed with a magnetic stirrer. Once mixed the autoclave was assembled and placed in an oven at 200 °C and left for 24 hours. The synthesised product was washed with butanol and filtered using vacuum filtration then left to dry at 80 °C in a drying cabinet. The dried product was ground using a pestle and mortar then fired in a muffle furnace at 800 °C for 2 hours.

As with the industrial sample above, the alkoxide synthesis method produces a phase pure $Ce_{0.5}Zr_{0.5}O_2$ solid solution. Neutron diffraction shows this material also has oxygen *z* coordinate displacement of 0.13 Å, which is marginally smaller than the as provided industrial $Ce_{0.5}Zr_{0.5}O_2$ material with 1.5 Å. The significance of this oxygen *z* coordinate and its relationship to the cubic-tetragonal duality are described in Chapter 4, section 4.2.1 of this thesis.

The pXRD shows that solid solution ceria zirconia can be formed at low temperatures using an alkoxide precursor based solvothermal synthesis method. Only initial screening laboratory pXRD data was collected on this alkoxide synthesised $Ce_{0.5}Zr_{0.5}O_2$ sample, which was not of sufficient quality for Rietveld refinement, as such Figure 4.9 below only shows the neutron diffraction data acquired from Polaris bank 4. Due to limited sample and the poorly crystalline sample, the primary reflections for the vanadium can are observed and have been fitted as background. Note that the eleven 1-hour long neutron diffraction patterns were combined to improve the signal to noise ratio for this dataset.

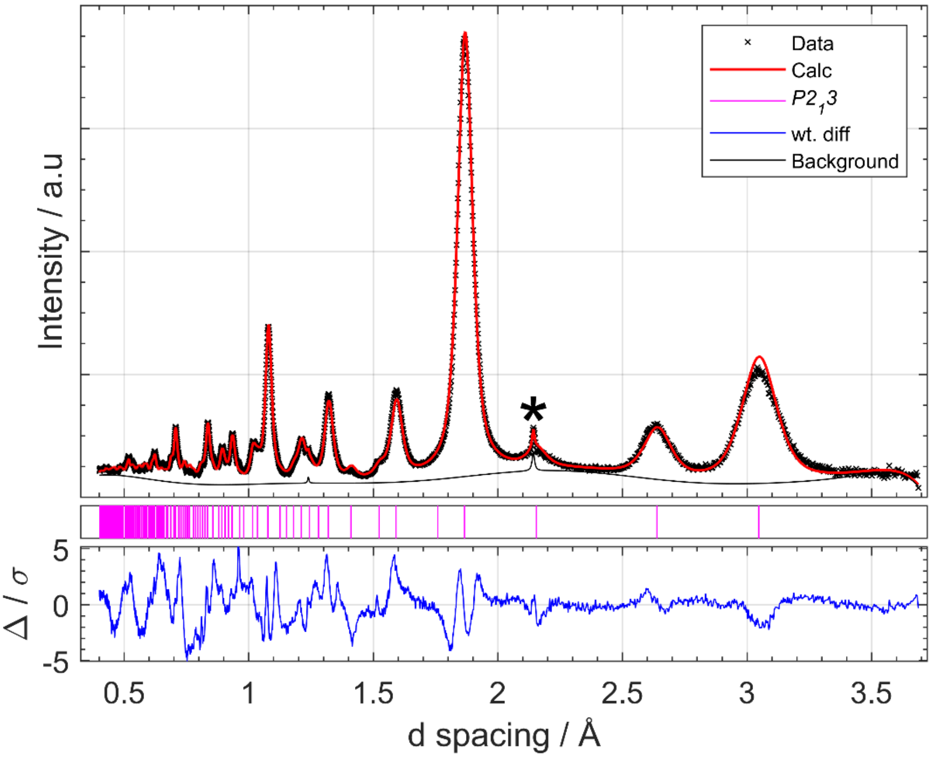

Figure 4.9: Rietveld refinement of alkoxide synthesised $Ce_{0.5}Zr_{0.5}O_2$ model refined against 5 banks of neutron data using the $P4_2/nmc$ structure. Data shown acquired on bank 4. Background shown due to primary vanadium can reflection fitted as background and indicated with an asterisk. Refined parameters are shown in Table 4.4.

Table 4.4: Refined parameters for alkoxide synthesised $Ce_{0.5}Zr_{0.5}O_2$ using the tetragonal $P4_2/nmc$ space group in the 2nd origin, a = 3.7322(6), c = 5.2759(14), a/c ratio = 0.7074 (ideal cubic ratio = 0.7071…). Calculated density = 6.6732 g/cm^3, oxygen 'displacement' from cubic z coordinate = 0.2509 (0.132 Å), wR = 1.78 %.

Atom	Label	Wyck.	*x*	*y*	*z*	Uiso / Å^2	Occ.
Ce Zr	Ce Zr	2a	0.25	-0.25	0.25	0.00729(11)	0.5 0.5
O	O	4d	0.25	0.25	0.47491(16)	0.01743(15)	1

4.3 Combined average and local structure investigation: RMCProfile

4.3.1 Initial setup for the $Ce_{0.5}Zr_{0.5}O_2$ industrial model

Initial setup of the RMC model for the as-provided industrial $Ce_{0.5}Zr_{0.5}O_2$ sample follows the method outlined in Chapter 2. The model generated was fitted against neutron Bragg diffraction (Polaris bank 4), neutron total scattering and X-ray total scattering data using a 12 × 12 × 12 fluorite supercell. The cubic fluorite base unit cell was chosen for the same reasons as the $Ce_{0.75}Zr_{0.75}O_2$ F800 sample discussed in Chapter 4. Figure 4.10 below shows the starting model used in sub-figure D_1.

The experimental PDF was heavily impacted by the small crystallite size of the industrially provided $Ce_{0.5}Zr_{0.5}O_2$ sample, this effect is observed as significant dampening towards the higher *r* distances of the PDF. RMCProfile is currently incapable of simulating this ~ 50 nm crystallite size effect with the 6.3 nm^3 supercell sizes explored, to account for this feature of the data an 'enhancement' function was used. The enhancement function was an inverted application of the spdiameter function used in PDFgui[16] used to enhance the experimental G(r) rather than dampening a model. A crystallite size of 50 nm was chosen based on preliminary PDFgui fitting of the dampening profile observed.

No interstitial oxygen of note was observed via Rietveld refinement of the Bragg diffraction data, or via RMC modelling using a trial interstitial included model, in both trial studies meaningful interstitial site occupancy was rejected by the refined models.

4.3.2 Initial setup for the $Ce_{0.5}Zr_{0.5}O_2$ alkoxide model

Initial setup of the RMC model for the alkoxide synthesised $Ce_{0.5}Zr_{0.5}O_2$ sample follows the method outlined in Chapter 2. The model was fitted against a neutron diffraction pattern (Polaris bank 4) and neutron total scattering data using a 12 × 12 × 12 fluorite supercell. The cubic fluorite base unit cell was chosen for the same reasons as the $Ce_{0.75}Zr_{0.75}O_2$ F800 sample discussed in Chapter 4.

Due to limited crystallite size significantly impacting the relative intensity of the PDF patterns generated for the alkoxide synthesised $Ce_{0.5}Zr_{0.5}O_2$ sample the same crystallite 'enhancement' function described for the industrially provided RMC model was applied to the G(r) PDF pattern. This function was an inverted application of the spdiameter function used in PDFgui, with a crystallite size of 50 nm chosen based on preliminary PDFgui fitting of the dampening profile observed which was very similar to the industrially provided sample.

During initial refinements an unexpectedly large number of oxygen atoms moved to the initially unoccupied 'interstitial' 4b site, this 'oxygen migration' effect was included in subsequent RMC models via the mechanism to allow oxygen atoms to swap between the 8c fluorite oxygen site and the 4b interstitial oxygen site, effectively probing the concentration of Frenkel type oxygen defects.

Caution should be employed when drawing conclusions from the RMC supercell model generated from the alkoxide synthesised $Ce_{0.5}Zr_{0.5}O_2$ due to the limited quality and types of data used, namely the sole dependence on neutron data and the introduction of significant artefacts due to the crystallite size enhancement function. While this caution should be noted, the sense of the model was rigorously checked and provided no clear indication of the conclusions having been driven by data artefacts.

4.3.3 Initial setup for the κ-$CeZrO_4$ SRMO1050 model

The initial setup of the RMC model follows the method described in Chapter 2 with the following considerations. The initial structural model chosen was the $P2_13$ (2 × 2 × 2 fluorite supercell) structure with idealised fluorite atomic coordinates and interstitial sites. This ‘idealised’ modification was made to better characterise how the model deviates from the fluorite sub-units to allow for meaningful comparison across different materials studied by RMCProfile using fluorite unit cells throughout this thesis. Given the somewhat unexplained preference for specific occupied interstitial sites highlighted in the Bragg diffraction the choice was made to use idealised fluorite supercell oxygen coordinates and occupancies with 0 % interstitial oxygen. This was done to avoid confirmation bias between the Bragg model and the RMC model on the types of oxygen disorder present. The RMC model required longer run times than other atom equivalent models generated which may be in part due to this deliberate omission of starting oxide disorder. Specifically no starting interstitial oxygen was chosen for two reasons, first the interstitial oxygen occupancy in the Rietveld models displayed in Table 4.4 were varied and non-uniform, which would inherently bias the starting RMC models. Secondly omitting any starting interstitial oxygen site occupancy is less likely to provide confirmation bias for the presence of interstitial oxygen as either uniform or non-uniform across the 32 interstitial oxygen sites. Approaching the model in this manner was a step to avoid imposing the conclusions of the Rietveld model into the RMCProfile generated supercell allowing it to reach data driven configurations independent to the human influence over the Rietveld modelling.

To improve resolution of the significant cation ordering present, the model was simultaneously fitted against X-ray total scattering data in addition to neutron total scattering and neutron Bragg data. Figure 4.10 shows the final fitted supercell (A_2), the fitted supercell overlaid in a single unit cell (B_2, C_2) and the initial unit cell atom arrangement used (D_2) alongside the Fluorite unit cell equivalent used to fit the industrially provided $Ce_{0.5}Zr_{0.5}O_2$ sample.

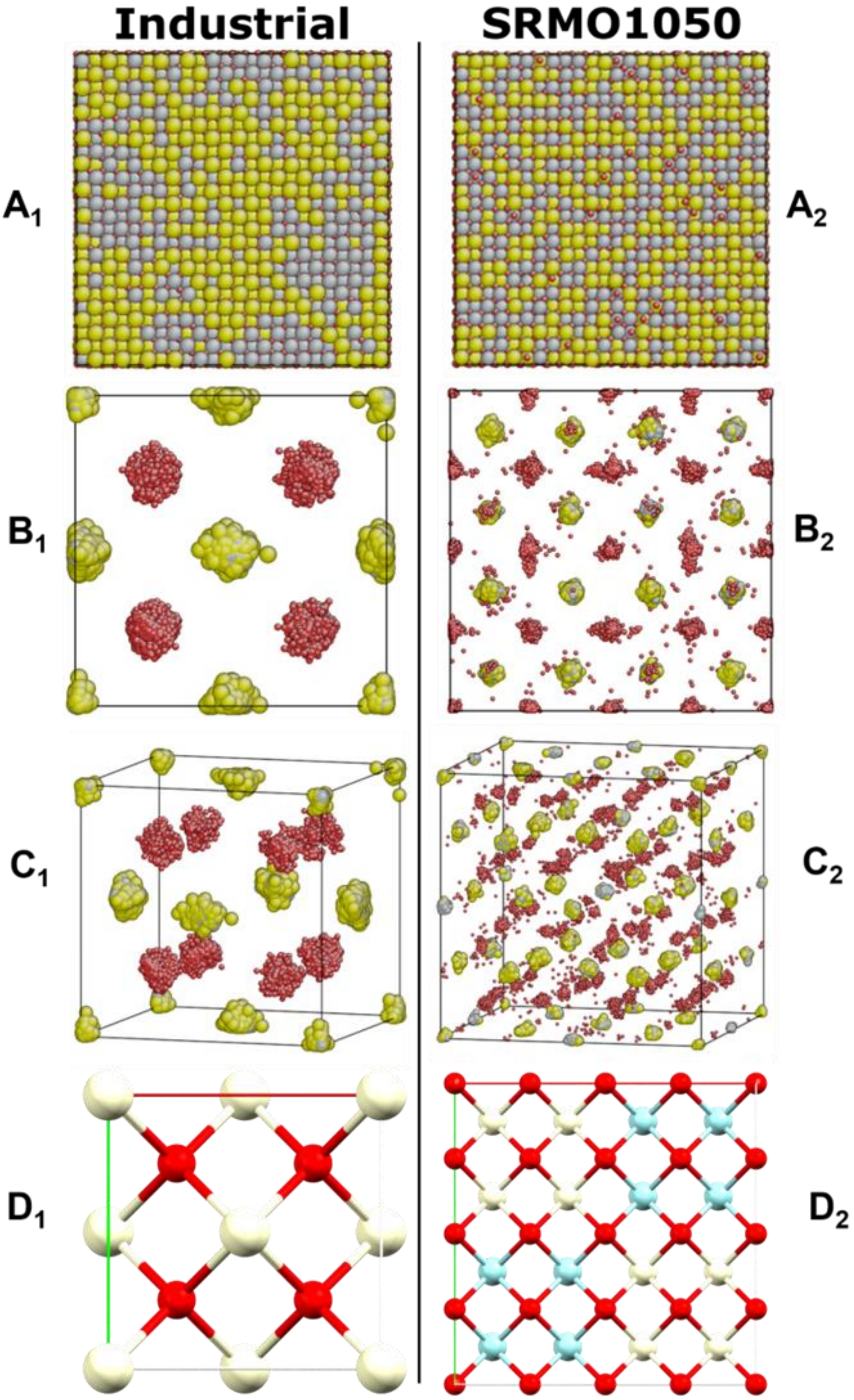

Figure 4.10: Models generated from RMC based on the fluorite unit cell. A) RMC generated supercell containing 20736 atoms. B) Supercell collapsed into a single fluorite unit cell, viewing angle from a single face. C) Viewing angle offset for additional perspective, yellow = cerium, grey = zirconium, red = oxygen. D) Classical view of the starting model. red = regular oxygen site, white = metal site, pink = interstitial oxygen site. Left, #$_1$*) 12 × 12 × 12 supercell model generated using experimental data of the as-provided industrial* $Ce_{0.5}Zr_{0.5}O_2$ *sample. Right, #*$_2$*) 6 × 6 × 6 supercell model generated using experimental data of the SRMO1050 treated* $Ce_2Zr_2O_8$ *sample.*

4.3.4 Results of RMC fitting of industrially provided $Ce_{0.5}Zr_{0.5}O_2$ data

Figure 4.11 shows the RMC model calculated fits against the observed neutron Bragg, neutron G(r) PDF and X-ray G(r) PDF data of the as-provided industrial $Ce_{0.5}Zr_{0.5}O_2$ sample. The fits were obtained using the 12 × 12 × 12 supercell with 20736 discrete atoms, 2,131,755 generated moves and 538,481 accepted moves over 24 hours of run time. In all compared datasets the model fits the observed data well across the entire fitted range.

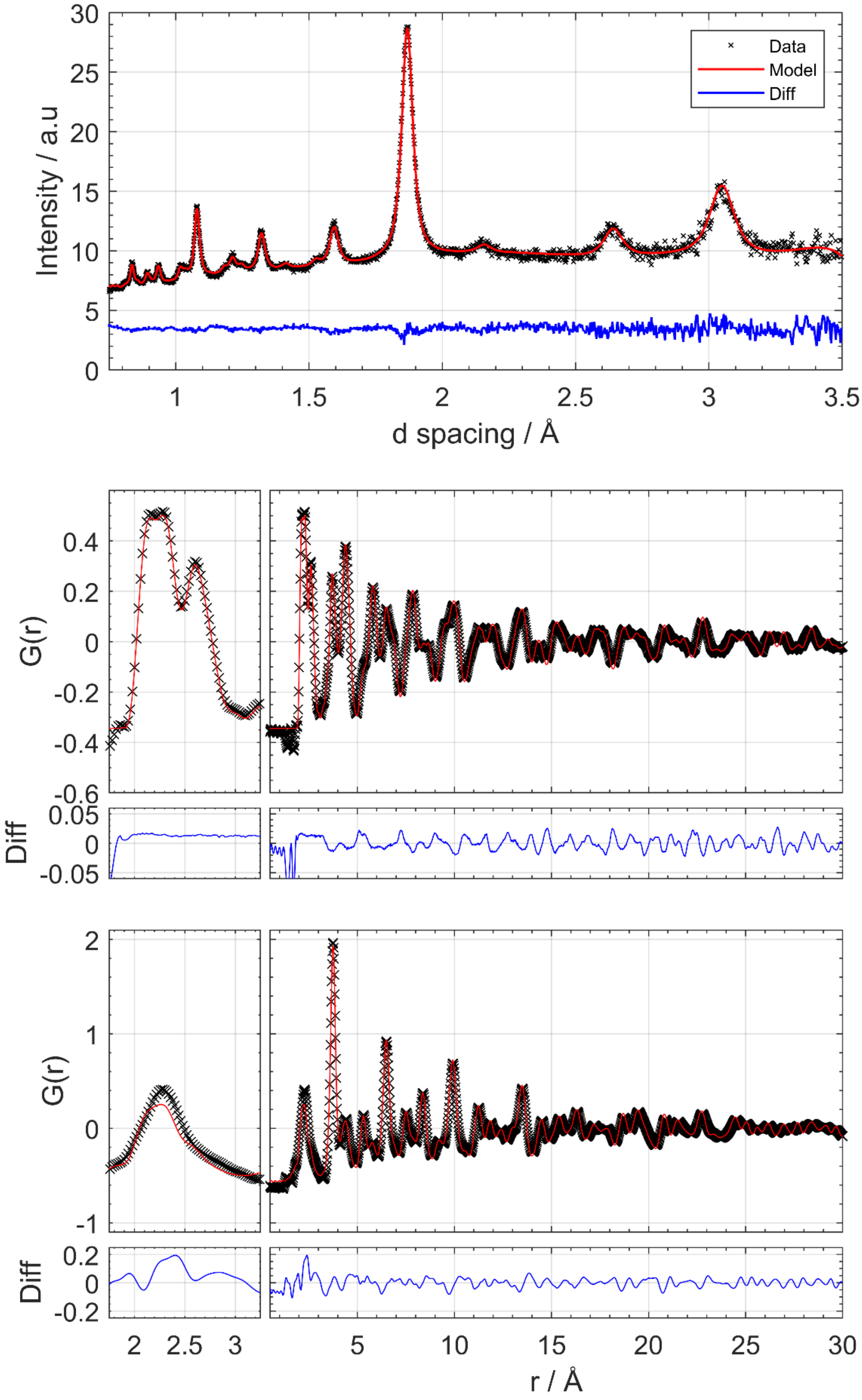

Figure 4.11: Datasets and calculated patterns from the RMCProfile generated 12 × 12 × 12 supercell for the as-provided industrial Ce$_{0.5}$Zr$_{0.5}$O$_2$ sample. Top) TOF neutron data acquired on Polaris bank 3. Middle) neutron pair distribution function acquired on Polaris. Bottom) X-ray pair distribution function acquired on the I15-1 beamline at the Diamond Light Source.

Figure 4.12 shows the atomic displacement histogram generated from the RMCProfile generated model for the industrial $Ce_{0.5}Zr_{0.5}O_2$ material. The most notable features of this displacement histogram are the broad but well-defined oxygen profile and the highly similar profiles of both cations present. The broad oxygen displacement profile shows a range of displacements which is not expected from thermal motion alone, this suggests that there may be two or more oxygen displacement environments, such as would be the case if the sample existed as crystallites/nanodomains with range of cation ratios. In this case, Zr rich regions would be expected to have larger O displacements as the local environments approach that of tetragonal ZrO_2 while Ce rich regions would be expected to be more cubic CeO_2 like where oxygen displacement from the ideal cubic site is defined by thermal motion alone.

The highly similar cation displacement profiles however indicate that the cations remain well mixed and in equivalent average environments when compared to the ideal fluorite structure.

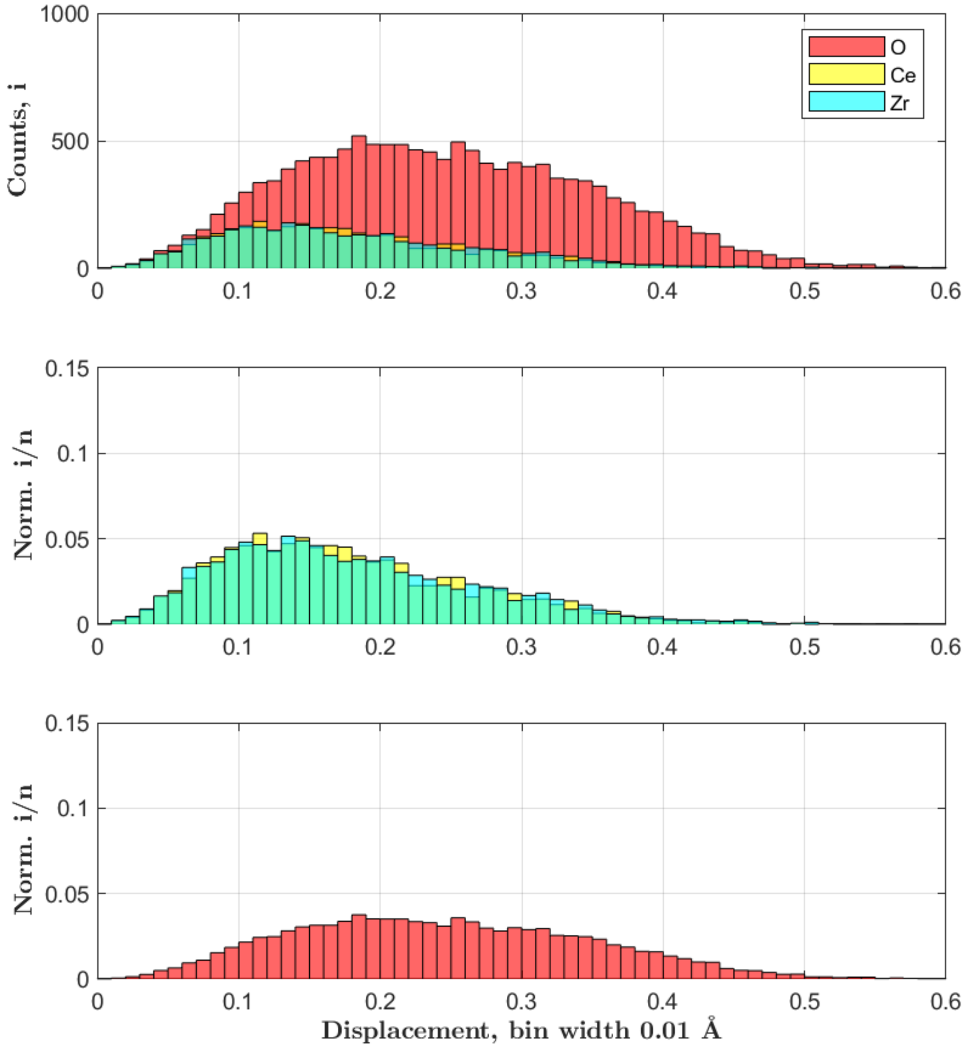

Figure 4.12: Top) Histogram of atomic displacement counts by species for the industrially provided $Ce_{0.5}Zr_{0.5}O_2$ *sample. Middle) Cerium (yellow) and zirconium (cyan) displacements normalised to relative atom count. Bottom) Bulk oxygen (red) normalised to relative atom count. Counts, Total = 20,736; Ce = 3456; Zr = 3456; O = 13824. Displacement distance measured from the sub-cell* $Fm\bar{3}m$ *idealised coordinates.*

Figure 4.13 shows the mean cation site occupancy of the 12 × 12 × 12 fluorite supercell reduced to the 1728 fluorite unit cells used to generate the supercell. The fluorite structure has 4 symmetry related cation sites which are all expected to have approximately equal cation occupancy in the case of a solid solution material with equal cation composition. This is shown to be true for the RMCProfile generated model showing all four sites have approximately Ce = ~50 % and Zr = ~50 %. During Rietveld refinement no oxygen vacancies were noted as such the model was constructed with full oxygen occupancy, no interstitial oxygen sites were indicated through the RMCProfile model fitting process or during Rietveld refinement, as such the 8 oxygen sites were not probed further as occupancy profiles would be uninformative.

Primitive site IDs (*P*1) 1-4 are the symmetrically equivalent Ce/Zr occupied 4a 0, 0, 0 $m\bar{3}m$ site and 8c 5-12 the being the symmetrically equivalent ¼, ¼, ¼, -43*m* O occupied site of the original $Fm\bar{3}m$ structure, P1 site IDs and ideal atomic coordinates are shown in Table 4.5.

Table 4.5: P1 transcription of the $Fm\bar{3}m$ *unit cell of the RMCProfile model of industrially provided* $Ce_{0.5}Zr_{0.5}O_2$ *with final site occupancy of the 1728 base unit cells.*

Atom	***P*1 Site ID**	**Wyck.**	***x***	***y***	***z***	**Occ. / %**
Ce : Zr	1	4a	0	0	0	45.4 : 54.6
Ce : Zr	2	4a	0.5	0.5	0	53.2 : 46.8
Ce : Zr	3	4a	0.5	0	0.5	50.2 : 49.8
Ce : Zr	4	4a	0	0.5	0.5	51.2 : 48.8
O	5	8c	0.25	0.25	0.25	1
O	6	8c	0.75	0.75	0.25	1
O	7	8c	0.75	0.25	0.75	1
O	8	8c	0.25	0.75	0.75	1
O	9	8c	0.75	0.75	0.75	1
O	10	8c	0.25	0.25	0.75	1
O	11	8c	0.25	0.75	0.25	1
O	12	8c	0.75	0.25	0.25	1

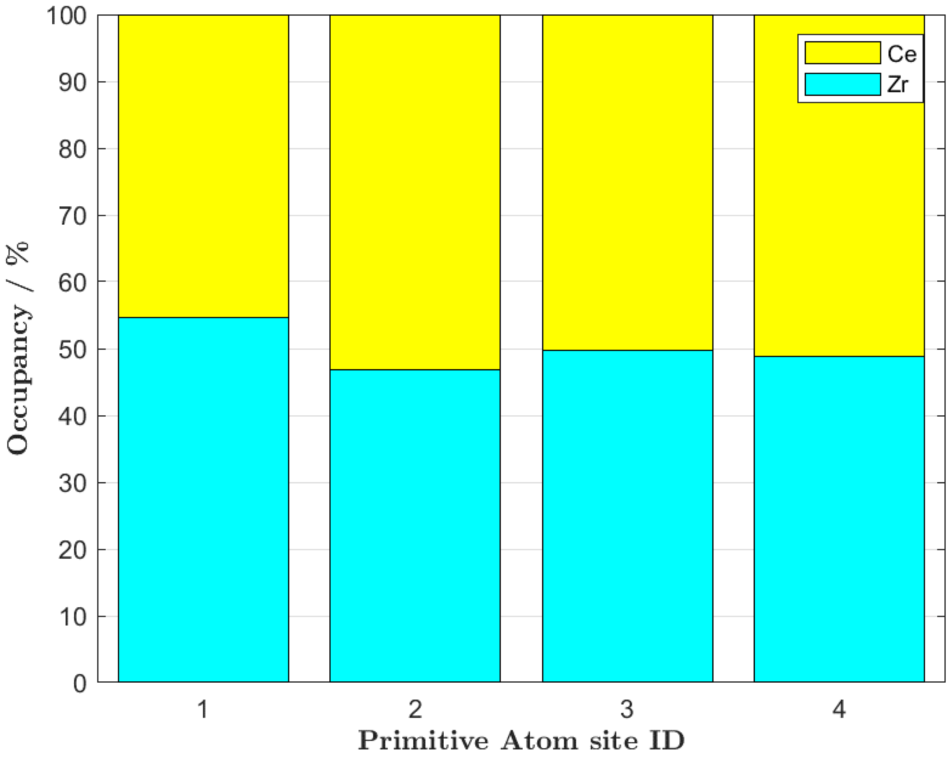

Figure 4.13: Cation site occupancy by individual unit cell cation sites for the as-provided industrial $Ce_{0.5}Zr_{0.5}O_2$ *sample. All sites are symettrically equivlent in the original structure.*

Figure 4.14 shows the nearest cation neighbour distances based on cation species. Based on the *P*4$_2$/*nmc* Rietveld refinements shown in Figure 4.3 and Table 4.1 for this sample the average metal-metal nearest neighbour distance was expected to be 3.7344(6) Å (lattice parameter *a*), this is approximately true for Ce – Zr neighbours where the mean atom-atom distance was 3.733 Å. Ce – Ce and Zr – Zr neighbours showing significant divergence from the average with atom-atom distances of 3.779 Å and 3.715 Å, respectively. The model also showed a significant preference for like-like cation neighbours well above that expected from statistical deviation, with Ce – Ce, Ce- Zr and Zr – Zr observed/expected ratios of occurrences being 1.15, 0.83 and 1.16, respectively. This supports the hypothesis that the sample exists as discrete crystallites or nano-domains with a non-uniform range of cerium to zirconium ratios.

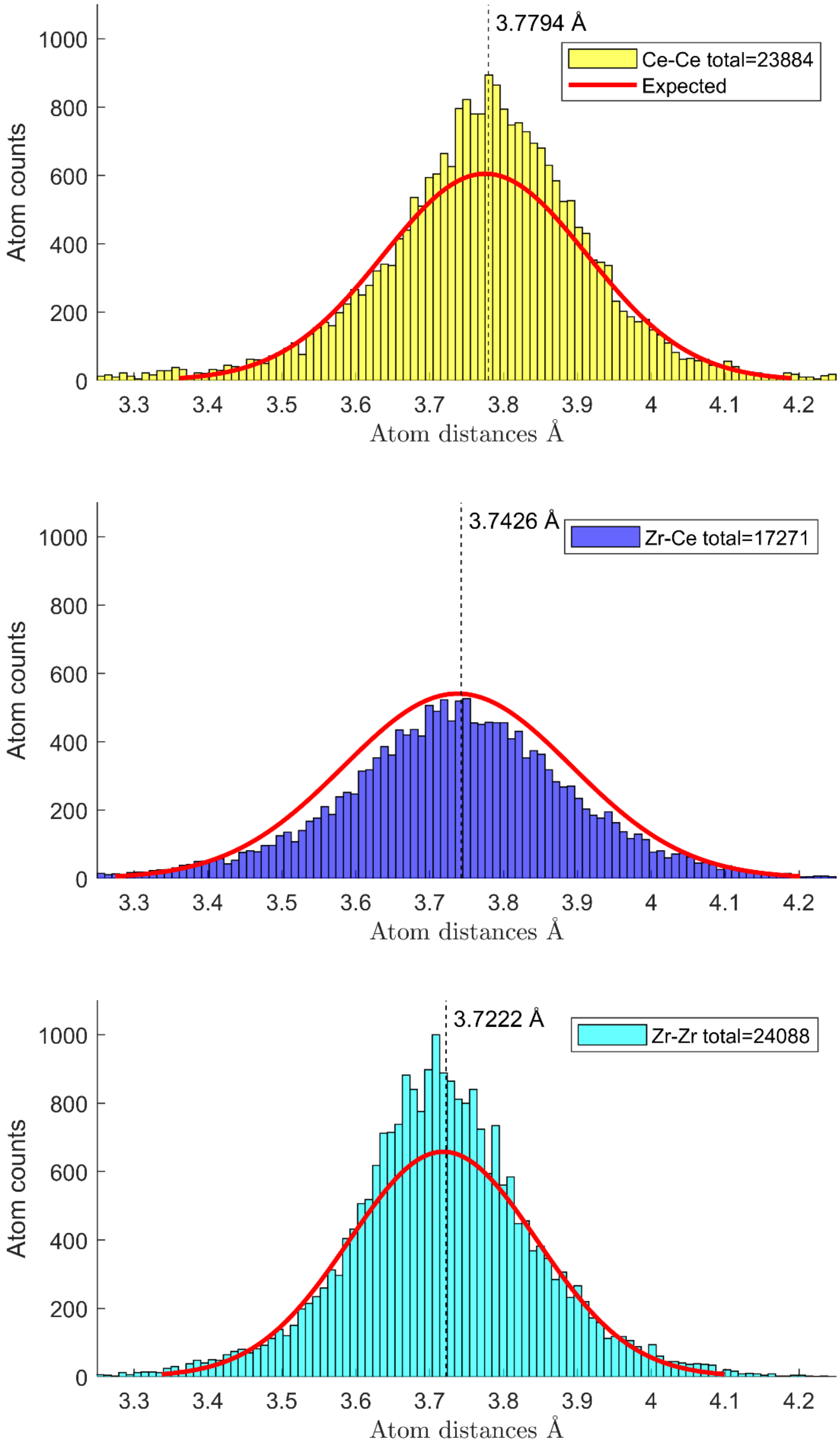

Figure 4.14: Histograms of nearest neighbour cation count and distance by species for the industrially provided Ce$_{0.5}$Zr$_{0.5}$O$_2$ material. Top) Ce-Ce cation neighbour distances. Middle) Ce-Zr cation neighbour distances. Bottom) Zr-Zr cation neighbour distances. Red 'expected' line indicates profile and intensity for a statistically defined solid solution. Dashed line shows mean atom-atom distance for the respective pairs.

Figure 4.15 shows the Clapp configuration analysis of the industrially provided $Ce_{0.5}Zr_{0.5}O_2$. Clapp configuration analysis focuses solely on cation ordering and highlights occurrences of symmetrically unique 13 cation clusters (1 central, 12 nearest neighbours in a face-centred cubic arrangement) arrangements. In a binary system there are 144 unique configurations, and the occurrences of these configurations are compared with the statistical probability of their occurrence and plotted as a multiple of the standard deviation away from the statistically defined probable number of occurrence for each configuration. Dotted lines indicate 3 standard deviations above and below from the statistically random predicted number of occurrences which is used as a test of significance.

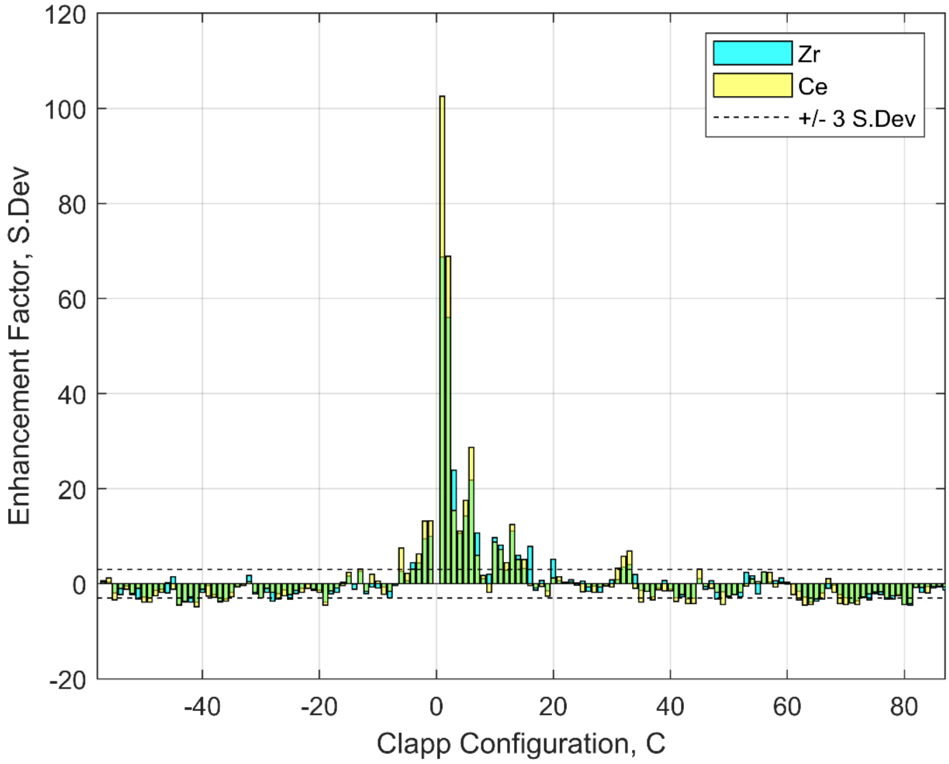

Figure 4.15: Histogram of Clapp configurations observed within the 12 × 12 × 12 supercell for the as-provided industrial $Ce_{0.5}Zr_{0.5}O_2$ sample.

Figure 4.16 shows how the enhanced Clapp configurations link to each other in single mutation steps. The diagram is shown for completeness but shows what is already well established for this model in Figure 4.14 and Figure 4.15, that the local atomic configurations describe cation rich nano-domains of Ce and Zr.

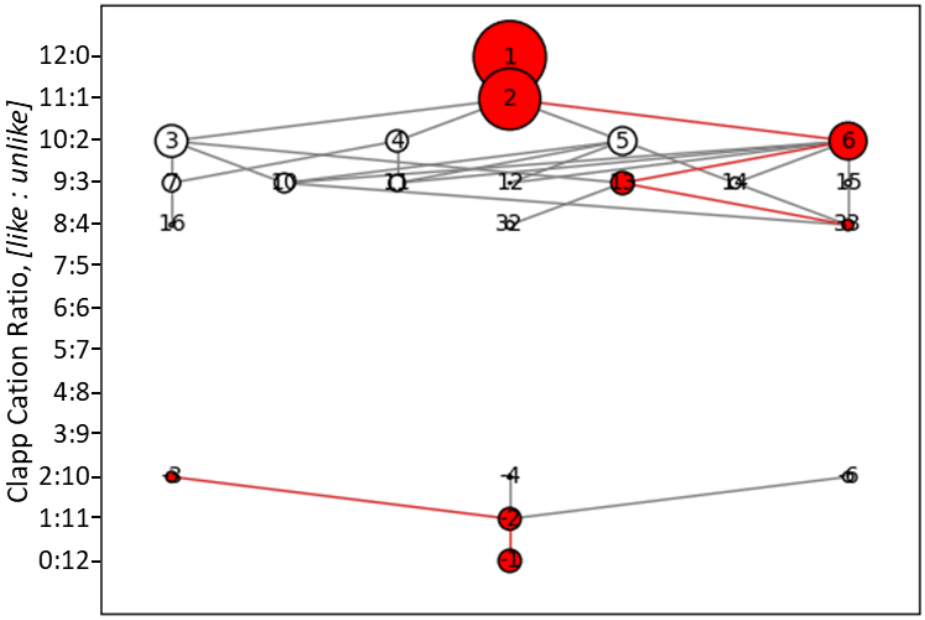

Figure 4.16: Diagram shows single mutation linked Clapp configurations enhanced in the industrially provided sample, red indicates the most enhanced configuration in group, circle sizes correspond to the magnitude of enhancement observed.

The Clapp configuration analysis for this RMCProfile generated model using combined neutron Bragg, n-PDF and X-PDF data clearly shows significant levels of cation clustering are present within the model with both cation species showing the same enhanced configurations. This analysis clearly supports a hypothesis of cation rich crystallites/nanodomains where the average bulk material is comprised of crystallites/domains with a range of cation compositions.

Combined with the rest of the analysis undertaken on this RMC generated model indicates that the bulk structure of the industrially provided $Ce_{0.5}Zr_{0.5}O_2$ sample exists as an average cerium zirconium oxide solid solution where cerium and zirconium atoms are equivalent. This uniformity ceases on the local scale where there is ~15 % more Ce-Ce cation neighbours showing longer than average distances and ~16 % more Zr-Zr cation neighbours showing shorter than average distances. This indicates that the average bulk solid solution is comprised of local regions of off-stochiometric ratios of cerium and zirconium.

4.3.5 Results of RMC fitting of alkoxide synthesised $Ce_{0.5}Zr_{0.5}O_2$ data

Caution is advised when drawing conclusions from the model generated for the alkoxide synthesised $Ce_{0.5}Zr_{0.5}O_2$ sample due to the limited data quality and range of data types used. Due to limited sample volume the collected neutron data were not as high quality as the neutron total scattering data collected for other samples discussed in this thesis. X-ray data were collected on a separate batch but the sample analysed was found to be a true tetragonal unit cell where the a/c ratio deviated significantly from 0.7071 making it inconsistent with the observed neutron diffraction data. While the samples were initially screened using a laboratory X-ray diffractometer this inconsistency was only observed when fitting the data and noted too late into this work to remake the samples and acquire the required data. The same batch of sample was not used due to the full volume of the original batch being used to collect the neutron diffraction data leaving it in an activated state. A subsample was not kept due to significant uncertainty related to the likelihood of the I15-1 experiment which suffered five separate cancellations and finally occurred 2 years, 2 months and 17 days after the original scheduled date, the cause of these cancellations were a mix of beamline/instrument component failures and Covid-19 restrictions.

Figure 4.17 shows the RMC model calculated fits against the observed neutron Bragg diffraction and neutron G(*r*) PDF data of the alkoxide synthesised $Ce_{0.5}Zr_{0.5}O_2$ sample. The fits were obtained using a the 12 × 12 × 12 supercell with 27648 discrete atoms with 5,838,468 generated moves and 1,799,711 accepted moves over 24 hours of run time. In all compared datasets the model fit the observed data reasonably across the entire fitted range. The primary vanadium can Bragg reflection is marked with an asterisk for clarity.

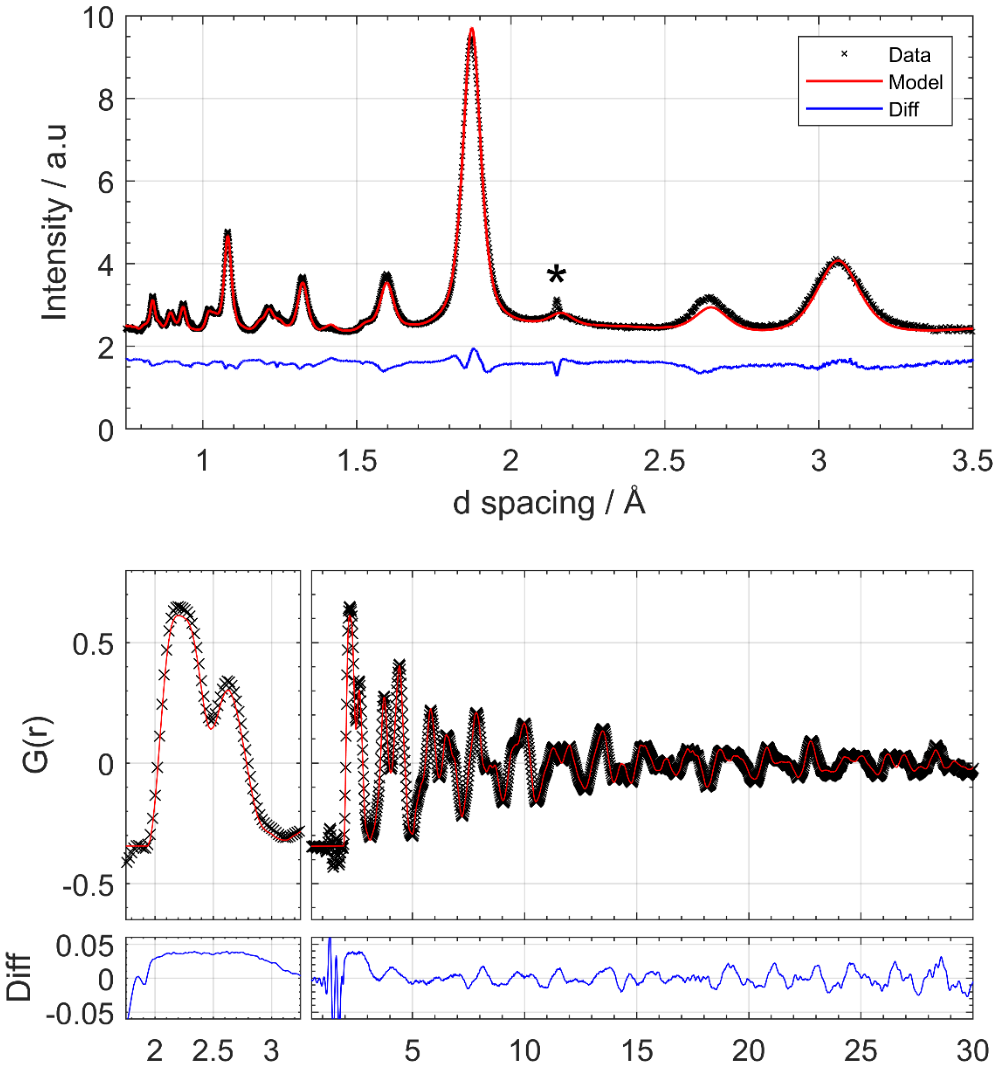

Figure 4.17: Datasets and calculated patterns from the RMC generated 12 × 12 × 12 supercell for the Alkoxide synthesised Ce$_{0.5}$Zr$_{0.5}$O$_2$ sample. Top) TOF neutron data acquired on Polaris bank 4, primary V metal reflection marked for clarity . Bottom) 0-30 Å neutron pair distribution function acquired on Polaris.

Figure 4.18 shows the atomic displacement histogram generated from the RMC supercell model for the alkoxide synthesised Ce$_{0.5}$Zr$_{0.5}$O$_2$ sample. The observed oxygen displacement profile is broad resembling close to that observed for the industrially provided sample, although more uniform throughout. The cerium and zirconium displacements show both cations appear equally displaced indicating similar average local environments for both cations. The interstitial oxygen present appears to be spread across a range of displacements with no clear preferred average displacement.

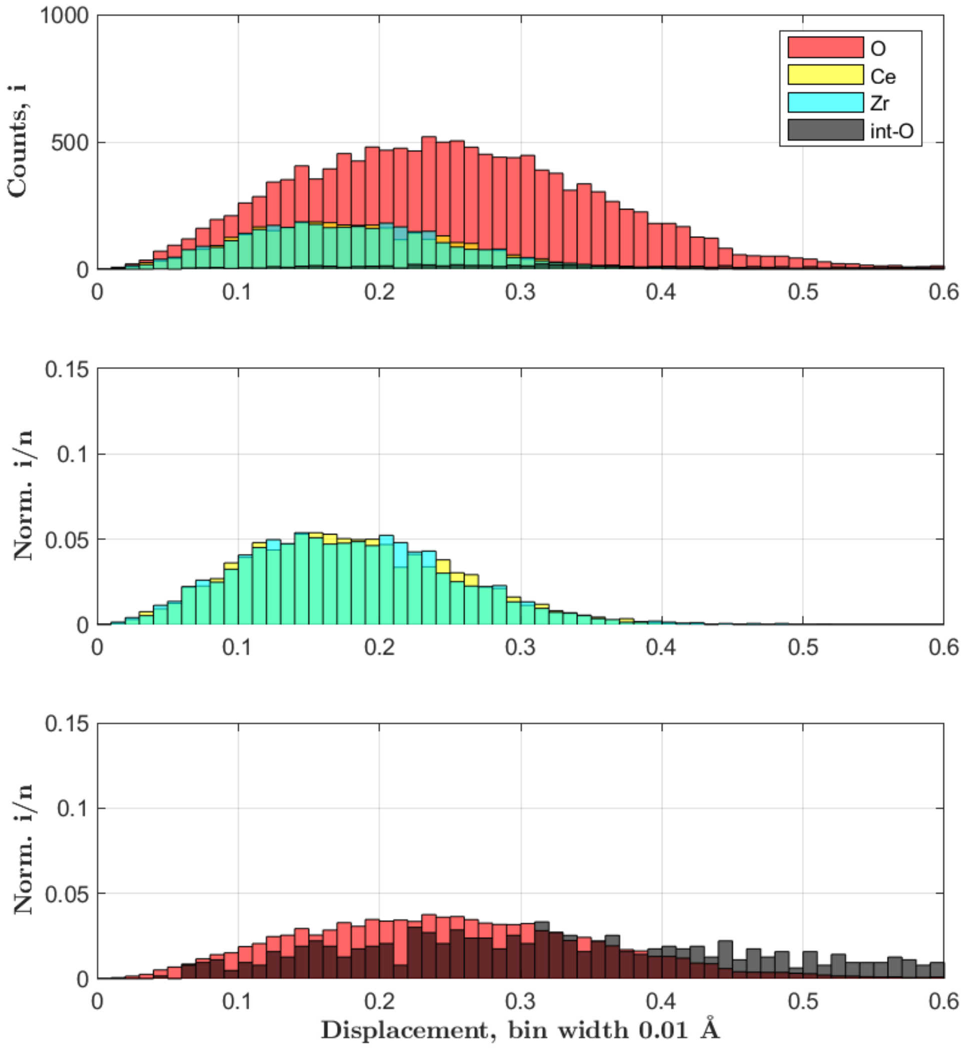

Figure 4.18: Top) Histogram of atomic displacement counts by species for the Alkoxide synthesised $Ce_{0.5}Zr_{0.5}O_2$ *sample. Middle) Cerium (yellow) and zirconium (cyan) displacements normalised to relative atom count. Bottom) Bulk oxygen (red) and interstitial oxygen (black) normalised to relative atom count. Counts, Ce = 3456; Zr = 3456; O = 13824, int-O = 649. Displacement distance measured from the* $Fm\bar{3}m$ *idealised coordinates.*

Figure 4.19 shows the mean cation site occupancy of the 12 × 12 × 12 fluorite supercell reduced to the 1728 fluorite unit cells used to generate the supercell. The fluorite structure has 4 symmetry related cation sites which are all expected to have approximately equal cation occupancy in the case of a bulk solid solution material with equal cation composition. This is shown to be true for the RMCProfile generated model showing all four sites have approximately Ce = ~50 % and Zr = ~50 %.

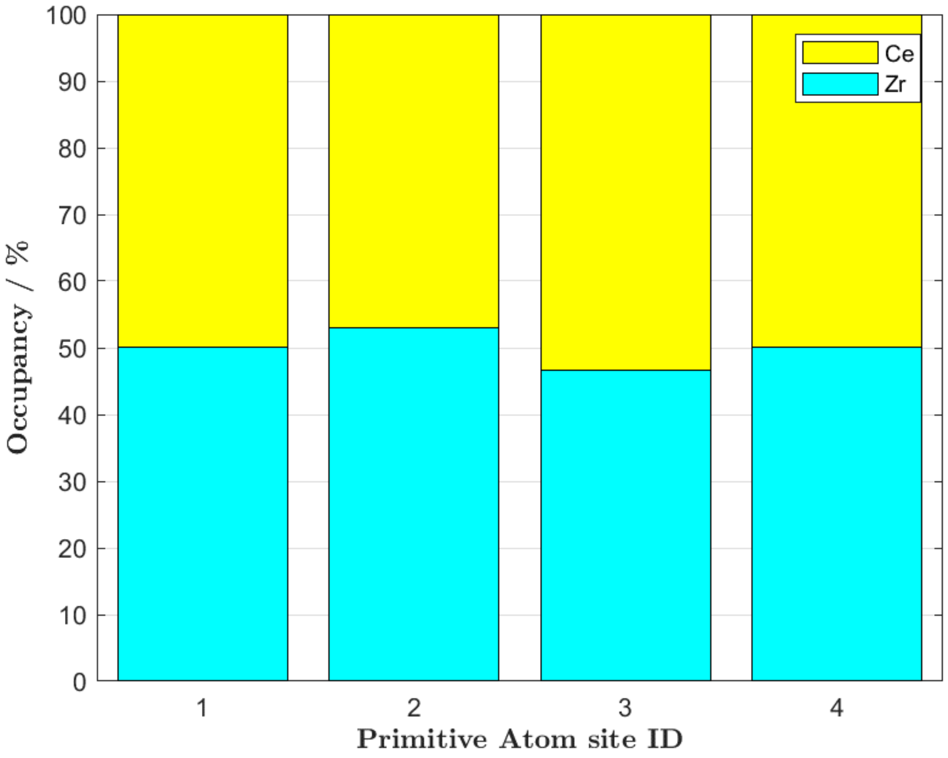

Figure 4.19: Cation site occupancy by individual unit cell cation sites for Alkoxide synthesised $Ce_{0.5}Zr_{0.5}O_2$ *sample. Sites (1-4) are the symmetrically equivalent 4a fluorite sites.*

Figure 4.20 shows the mean anion site occupancy histogram of the 12 × 12 × 12 fluorite supercell reduced to the 1728 fluorite unit cells used to generate the supercell. Oxygen vacancies appear to form approximately evenly from all of the originally occupied 8c oxygen sites and occupy the 4b interstitial oxygen sites evenly summing to 4.7 % of the total oxygen content. The model showed a strong preference for high Zr environments surrounding the occupied interstitial sites showing that 91.0 % of the interstitial oxygen cation neighbours were Zr atoms.

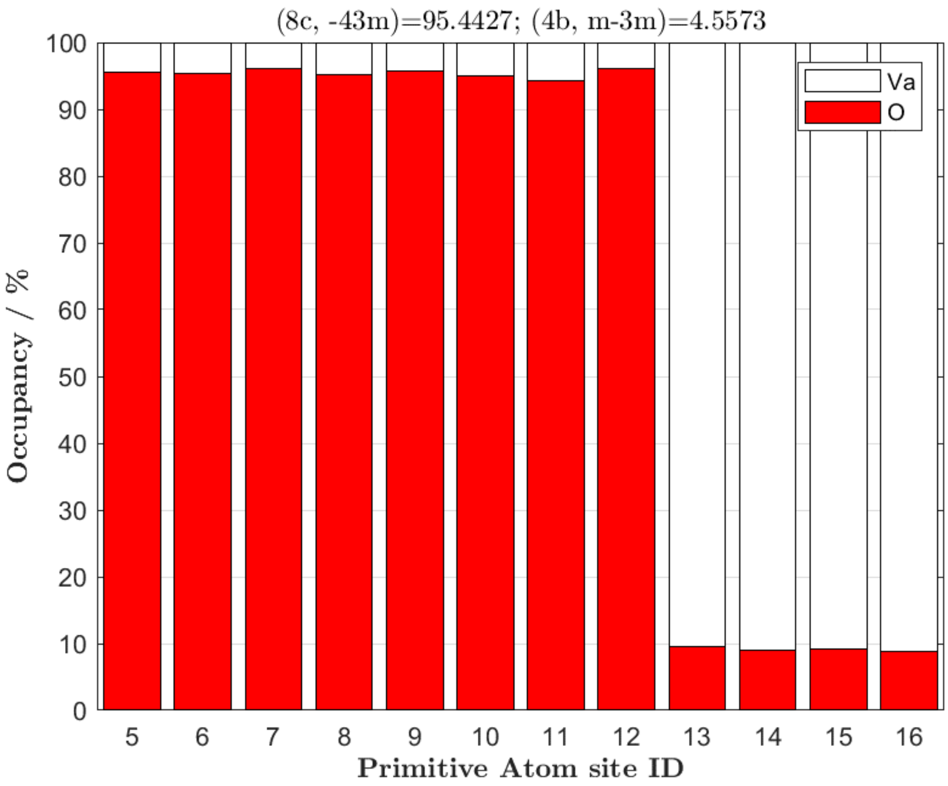

Figure 4.20: Oxygen site occupancy by individual unit cell oxygen and interstitial sites for the Alkoxide synthesised $Ce_{0.5}Zr_{0.5}O_2$ *sample. Sites (5-12) are symmetrically equivalent 8c bulk oxygen sites, while sites 13-16 are symmetrically equivalent 4b interstitial oxygen sites.*

Primitive site IDs (*P*1) 1-4 are the symmetrically equivalent Ce/Zr occupied 4a 0, 0, 0 $m\bar{3}m$ site and 5-12 the being the symmetrically equivalent 8c ¼, ¼, ¼, -43*m* O occupied site of the original $Fm\bar{3}m$ structure while 13-16 represent the interstitial oxygen 4b 0, 0, 0.5 $m\bar{3}m$ site. *P*1 site details and occupancy are shown in Table 4.6.

Table 4.6: P1 transcription of the $Fm\bar{3}m$ unit cell of the RMCProfile model of alkoxide synthesised $Ce_{0.5}Zr_{0.5}O_2$ with final site occupancy of the 1728 base unit cells.

Atom	***P*1 Site ID**	**Wyck.**	**x**	**y**	**z**	**Occ. / %**
Ce : Zr	1	4a	0	0	0	49.9 : 50.1
Ce : Zr	2	4a	0.5	0.5	0	47.0 : 53.0
Ce : Zr	3	4a	0.5	0	0.5	53.3 : 46.7
Ce : Zr	4	4a	0	0.5	0.5	49.8 : 50.2
O	5	8c	0.25	0.25	0.25	95.5
O	6	8c	0.75	0.75	0.25	95.4
O	7	8c	0.75	0.25	0.75	96.1
O	8	8c	0.25	0.75	0.75	95.3
O	9	8c	0.75	0.75	0.75	95.8
O	10	8c	0.25	0.25	0.75	95.0
O	11	8c	0.25	0.75	0.25	94.3
O	12	8c	0.75	0.25	0.25	96.2
O	13	4b	0	0	0.5	9.5
O	14	4b	0	0.5	0	9.0
O	15	4b	0.5	0	0	9.1
O	16	4b	0.5	0.5	0.5	8.9

Figure 4.21 shows the cation-cation nearest neighbour distances by cation species. There is a significant number of like-like neighbour pairings than expected based on cation composition alone. This shows that the RMC generated supercell indicates the presence of cation rich domains present within the sample, while mean cation-cation distance does differ by species, the magnitude of these differences remains small and may not be significant.

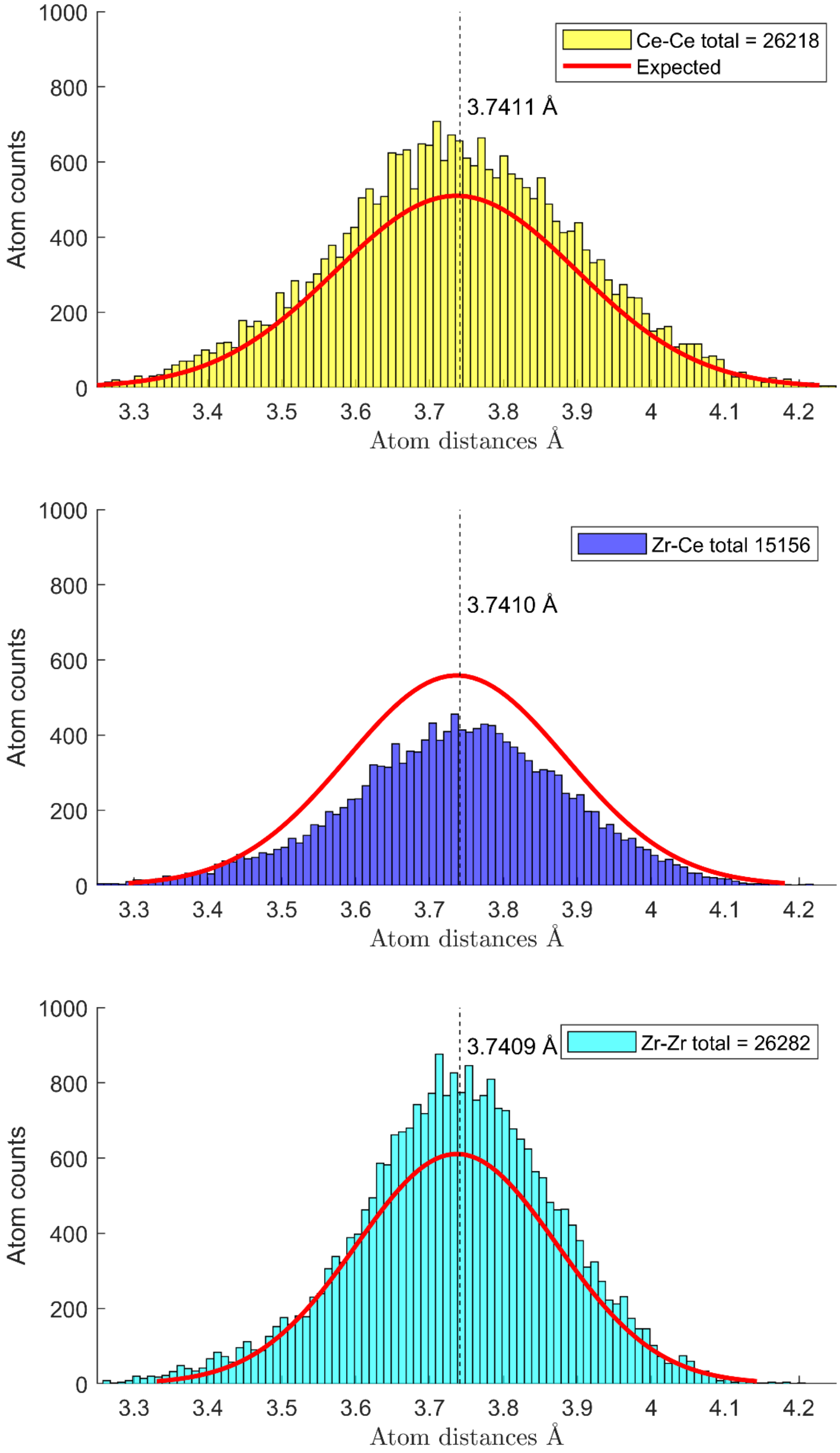

Figure 4.21: Histograms of nearest neighbour cation count and distance by species for the Alkoxide synthesised $Ce_{0.5}Zr_{0.5}O_2$ *sample. Top) Ce-Ce cation neighbour distances. Middle) Ce-Zr cation neighbour distances. Bottom) Zr-Zr cation neighbour distances. Red 'expected' line indicates profile and intensity for a statistically defined solid solution. Dashed line shows mean atom-atom distance for the respective pairs.*

Figure 4.22 shows the Clapp configuration analysis for the alkoxide synthesised $Ce_{0.5}Zr_{0.5}O_2$ model generated by RMCProfile. The analysis clearly shows cation rich nanodomains are the most enhanced local structure with C1 – C8 occurring significantly more than statistically expected. There is also additional enhanced configurations spanning all the way to the well-mixed 6 like, 6 unlike region of configurations showing that while there is cation clustering present, there are also more regions of specifically arranged cation mixing than statistically expected. Cerium and zirconium atoms appear to form near-identical local structures.

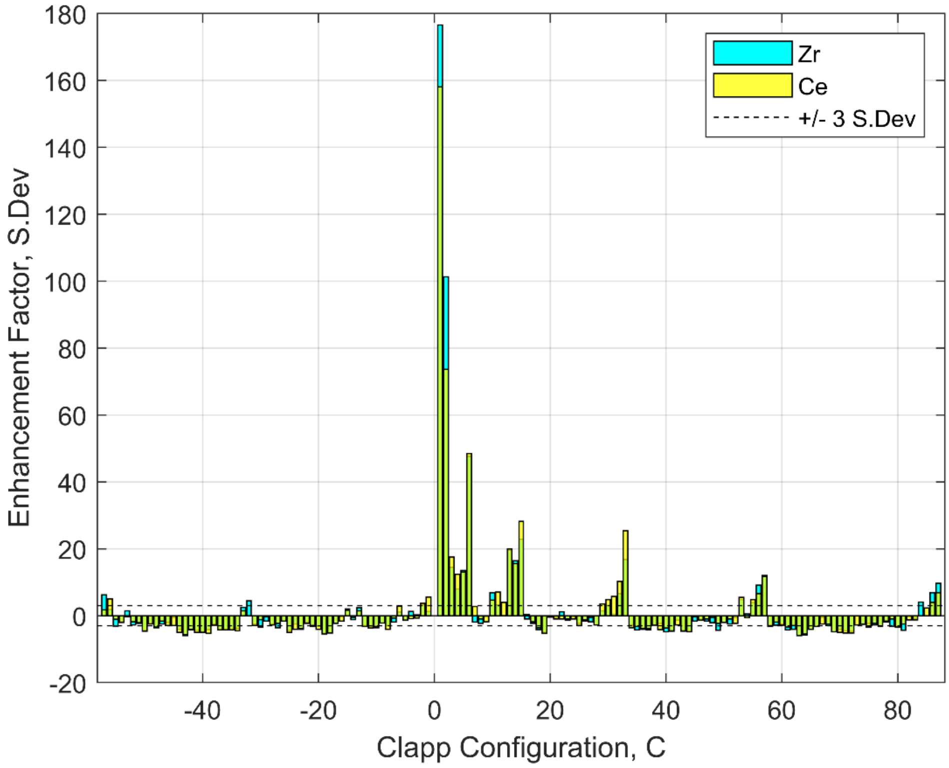

Figure 4.22: Histograms of Clapp configurations observed within the 12 × 12 × 12 fluorite supercell for the alkoxide synthesised $Ce_{0.5}Zr_{0.5}O_2$ sample.

Figure 4.23 shows a diagram linking the enhanced Clapp configurations for this model, showing that the primarily enhanced configurations describe cation rich clusters with specific cation arrangements spanning into the 'well-mixed' compositional regions.

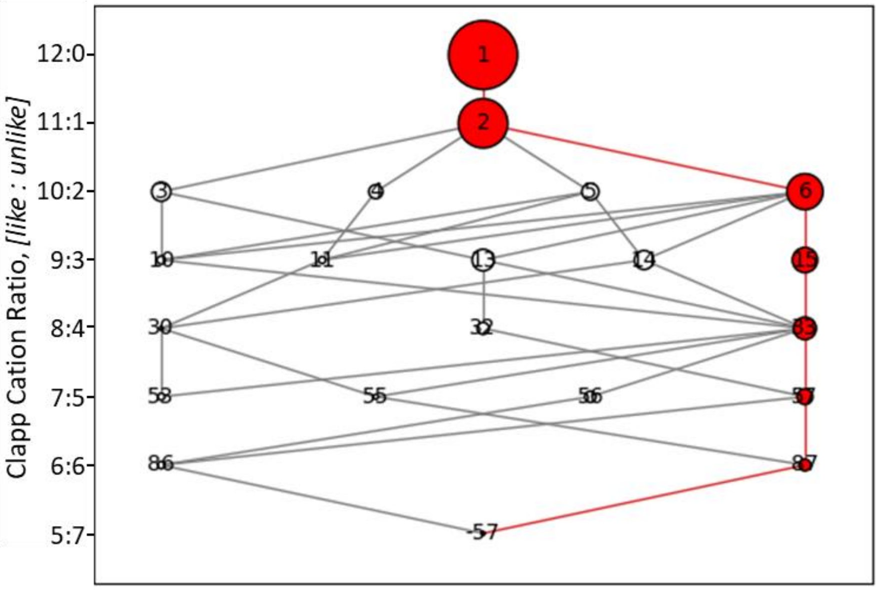

Figure 4.23: Diagram showing single mutation linked Clapp configuration for the Alkoxide synthesised sample, red indicates the most enhanced configuration in group, circle sizes correspond to the magnitude of enhancement observed.

While all conclusions drawn from this model should be done so with caution, the RMC model does indicate that the material is primarily comprised of cation rich regions with an enhanced number of specific local structures, these enhanced cation structures show near equal enhancement for both Ce centred and Zr centred configurations. When considered alongside the near-identical displacement profiles and cation-cation nearest neighbour distances the conclusions formed from this model are that the Cerium and Zirconium exist in near-cation segregated but otherwise equivalent environments. . Anion analysis indicates ~ 5 % of the overall oxygen is present in interstitial sites with a strong preference for Zr rich regions, Zr makes up ~ 90 % of the cation neighbours for occupied interstitial sites.

4.3.6 Results of RMC fitting of SRMO1050 κ-$CeZrO_4$ data

Figure 4.24 shows the fitted pattern of the RMCProfile generated 6 × 6 × 6 kappa supercell (12 × 12 × 12 fluorite supercell) is in good agreement with the observed neutron Bragg, n-PDF and X-PDF data. This model was run for 5,287,542 moves with a total of 2,001,815 accepted moves over 84 hours.

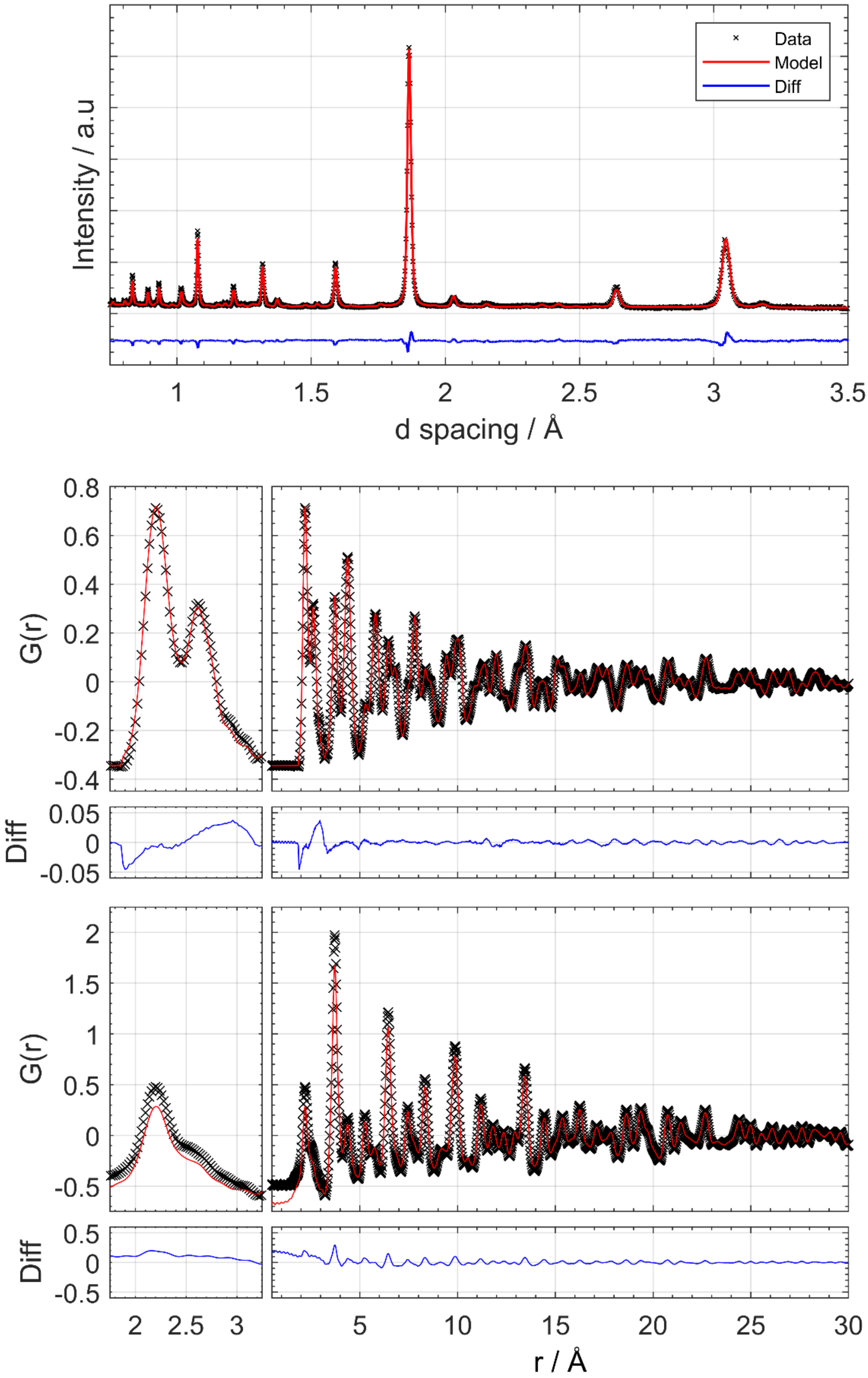

Figure 4.24: Datasets and calculated patterns from the RMC generated 6 × 6 × 6 kappa (12 × 12 × 12 fluorite) supercell for the SRMO1050 treated Ce$_{0.5}$Zr$_{0.5}$O$_2$ sample. Top) TOF neutron diffraction data acquired on Polaris bank 4. Middle) Neutron pair distribution function acquired on Polaris. Bottom) X-ray pair distribution function acquired on I15-1, Diamond Light Source.

Figure 4.25 shows a histogram of atomic displacements of the 1050SRMO treated κ-$CeZrO_4$ model which shows an oxygen displacement profile spread across a wide range indicating a range of oxygen environments are present. Cation displacements clearly differ with mean values of 0.12 Å for Zr and 0.18 Å for Ce clearly showing the preferred bulk environment of these two cations are not equivalent.

While the interstitial oxygen present appears to have a preferred environment close to the ideal interstitial coordinates this is heavily biased by a very uneven interstitial occupancy profile shown later in Figure 4.29 making broad conclusions drawn from the interstitial displacements potentially misleading.

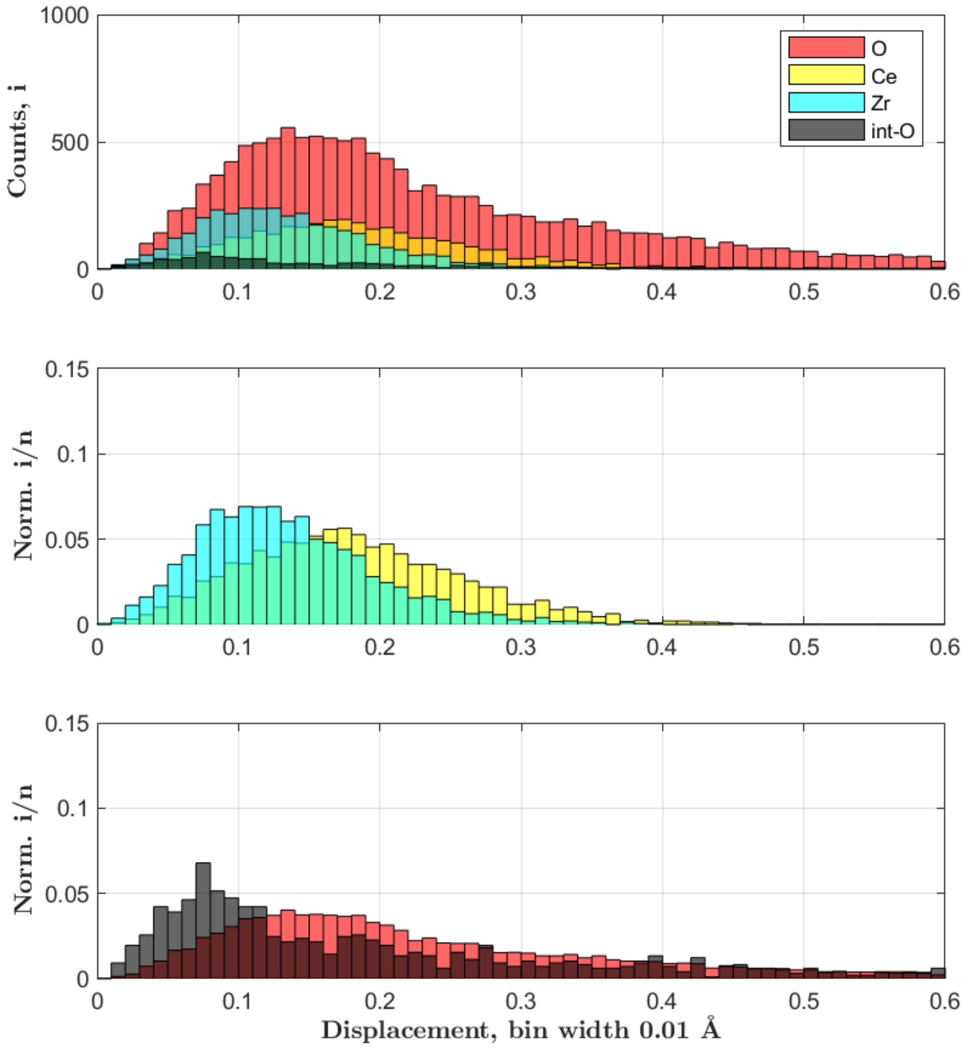

Figure 4.25: Top) Histogram of atomic displacement counts by species for the SRMO1050 treated sample. Middle) Cerium (yellow) and zirconium (cyan) displacements normalised to relative atom count. Bottom) Bulk oxygen (red) and interstitial oxygen (black) normalised to relative atom count. Counts, Total = 20,736; Ce = 3456; Zr = 3456; O = 12946, int-O = 878. Displacement distance measured from the sub-cell $Fm\bar{3}m$ *idealised coordinates.*

Figure 4.26 shows the cation occupancy by unit cell site ID. Site IDs 1-16 were originally occupied by Ce while sites 17-32 were originally occupied by Zr. The majority of the cation sites show a strong preference for their original cation showing this long-range cation ordering has been mostly preserved. Due to the supercell and periodic nature of the supercell it is very possible for the alternating cation arrangement to be preserved without having the original sites occupied, as the cation ordering could ‘shift’, maintaining the relative alternating cation ordering while changing which of the subcell sites are effectively occupied. This become increasingly likely for RMC simulations with large number of accepted moves/swaps, in this case ~ 5.3 million moves/swaps were tried and ~ 2 million were accepted over 84 hours of run time. Due to this Figure 4.26 informs on the presence of bulk scale cation ordering but is incapable of confirming what local arrangements are present. Clapp configuration analysis proves to shine additional insight into the nature of local order and is indeed more suited for analysis of cation structures, and is discussed later.

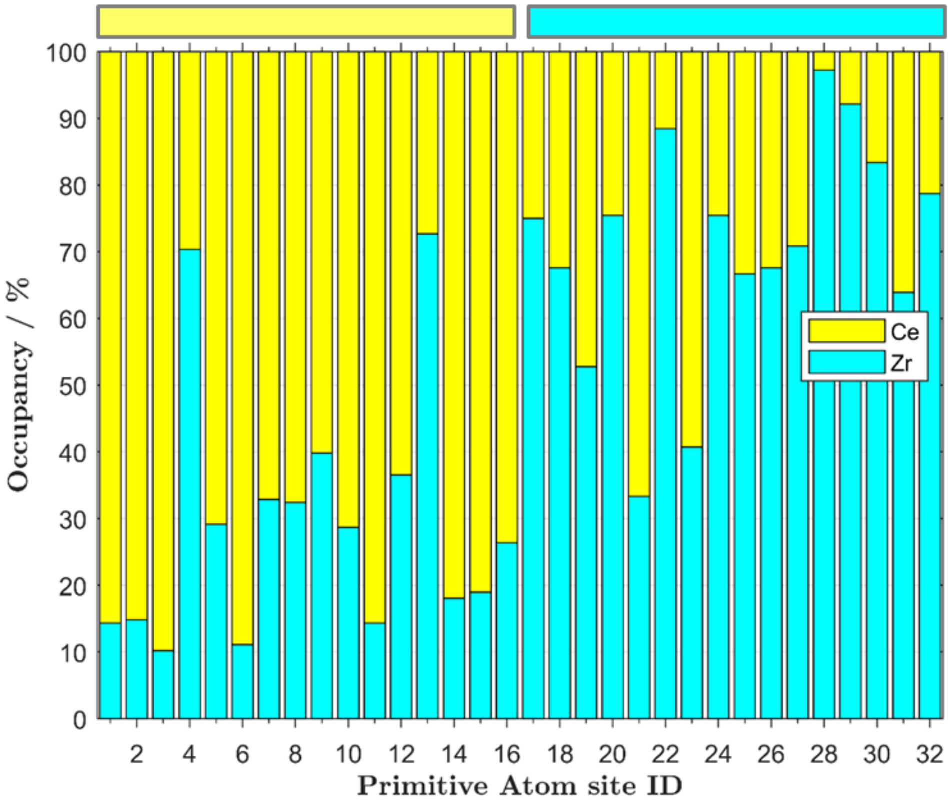

Figure 4.26: Cation site occupancy by individual unit cell cation sites for the SRMO1050 treated $Ce_{0.5}Zr_{0.5}O_2$ sample. Sites are related to the original structure as follows; Ce1/Zr1 (ID 1-4), Ce2/Zr2 (ID 5:16), Zr3/Ce3 (ID 17-20) and Zr4/Ce4 (ID 21-32). Original site occupancies indicated by the yellow/cyan overbars.

Figure 4.27 shows the nearest cation neighbour distances based on cation species for the SRMO1050 treated sample. Zr-Zr neighbours show a narrower profile of atom-atom distances than Ce-Zr and Ce-Ce, all three cation pairings show the same mean atom-atom distance. All neighbours match the intensity expected of a statistically defined composition with exceptional precision with occurrences of neighbours of Ce-Ce being 99.8 %, Ce-Zr being 100.0 % and Zr-Zr being 99.9 % of their statistically expected values. This level of precision indicates a strong preference for a stoichiometric mixture as would be the case for pyrochlore cation ordering where the 12 nearest neighbour cation shell for both Ce and Zr sites are comprised of 6 Ce sites and 6 Zr sites.

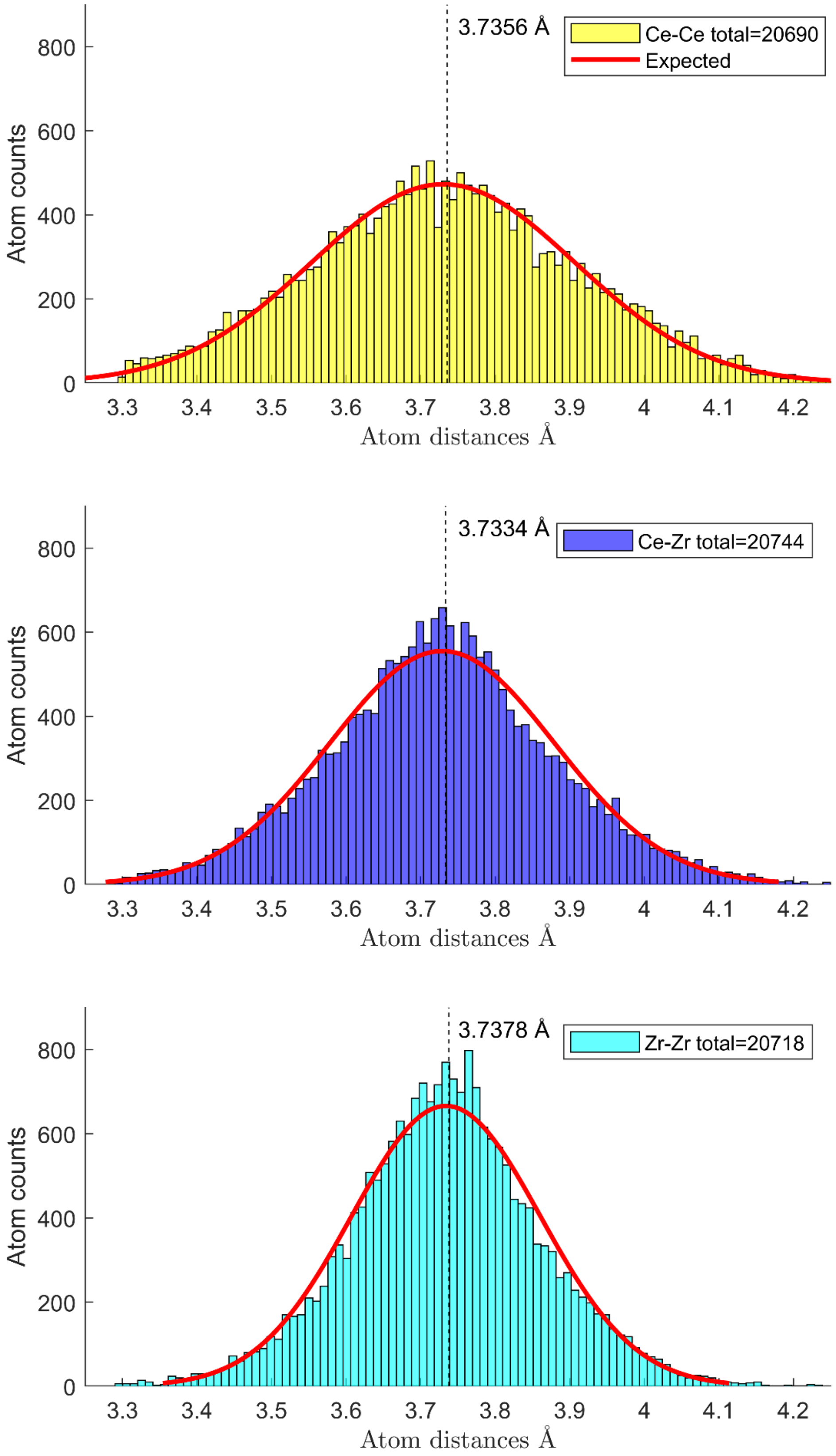

Figure 4.27: Histograms of nearest neighbour cation count and distance by species for the SRMO1050 treated $Ce_{0.5}Zr_{0.5}O_2$ sample. Top) Ce-Ce cation neighbour distances. Middle) Ce-Zr cation neighbour distances. Bottom) Zr-Zr cation neighbour distances. Red 'expected' line indicates profile and intensity for a statistically defined solid solution. Dashed line shows mean atom-atom distance for the respective pairs.

Figure 4.28 shows the oxygen site occupancy and the mean local cation environment of each of the 64 fluorite-like oxygen sites. This clearly shows that oxygen vacancies primarily form in sites where the majority of the nearest neighbour cations are Zr, this is consistent with the findings of Urban *et al*. in 2016[10] who claimed that oxygen vacancies primarily formed at the Zr surrounded oxygen sites O3 and O4. A significant outlier to this trend is site ID39, which shows 45 % of the 216 oxygen sites are vacant while 85% of the cation neighbours of that site are Ce, while unexpected, some vacancies in Ce surrounded oxygen sites was indicated by the 89 % mean occupancy of the Ce surrounded sites O1 and O2 detailed in Table 4.3. Given these two oxygen sites in the Rietveld model have a multiplicity of 4 the 89 % occupancy could be explained by 44 % from one site no longer constrained by symmetry, as such these two conclusions are not contradictory.

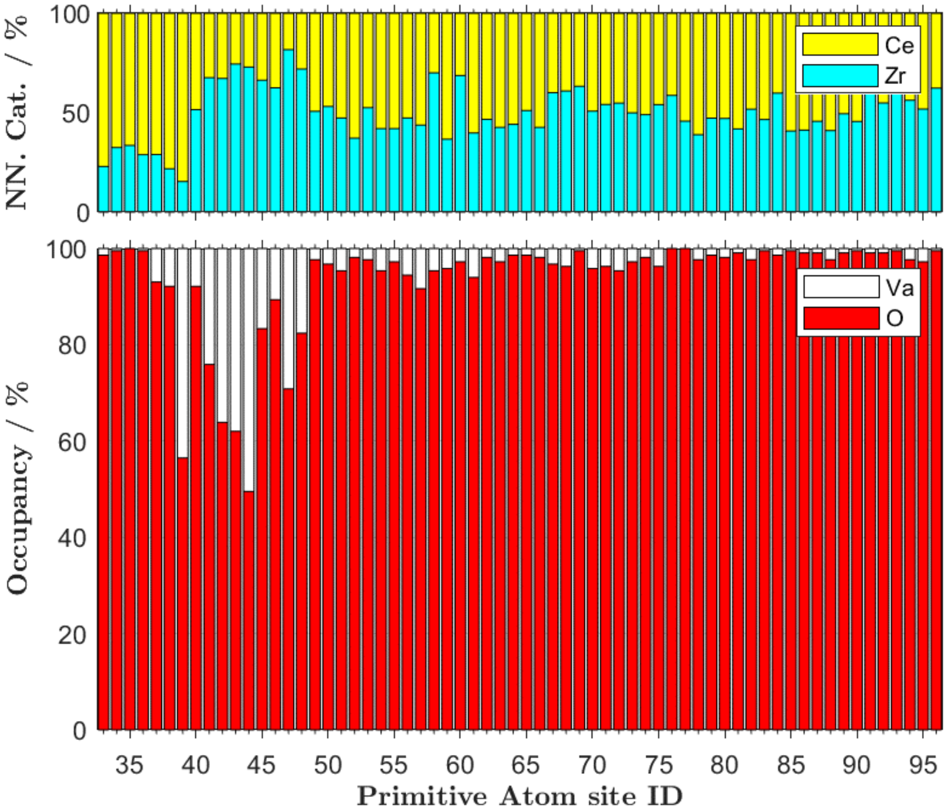

Figure 4.28: Oxygen site occupancy of the 64 fluorite-like sites for the SRMO1050 treated $Ce_{0.5}Zr_{0.5}O_2$ industrially provided sample. Each site ID represents 216 oxygen sites 6 × 6 × 6 kappa supercell (12 × 12 × 12 fluorite supercell). Mean nearest neighbour cation ratio of each oxygen site shown across the top of the figure. Interstitial O-sites not shown.

Figure 4.29 shows the interstitial site occupancy and mean local cation environments for each of the 32 interstitial oxygen sites. Somewhat unexpectedly the oxygen interstitial site occupancies show high occupancy percentages for a small number of interstitial sites. Notably, while Figure 4.29 shows the average cation environment of the site, when considering only occupied interstitial sites we find that the cation neighbours of occupied interstitial sites are 62.2 % Zr and 37.8 % Ce, indicating that both vacancies in the Fluorite oxygen lattice and occupied interstitial sites are both occurring in Zr rich local environments. This could be seen as support for a local displacement effect around Zr mini clusters encouraging oxygen vacancies during reduction[17], which in turn makes more easily accessible interstitial sites during re-oxidation resulting in both vacancies and interstitially occupied sites associated with Zr nearest cation neighbours.

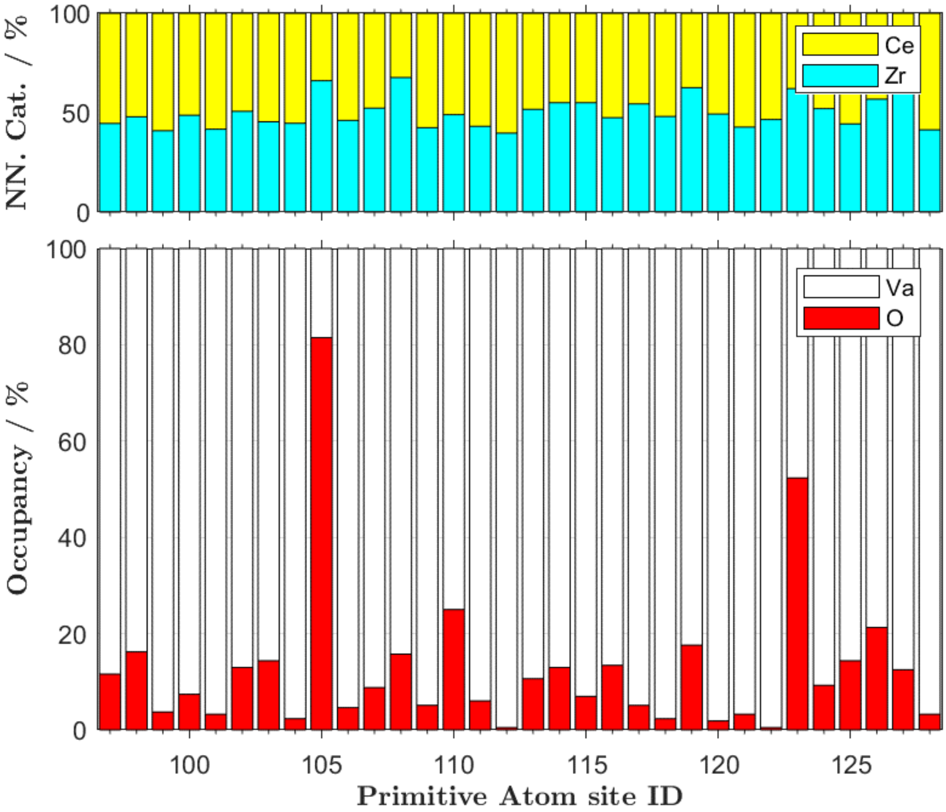

Figure 4.29: Interstitial oxygen site occupancy of the 32 interstitial sites for the SRMO1050 treated $Ce_{0.5}Zr_{0.5}O_2$ *industrially provided sample. Each site ID represents 216 interstitial oxygen sites across the 6 × 6 × 6 kappa supercell (12 × 12 × 12 fluorite supercell). Mean nearest neighbour cation ratio of each interstitial oxygen site shown across the top of the figure.*

Figure 4.30 shows the Clapp configuration analysis for the SRMO1050 model generated by RMCProfile. The model shows clear evidence of cation mixed ordering present such as the ideal kappa cation alternating structure represented by Clapp configuration 83. The Clapp configurations present show that the obtained model shows no evidence of cation clustering with the cation anti-site disorder present disrupting the ideal kappa configuration (C83) resulting in a significant enhancement of specific defect related configurations of like to unlike (negative C numbers indicate a configuration with unlike to like ratio instead) nearest neighbours of 6 to 6 (C71, C72, C76, C77, C81, C82), 7 to 5 (+/-C40, -C47, C49, +/-C51, +/-C52 and +/-C55) and 8 to 4 (+/-C26, +/-C28, +/-C29, and C30) one 9 to 3 (+/-C11). The observed cation ordering shows both Ce and Zr appear to be equivalent in their environments resulting in the near-mirrored profile of enhanced configurations, where both the positive (like) and negative (unlike) versions of the Clapp configuration are enhanced.

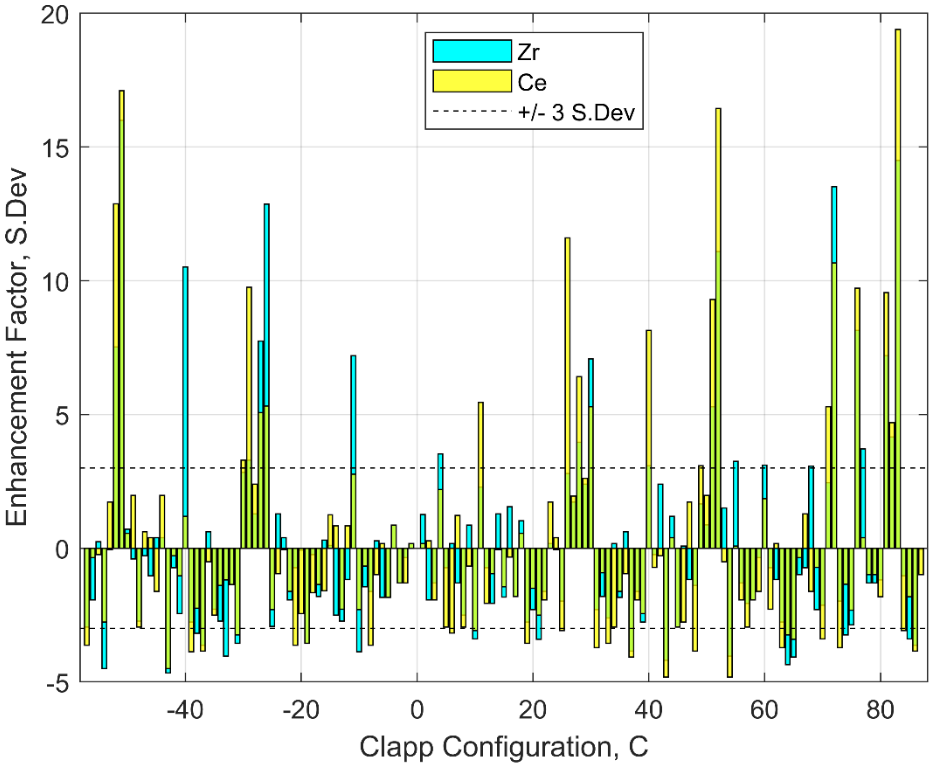

Figure 4.30: Histograms of Clapp configurations observed within the 6 × 6 × 6 kappa supercell (12 × 12 × 12 fluorite supercell) for the SRMO1050 treated $Ce_{0.5}Zr_{0.5}O_2$ industrially provided sample.

Figure 4.31 shows a diagram linking the enhanced Clapp configurations, notably most enhanced Clapp configurations at each cation ratio step are directly linked by single mutations and can be traced to *C83*, the ideal kappa arrangement. All other significantly enhanced configurations can be related to this degradation pathway by a one or two mutations, with *C*72, *C*76, *C*81, *C*51 and *C*-52 being key examples of this. Overall the Clapp analysis shows that the model describes a defective κ-$CeZrO_4$ structure where imperfect alternating cation ordering is present throughout the model with a range of cation anti-site disorder throughout the model rather than as a small subsection of concentrated cation disorder otherwise segregated from an alternating cation kappa structure.

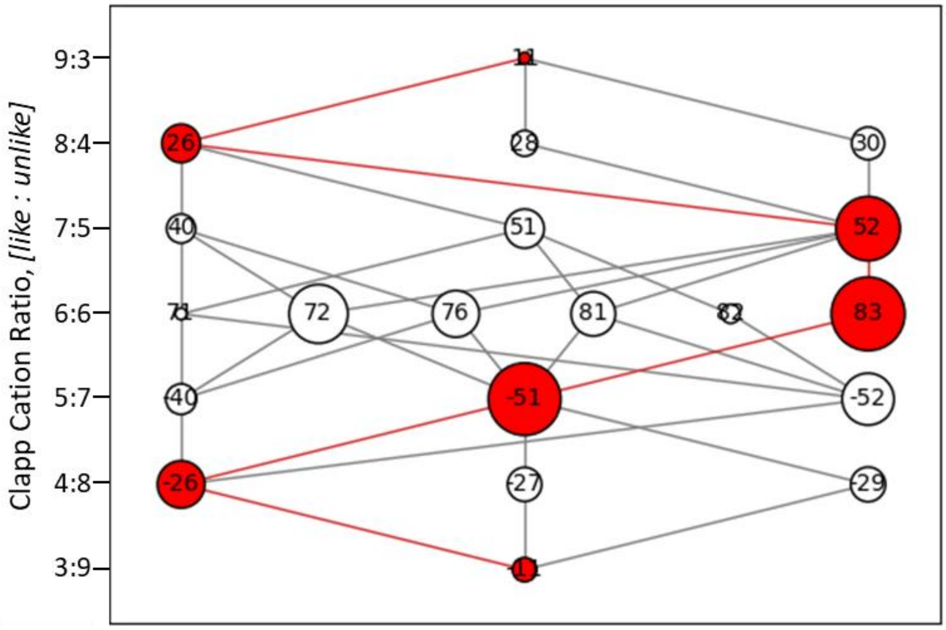

Figure 4.31: Diagram of single mutation linked Clapp configurations for the SRMO1050 treated $Ce_{0.5}Zr_{0.5}O_2$ sample, red indicates the most enhanced configuration in group, circle sizes correspond to the magnitude of enhancement observed.

4.4 Additional Analysis

4.4.1 Raman Spectroscopy

The four materials discussed in this chapter were also probed by Raman spectroscopy with the observed Raman spectra, the Raman spectra obtained from samples “Industrial as made” and “alkoxide synthesised” are shown in Figure 4.32, the Raman spectra obtained from samples “SRMO1050” and “SRMO1200” are shown in Figure 4.33.

Figure 4.32 shows the spectra obtained from the industrially provided and alkoxide synthesised $Ce_{0.5}Zr_{0.5}O_2$ samples, the primary Raman band of both spectra shown at 470 cm^{-1} is associated to the highly symmetric M-O bond distances of the $Fm\overline{3}m$ structure[18–21], however in both spectra this feature is broader than would be expected from an idealised fluorite structure. The industrially provided $Ce_{0.5}Zr_{0.5}O_2$ sample shows two additional Raman bands at 305 cm^{-1} and 630 cm^{-1} which match the approximate Raman shift expected for two of the major bands for the t-ZrO_2 ($P4_2/nmc$) structure. Curiously however the alkoxide synthesised sample does not have any strong Raman band at ~ 630 cm^{-1}. The Raman band at 630 cm^{-1} in Ce rich ceria zirconia systems has previously been accredited to defect structures related to Zr substitution in CeO_2[22], this would indicate that these defect structures are diminished in the alkoxide synthesised sample.

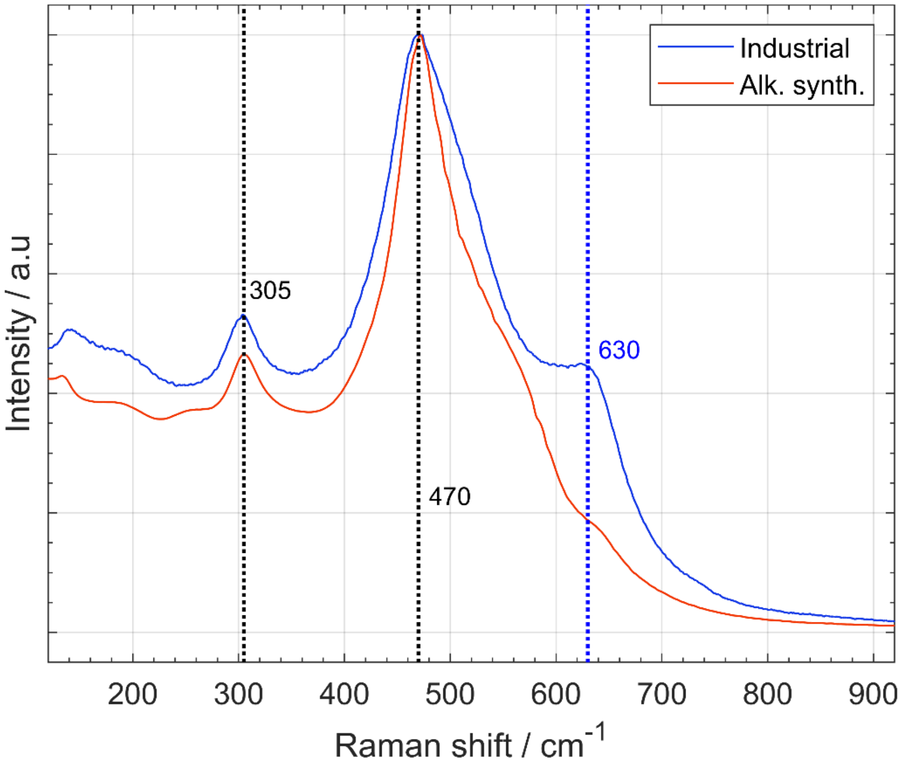

Figure 4.32: Raman spectra of as-made industrial and alkoxide synthesised $Ce_{0.5}Zr_{0.5}O_2$ *samples. Dotted lines are guides for the eye and are coloured based on which spectra the indicated Raman band appears in, black for both.*

Figure 4.33 shows the observed Raman spectra of the SRMO1050 and SRMO1200 treated samples. The observed Raman spectra shows 14 distinct peaks with several other minor peaks. This is in stark contrast to the relative simplicity of the industrially provided $Ce_{0.5}Zr_{0.5}O_2$ sample prior to SRMO treatment. The observed Raman spectra is a good match to those reported in the literature.[10,11] Notably the features of the SRMO1200 sample appear broadened to the point where several Raman bands present in the SRMO1050 sample are not visible in the SRMO1200 sample, although the significance of this difference is unknown, the major features remain in good agreement between the two samples.

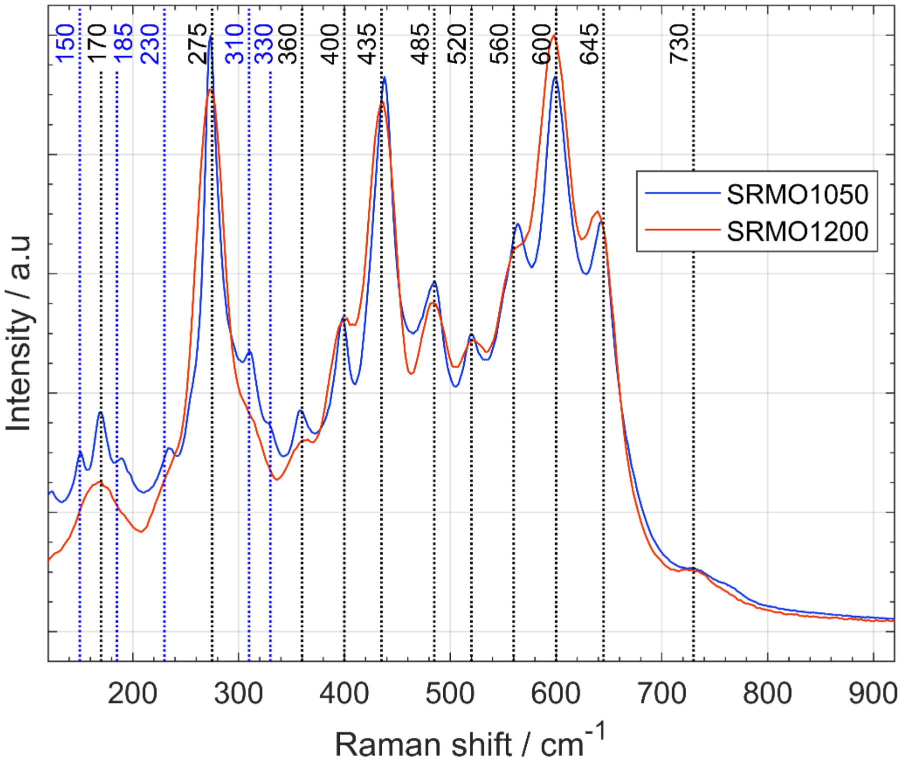

Figure 4.33: Raman spectra of SRMO1050 and SRMO1200 treated industrial $Ce_{0.5}Zr_{0.5}O_2$ *samples. Dotted lines are guides for the eye and are coloured based on which spectra the indicated Raman band appears in, black for both.*

Table 4.7 shows a list of the observed Raman bands in the SRMO1050 and SRMO1200 treated industrial $Ce_{0.5}Zr_{0.5}O_2$ materials alongside various literature references for the κ-$CeZrO_4$ phase.

Table 4.7: Observed Raman bands of experimental SRMO materials compared with literature references with the reduction temperatures of the SRMO treatments used.

	SRMO1050	***SRMO1200***	***Omata***[2]		***Urban***[10]	***Deng***[23]
	SR-1050	**SR-1200**	**SR-1050**	**SR-1300**	**SR-1500**	**SR-1000**
Wavenumber / cm^{-1}	**-**	**-**	**-**	**89**	**-**	**-**
	-	**-**	**-**	**101**	**105**	**-**
	-	**-**	**118**	**113**	**116**	**-**
	-	**-**	**-**	**121**	**124**	**136**
	150	**-**	**-**	**149**	**152**	**-**
	170	**170**	**170**	**167**	**170**	**174**
	185	**-**	**-**	**187**	**190**	**-**
	-	**-**	**-**	**200**	**-**	**-**
	230	**-**	**-**	**232**	**235**	**-**
	-	**-**	**-**	**256**	**247**	**-**
	275	**275**	**273**	**271**	**275**	**269**
	310	**-**	**300**	**309**	**312**	**302**
	330	**-**	**-**	**328**	**332**	**-**
	360	**360**	**-**	**356**	**360**	**-**
	400	**400**	**-**	**397**	**401**	**-**
	435	**435**	**436**	**437**	**442**	**438**
	485	**485**	**565**	**486**	**490**	**477**
	520	**520**	**601**	**520**	**523**	**-**
	-	**-**	**643**	**-**	**554**	**-**
	560	**560**	**-**	**562**	**564**	**-**
	600	**600**	**-**	**598**	**601**	**602**
	645	**645**	**-**	**643**	**644**	**-**
	730	**730**	**763**	**730**	**734**	**-**

4.4.2 I15-1 in-situ X-PDF study on SRMO treated industrial $Ce_{0.5}Zr_{0.5}O_2$

An in-situ X-PDF study of the SRMO treatment was undertaken at the Diamond Light Source using the I15-1 X-PDF beamline, the details of this experiment are described in further detail in chapter **2.**

Figure 4.34 shows the contour plot of Bragg diffraction for the *in-situ* reduction of the as-provided industrial $Ce_{0.5}Zr_{0.5}O_2$ material for temperatures between 910-1520 °C. The pyrochlore cation ordering supercell reflections can be seen forming from ~ 1050 °C with the (4 0 0) reflection at 2.48 Å first visible, while the (1 1 1) reflection at 6.35 Å clearly observable by 1100 °C. While the cation ordering reflections are initially observed at ~ 1050 °C these reflections continue to slowly grow until ~ 1400 °C.

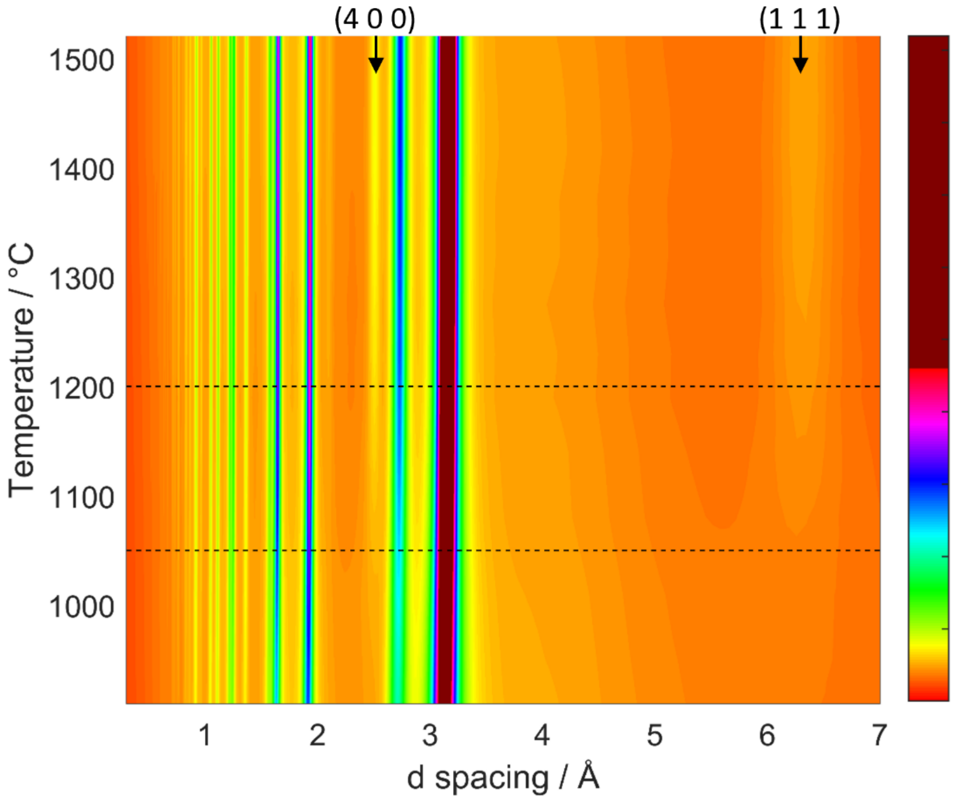

Figure 4.34: Thermal contour plot for in-situ SRMO1500 treatment of the industrially provided $Ce_{0.5}Zr_{0.5}O_2$ sample. Dashed lines at 1050 °C and 1200 °C as temperatures of interest for other samples discussed in this chapter. Pyrochlore cation ordering supercell reflections (4 0 0) and (1 1 1) indicated for clarity.

Figure 4.35 shows the observed X-ray diffraction patterns used to generate the contour plot shown in Figure 4.34 along with the refined phase fraction of the precursor pseudo-cubic phase and the target reduced pyrochlore phase. Between room temperature (0 % power) and 910 °C (20 % power) lattice expansion and relative reflection intensity shifts were observed for the reflections at 3.05 Å (1 0 1) and 2.65 Å (1 1 0). At 910 °C no supercell reflections were observed indicating no bulk pyrochlore cation ordering had occurred.

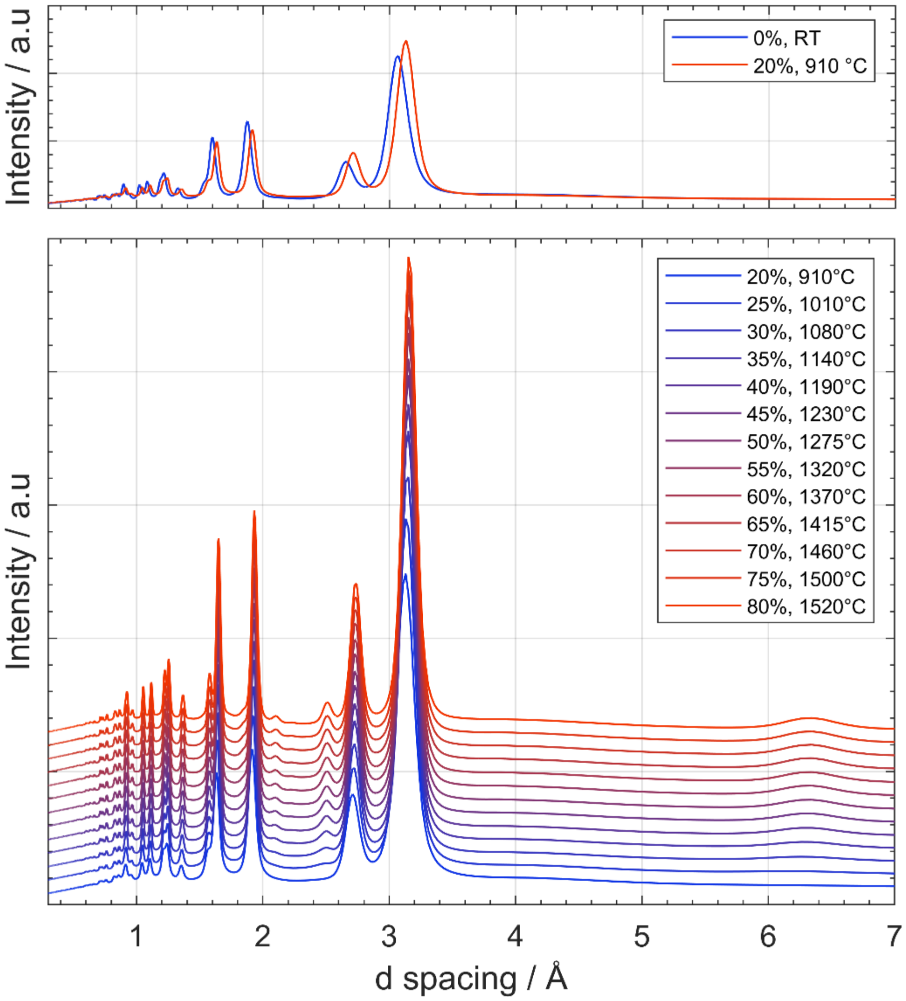

Figure 4.35: Observed in-situ diffraction patterns of the industrial $Ce_{0.5}Zr_{0.5}O_2$ *sample undergoing high temperature reduction. Top) Diffraction patterns taken at RT and ~ 910 °C overlapped. Bottom) Offset waterfall plot of diffraction patterns taken between ~ 910 °C and ~ 1520 °C. Legend) HELIOS IR Furnace power % and temperature calibration.*

Figure 4.36 shows two key parameters from a sequential Rietveld refinement of the high temperature reduction diffraction data shown in Figure 4.35, room temperature data points excluded for clarity. Rietveld refinement shows bulk cation ordering initially occurs between 910 °C and 1010 °C boasting ~ 20% cation ordering after 10 minutes at 1010 °C. While the observed Rietveld refinements indicate only 85 % cation ordering achieved by 1500 °C, caution is advised as the pseudo-cubic cation disordered phase has no unique reflections by principle. The driving factors for this dual phase refinement are the intensity mismatch between the bulk and supercell reflections, this results in a significant increase in uncertainty for the cation disordered component as it becomes a minor contribution to the data. For this reason the model is expected to lose sensitivity at high pyrochlore to pseudo-cubic ratios where the intensity mismatch becomes a drastically smaller contribution to the data. With this caveat in mind it is unclear if full cation ordering was achieved for 1500 °C or 1520 °C where the refined phase ratio being an artifact of overfitting. While the data has been modelled as two unique phases in these dual phase refinements shown, the material itself should be considered domains of cation disorder/order. The trend observed between 1080 °C and 1460 °C appears to be robust and meaningful.

The shift in phase fraction change rate is matched in the lattice parameter *a* of the pyrochlore phase across the same temperature range. When considering the atomic structures of the two phases, the key differences are the cation ordering and oxygen deficiency present in the pyrochlore phase, both structural features would result in a unit cell expansion and are likely to be occurring simultaneously due to their dependence on the reduction of Ce^{4+} to Ce^{3+}, rather it can be considered that ~20 % of the bulk material is resilient to reduction and requires higher temperatures to fully achieve pyrochlore cation ordering. This observation is in good agreement with the combined neutron and X-ray Rietveld refinement of SRMO1050 and SRMO1200 discussed earlier in this chapter, where anti-site cation disorder of 19.6 % and 11.0 % was observed. The SRMO1050 combined neutron and X-ray Rietveld refinement showed cation anti-site disorder of 19.6 % which is significantly lower than that observed in the in-situ pyrochlore formation for the same temperature 1050 °C. This could indicate that the phase transition at 1050 °C was incomplete within the 10 minute holds during the in-situ experiment, but reached ~80% cation ordering at the same temperature when left for 4 hours.

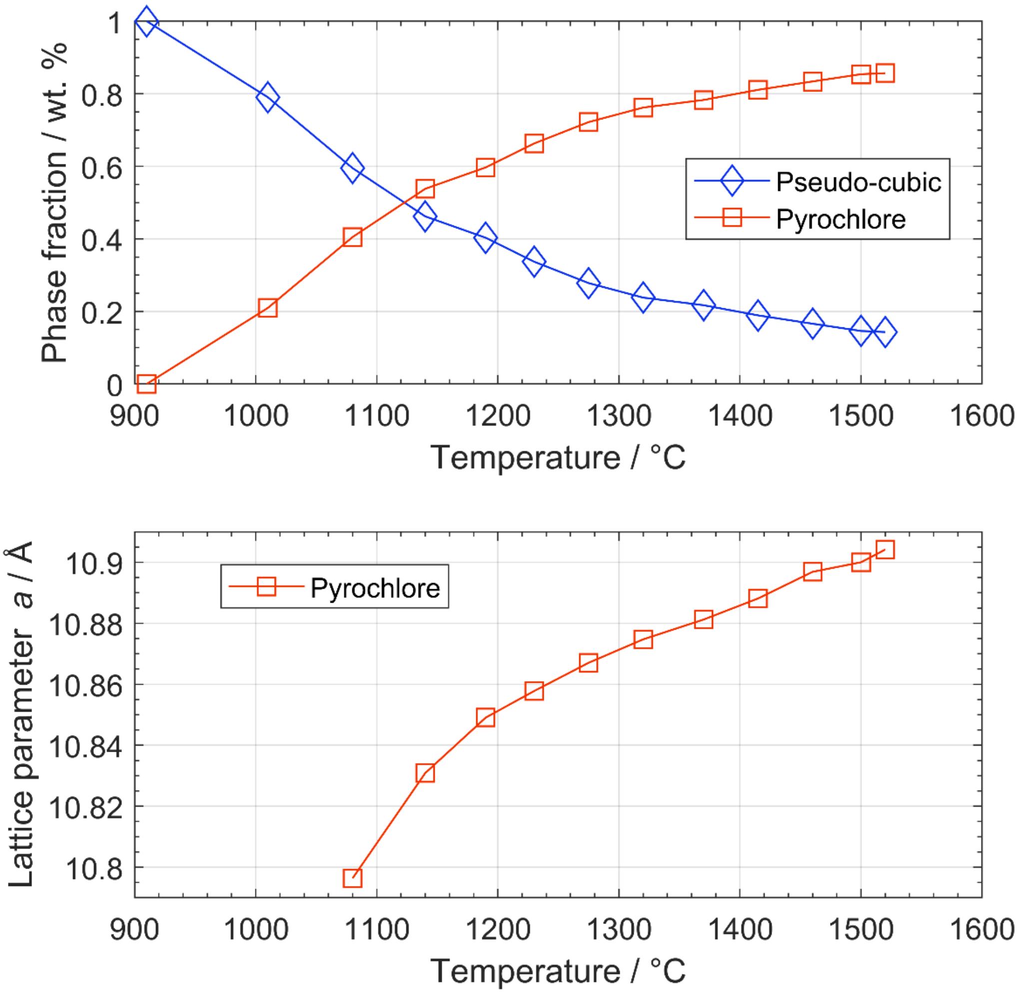

Figure 4.36: Top) Rietveld refined phase fraction of pseudo-cubic as-made material and post reduction pyrochlore phase by temperature. Bottom) Rietveld refined lattice parameter a of the evolving pyrochlore phase.

Figure 4.37 shows three Rietveld refinements at 900 °C, 1190 °C and 1520 °C highlighting the fitting approach employed to extract phase fraction information of the mixed cation site pseudo-cubic ($P4/nmc$) and the cation ordered pyrochlore ($Fd\bar{3}m$) phases co-existence over an extended temperature range. While phase co-existence at the extremes of the temperature range (t = 910 and t = 1500+) cannot be unambiguously confirmed due to the significant reflection overlap and relative low intensity of the pyrochlore cation ordering supercell reflections, the trends observed during cation ordering are robust.

Notably, at low phase fractions the pyrochlore supercell reflections suffer from crystallite size or strain related broadening more than the bulk pseudo-cubic reflections until the data observed for 1230 °C shown in Table 4.8 below. This broadening observation implies the formation of cation ordering occurs as expanding nano-domains which could explain the two stage formation profile observed in Figure 4.36 above, where cation ordered nano-domain expansion is dominant until ~1200 °C at which point sheer strain-like defects forming cation mismatched domain boundaries between the nanodomains would need to be overcome to continue crystalline ordering.

*Table 4.8: Refined phase fractions and size/strain related broadening observations of the pyrochlore cation ordered phase fitted as crystallite size. ~ indicates use of a fixed value due to refinement instability. 1+ indicates 'bulk crystalline' a fixed value of 10 µm due to no significant size/strain broadening observed. Values marked with * show high degrees of uncertainty in the fitting.*

Temp / °C	Phase	Frac.	C.S / µm	Temp / °C	Phase	Frac.	C.S / µm
RT	Pseudo-Cubic Pyrochlore	1.0 0.0	0.011 N/A	1275	Pseudo-Cubic Pyrochlore	0.278 0.722	1+ 1+
910	Pseudo-Cubic Pyrochlore	1.0 0.0	0.018 N/A	1320	Pseudo-Cubic Pyrochlore	0.238 0.762	1+ 1+
1010	Pseudo-Cubic Pyrochlore	0.791 0.209	0.0636 ~0.01	1370	Pseudo-Cubic Pyrochlore	0.217 0.783	1+ 1+
1080	Pseudo-Cubic Pyrochlore	0.595 0.405	1+ ~0.015	1415	Pseudo-Cubic Pyrochlore	0.189 0.811	1+ 1+
1140	Pseudo-Cubic Pyrochlore	0.462 0.538	1+ 0.0561	1460	Pseudo-Cubic Pyrochlore	0.166 0.834	1+ 1+
1190	Pseudo-Cubic Pyrochlore	0.403 0.597	1+ 0.0989	1500	Pseudo-Cubic Pyrochlore	0.146* 0.854*	1+ 1+
1230	Pseudo-Cubic Pyrochlore	0.337 0.663	1+ 1+	1520	Pseudo-Cubic Pyrochlore	0.143* 0.857*	1+ 1+

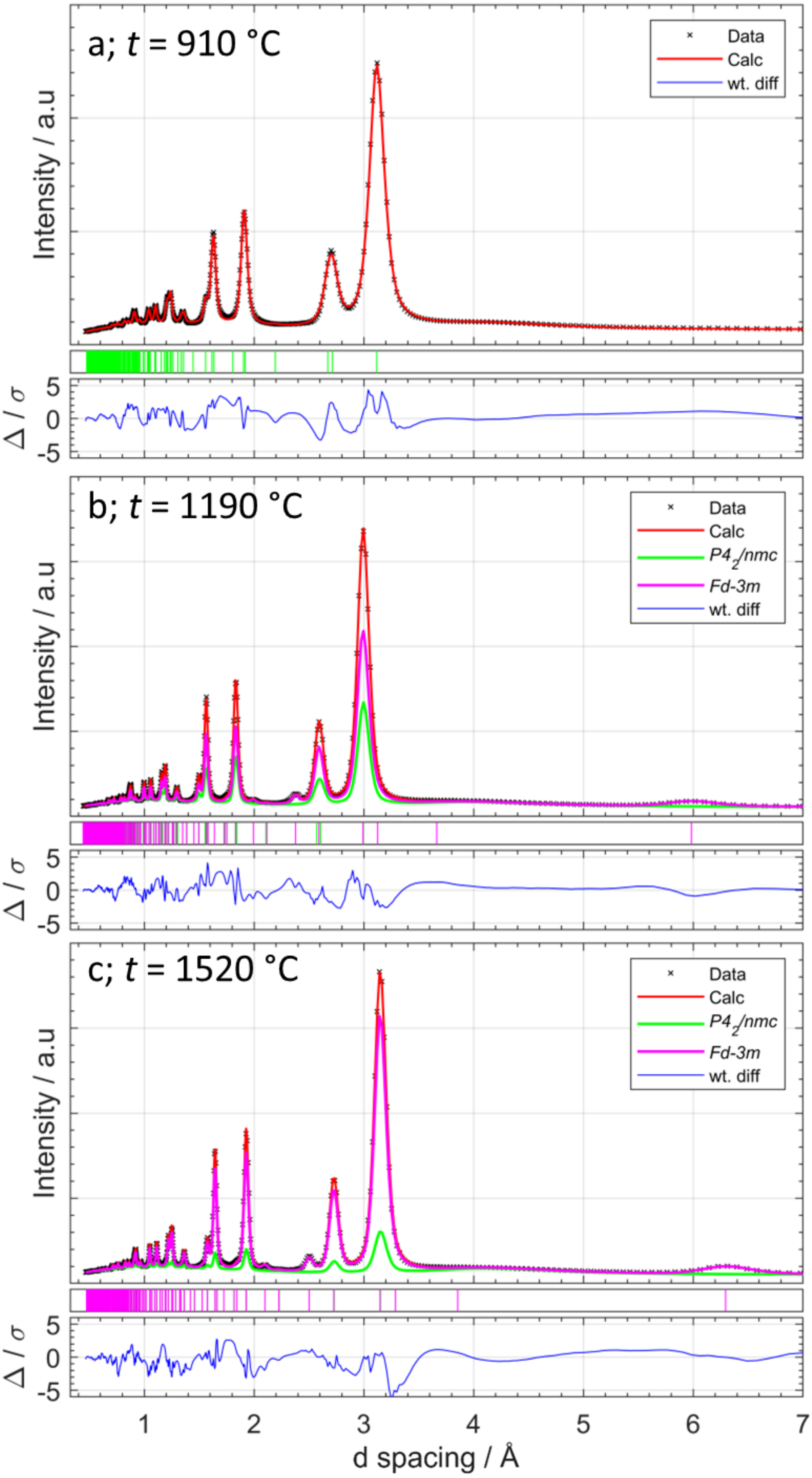

Figure 4.37: Rietveld refinements of in-situ observed pseudo-cubic to pyrochlore phase transition at three key temperatures. a) t = 910 °C, some limited evidence of cation ordering. b) t = 1190 °C, significant evidence of cation ordering, magnitude of supercell reflections is insufficient to explain bulk reflections. c) t = 1520 °C, supercell reflection intensity closer to that expected for full cation ordering.

Figure 4.38 shows the obtained X-PDFs of the in-situ high temperature reduction of the industrial $Ce_{0.5}Zr_{0.5}O_2$ sample. While no clear evidence of average structure change was observed between RT and ~910 °C in the Bragg diffraction patterns above, clear evidence of change was observed in the X-PDFs for these temperatures. Notably the profile of the first M-O peak at ~2.1 Å shown in Figure 4.38.A dramatically changes in profile indicating a decrease in disorder with better defined M-O bond distances when reduced at 910 °C. The differences observed in the ~ 900 °C to ~ 1520 °C range are subtle and observed below 1140 °C (35 % power), above which no further changes were observed. Notably these subtle changes consisted of sharper/better defined features across the whole *r* range observed with the largest differences observed for the first M-O (2.1 Å) distance where a low-r shoulder grew with temperature while a high-r shoulder shrank. The first O-O (2.4 Å to 2.8 Å) pair distances became more defined with temperature clearly showing at least 2 peaks. The second M-O distance (4.5 Å) lost definition and overall intensity. Linear thermal expansion cannot fully explain the *r* shift observed in Figure 4.38 as this distinct shift clearly stops by 1140 °C and is more pronounced in the peaks with large M-M contributions. The sample was held at 1520 °C under 4 % H_2 in Ar for over 2 hours with no change in the observed diffraction pattern or X-PDF observed.

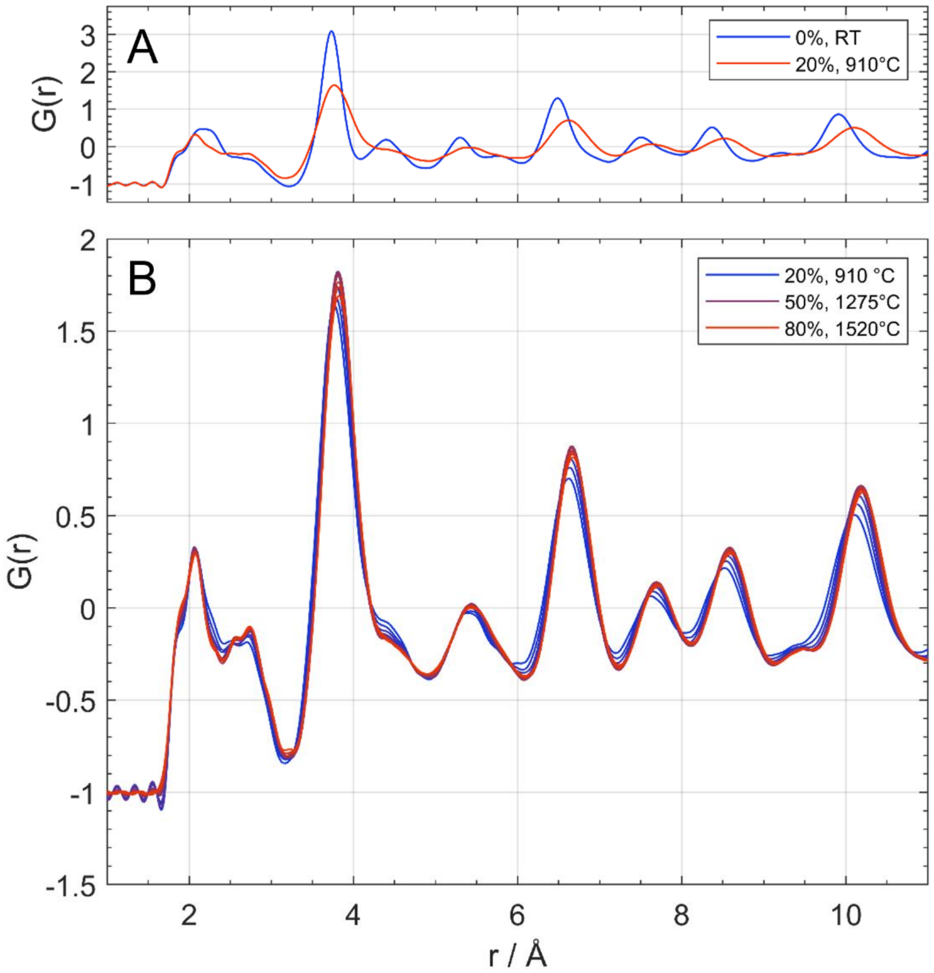

Figure 4.38: Observed in-situ X-PDF patterns of the industrial $Ce_{0.5}Zr_{0.5}O_2$ *sample undergoing high temperature reduction. Top) X-PDF patterns taken at RT and ~910 °C . Bottom) XPDF patterns taken between ~ 910 °C and ~ 1520 °C. Legend) HELIOS IR Furnace power % and temperature calibration.*

These results heavily imply that most of the local structural changes during high temperature reduction occur prior to 900 °C although only reach bulk cation ordering visible via Bragg diffraction after ~ 1200 °C.

Figure 4.39 shows the observed X-ray diffraction patterns of the in-situ mild oxidation of the industrial $Ce_{0.5}Zr_{0.5}O_2$ sample after being reduced in-situ. The reduced sample was cooled to RT under 4 % H_2 in Ar before being exposed to air followed by a mild oxidation treatment. The mild oxidation from pyrochlore to kappa was rapid with a clear decrease in lattice parameters evidenced by the observable peak shift to lower d-spacing. The shift was complete by the second scan obtained 1 minute after 5 % furnace power was applied (~260 °C, temperature held for 15 minutes at each heating step, scans acquired at 10 minutes are shown). No further change was observed in the X-ray Bragg diffraction pattern on subsequent scans up to 1010 °C (25 % furnace power)

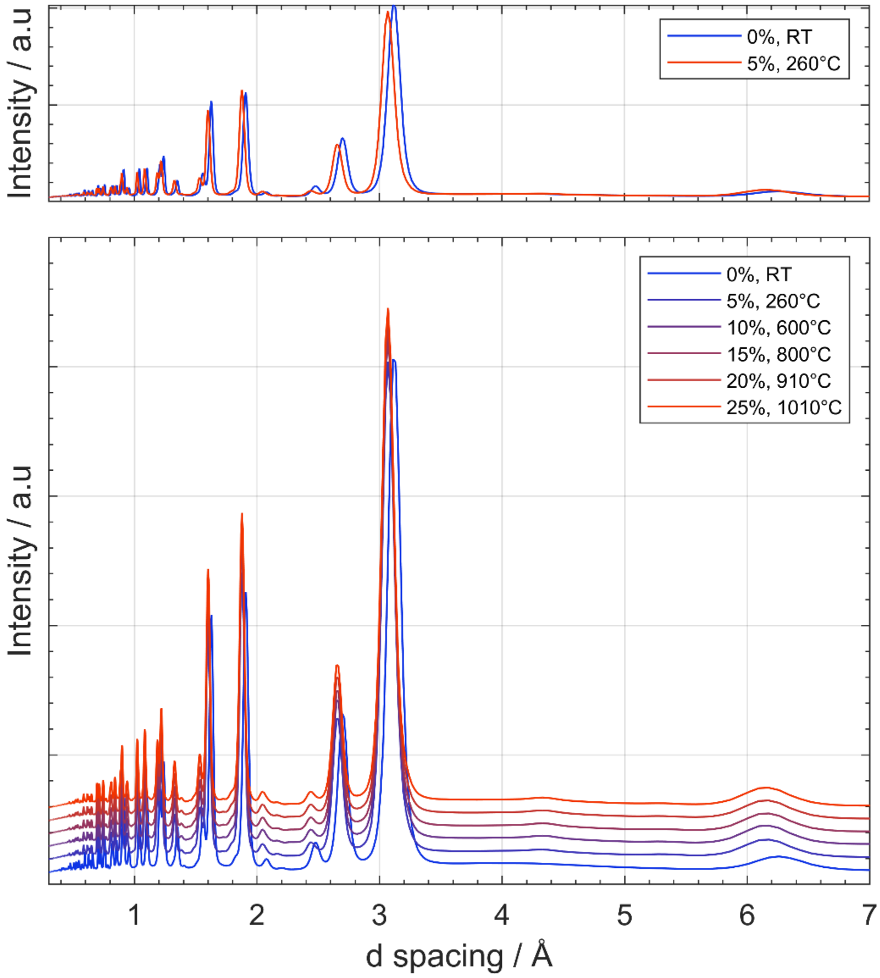

Figure 4.39: X-ray Bragg diffraction patterns of in-situ oxidation of post high temperature reduced industrial $Ce_{0.5}Zr_{0.5}O_2$ *sample. Top) Diffraction patterns taken at RT and ~260 °C overlapped. Bottom) Offset waterfall plot of diffraction patterns taken between RT and 1010 °C.*

Figure 4.40 shows the X-PDFs obtained during the in-situ oxidation of the high temperature reduced industrial $Ce_{0.5}Zr_{0.5}O_2$ sample. Nearly all changes occur between RT and 260 °C with a clear contraction of lattice parameters, broadening of the first M-O (2.1 Å) distance and a significant dampening of the first O-O (2.4 Å to 2.8 Å) distance. Only minor differences in relative peak intensity is observed between 260 °C and 600 °C with no further changes observed above 600 °C.

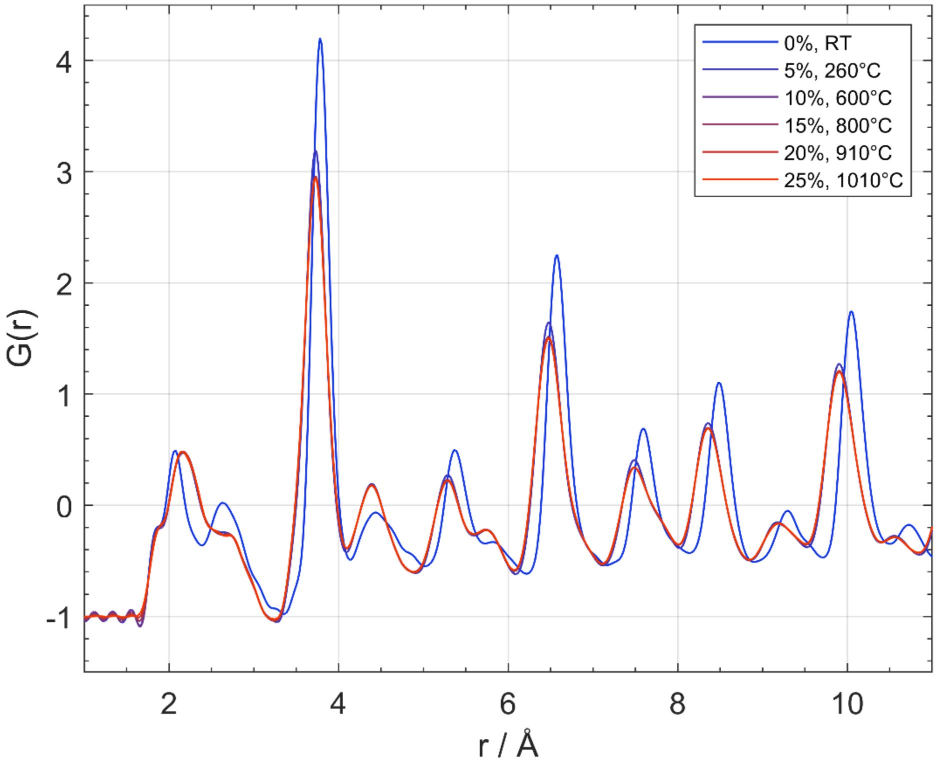

Figure 4.40: X-PDF patterns of in-situ oxidation of post high temperature reduced industrial $Ce_{0.5}Zr_{0.5}O_2$ *sample.*

Figure 4.41 shows the as-made, post reduction and post oxidation Bragg diffraction and X-PDF patterns of the in-situ SRMO treatment of the industrial $Ce_{0.5}Zr_{0.5}O_2$ sample. Reduction of the $Ce_{0.5}Zr_{0.5}O_2$ solid solution to the $Ce_2Zr_2O_7$ pyrochlore showed clear change the local structure of the material. Oxidation to the κ-$CeZrO_4$ phase preserves the cation ordering fluorite supercell reflections (4 0 0) (hkl) and (1 1 1) (hkl) observed via Bragg diffraction. The local structure changes show a return to a Fluorite local environment highly similar to the cation disordered fluorite with only minor peak intensity differences showing evidence of cation ordering via X-PDF showing that while long range cation ordering is preserved, the average local atomic structure is truly Fluorite-like.

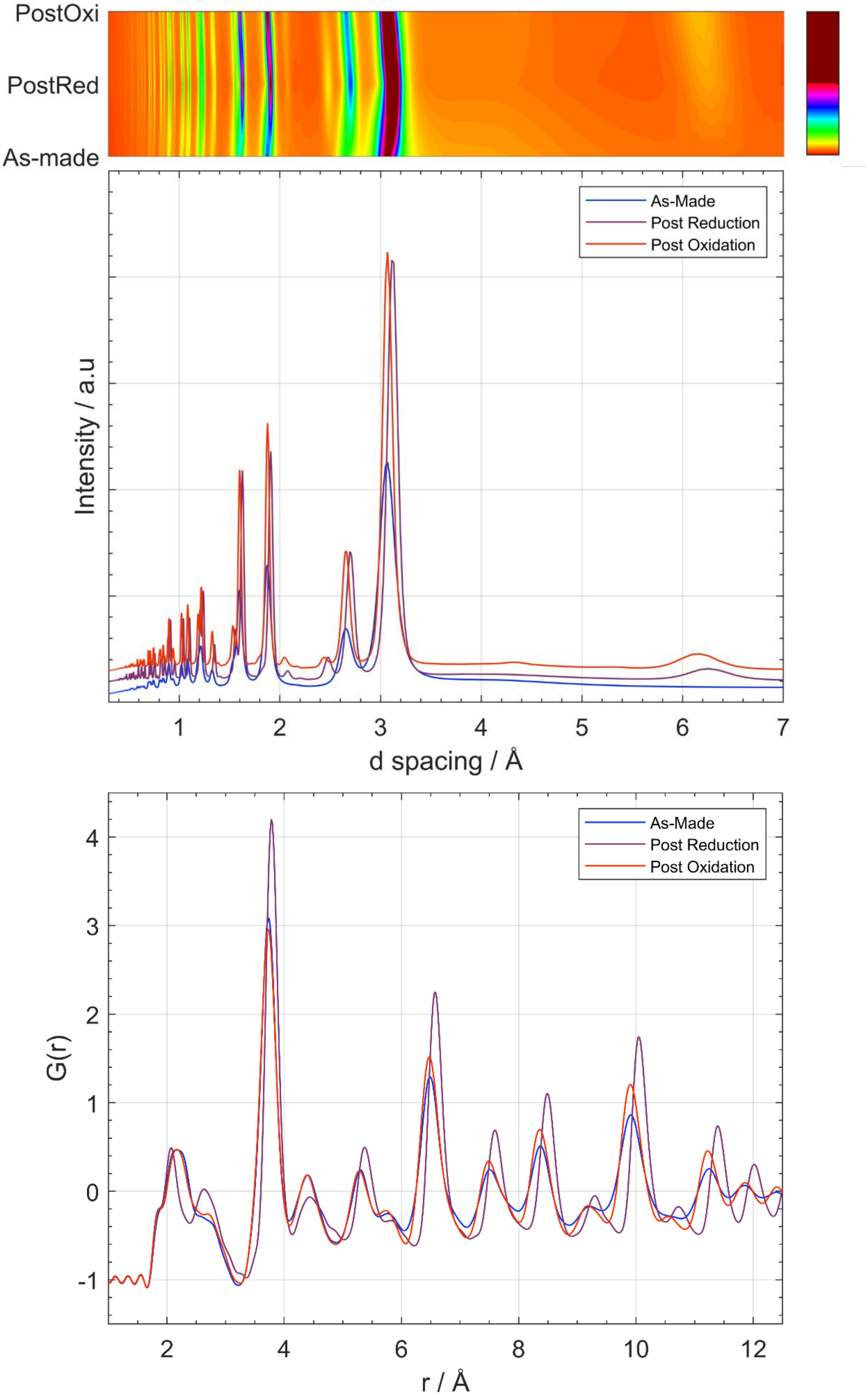

Figure 4.41: As-made, post reduction and post oxidation datasets of the in-situ SRMO treated industrial $Ce_{0.5}Zr_{0.5}O_2$ *sample. Top) Observed X-ray diffraction patterns with heatmap. Bottom) X-PDFs.*

4.5 Discussion and Conclusions

Rietveld analysis of the average structure for an as-provided industrial $Ce_{0.5}Zr_{0.5}O_2$ sample and the $Ce_{0.5}Zr_{0.5}O_2$ alkoxide synthesised sample show both can be modelled as pseudo-fluorite mixed metal oxides in the $P4_2/nmc$ space group consistent with the t'-$Ce_{0.5}Zr_{0.5}O_2$ phase described in literature. The primary features of this average structure model are a cubic arrangement of cation sites occupied by both cerium and zirconium ions with the oxygen sites z coordinate displaced away from the ideal fluorite arrangement. Differences between the Rietveld refined models of the as-provided industrial sample and the alkoxide synthesised sample are minor and within probable error given the poorly crystalline diffraction patterns showing no discernible difference in the average structure of these two preparation methods.

RMCProfile fitting of a 12 × 12 × 12 supercell based on the fluorite structure against combined neutron and X-ray total scattering data obtained for the as-provided industrial $Ce_{0.5}Zr_{0.5}O_2$ generated a model with interesting characteristics. While the sample can be described as an average cation mixed fluorite structure, the model generated shows nano-scale cation segregated domains where Zr – Zr cation neighbours are closer while Ce – Ce cation neighbours are further apart than the average site distance defined by the Rietveld refined lattice parameters. Solid solution $Ce_{0.5}Zr_{0.5}O_2$ has been reported be meta-stable and segregation into various forms of cation rich domains has been observed in the literature before,[17,24] where bulk segregation is expected when heated above 1000 °C in air.[25] In addition to this the oxygen displacement profile is remarkably different to that shown for the F800 $Ce_{0.75}Zr_{0.25}O_2$ material in Chapter 3 showing a broadened profile which supports two or more oxygen environments. The cation clustering, divergent cation-cation distances and broadened oxygen displacement all support the hypothesis that the as-provided industrial material studied exists as discrete Ce/Zr rich crystallites/nanodomains and not as a uniform statistically cation mixed oxide often described as a true solid solution.

RMCProfile fitting of a 12 × 12 × 12 supercell based on the fluorite structure against neutron Bragg and PDF data obtained for the alkoxide synthesised $Ce_{0.5}Zr_{0.5}O_2$ sample generated a model with cation segregated nano-domains with ~ 5 % of the total oxygen in interstitial sites with ~90 % cation neighbours being Zr atoms. Unlike the SRMO1050 treated $Ce_{0.75}Zr_{0.25}O_2$ sample discussed in Chapter 4 the alkoxide synthesised $Ce_{0.5}Zr_{0.5}O_2$ also showed enhanced occurrences of cation mixed structures in addition to the nano-domains indicating a very non-homogeneous local structure.

The Rietveld refined results of the SRMO1050 and SRMO1200 treated $Ce_{0.5}Zr_{0.5}O_2$ materials clearly show a degree of pyrochlore cation ordering was achieved in these samples, however the dual X-ray/neutron diffraction probe approach highlighted the resulting κ-$CeZrO_4$ phase had significant levels of cation anti-site disorder present, ~18 % and ~11 % for SRMO1050 and SRMO1200. This indicates that initial reduction to pyrochlore at 1050 °C or 1200 °C for 4 hours was insufficient for complete cation ordering highlighting the process has a temperature dependence. This agrees with the conclusions of Urban *et al.* in 2016 who showed that higher reduction temperatures of 1500 °C were required to form a fully cation ordered $Ce_2Zr_2O_7$ pyrochlore. The magnitude and types of oxygen disorder were approximately equivalent across both κ-$CeZrO_4$ phase samples studied with the SRMO1200 κ-$CeZrO_4$ phase showing slightly more oxygen interstitials and a more even oxygen site splitting for O7. In both samples the oxygen sites surrounded by four Zr showed the largest vacancies. Significant oxygen disorder throughout the bulk of this material could help explain the significant difference in oxygen release temperature and rate between the κ-$CeZrO_4$ and the bulk cation disordered t'-$Ce_{0.5}Zr_{0.5}O_2$ phases.

The RMCProfile generated 6 × 6 × 6 cation ordered supercell (12 × 12 × 12 fluorite supercell) model for the SRMO1050 treated industrial $Ce_{0.5}Zr_{0.5}O_2$ sample which was fitted against neutron Bragg, neutron PDF and X-ray PDF data, showed a defective cation ordered structure with significant oxygen disorder. The average cation sites showed significant cation ordering which is consistent with the anti-site disorder observed via the Rietveld refinements discussed above. Cerium and zirconium average displacement profile were different however cation-cation distances remained close to the expected lattice parameter defined value and independent of cation species. The local scale single shell cation composition remained extremely close to the stoichiometrically expected composition with no evidence of significant cation rich nanodomains forming.

The Frenkel type oxygen defects, namely the occupied interstitial sites and vacant fluorite-like oxygen sites were primarily surrounded by Zr ions which is consistent with the $A_2B_2O_6O'$ pyrochlore structure. The RMCProfile refined model showed a strong preference for a small subset (1-3) of significantly occupied interstitial sites.

Clapp configuration analysis of the local cation structure shows significantly enhanced configurations for not just the pyrochlore cation ordering (C83) but also a significant amount of single, double, or triple defect related structures implying the existence of a defective structure throughout the model rather than regions of cation order in an otherwise cation disordered lattice.

Conclusions from the in-situ I15-1 study of the SRMO treatment undertaken on the industrial $Ce_{0.5}Zr_{0.5}O_2$ sample showed that the main local structure changes on reduction occurred below 910 °C with the average structure cation ordering visible via to Bragg diffraction at 1050 °C with no further changes noted above 1400 °C. These average structure changes were not mirrored by any significant changes in the observed X-PDFs of which showed no further change above 1140 °C. The sample was held at 1520 °C for over 2 hours and showed absolutely no difference in the observed Bragg diffraction or the X-PDF patterns during the hold at 1520 °C. It is believed that significant cation ordered nano-domains had already formed prior to 1200 °C and joining of these nano-domains is what was observed in the Bragg diffraction above this temperature. Oxidation of the reduced $Ce_2Zr_2O_7$ pyrochlore was rapid and occurred at a very low temperature, the X-PDF pattern of the resultant κ-$CeZrO_4$ phase. The κ-$CeZrO_4$ phase is a fluorite supercell structure with local cation ordering with the local composition matching the average composition, resulting in remarkably few visual differences between the observed X-ray PDF of the untreated solid solution $Ce_{0.5}Zr_{0.5}O_2$ and the cation ordered κ-$CeZrO_4$ phase, confirming a local fluorite-like structure alongside supercell cation ordering observed clearly via Bragg diffraction.

Overall, this chapter details various forms of cation and anion disorder observed in a subset of cerium zirconium oxide samples with equal cerium and zirconium ratios. Most notably is that the cation ordering of the κ-$CeZrO_4$ phase shows a significant temperature dependence of the pyrochlore reduction intermediate step, however the while almost twice as much cation disorder is observed when pyrochlore reduction is performed at 1050 ° compared to 1200 °C, the types and magnitudes of oxide disorder appear to be highly comparable. RMCProfile modelling also indicates that the partial cation ordering is present throughout the bulk material as single and double substituted cation order rather than discreet κ-$CeZrO_4$ crystallites or perfectly ordered nanodomains. This conclusion is supported by in-situ observations showing that while partial cation ordering is relatively accessible at reduction temperatures of > 1000 °C, the pyrochlore phase formation follows a two step process where cation disorder can persist at temperatures up to ~1500 °C.

Alongside the details studies of the κ-$CeZrO_4$ phase, two solid solution ceria zirconia samples were studied, a industrially provided “as-made” sample and “alkoxide synthesised”. It is shown that while both samples highly similar bulk structures, the local structures formed are distinctly different, further highlighting the importance of synthesis route and sample history.

4.6 Bibliography

1 S. Otsuka-Yao-Matsuo, T. Omata, N. Izu and H. Kishimoto, *J. Solid State Chem.*, 1998, **138**, 47–54.

2 T. Omata, H. Kishimoto, S. Otsuka-Yao-Matsuo, N. Ohtori and N. Umesaki, *J. Solid State Chem.*, 1999, **147**, 573–583.

3 J. B. Thomson, A. Robert Armstrong and P. G. Bruce, *J. Am. Chem. Soc.*, 1996, **118**, 11129–11133.

4 J. B. Thomson, A. Robert Armstrong and P. G. Bruce, *J. Solid State Chem.*, 1999, **148**, 56–62.

5 T. Masui, T. Ozaki, G. Y. Adachi, Z. Kang and L. R. Eyring, *Chem. Lett.*, 2000, 840–841.

6 Y. Nagai, T. Yamamoto, T. Tanaka, S. Yoshida, T. Nonaka, T. Okamoto, A. Suda and M. Sugiura, *Catal. Today*, 2002, **74**, 225–234.

7 H. F. Wang, Y. L. Guo, G. Z. Lu and P. Hu, *Angew. Chem - Int. Ed.*, 2009, **48**, 8289–8292.

8 T. Yamamoto, A. Suzuki, Y. Nagai, T. Tanabe, F. Dong, Y. Inada, M. Nomura, M. Tada and Y. Iwasawa, *Angew. Chem - Int. Ed.*, 2007, **46**, 9253–9256.

9 H. Kishimoto, T. Omata, S. Otsuka-Yao-Matsuo, K. Ueda, H. Hosono and H. Kawazoe, *J. Alloys Compd.*, 2000, **312**, 94–103.

10 S. Urban, P. Dolcet, M. Möller, L. Chen, P. J. Klar, I. Djerdj, S. Gross, B. M. Smarsly and H. Over, *Appl. Catal. B Environ.*, 2016, **197**, 23–34.

11 S. Urban, I. Djerdj, P. Dolcet, L. Chen, M. Möller, O. Khalid, H. Camuka, R. Ellinghaus, C. Li, S. Gross, P. J. Klar, B. Smarsly and H. Over, *Chem. Mater.*, 2017, **29**, 9218–9226.

12 S. N. Achary, S. K. Sali, N. K. Kulkarni, P. S. R. Krishna, A. B. Shinde and A. K. Tyagi, *Chem. Mater.*, 2009, **21**, 5848–5859.

13 Y. Ding, Z. Wang, Y. Guo, Y. Guo, L. Wang and W. Zhan, *Catal. Today*, 2019, **327**, 262–270.

14 T. Wakita and M. Yashima, *Acta Crystallogr. Sect. B Struct. Sci.*, 2007, **63**, 384–389.

15 J. B. Thomson, A. R. Armstrong and P. G. Bruce, *Chem. Commun.*, 1996, **7863**, 1165–1166.

16 C. L. Farrow, P. Juhas, J. W. Liu, D. Bryndin, E. S. Božin, J. Bloch, T. Proffen and S. J. L. Billinge, *J. Phys. Condens. Matter*, 2007, **19**, 335219.

17 T. A. Lee, C. R. Stanek, K. J. McClellan, J. N. Mitchell and A. Navrotsky, *J. Mater. Res.*, 2008, **23**, 1105–1112.

18 S. Damyanova, B. Pawelec, K. Arishtirova, M. V. M. Huerta and J. L. G. Fierro, *Appl. Catal. A Gen.*, 2008, **337**, 86–96.

19 V. Sánchez Escribano, E. Fernández López, M. Panizza, C. Resini, J. M. Gallardo Amores and G. Busca, *Solid State Sci.*, 2003, **5**, 1369–1376.

20 Y. Xu, F. Wang, X. Liu, Y. Liu, M. Luo, B. Teng, M. Fan and X. Liu, *J. Phys. Chem. C*, 2019, **123**, 18889–18894.

21 S. Wang, W. Wang, J. Zuo and Y. Qian, *Mater. Chem. Phys.*, 2001, **68**, 246–248.

22 M. Yashima, H. Arashi, M. Kakihana and M. Yoshimura, *J. Am. Ceram. Soc.*, 1994, **77**, 1067–1071.

23 J. Deng, Z. Li, S. Li, X. Yin, M. Li, J. Wang, Y. Chen and Y. Chen, *Appl. Catal. A Gen.*, 2022, **646**, 118831.

24 E. Mamontov, R. Brezny, M. Koranne and T. Egami, *J. Phys. Chem. B*, 2003, **107**, 13007–13014.

25 Y. Nagai, T. Nonaka, A. Suda and M. Sugiura, *R&D Rev. Toyota CRDL*, 2002, **37**, 20–27.

Chapter 5: Other Ceria Zirconia materials

5.1 Introduction

As part of this study several other cerium containing materials were studied albeit in not as much detail as the $Ce_{0.75}Zr_{0.25}O_2$ and $Ce_{0.5}Zr_{0.5}O_2$ materials discussed in previous chapters. These additional materials include two thermal treatments of the $Ce_{0.25}Zr_{0.75}O_2$ composition of cerium zirconium oxide, Ti doped cerium zirconium oxides and an study on Ce doped anatase titanium oxides.[1]

Ti substituted cerium oxides[2,3] have gained a lot of interest for their improved catalysis of the water gas shift (WGS) reaction,[4–6] beyond that of mixtures of CeO_2 and TiO_2. TiO_2 is a capable catalytic material in its own right and displays a versatile mix of photocatalytic properties and accessible nano-structures such as rods[7], wires[8] and tubes are well documented and have been shown to have a dramatic impact on the obtained properties of the photocatalyst, allowing for a large degree of optimisation with the material, and it’s extended applications in electrochemistry.[9]

One of the major obstacles for TiO_2 photocatalysts is the large bandgap which limits its absorption to the UV region, as such a key focus of TiO_2 photocatalytic research is into reduction of the bandgap to a more accessible level.[10] Ce doped titanium oxides have been investigated for reducing the bandgap and improving the overall photocatalytic properties of TiO_2[1,11] which have important applications in water splitting, and the formation of H_2 for use as an alternative energy source to fossil fuels.[12]

This chapter deals with the work undertaken in investigating various mixed metal oxides and their suitability for further study via combined X-PDF, n-PDF and Bragg diffraction data analysis of local structure using RMCProfile.

5.2 $Ce_{0.25}Zr_{0.75}O_2$

Two samples of $Ce_{0.25}Zr_{0.75}O_2$ were studied to complete a composition & treatment study with the $Ce_{0.75}Zr_{0.25}O_2$ and $Ce_{0.5}Zr_{0.5}O_2$ samples discussed in Chapters 3 and 4 of this thesis. While neither of the $Ce_{0.25}Zr_{0.75}O_2$

composition samples (F800 & SRMO1050) were fully analysed via RMCProfile, they provide valuable insights into the thermal stability of the $Ce_{1-x}Zr_xO_2$ material under reducing conditions and highlight key areas of difficulty when applying complicated analysis methods, as such the combined X-ray and neutron Bragg diffraction analysis of $Ce_{0.25}Zr_{0.75}O_2$ samples after either firing in air at 800 °C for 4 hours (F800) or reduction under H2 at 1050 for 4 hours, cooled to room temperature then fired to 400 °C for 2 hours (SRMO1050) F800 is discussed here.

5.2.1 $Ce_{0.25}Zr_{0.75}O_2$ - F800

Figure 5.1 shows the observed diffraction pattern and Rietveld refined model fit for the $Ce_{0.25}Zr_{0.75}O_2$ F800 sample which shows a single tetragonal *P*4/*nmc* phase. The observed data are in good agreement for both X-ray and neutron data with no reflections observed with a d spacing above 3.2 Å. The X-ray and neutron diffraction combined refinement confirmed the assumption that the $Ce_{0.25}Zr_{0.75}O_2$ F800 material could be described as a single tetragonal *P*4/*nmc* phase with no evidence of oxygen or cation disorder observed as expected from liturature.[13–15] Table 5.1 shows the fitted parameters for the $Ce_{0.25}Zr_{0.75}O_2$ F800 sample.

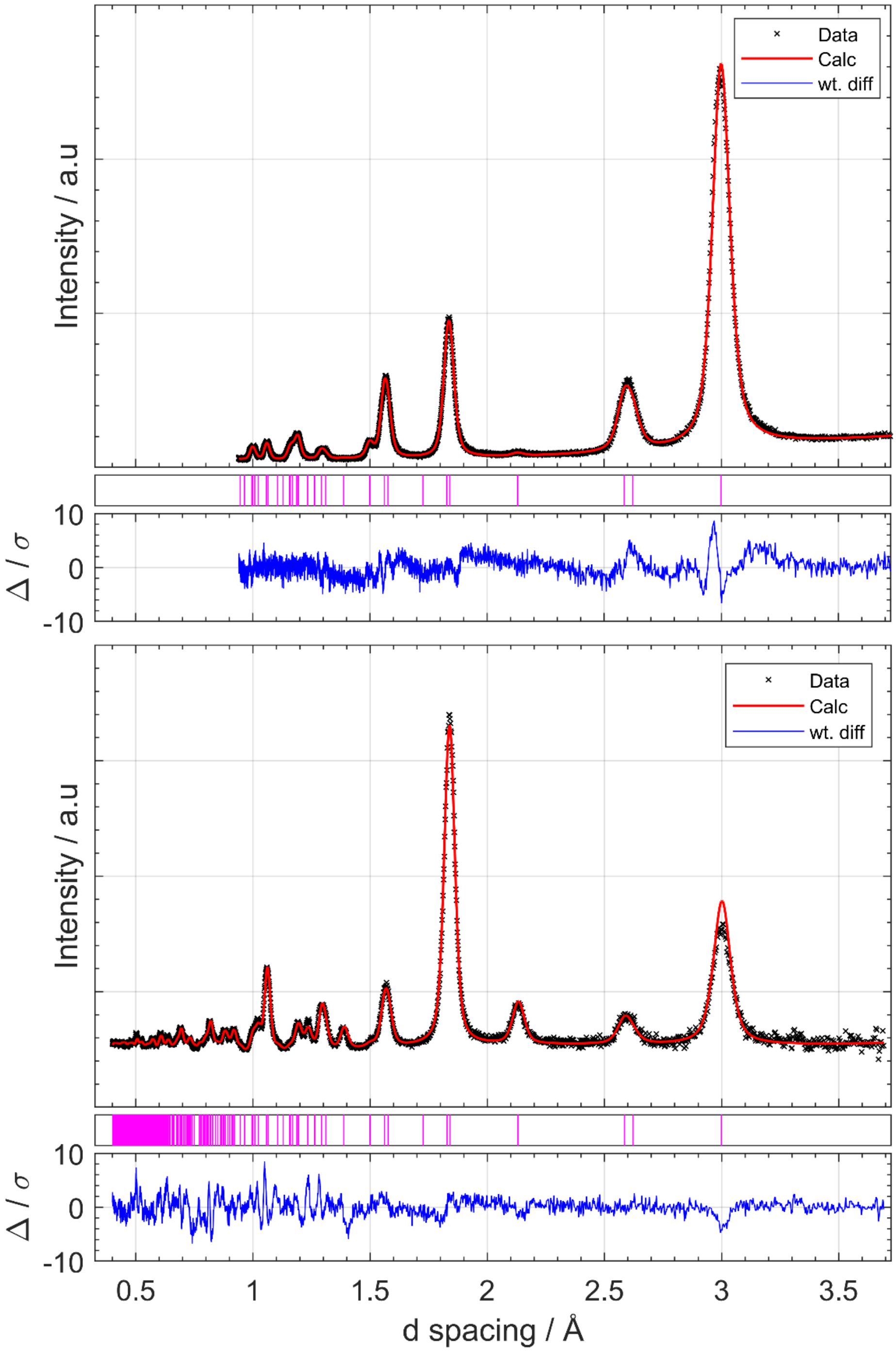

Figure 5.1: Rietveld refinements of $Ce_{0.25}Zr_{0.75}O_2$ F800, model refined against 5 banks of neutron data and 1 bank of X-ray data using the $P4_2/nmc$ structure, refined parameters shown in Table 5.1; Top) X-ray data obtained from a monochromatic Cu K-α1 laboratory diffractometer. Bottom) Neutron data obtained from Polaris, bank 4 shown.

Table 5.1: Refined parameters for F800 $Ce_{0.25}Zr_{0.75}O_2$ using the tetragonal $P4_2/nmc$ space group in the 2nd origin, a = 3.6564(2) Å, c = 5.2437(6) Å, a/c ratio = 0.6973 (ideal cubic ratio = 0.7071…). Calculated density = 6.4165 g/cm^3, oxygen 'displacement' from cubic z coordinate = 0.0439 (0.230 Å), wR = 3.43 %.

Atom	**Label**	**Wyck.**	***x***	***y***	***z***	**Uiso / Å^2**	**Occ.**
Ce Zr	Ce Zr	2a	0.25	-0.25	0.25	0.00623(12)	0.25 0.75
O	O	4d	0.25	0.25	0.45611(2)	0.01222(18)	1

5.2.2 $Ce_{0.25}Zr_{0.75}O_2$ - SRMO1050

Figure 5.2 and Figure 5.3 show the observed neutron and X-ray diffraction patterns for the same $Ce_{0.25}Zr_{0.75}O_2$ material shown in Figure 5.1 after having experienced a high temperature reduction at 1050 °C for 4 hours, cooled to room temperature and heated to 400 °C for 1 hour under air, consistent with the SRMO1050 treatment described in Chapters 4 and 5. Clear phase segregation is observed with Rietveld refined cation occupancies implying phase segregation to nominally tetragonal ZrO_2 ($Ce_{0.05}Zr_{0.95}O_2$) and cubic $Ce_{0.45}Zr_{0.55}O_2$. Unlike the $Ce_{0.75}Zr_{0.25}O_2$ material, some pyrochlore like cation ordering is observed and is most clear as peaks in the difference curve at 2.1 Å and 2.4 Å in the bottom section of Figure 5.2 and at 6.0 Å in Figure 5.3. These reflections indicative of cation ordering however are too low intensity to reliably model in a multiphase refinement of closely related, heavily overlapping features, thus the simpler $Fm\bar{3}m$ cubic "sub-cell" model was used instead with the observed supercell reflections left unmodelled. This immediate phase segregation, and low intensity of the cation ordering supercell reflections are the primary reasons the $Ce_{0.25}Zr_{0.75}O_2$ composition was not explored further for further analysis and RMC modelling, these samples are discussed here for completeness of the F800 and SRMO1050 treated $Ce_{0.75}Zr_{0.25}O_2$ and $Ce_{0.5}Zr_{0.5}O_2$ samples discussed in Chapters 3 and 4.

Comparing the $Ce_{0.05}Zr_{0.95}O_2$ $P4_2/nmc$ refined phase (tetragonal ~ZrO_2) present in the $Ce_{0.25}Zr_{0.75}O_2$ SRMO1050 sample to a liturature ZrO_2 $P4_2/nmc$ sample studied with neutron diffraction by Bouvier *et. al*[16]*;* it is unclear if there is significant Ce present in the Zr rich $P4_2/nmc$ phase as lattice parameters indicate a slight unit cell expansion, while the *a* / *c* ratio indicates limited impact on the distortion observed in tetragonal ZrO_2.

Table 5.2: Literature vs experimental parameters for tetragonal ZrO_2/$Ce_{0.05}Zr_{0.95}O_2$ in phase segregated $Ce_{0.25}Zr_{0.75}O_2$ post SRMO1050 treatment. O site z coordinate for P. Bouvier's model was adjusted by 0.5 - z to match the same $P4_2/nmc$ space group setting used.

Sample	***a* / Å**	***c* / Å**	***a* / *c* ratio**	**O^{2-} *z* coord.**
ZrO_2 P. Bouvier[16]	3.5794(2)	5.1647(7)	0.6941	0.4518(4)*
ZrO_2 Chen *et al*[17]	3.5964(3)	5.1685(8)	0.6958	-
ZrO_2 Materials Project[18]	3.60	5.23	0.69	-
$Ce_{0.05}Zr_{0.95}O_2$ This work	3.6169(2)	5.2126(5)	0.6939	0.4470(2)

The $Fm\bar{3}m$ refined phase shown in Table 5.4 is likely the κ-$CeZrO_4$ phase, however due to the complexity of κ-$CeZrO_4$ phase refinements detailed in Chapter 4 of this thesis a two phase model of tetragonal ~ZrO_2 and κ-$CeZrO_4$ was not stable enough to provide useful insights, so these "sub-cell" reflections were modelled with a cubic unit cell ($Fm\bar{3}m$) of composition $Ce_{0.25}Zr_{0.75}O_2$ with the composition allowed to refine.

While refinement of the κ-$CeZrO_4$ phase was impractical, the relative intensities of the supercell reflections likely indicates that a significant amount of Ce-Zr anti-site disorder is present. The supercell lattice parameters ($Fm\bar{3}m$ lattice parameter *a* × 2) 10.460(2) Å fall short of those observed for the κ-$CeZrO_4$ phases observed in the $Ce_{0.5}Zr_{0.5}O_2$ compositions of 10.53 Å; this could be due to off-stoichiometry with most of the anti-site disorder present being in the form of Zr on Ce sites, also indicated in the refined cation occupancies driven by relative intensities of the observed reflections.

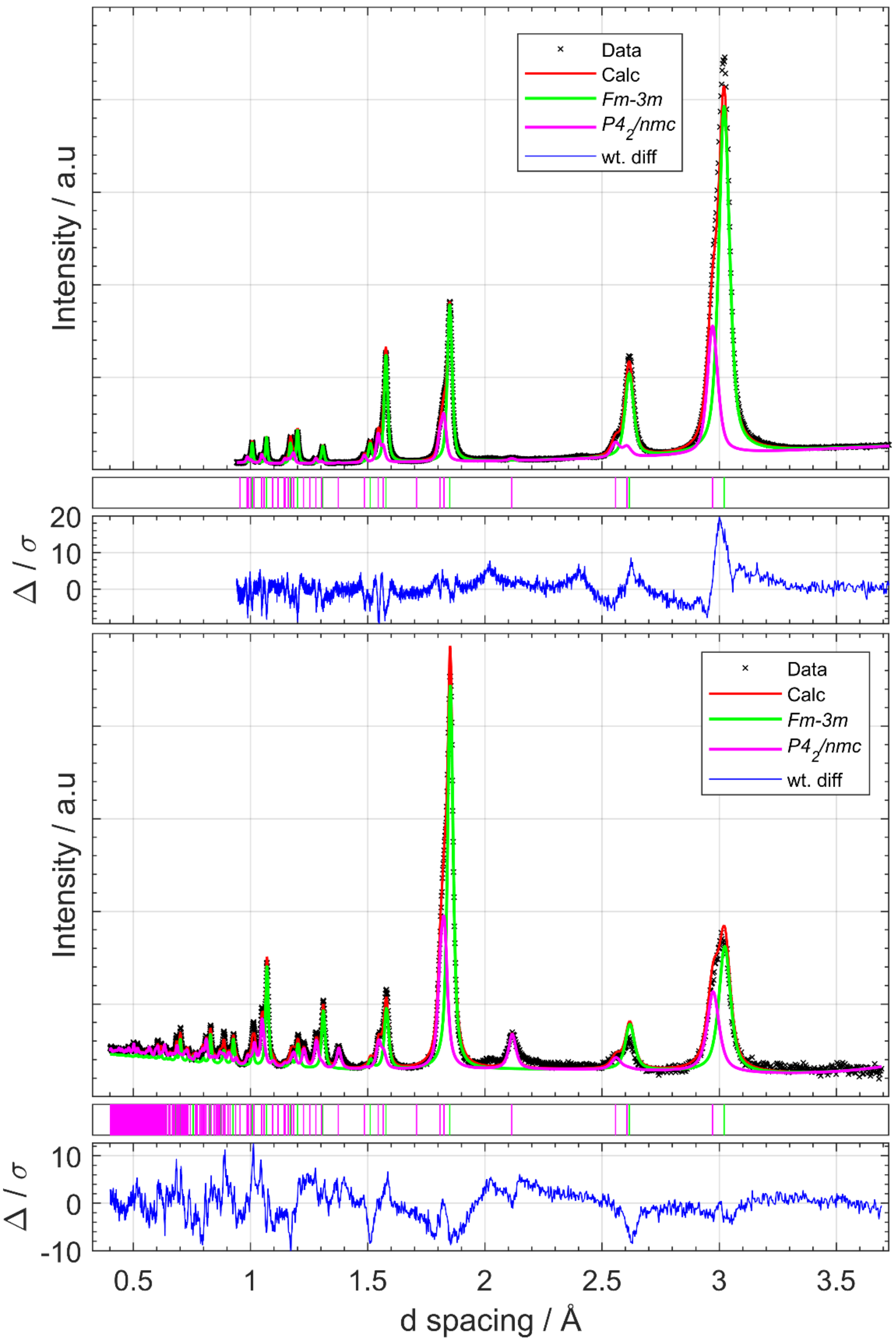

Figure 5.2: Rietveld refinement of $Ce_{0.25}Zr_{0.75}O_2$ *SRMO1050 fitted with a two phase model,* $P4_2/nmc$ tetragonal phase and a $Fm\bar{3}m$ *cubic model. Refined parameters are shown in Table 5.3. Top) X-ray data shown obtained from a monochromatic Cu K-α1 laboratory diffractometer. Bottom) Neutron TOF data obtained from Bank 4 showing X-ray/neutron scattering contrast. Refined parameters are shown in Table 5.3 and Table 5.4*

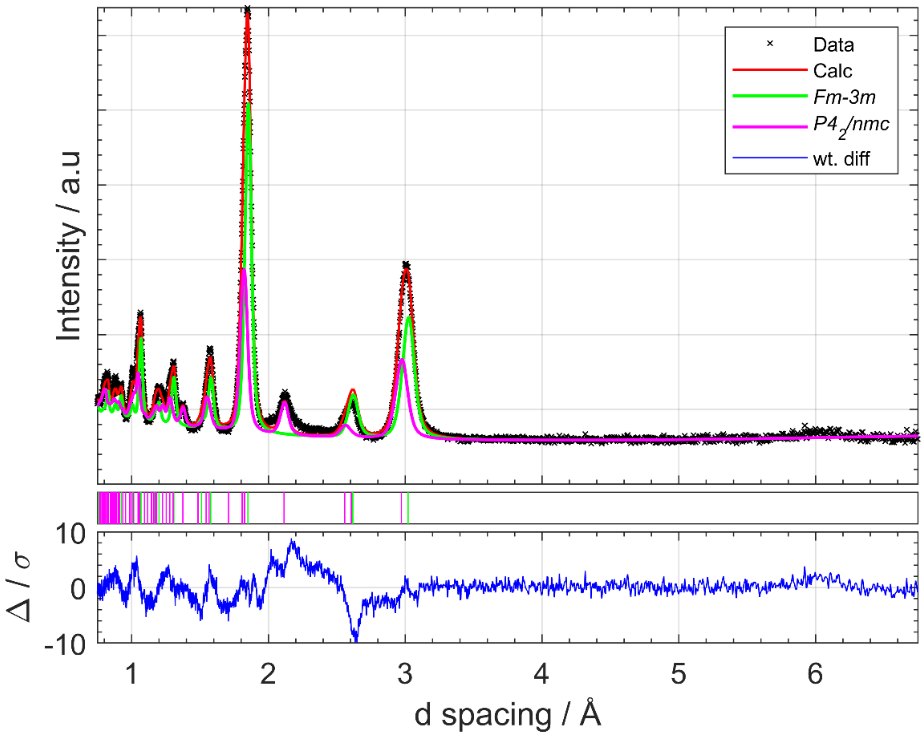

Figure 5.3: Rietveld refinement of $Ce_{0.25}Zr_{0.75}O_2$ SRMO1050 fitted with a two phase model, $P4_2/nmc$ tetragonal phase and a *$Fm\bar{3}m$ cubic model. Refined parameters are shown in Table 5.3 and Table 5.4. Neutron TOF data shown obtained from Polaris Bank 4.*

Table 5.3: Refined tetragonal parameters for the two phase refinement of SRMO1050 $Ce_{0.75}Zr_{0.25}O_2$ using the tetragonal $P4_2/nmc$ space group in the 2nd origin, a = 3.6169(2) Å, c = 5.2126(5) Å, a/c ratio = 0.6939 (ideal cubic ratio = 0.7071…). Calculated density = 6.1067 g/cm^3, oxygen 'displacement' from cubic z coordinate = 0.053 (0.276 Å), phase fraction = 0.296(2), combined wR = 3.31 %.

Atom	**Label**	**Wyck.**	***x***	***y***	***z***	**Uiso / Å^2**	**Occ.**
Ce	Ce	2a	0.25	-0.25	0.25	0.0064(2)	0.044(6)
Zr	Zr						0.956(6)
O	O	4d	0.25	0.25	0.4470(2)	0.0026(2)	1

Table 5.4: Refined cubic parameters for the dual phase refinement of SRMO1050 $Ce_{0.25}Zr_{0.75}O_2$ using the cubic $Fm\bar{3}m$ space group, a = 5.2302(12) Å. Calculated density = 6.71 g/cm^3, phase fraction = 0.704(2) , combined wR = 6.03 %.

Atom	**Label**	**Wyck.**	***x***	***y***	***z***	**Uiso / Å^2**	**Occ.**
Ce	Ce	4a	0.0	0.0	0.0	0.01696(18)	0.441(7)
Zr	Zr						0.559(7)
O	O	8c	0.25	0.25	0.25	0.0273(3)	1

5.3 $Ce_{1-(x+y)}Ti_xZr_yO_2$

Cerium zirconium oxide samples with 40% of the zirconium substituted for titanium were studied due to the significant reduction in temperature at which reflections related to pyrochlore cation ordering were experimentally observed, only requiring reduction at 900 °C to form the supercell reflections associated to pyrochlore cation arrangements. This reduction in reduction temperature required to achieve pyrochlore cation ordering provides a significant improvement over the higher temperature reductions required to achieve cation ordering in the $Ce_{0.5}Zr_{0.5}O_2$ system which requires temperatures above 1000 °C, with full cation ordering only being achieved above around 1500 °C. κ-$CeZrO_4$ phases synthesised at 1500 °C however show large crystallite sizes and poor overall OSC properties[19,20], showing that the improved OSC properties are not a direct result of the pyrochlore-like cation ordering. This decrease in properties is often accredited to loss of surface area, however surface area alone fails to capture bulk oxygen mobility[21] often observed in ceria zirconia materials. A alternative hypothesis is that the loss of properties is more likely related to the destruction of key oxygen defect sites[22,23], another side effect of sintering. Thus a cation ordered cerium zirconium oxide material prepared at relatively low temperatures is an attractive material to study from perspectives of both beneficial properties and the interesting structural questions raised.

F800 and SRMO900 treatments for the composition $Ce_{0.3}Zr_{0.5}Ti_{0.2}O_2$ were investigated but no phase pure SRMO900 sample was achieved with all attempts resulting in significant phase segregation into a complicated mixture, the F800 treated sample of this composition is not included as it provides limited benefit when investigated and discussed in isolation. As such no results for the $Ce_{0.3}Zr_{0.5}Ti_{0.2}O_2$ composition are discussed in this thesis.

5.3.1 $Ce_{0.5}Ti_{0.2}Zr_{0.3}O_2$ - F800

Figure 5.4 shows the X-ray and neutron observed diffraction pattern for sample $Ce_{0.5}Zr_{0.3}Ti_{0.2}O_2$ F800. The X-ray data were obtained at the I15-1 XPDF beamline at the DLS. Notably, the Rietveld refined model in the

P4/nmc space group is in good agreement with the X-ray diffraction pattern, however the neutron data shows a significant mismatch in the 1 0 2 (hkl) reflection at 2.18 Å. As discussed in Chapter 3 this reflection is associated to the tetragonal distortion of the oxygen site, however oxygen distortion alone is incapable of describing the intensity mismatch observed for this sample. Unlike other air heated samples discussed in this thesis a significant amount of oxygen vacancies were implied by Rietveld refinement of the observed neutron diffraction data. Explorative refinement of metal site occupancies proved unstable, but ultimately implied that the metal site may not account for the full 0.2 Ti occupancy. When the number of oxygen vacancies are considered, the magnitude exceeds that which the cerium present could charge balance for with full Ce^{3+}. These factors combined show that the obtained model which fits well for X-ray data is incapable of fully describing the subtleties of this sample. The reduction of Zr^{4+} or Ti^{4+} to a 3+ charge state is possible, however Ti and Zr are most common and stable in the 4+ charge state, with the data collection conditions approximately ambient temperature and atmosphere (neutron data collection from sample packed into a vanadium can in air) this explanation remains unlikely. Refined parameters discussed here are shown in Table 5.5.

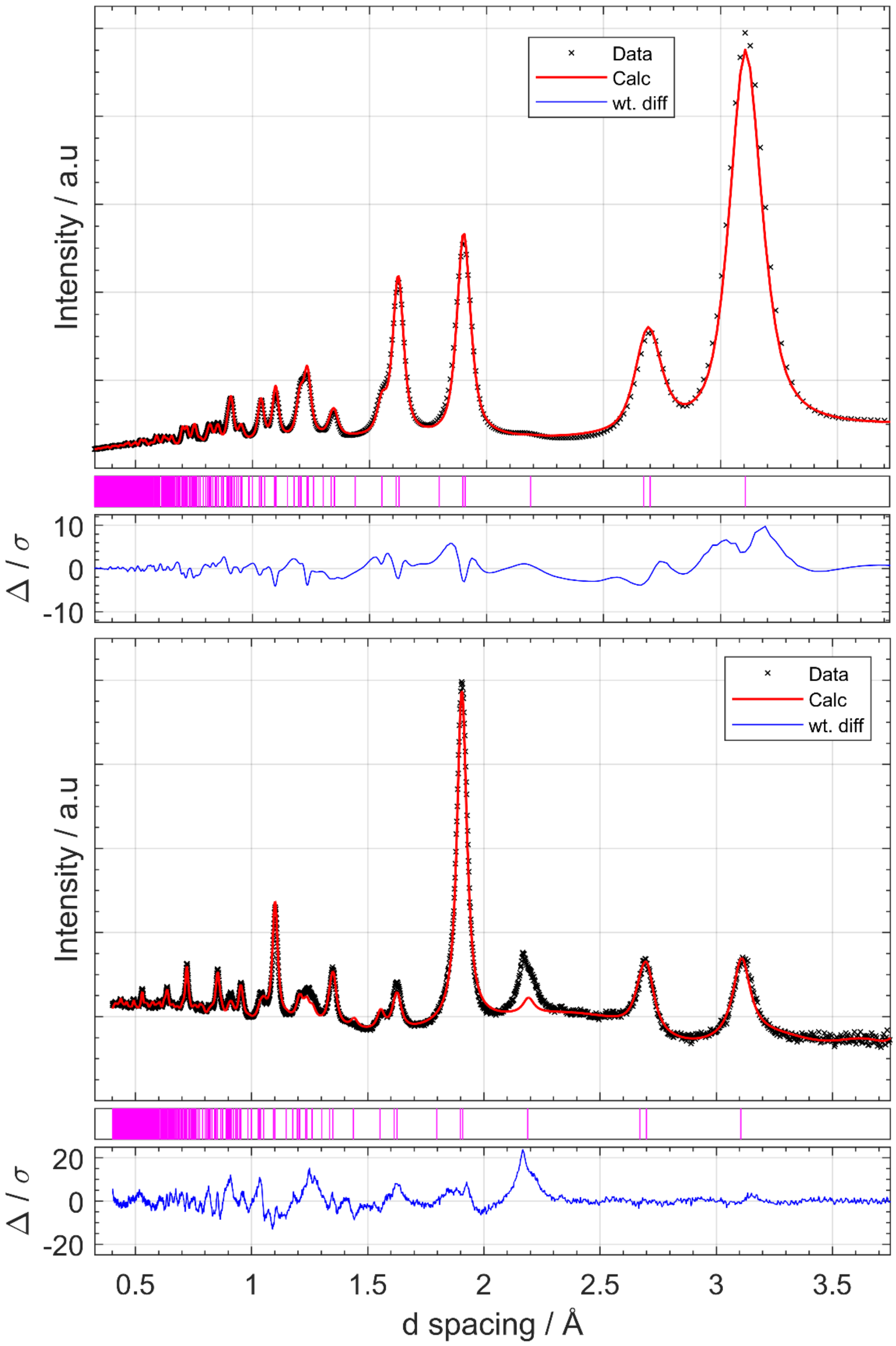

Figure 5.4: Rietveld refinements of $Ce_{0.5}Zr_{0.3}Ti_{0.2}O_2$ F800, model refined against 5 banks of neutron data and 1 bank of X-ray data using the $P4_2/nmc$ structure; Top) X-ray diffraction data obtained from the I15-1 XPDF beamline at DLS. Bottom) Neutron data obtained from Polaris, bank 4 shown.

Table 5.5: Refined parameters for F800 $Ce_{0.5}Zr_{0.3}Ti_{0.2}O_2$ using the tetragonal $P4_2/nmc$ space group in the 2nd origin, a = 3.8181(9) Å, c = 5.3433(15) Å, a/c ratio = 0.7146 (ideal cubic ratio = 0.7071…). Calculated density = 5.7144 g/cm^3, oxygen 'displacement' from cubic z coordinate = 0.267 (0.143 Å), wR = 4.28 %.

Atom	**Label**	**Wyck.**	***x***	***y***	***z***	**Uiso / Å^2**	**Occ.**
Ce	Ce	2a	0.25	-0.25	0.25	0.00157(19)	0.5
Zr	Zr						0.3
Ti	Ti						0.2
O	O	4d	0.25	0.25	0.47330(18)	0.0681(13)	0.845(2)

5.3.2 $Ce_{0.5}Ti_{0.2}Zr_{0.3}O_2$ - SRMO900

Figure 5.5 shows the observed X-ray and neutron diffraction patterns of SRMO900 treated $Ce_{0.5}Zr_{0.3}Ti_{0.2}O_2$ with the calculated fits from a Rietveld refined Ti doped κ-$CeZrO_4$ phase which is in relative agreement. Visual inspection of the fit and data show some immediate areas of mismatch, nominally the lack of any discernible intensity for the 1 1 1 reflection in the neutron data for bank 2 (bottom on Figure 5.5) while the X-ray diffraction pattern highlights clear intensity indicating pyrochlore like cation supercell ordering.

Unconstrained explorative free metal occupancy refinement indicated the Ti occupied preferentially the Zr superlattice with minimal levels of Ce/Zr anti-site disorder present, while refinement of interstitial oxygens indicated a much larger interstitial occupancy than observed in the κ-$CeZrO_4$ discussed in Chapter 4 accounting for 12 % of the refined total oxygen occupancy. Overall stoichiometry was constrained for the final refinements presented in Table 5.6, however oxygen vacancies were explored at various stages during the refinement process and consistently found to refine to approximately full overall oxygen occupancy, so to aid refinement stability total O was constrained to full occupancy.

While all anomalies within the data have not been fully accounted for by the refined model, it is clear that cation ordering and interstitial oxygen are present within the material in significant concentrations. It can also be deduced that the Ti present preferentially occupies the Zr sites, and may additionally occupy some interstitial sites, although exploring this possibility with a three metal cation ordered structure with possible anti-site disorder and significant oxygen disorder and overall low symmetry is challenging for Rietveld refinement analysis of powder X-ray/neutron diffraction data. Careful use of RMCProfile could assist in eluding to the nature of the unexplained disorder present as no clear phase segregation is observed. The use of neutron PDF could also provide insight into the nature of the Ti present, making this material an attractive topic for further study.

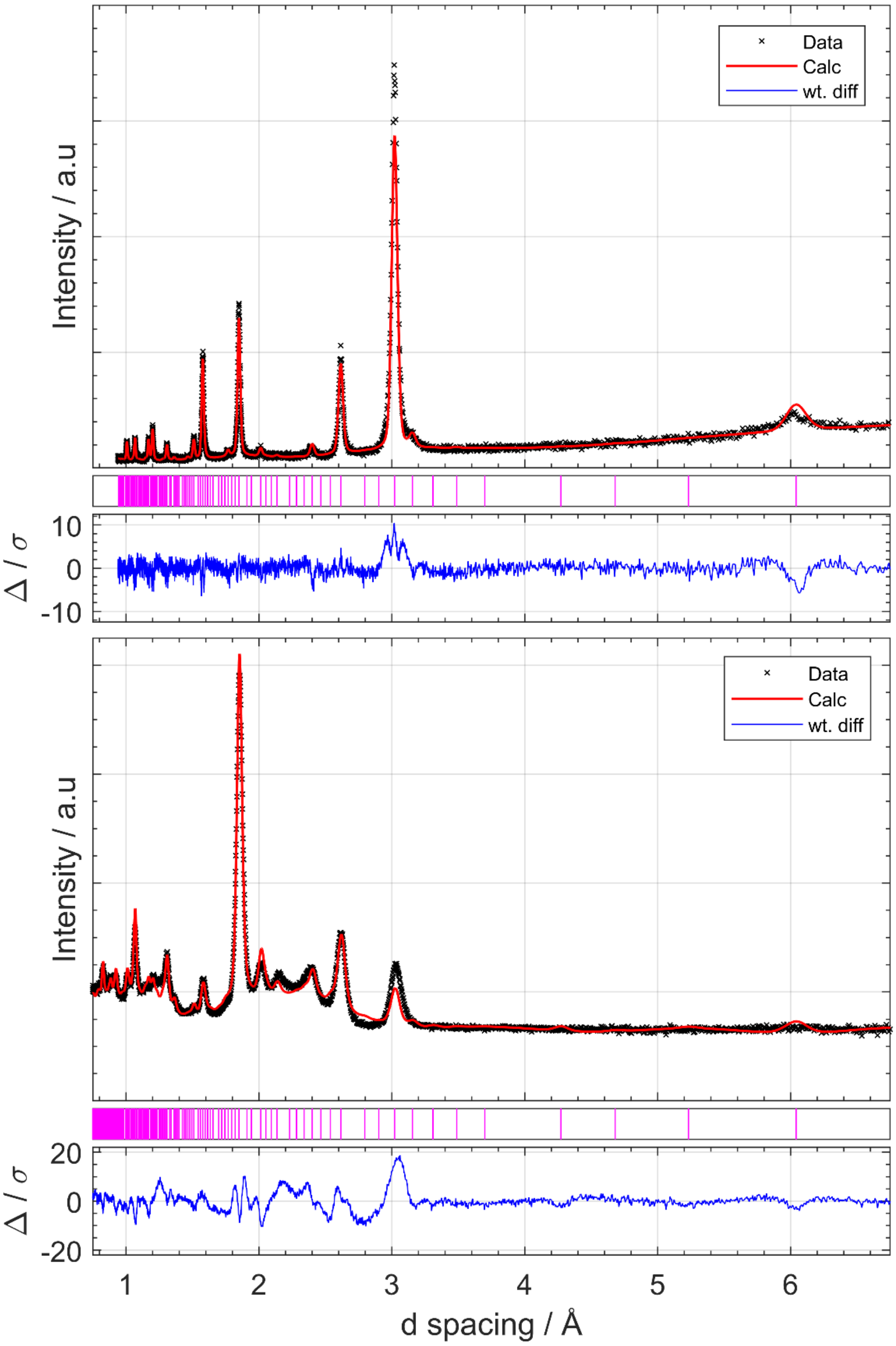

Figure 5.5: Rietveld refinement of $Ce_{0.5}Zr_{0.3}Ti_{0.2}O_2$ SRMO900 fitted with a Ti doped κ-$CeZrO_4$ phase based on the structure refined in Chapter 4. Refined parameters are shown in Table 5.6. Top) X-ray data shown obtained from a monochromatic Cu K-α1 laboratory diffractometer showing the primary cation ordering reflection 6.0 Å. Bottom) Neutron TOF data obtained from Bank 2 showing X-ray/neutron scattering contrast.

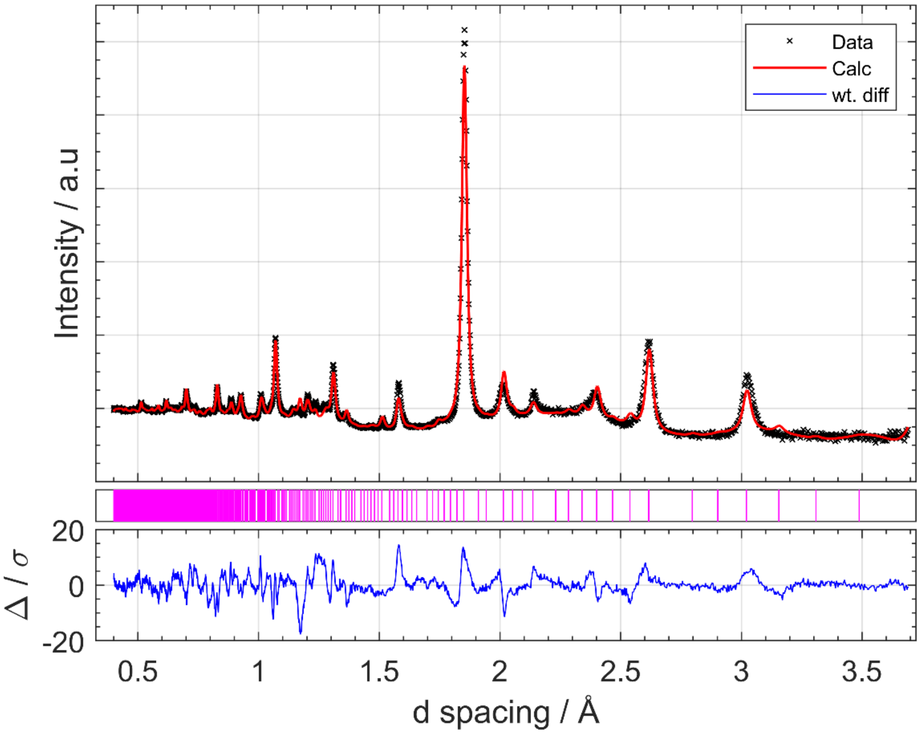

Figure 5.6: Rietveld refinement of $Ce_{0.5}Zr_{0.3}Ti_{0.2}O_2$ *SRMO900 fitted with a Ti doped κ-*$CeZrO_4$ *phase. Refined parameters are shown in Table 5.6. Neutron TOF data shown obtained from Polaris Bank 4.*

*Table 5.6: Refined parameters for SRMO900 κ-$CeZrO_4$ using the $P2_13$ space group, a = 10.4636(5) Å. Calculated density = 6.4475 g/cm^3, wR = 3.35 %, * Oint3 and Oint4 showed no evidence of oxygen occupancy, however they are included for completeness.*

Atom	Label	Wyck.	x	y	z	Uiso / Å^2	Occ.
Ce	Ce1	4a	0.124	0.1240	0.1240	0.0128(3)	0.898(3)
Ti	Ti1						0.102(3)
Zr	Zr1						0
Ce	Ce2	12b	0.123	0.3715	0.3752		
Ti	Ti2						0.102(3)
Zr	Zr2						0
Ce	Ce3	4a	0.633	0.6327	0.6327		0.102(3)
Ti	Ti3						0.298(3)
Zr	Zr3						0.6
Ce	Ce4	12b	0.625	0.8683	0.8695		0.102(3)
Ti	Ti4						0.298(3)
Zr	Zr4						0.6
O	O1	4a	-0.021	-0.021	-0.021	0.00507(17)	0.822(13)
O	O2	4a	0.261	0.261	0.261		0.781(22)
O	O3	4a	0.458	0.458	0.458		0.392(17)
O	O4	4a	0.726	0.726	0.725		0.696(22)
O	O5	12b	0.242	0.248	-0.010		0.956(11)
O	O6	12b	0.242	0.248	0.505		0.979(11)
O	O7	12b	-0.001	-0.005	0.240		0.518(7)
O	O7-split	12b	0.002	-0.008	0.320		0.482(7)
O	O8	12b	-0.006	0.011	0.709		0.837(10)
O	Oint1	12b	0.513	0.177	0.102	0.0007(14)	0.312(8)
O	Oint2	12b	0.915	0.124	0.091		0.353(5)
O	Oint3*	4a	0.875	0.875	0.875	N/A	0
O	Oint4*	4a	0.375	0.375	0.375		0

5.4 $Ce_xTi_{1-x}O_2$ materials

A neutron diffraction study on Ce inclusion into the TiO_2 anatase structure was undertaken on samples synthesised via a solvothermal route at 240 °C by de Lima[1] for photocatalysis. The samples of $Ce_xTi_{1-x}O_2$ (x = 0.005, 0.01, 0.05 and 0.1) were studied using XANES spectroscopy and found that the low Ce at. % samples (x = 0.005 and 0.01) showed Ce oxidation states close to 3+; this could be extended to the x= 0.05 and 0.1 samples by the addition of lactic acid. In-situ XANES showed that firing these samples showed an oxidation of Ce^{3+} to Ce^{4+} at temperatures above 200 °C.

Samples of composition $Ce_xTi_{1-x}O_2$ for x = 0, 0.01, 0.05 and 0.1 were studied as made and fired at 400 °C in air for 4 hours. Data collection pre-dated the work undertaken in this Thesis however data analysis of these samples was included in the project due to the relevance of the use of neutron total scattering to study Ce containing oxide materials.

The obtained neutron diffraction Rietveld fits are shown in Figure 5.7. The strongest reflection for V metal from the vanadium sample can is indicated by an asterisk in each dataset shown, and this reflection appears more clearly in the fired 10% Ce sample due to the significantly lower sample volume resulting in a larger relative volume of the vanadium can sampled.

Figure 5.8 shows the trends observed in the refined lattice parameters, cell volume, a / c ratio, and oxygen z coordinate for which neutron diffraction has meaningful sensitivity. While the trends observed in the lattice parameters and volume don't show a clear linear trend, when the a/c ratio is a clear shift towards a less tetragonally distorted unit cell is observed. This trend is matched with the shift observed in oxygen z coordinate. While the original aim of this study was to resolve the nature of the Ce present via the use of PDF data, the insights of neutron diffraction alone show significant evidence of the bulk TiO_2 anatase structure showing key linear trends in the a/c ratio and oxygen z coordinate, showing a clear shift towards a more cubic arrangement of atoms, implying that the cerium is present within the bulk material. Vegard's law[24] is a valuable tool in materials chemistry and is derived from a observation where the lattice parameters of a solid solution could be described by the weighted mean of its constituents, most useful for binary solid solutions. However due to only having a small portion of the relative Ce-Ti occupancy ratio and the drastically different local atomic arrangements for TiO_2 (where Ti is 6 coordinated) and CeO_2 (where Ce is 8 coordinated), the solid solution approximation cannot be fulfilled as the native CeO_2 and anatase TiO_2 structures are too distinct to have a linear transformation, as such Vegard's Law was not applied to this study, as the a / c ratio and oxygen displacement were deemed indicative enough of observation of a linear relationship between Ce doping and bulk TiO_2 properties.

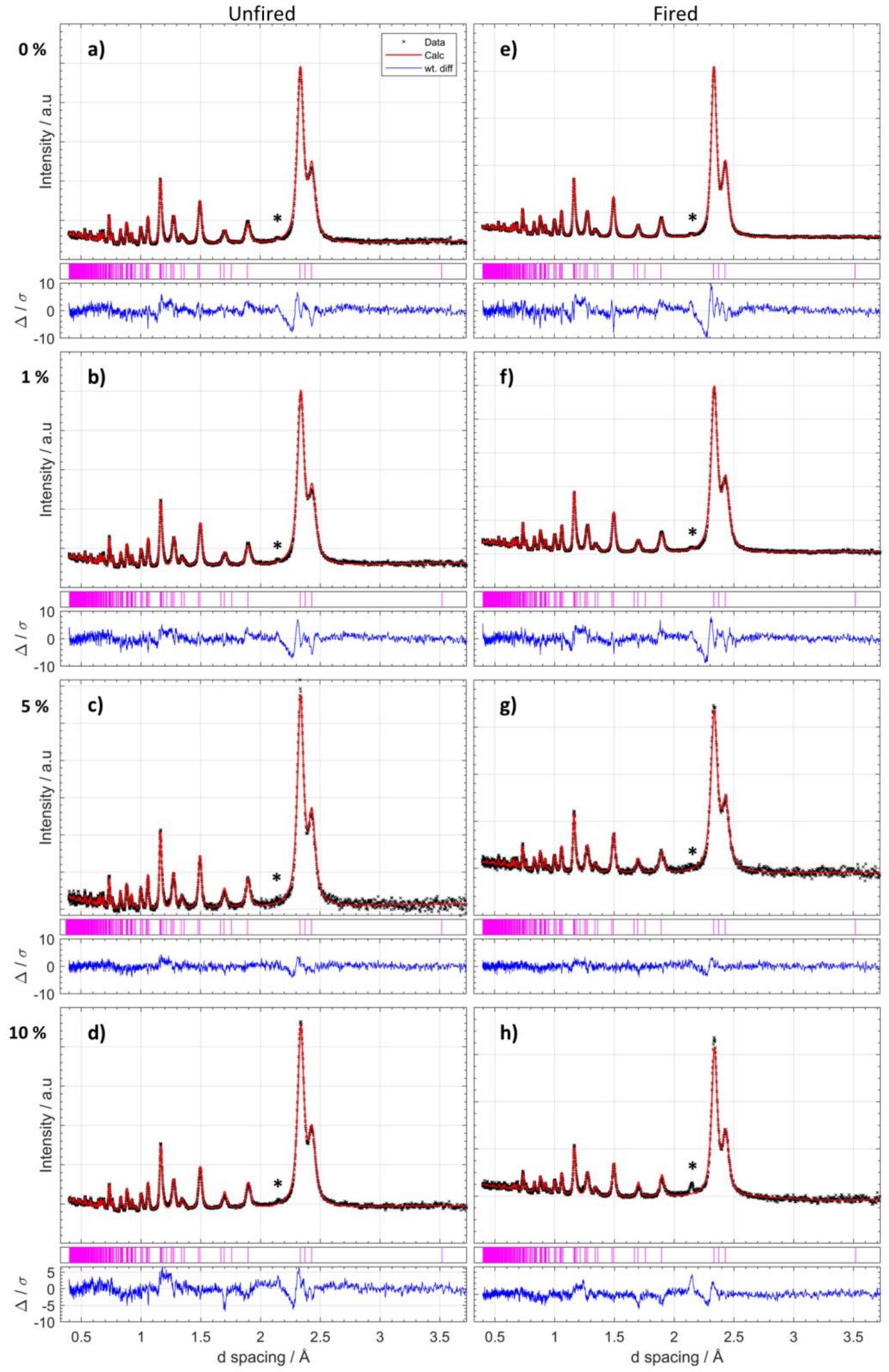

Figure 5.7: Obtained Rietveld refined models and neutron diffraction patterns for $Ce_xTi_{1-x}O_2$ samples and obtained fits against 5 banks of neutron data collected on Polaris, bank 3 shown. a) TiO_2 anatase. b) x= 0.01 Ce-TiO_2. c) x = 0.05 Ce-TiO_2. d) x = 0.1 Ce-TiO_2. e) TiO_2 anatase fired in air. f) x = 0.01 Ce-TiO_2 fired in air. g) x = 0.05 Ce-TiO_2 fired in air. h) x = 0.1 Ce-TiO_2 fired in air. Refined parameter trends visually displayed in Figure 5.8 with values displayed in Table 5.8.

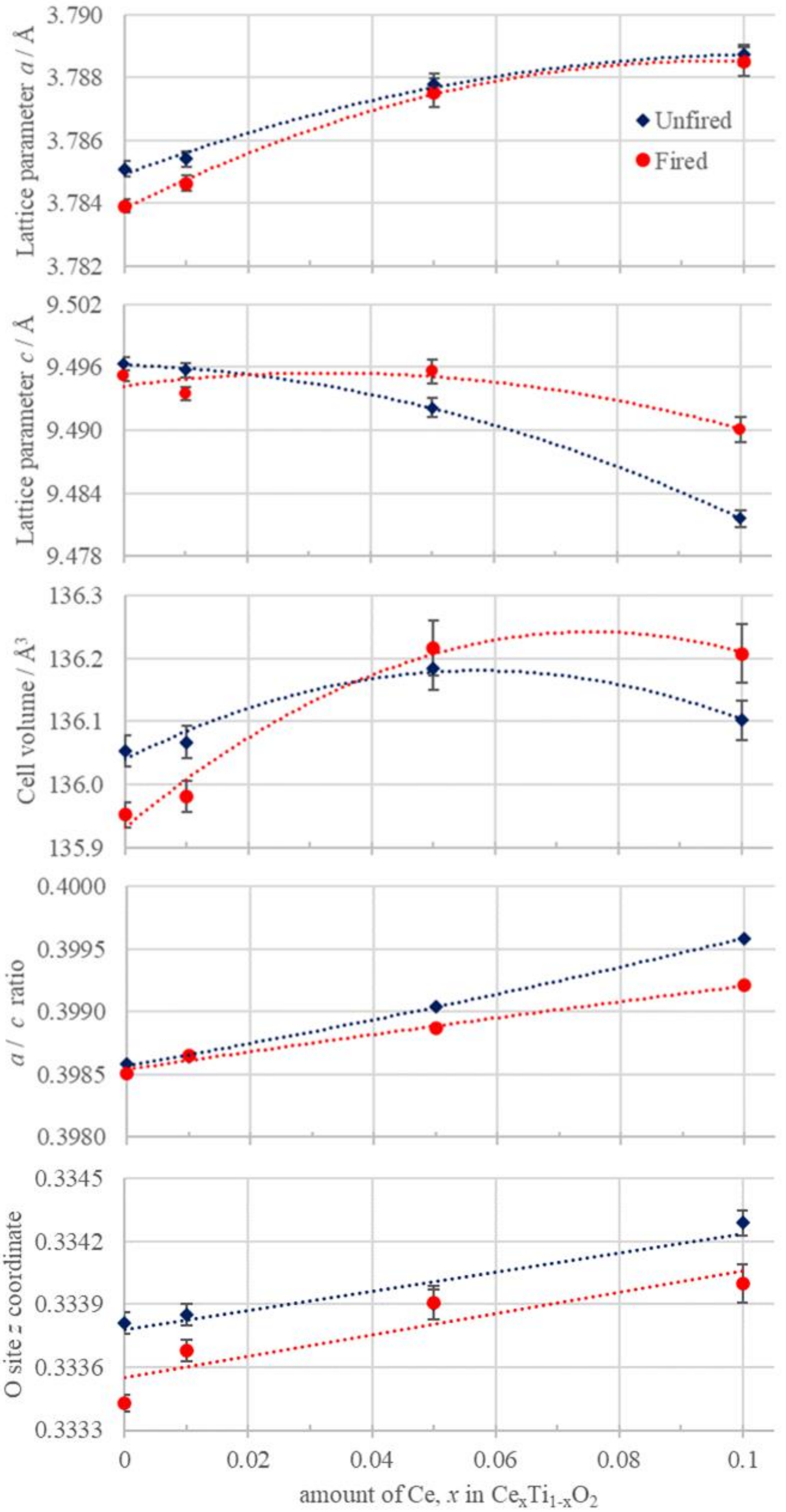

Figure 5.8: Refined lattice parameters, cell volume, a/c ratio and O site z coordinate for anatase $Ce_xTi_{1-x}O_2$ samples studied by neutron diffraction, x = 0, 0.01, 0.05 and 0.1. Dashed lines added as a guide for the eye. Values shown in Table 5.8, obtained fits and raw data shown in Figure 5.7.

Table 5.7: Crystal structure of anatase in the $I4_1/amd$ space group. The refined models had a fixed occupancy of Ce substituted onto the Ti site. Sample specific refined parameters shown in Table 5.8 below. Oxygen z coordinate obtained from Horn et. al.[25]

Atom	**Label**	**Wyck.**	***x***	***y***	***z***
Ti	Ti1	4a	0	0.75	0.125
O	O1	8e	0	0.25	0.3331*

Table 5.8: Refined parameters from experimentally acquired neutron diffraction data on Ce containing TiO_2 and after a firing treatment. Calculated density and weighted residual (wR) included.

Sample	**Ce / %**	**Calc. Den. g / cm^3**	**wRp %**	***a* / Å**	***c* / Å**	***a* / *c* ratio**	**O^{2-} *z* coord.**
				Unfired			
TiO2-0	0	3.9006	2.00	3.7850(3)	9.4964(6)	0.39858	0.33381(5)
TiO2-1	1	3.9453	1.92	3.7854(3)	9.4957(7)	0.39864	0.33385(5)
TiO2-5	5	4.1217	2.60	3.7878(3)	9.4922(9)	0.39904	0.33390(7)
TiO2-10	10	4.3493	1.88	3.7887(3)	9.4816(8)	0.39959	0.33429(6)
				Fired			
TiO2-F0	0	3.9035	2.80	3.7839(2)	9.4952(5)	0.39851	0.33343(4)
TiO2-F1	1	3.9478	2.37	3.7846(2)	9.4935(6)	0.39865	0.33368(5)
TiO2-F5	5	4.1208	3.65	3.7875(4)	9.4956(11)	0.39887	0.33391(8)
TiO2-F10	10	4.3459	2.86	3.7885(5)	9.4900(12)	0.39921	0.33400(9)

X-ray total scattering data were collected on these samples at I15-1 using an X-ray wavelength of 0.161669 Å. The data were processed in an identical manner taking into account the relative elemental compositions of each sample with a usable Q-max of 26 Å^{-1}. The obtained X-ray PDF patterns are shown in Figure 5.9. For the unfired samples some impact on the short range (1-5 Å) PDF is observed with relatively minimal impact on the medium range structure. The fired materials however show an entirely different story with significant difference observed in the low *r* distances of the PDFs coupled with a clear decrease the medium range structure. Caution is advised when correlating the PDF qualities here as especially for the x = 0.1 materials the standardised processing approach likely does not provide PDF’s of equivalent quality, the standardised normalisation approach was in part to highlight these differences that increasing Ce content had on the materials studied here. A more individual processing of the total scattering data would be required if the RMC method were to be applied to data like these observed.

A complimentary way of viewing the effect of Ce here is to also view the total scattering pattern in Q prior to Fourier transform to the PDF. Figure 5.10 shows the 8 processed total scattering datasets in Q for the x = 0, 0.01, 0.05 and 0.1 $Ce_xTi_{1-x}O_2$ fired and unfired samples. Large broad features correlating with Ce content and more distinct for the fired sample series are observed, note all known non-sample background contributions have been removed.

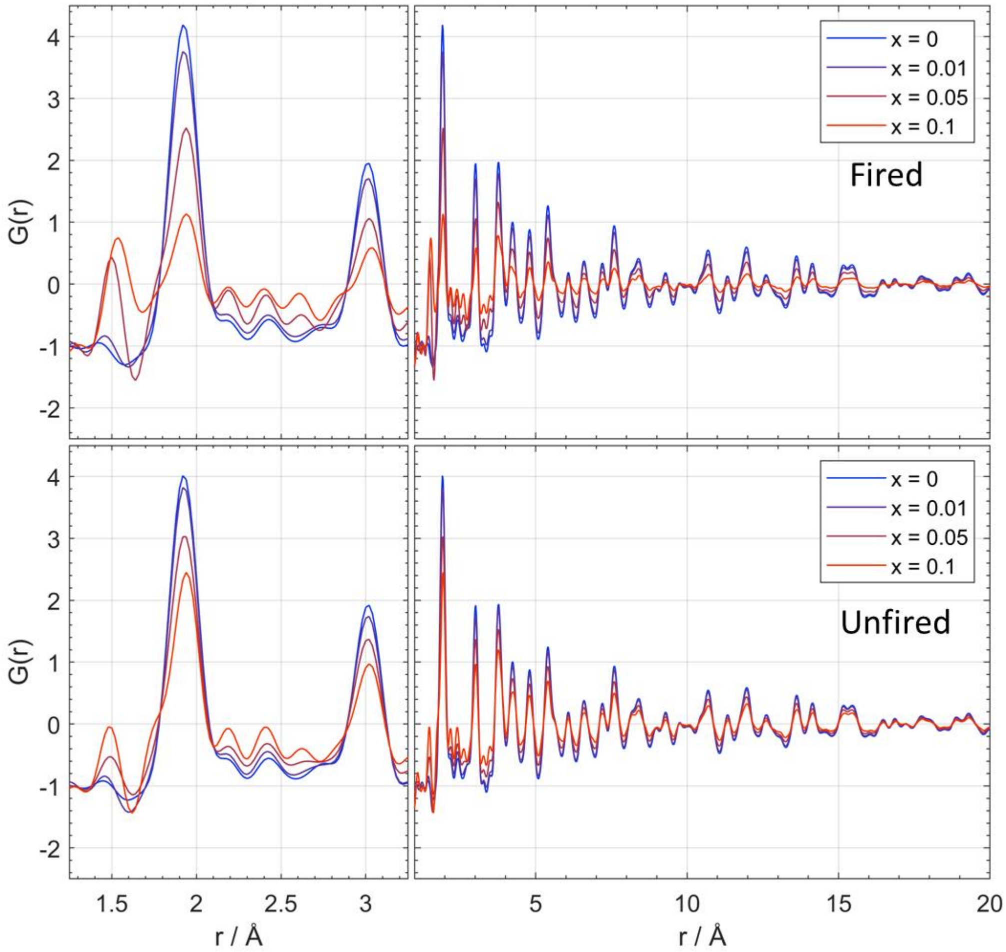

Figure 5.9: Obtained X-ray PDFs for Ce containing TiO_2 samples studied. Top) Fired samples overlaid with a inset focusing on the short 1.25 to 3.25 Å region Bottom) Unfired samples overlaid with a inset focusing on the short 1.25 to 3.25 Å region.

From this data it is indicated that the firing step causes formation of an amorphous structure in the material, implying that the morphology of the Ce present changes with firing. It is unclear from the data if this is clusters of CeO_x embedded in a TiO_2 matrix or a forming surface coated of CeO_2. For the unfired samples it is clear that the Ce is not present as an amorphous phase of meaningful dimensions, implying that the Ce is more likely dispersed throughout the structure causing generalised local disruption which cluster upon firing. Due to the clear non-crystalline anomalies within this data no small box PDF fitting is reported.

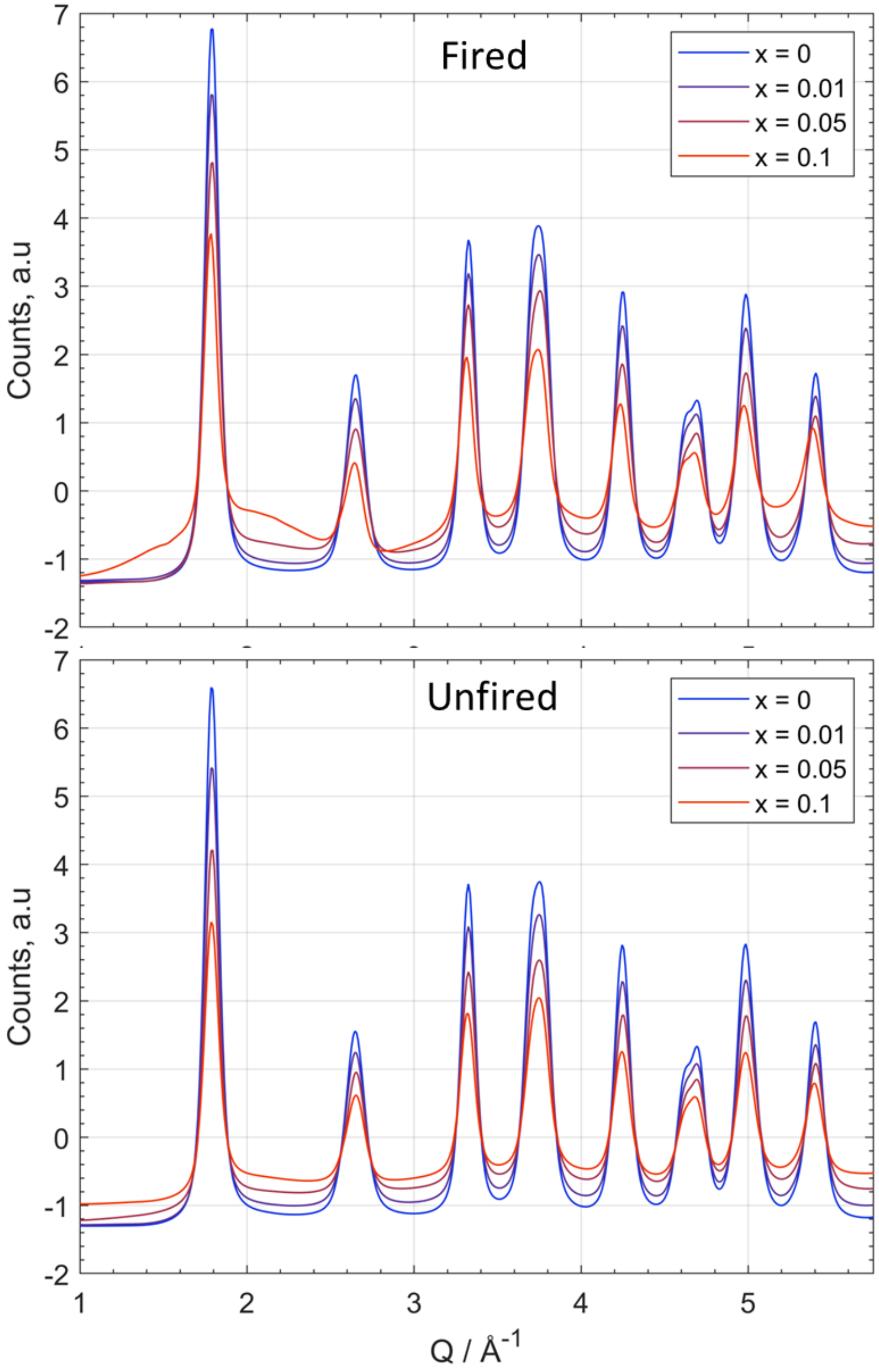

Figure 5.10: Total scattering patterns plotted in Q space highlighting the broad amorphous features present in the data post firing.

5.4 Conclusions

This chapter reports the preliminary assessment of X-ray and neutron scattering data from some cerium-oxide materials to assess what information might be obtained about the disorder present in their structures.

The $Ce_{0.25}Zr_{0.75}O_2$ composition shows limited phase stability under high temperature reductive conditions eliminating the possibility of studying the sample post reduction via PDF analysis and the RMC method. The material appears to remain a solid solution at 800 °C under air which allows for further investigation into the local structure making $Ce_{0.25}Zr_{0.75}O_2$ F800 an attractive subject for comparison with the $Ce_{0.75}Zr_{0.25}O_2$ F800 and industrially provided $Ce_{0.5}Zr_{0.5}O_2$ (F800) materials. The aim of such a study would be to determine the degree of solid-solution homogeneity between the cerium and zirconium present.

The $Ce_{0.5}Zr_{0.3}Ti_{0.2}O_2$ samples show anomalous features in the neutron diffraction patterns likely related to inherent structural disorder of the titanium content, namely the possibility of various possible sites for Ti within the structure. The exact nature of titanium in these samples could not be distinguished by powder X-ray and neutron diffraction. Pyrochlore like cation ordering was observed with reduction at 900 °C, and this cation ordering was visible via X-ray diffraction but showed unexpected behaviour in the neutron diffraction patterns with the 1 1 1 reflection visible to X-rays but showed no intensity in the neutron data. The $Ce_{0.3}Zr_{0.5}Ti_{0.2}O_2$ composition was also studied but found to be unstable under reduction conditions of 900 °C, making valuable insights using the PDF method unlikely.

The neutron total scattering study on Ce containing TiO_2 (0 - 10 %) sample pre and post firing showed a clear linear relationship for tetragonality (a / c ratio) and the oxygen site z coordinate of the bulk unit cell and the doped Ce content. In the original work on these materials it was established with TEM and electron energy loss spectroscopy that the Ce was present throughout the sample but the question remained, was this a surface coating of Ce, or was the Ce within the bulk of the samples. X-PDF data were collected to begin addressing this question and show that while local structure changes are observed in the unfired sample, firing the samples significantly increased these local structure differences. Inspection of the total scattering ‘Bragg’ data it is clear that a significant near-amorphous phase manifests after firing, likely 0.5-1 nm domains of CeO_x which significantly impact the required normalisations of the X-ray PDFs which were performed using a standardised approach for the 8 samples studied.

The preliminary conclusions of the neutron diffraction show strong evidence of the anatase TiO_2 structure accommodating discrete Ce through slight expansion of the *a* lattice parameter and significant contraction of the *c* lattice parameter of the anatase structure with increasing Ce content via neutron Bragg diffraction. This average structure impact is stronger for the unfired samples than the fired samples and could be explained by the formation of CeO_x nano-domains post firing which is strongly supported by the X-PDF data obtained. The observed data are applicable for further study via the addition of neutron PDF analysis coupled with the RMC method to gain insights into the local environments for Ti and Ce along with the implications of localised O defects.

5.5 Bibliography

1 J. Fonseca De Lima, M. H. Harunsani, D. J. Martin, D. Kong, P. W. Dunne, D. Gianolio, R. J. Kashtiban, J. Sloan, O. A. Serra, J. Tang and R. I. Walton, *J. Mater. Chem. A*, 2015, **3**, 9890–9898.

2 Z. J. Bo, Lintao, G. Maochu, W. J. Li, L. Z. Min, Z. Ming and Y. Chen, *J. Hazard. Mater.*, 2007, **143**, 516–521.

3 D. Devaiah, L. H. Reddy, S. E. Park and B. M. Reddy, *Catal. Rev. - Sci. Eng.*, 2018, **60**, 177–277.

4 T. Montini, M. Melchionna, M. Monai and P. Fornasiero, *Chem. Rev.*, 2016, **116**, 5987–6041.

5 Z. Fei, Y. Yang, M. Wang, Z. Tao, Q. Liu, X. Chen, M. Cui, Z. Zhang, J. Tang and X. Qiao, *Chem. Eng. J.*, 2018, **353**, 930–939.

6 P. Li, Y. Xin, Q. Li, Z. Wang, Z. Zhang and L. Zheng, *Environ. Sci. Technol.*, 2012, **46**, 9600–9605.

7 K. Santhi, M. Navaneethan, S. Harish, S. Ponnusamy and C. Muthamizhchelvan, *Appl. Surf. Sci.*, 2020, **500**, 144058.

8 J. E. Graves, M. E. A. Bowker, A. Summer, A. Greenwood, C. Ponce de León and F. C. Walsh, *Electrochem. commun.*, 2018, **87**, 58–62.

9 F. C. Walsh, L. F. Arenas and C. Ponce de León, *J. Chem. Technol. Biotechnol.*, 2018, **93**, 3073–3090.

10 C. Dette, M. A. Pérez-Osorio, C. S. Kley, P. Punke, C. E. Patrick, P. Jacobson, F. Giustino, S. J. Jung and K. Kern, *Nano Lett.*, 2014, **14**, 6533–6538.

11 N. Yan, Z. Zhu, J. Zhang, Z. Zhao and Q. Liu, *Mater. Res. Bull.*, 2012, **47**, 1869–1873.

12 M. Ge, J. Cai, J. Iocozzia, C. Cao, J. Huang, X. Zhang, J. Shen, S. Wang, S. Zhang, K. Q. Zhang, Y. Lai and Z. Lin, *Int. J. Hydrogen Energy*, 2017, **42**, 8418–8449.

13 M. Yashima, *Catal. Today*, 2015, **253**, 3–19.

14 P. Duran, M. Gonzalez, C. Moure, J. R. Jurado and C. Pascual, *J. Mater. Sci.*, 1990, **25**, 5001–5006.

15 R. Di Monte and J. Kašpar, *Top. Catal.*, 2004, **28**, 47–58.

16 P. Bouvier, E. Djurado, G. Lucazeau, C. Ritter and A. J. Dianoux, *Int. J. Inorg. Mater.*, 2001, **3**, 647–654.

17 L. Chen, T. Mashimo, E. Omurzak, H. Okudera, C. Iwamoto and A. Yoshiasa, *J. Phys. Chem. C*, 2011, **115**, 9370–9375.

18 A. Jain, S. P. Ong, G. Hautier, W. Chen, W. D. Richards, S. Dacek, S. Cholia, D. Gunter, D. Skinner, G. Ceder and K. A. Persson, *APL Mater.*, 2013, **1**, 011002.

19 S. Urban, P. Dolcet, M. Möller, L. Chen, P. J. Klar, I. Djerdj, S. Gross, B. M. Smarsly and H. Over, *Appl. Catal. B Environ.*, 2016, **197**, 23–34.

20 S. Urban, I. Djerdj, P. Dolcet, L. Chen, M. Möller, O. Khalid, H. Camuka, R. Ellinghaus, C. Li, S. Gross, P. J. Klar, B. Smarsly and H. Over, *Chem. Mater.*, 2017, **29**, 9218–9226.

21 S. Damyanova, B. Pawelec, K. Arishtirova, M. V. M. Huerta and J. L. G. Fierro, *Appl. Catal. A Gen.*, 2008, **337**, 86–96.

22 E. Mamontov, R. Brezny, M. Koranne and T. Egami, *J. Phys. Chem. B*, 2003, **107**, 13007–13014.

23 T. Proffen, S. J. L. Billinge, T. Egami and D. Louca, *Zeitschrift fur Krist.*, 2003, **218**, 132–143.

24 L. Vegard, *Zeitschrift für Phys.*, 1921, **5**, 17–26.

25 M. Horn, C. F. Schwebdtfeger and E. P. Meagher, *Zeitschrift für Krist. - Cryst. Mater.*, 2014, **136**, 273–281.

Chapter 6: Cross chapter results and Future Work

This chapter briefly covers cross chapter tends which aren't explicitly covered in Chapters 3, 4 or 5.

1 $Ce_{1-x}Zr_xO_2$ trends

Chapters 3, 4 and 5 individually discuss various compositions of $Ce_{1-x}Zr_xO_2$ and compare the results of two or more treatments. This chapter addresses some of the cross compositional trends in lattice parameters, oxygen z coordinate and *a* / *c* ratios across the F800 treated $Ce_{1-x}Zr_xO_2$ samples which nominally all present as bulk solid solution materials when studied with X-ray or neutron Bragg diffraction.

Figure 6.1 shows the Rietveld refined parameters from the cerium zirconium oxides fired in air at 800 °C reported throughout this thesis. Lattice parameter trends across the F800 treated samples for the x = 0.25, 0.5 (industrially provided and alkoxide synthesised) and 0.75 compositions show close to linear trend, however inspection of the *a* / *c* ratio shows that the tetragonal distortion in the cation lattice is only present in the $Ce_{0.25}Zr_{0.75}O_2$ composition. The $Ce_{0.5}Zr_{0.5}O_2$ and $Ce_{0.75}Zr_{0.25}$ compositions studied show an approximate cubic lattice. The oxygen z coordinate displacement which breaks the cubic symmetry shows a clear linear trend across the full composition range studied, highlighting the importance of neutrons in this study as X-rays alone are insensitive oxygen cerium zirconium oxides where conclusions drawn solely from the cation lattice would entirely miss this duality.

Initial analysis of the neutron PDF data reveals a shifting towards the simulated phase pure ZrO_2 with higher Zr content. The $Ce_{0.5}Zr_{0.5}O_2$ and $Ce_{0.25}Zr_{0.75}O_2$ samples are evidently mixed phase, showing features of both cubic fluorite phase and the tetragonal ZrO_2 phase, most noticeable by the peak clusters at 4 Å and 10 Å. The $Ce_{0.75}Zr_{0.25}O_2$ material shows predominantly fluorite features indicating relative phase purity. One anomaly observed is the relative peak intensity of the first O-O peak across all datasets when compared with calculated intensities, it is clearly visible at ~2.6 Å.

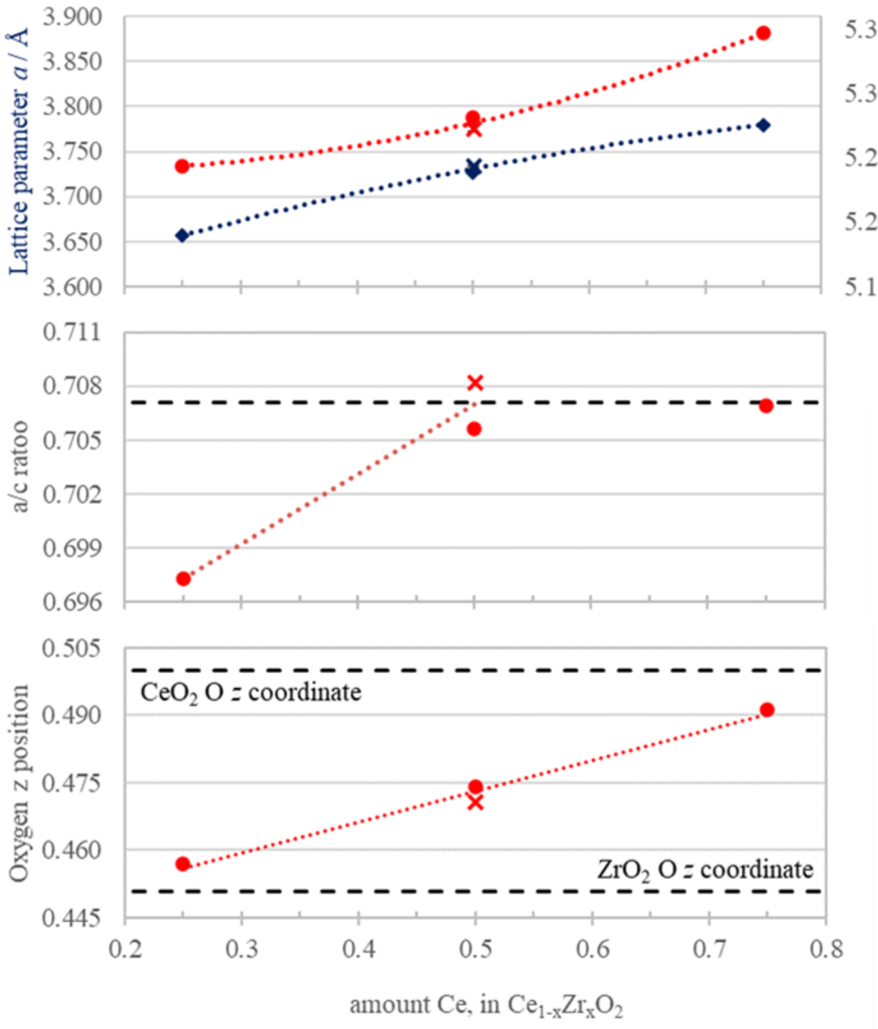

Figure 6.1: Rietveld refined parameters for x = 0.25, 0.5 and 0.75 in $Ce_{1-x}Zr_xO_2$ *discussed in Chapters 3, 4 and 5. Alkoxide synthesised sample marked as a X. Cubic a / c ratio for the* $P4_2/nmc$ *ceria zirconia structure marked in black dashed line. Oxygen z coordinates for cubic CeO2 and tetragonal ZrO2 labelled and marked for dashed black lines. Coloured dotted lines shown as guides to the eye.*

Figure 6.2 shows the neutron PDF patterns for the Johnson Matthey provided $Ce_{0.25}Zr_{0.75}O_2$, $Ce_{0.5}Zr_{0.5}O_2$ and $Ce_{0.75}Zr_{0.25}O_2$ F800 with simulated patterns for CeO_2 and ZrO_2. The visually observed trends in the n-PDF patterns show a gradual transition from a CeO_2 like structure to a ZrO_2 like structure with increasing Zr content. The first features at ~ 2.2 Å are particularly insightful showing sharp M-O bonds for the $Ce_{0.25}Zr_{0.75}O_2$ and $Ce_{0.75}Zr_{0.25}O_2$ with the $Ce_{0.5}Zr_{0.5}O_2$ feature showing what presents as a convolution of both. While these features are sharper than the simulated patterns, it is not uncommon in PDF data for the first atom-atom correlations to be sharper than the simulated model, this is due to the correlated motion of atoms resulting in a much sharper well-defined atom-atom distance for bonded atoms.

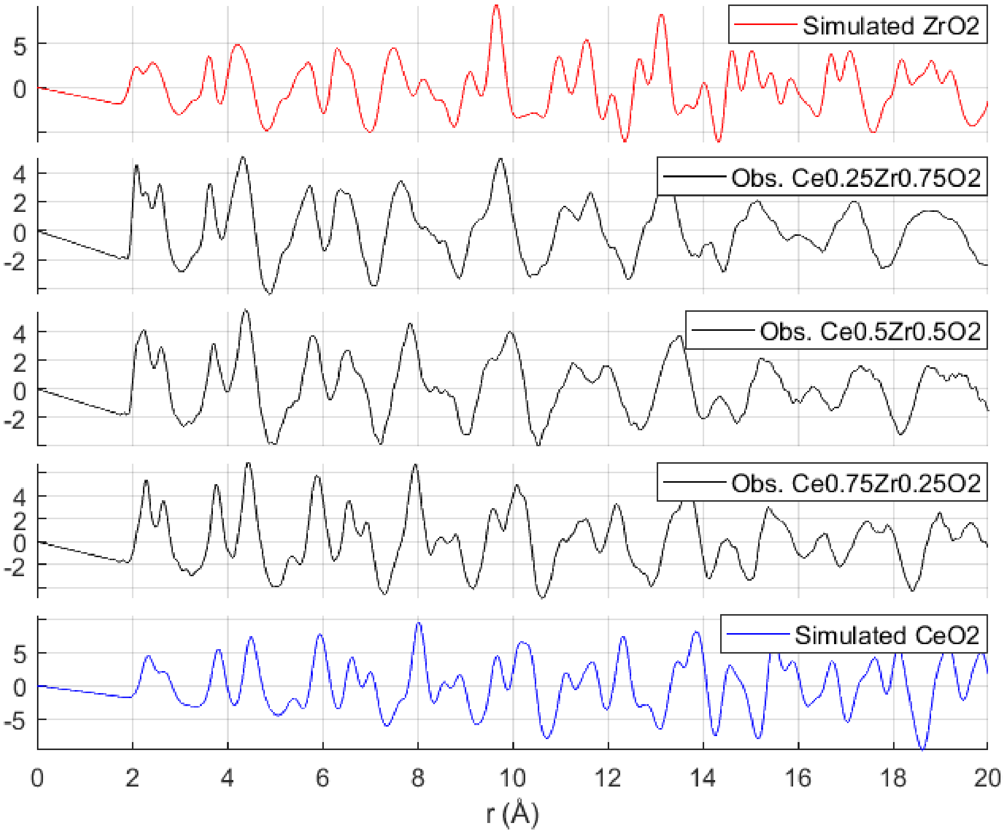

Figure 6.2: Observed and simulated neutron PDF data of various ceria zirconia compositions. Data acquired from the Polaris neutron diffractometer at the ISIS neutron and muon source.

Future work

Comprehensive reverse Monte Carlo studies have been completed across several ceria zirconia materials including the structurally challenging κ-$CeZrO_4$ phase highlighting the existence of interstitial oxygen in several of the samples studied, further work characterising oxygen defects in a range of ceria-zirconia materials would likely prove insightful.

Initial analysis of $Ce_{0.25}Zr_{0.75}O_2$ materials highlighted thermal instability under reducing conditions resulting in bulk phase segregation into clearly phase segregated compositionally different tetragonal and cubic ceria zirconia with some cation ordering when heated to 1050 °C. However a full study on a expanded compositional/synthesis route range of $Ce_{1-x}Zr_xO_2$ materials fired at 800 °C in air providing insight for characterising local preferred structures for otherwise apparently equivalent materials known to have variable properties based on synthesis route.

The Ce spiked TiO_2 samples discussed in chapter 5 show a linear effect on the a / c lattice parameter ratio and oxygen z coordinate of the bulk material as a function of added Ce content, showing that the added Ce has an impact on the bulk structural properties of the TiO_2. Firing these samples appears to have minimal impact on the observed Bragg diffraction, however the X-ray total scattering shows evidence of an amorphous contribution post firing. Employing the RMC method may yield insights into the local nature of the Ce prior to firing with a in-situ X-ray PDF study focusing on the temperatures leading up to 400 °C, easily attainable with use of capillaries and the Hot Air Blower at I15-1 being suitable to observe the formation of this near amorphous feature. Careful processing of the total scattering would be required due to the significant impact Ce content and the presence of broad diffuse scattering has on the obtained PDF's.

RMC modelling of a anatase TiO_2 supercell of sufficiently large scale (at least 80 Å in the lowest dimension) should lead to insights on the local nature of the Ce in the unfired samples and may provide useful insights in the fired samples with amorphous contributions, however careful consideration must be taken on how to characterise the tetragonal unit cell and quantify in a meaningful way, the local environments of the Ce present. The existing applications of the Clapp configuration analysis are limited to BCC or FCC arrangements of cations, and given the distinct difference in local coordination between CeO_2 and TiO_2 a novel analysis method would be required to extract meaning from even the most idealised supercell.

Further development of a solid understanding of the solid solution states of ceria zirconia would allow for the extension to Ti or rare earth doped cerium zirconium oxides which form a large portion of the research surrounded cerium zirconium oxides.

While the latest versions of RMCProfile have multiple phase comparability, the application of this is to describe two independent discrete large box models with no interaction, an assumption which loses accuracy when studying nano-crystalline materials.